

TRINITY COLLEGE DUBLIN  
School of Genetics and Microbiology  
Smurfit Institute of Genetics



**BLOOD-RETINA BARRIER REGULATION  
AND STERILE INFLAMMATION IN RETINAL  
HOMEOSTASIS AND DISEASE**

A thesis submitted to Trinity College Dublin, the University of Dublin for the  
degree of Doctor of Philosophy

**Lucia Celkova, M.Sc.**

2019

## DECLARATION

---

I declare that this thesis has not been submitted as an exercise for a degree at this or any other university and it is entirely my own work.

I agree to deposit this thesis in the University's open access institutional repository or allow the Library to do so on my behalf, subject to Irish Copyright Legislation and Trinity College Library conditions of use and acknowledgement.

I consent to the examiner retaining a copy of the thesis beyond the examining period, should they so wish (EU GDPR May 2018).



.....  
Lucia Celkova

## SUMMARY

---

Age-related macular degeneration (AMD) is the leading cause of central vision loss and blindness in the elderly and also the primary cause of visual impairment in industrialised countries. It results from the progressive loss of photoreceptor cells in the macula, a highly specialised region in the central retina responsible for high acuity and colour vision, and is thought to occur secondary to the damage of the underlying retinal pigment epithelium (RPE). Although the disease prevalence is expected to rise in the coming years, the current therapeutic strategies remain limited. Recently, AMD has been associated with a state of chronic local low-grade inflammation in the retina. Dichotomous roles for the NLRP3 inflammasome, a large multiprotein oligomeric complex of the innate immune response, and its effector cytokine IL-18 have been implicated in the disease development and progression, as being protective in the neovascular (wet) AMD and pathological in the non-neovascular (dry) AMD, respectively.

In the present study, the effects of systemic IL-18 administration were investigated in the JR5558 mouse strain, a novel genetic model of spontaneous retinal neovascularisation, as an alternative to the previously used laser-induced animal model of wet AMD. The JR5558 mice develop spontaneous chorio-retinal lesions accompanied by vascular leakage soon after birth, followed by a gradual decline in their number and severity. It was demonstrated that IL-18 could prevent progression of developing neovascular lesions as well as enhance regression of fully established lesions in this animal model, providing further evidence for its therapeutic potential in the treatment of wet AMD. In addition, the mechanism(s) by which IL-18 could exert its anti-angiogenic and anti-permeability functions were explored in a number of *in vivo* and *in vitro* assays. In line with previously published reports, IL-18 was found to regulate the secretion of vascular endothelial growth factor (VEGF), the main driver of the pathological changes observed in neovascular AMD as well as in the JR5558 mouse model. Furthermore, IL-18 could promote the wound-healing process in the RPE and controlled the expression of tight junction proteins in endothelial cells to regulate the paracellular transport.

It is now widely accepted that the inflammasome components are present in and around the RPE of AMD patients. This was confirmed by immunohistochemical staining of specimens from human donors diagnosed with geographic atrophy, the end-stage form of dry AMD. The role of the inflammasome complex and/or its effector cytokines IL-18 and IL-1 $\beta$  in retinal and RPE homeostasis, however, remains unclear. The RPE serves many important support functions to maintain the proper visual responses in the retina. Most importantly, it

is responsible for the upkeep of rod and cone photoreceptors by phagocytosing shed tips of their outer segments on daily basis. Studying the molecular changes in the RPE in response to photoreceptor outer segment (POS) phagocytosis *in vitro* and *in vivo*, a novel link has been established between the daily POS phagocytosis and inflammasome activation in the RPE as part of the normal RPE physiology. Exploiting serum starvation as the means of autophagy induction *in vitro*, it was observed that autophagy activation could slow down VEGF secretion by the RPE, suggesting that the POS phagocytosis might be an important regulator of VEGF synthesis in retinal homeostasis.

The inner blood-retina barrier (iBRB) has evolved in order to protect the delicate tissue of the retina from potential blood-borne toxicity and maintain healthy local microenvironment and homeostasis. The breakdown of the iBRB integrity has been associated with multiple blinding retinal conditions and several disease-related factors have been shown to modify the barrier properties to increase vascular leakage. The control of the iBRB permeability in normal retinal physiology, however, remains poorly understood.

Therefore, the regulation of the iBRB permeability in retinal homeostasis was addressed in a series of *in vivo* experiments, examining vascular leakage at 8 AM and 8 PM in several different mouse strains. It was observed that the iBRB is physiologically a very dynamic structure, with its barrier properties cycling periodically during the day. In addition, a model of physiological iBRB regulation was proposed whereby the iBRB permeability is under the control of circadian rhythms and can be modulated by local factors, such as IL-18 and/or VEGF. These findings not only provide more insight into the iBRB regulation in normal retinal homeostasis, but also have major clinical implications for drug delivery and development of new therapeutics for retinal diseases as well as provide a basis for novel approaches to modelling the disease pathology associated with geographic atrophy that would better reflect the phenotype observed in patients with dry AMD.

## ACKNOWLEDGEMENTS

---

First and foremost, my sincere gratitude goes to my supervisor Dr. Matt Campbell for giving me the fantastic opportunity of becoming a member of his team and working on this interesting project. I am very grateful for his professional guidance and help over the past 4 years. Matt truly is an inspirational leader and scientist and I much appreciate not only his academic advice, but also his patience and all the personal support he provided, especially towards the end of my PhD. I would also like to thank Dr. Sarah Doyle for her invaluable insights and expert advice on the immunology-related aspects of my project.

My thanks also belongs to all members of the Campbell lab, present and past, for their friendship, support and help during my time as a PhD student and for making the lab such an enjoyable and fun environment to work. Thanks Natalie, Ema, John, Chris, Eoin, Conor and Nicole!

I would also like to thank everyone in the Humphries and Farrar labs, ruling over the third floor of the Smurfit, for always being so helpful and friendly. Thanks to all the attendants and technicians in our animal unit, Charlie, Caroline, Dave and Monica, for being ready to answer all my queries. Thanks also to Brenda, Paul, Dave, Rachel and all the technical, administrative and support staff as well as everyone in the Department for making it the place it is.

Special thanks to my parents who kindled a spark of curiosity in me when I was but a small child, both in their own way, always encouraged me in all my endeavours and supported me in all the ways they could.

Last but not least, thanks to Lukas for his constant love and care, for sharing with me all the ups and downs of everyday life, supporting me in everything I do, no matter how big or small, and never giving up at trying to understand what my research is about. Thank you for all the laughs and joy that you bring to my life!

# TABLE OF CONTENTS

---

Declaration.....	ii
Summary .....	iii
Acknowledgements.....	v
List of figures .....	x
List of tables.....	xiii
List of abbreviations.....	xiv
<b>Chapter 1: General introduction .....</b>	<b>1</b>
1.1 Anatomy and physiology of the retina.....	2
1.1.1 Cellular and histological organisation of the retina.....	3
1.1.1.1 Photoreceptor layer.....	3
1.1.1.2 External limiting membrane .....	9
1.1.1.3 Outer nuclear layer .....	10
1.1.1.4 Outer plexiform layer .....	10
1.1.1.5 Inner nuclear layer .....	14
1.1.1.6 Inner plexiform layer .....	14
1.1.1.7 Ganglion cell layer.....	18
1.1.1.8 Nerve fibre layer.....	19
1.1.1.9 Internal limiting membrane .....	20
1.1.2 Glial cells of the retina .....	20
1.1.3 Retinal pigment epithelium .....	23
1.1.4 Blood supply of the retina .....	27
1.2 Blood-retina barrier.....	29
1.2.1 Transport across the BRB .....	30
1.2.2 Tight junctions.....	32
1.2.3 The neurovascular unit .....	32
1.3 Age-related macular degeneration .....	33
1.3.1 Prevalence and epidemiology of AMD .....	34
1.3.2 End-stage forms of AMD .....	35
1.3.3 Risk factors in AMD .....	35
1.3.4 Clinical hallmarks of AMD.....	35
1.3.4.1 Drusen deposition.....	36
1.3.4.2 Lipofuscin accumulation .....	37

1.3.4.3 RPE cell death .....	37
1.3.5 Current therapies for AMD .....	38
1.4 Sterile inflammation in AMD pathology .....	39
1.4.1 Immune privilege of the eye .....	39
1.4.2 Para-inflammation in the aging retina .....	40
1.4.3 The complement system.....	41
1.4.4 The NLRP3 inflammasome.....	41
1.4.4.1 Structure and assembly of the inflammasome complex .....	42
1.4.4.2 Activation of the inflammasome complex .....	42
1.4.4.3 Role in AMD pathology .....	44
1.4.5 Interleukin-18.....	47
1.4.5.1 Role in AMD pathology .....	47
1.5 Objectives .....	48
<b>Chapter 2: Materials and methods.....</b>	<b>50</b>
2.1 Buffer compositions.....	51
2.2 Animal studies .....	51
2.2.1 IL-18 administration in JR5558 mice .....	52
2.3 Cell culture and <i>in vitro</i> experiments.....	52
2.3.1 Cell counting procedure .....	53
2.3.2 IL-18 treatment.....	54
2.3.3 VEGF treatment .....	54
2.3.4 Inflammasome activation .....	54
2.3.5 POS treatment .....	55
2.3.6 Serum starvation.....	55
2.4 Protein analysis .....	55
2.4.1 Sample preparation and protein extraction .....	55
2.4.2 Bicinchoninic acid (BCA) assay .....	56
2.4.3 Sodium dodecyl sulphate polyacrylamide gel electrophoresis (SDS-PAGE).....	57
2.4.3.1 Pouring an SDS-PAGE gel.....	57
2.4.3.2 Preparing protein samples for SDS-PAGE .....	58
2.4.3.3 Running an SDS-PAGE gel .....	59
2.4.4 Western blotting.....	59
2.4.4.1 Semi-dry electrophoretic protein transfer.....	59
2.4.4.2 Immunodetecting proteins of interest .....	60

2.4.4.3 Western blot development and analysis .....	61
2.4.5 Enzyme-linked immunosorbent assay (ELISA).....	62
2.5 Gene expression analysis .....	64
2.5.1 Sample preparation.....	64
2.5.2 RNA extraction .....	64
2.5.3 Polymerase chain reaction (PCR) arrays.....	65
2.6 Histology and immunofluorescence staining.....	70
2.6.1 Paraffin-embedding and sectioning of mouse eyes.....	70
2.6.2 Haematoxylin and eosin (H&E) staining .....	70
2.6.3 RPE flatmount preparation and staining .....	71
2.6.4 Immunohistochemistry of human sections.....	72
2.7 Functional <i>in vitro</i> measurements .....	73
2.7.1 Cell viability assay .....	73
2.7.2 Wound-healing (scratch) assay .....	73
2.7.3 Transendothelial electrical resistance (TEER) measurement.....	74
2.8 Functional <i>in vivo</i> measurements.....	74
2.8.1 Fluorescein angiography (FA) imaging .....	74
2.8.2 Electroretinography (ERG) .....	75
2.9 Statistical analysis .....	76
<b>Chapter 3: IL-18 efficacy in a mouse model of spontaneous retinal neovascularisation and its mechanism of action .....</b>	<b>77</b>
3.1 Introduction.....	78
3.2 Results.....	80
3.2.1 Spontaneous neovascular lesions disrupt retinal architecture in JR5558 mice.....	80
3.2.2 IL-18 prevents progression and enhances regression of JR5558 lesions .....	82
3.2.3 IL-18 regulates VEGF secretion <i>in vivo</i> and <i>in vitro</i> .....	91
3.2.4 IL-18 promotes RPE wound-healing <i>in vitro</i> .....	95
3.2.5 IL-18 regulates tight junction protein expression in endothelial cells <i>in vitro</i> .....	95
3.3 Discussion .....	98
<b>Chapter 4: Diurnal processing of the NLRP3 inflammasome in RPE homeostasis ..</b>	<b>104</b>
4.1 Introduction.....	105
4.2 Results.....	106
4.2.1 Inflammasome components are present in human AMD tissue samples.....	106



4.2.2	Detection of inflammasome activation in the RPE <i>in vitro</i> .....	109
4.2.3	Molecular response of the RPE to POS phagocytosis <i>in vivo</i> and <i>in vitro</i> .....	113
4.2.4	Serum starvation regulates VEGF production by the RPE <i>in vitro</i> .....	125
4.3	Discussion .....	128
<b>Chapter 5: Regulation of the inner blood-retina barrier in retinal homeostasis.....</b>		<b>131</b>
5.1	Introduction.....	132
5.2	Results.....	135
5.2.1	VEGF regulates endothelial barrier properties <i>in vitro</i> .....	135
5.2.2	Functional changes in the iBRB permeability at 8 AM and 8 PM <i>in vivo</i> .....	136
5.2.3	IL-18 regulates the iBRB permeability <i>in vivo</i> .....	139
5.2.4	The iBRB permeability cycling is under circadian control.....	153
5.3	Discussion .....	160
<b>Chapter 6: General discussion and future perspectives.....</b>		<b>164</b>
6.1	Therapeutic potential of IL-18 in neovascular AMD .....	165
6.2	A novel link between POS phagocytosis and inflammasome activation in the RPE ..	167
6.3	Circadian regulation of the iBRB permeability in retinal homeostasis .....	168
References.....		172
Appendix		

## LIST OF FIGURES

---

Figure 1.1: Cellular and histological organisation of the retina.....	4
Figure 1.2: Support functions of the retinal pigment epithelium (RPE).....	24
Figure 1.3: Blood supply of the retina .....	28
Figure 1.4: Components of the blood-retina barrier .....	31
Figure 1.5: Mechanism of the NLRP3 inflammasome complex formation.....	43
Figure 1.6: The NLRP3 inflammasome controversy in AMD pathology.....	46
Figure 3.1: Effect of spontaneous neovascular lesion development on retinal architecture in JR5558 mice.....	81
Figure 3.2: Detection of spontaneous chorio-retinal lesions in JR5558 mice .....	81
Figure 3.3: Detection of vascular leakage sites in JR5558 mice .....	82
Figure 3.4: Development of vascular leakage sites in JR5558 mice over time .....	83
Figure 3.5: IL-18 in the progression of developing JR5558 vascular leakage sites .....	85
Figure 3.6: IL-18 in the progression of developing JR5558 chorio-retinal lesions .....	86
Figure 3.7: IL-18 in the regression of established JR5558 vascular leakage sites.....	87
Figure 3.8: IL-18 in the regression of established JR5558 chorio-retinal lesions .....	88
Figure 3.9: Effect of IL-18 on rod function in JR5558 mice .....	89
Figure 3.10: Effect of IL-18 on cone function in JR5558 mice .....	90
Figure 3.11: Effect of IL-18 on VEGF production in the JR5558 retina.....	92
Figure 3.12: Effect of IL-18 on VEGF production <i>in vitro</i> in hFRPE cells .....	93
Figure 3.13: Effect of IL-18 on RPE cell viability <i>in vitro</i> .....	94
Figure 3.14: Effect of IL-18 on RPE wound-healing <i>in vitro</i> (representative images) .....	96
Figure 3.15: Effect of IL-18 on RPE wound-healing <i>in vitro</i> (quantification).....	97
Figure 3.16: Effect of IL-18 on tight junction protein expression <i>in vitro</i> in bEnd.3 cells ..	98
Figure 4.1: Inflammasome components in healthy and GA-affected human maculae.....	108
Figure 4.2: Inflammasome effector cytokines in healthy and GA-affected human maculae ..	109
.....	
Figure 4.3: Effect of standard inflammasome activation on RPE protein secretion <i>in vitro</i> ...	110
.....	
Figure 4.4: Detection of inflammasome components intracellularly <i>in vitro</i> in hFRPE cells..	111
.....	
Figure 4.5: Effect of extended inflammasome activation on RPE cell viability <i>in vitro</i> ...	112

Figure 4.6: Autophagy gene expression in the RPE <i>in vivo</i> at 8 PM relative to 8 AM .....	114
Figure 4.7: Inflammasome gene expression in the RPE <i>in vivo</i> at 8 PM relative to 8 AM.....	117
Figure 4.8: Patterns of IL-18 and caspase-1 expression in the RPE <i>in vivo</i> at 8 AM and 8 PM.....	120
Figure 4.9: Autophagy gene expression in response to POS treatment <i>in vitro</i> in hFRPE cells .....	121
Figure 4.10: IL-18 secretion in response to POS treatment <i>in vitro</i> in hFRPE cells.....	124
Figure 4.11: Effect of serum starvation on VEGF production <i>in vitro</i> in hFRPE cells.....	126
Figure 4.12: Effect of serum starvation on RPE cell viability <i>in vitro</i> .....	127
Figure 4.13: Effect of serum starvation on endothelial cell viability <i>in vitro</i> .....	128
Figure 5.1: Feedback loops of the mammalian core circadian genes .....	134
Figure 5.2: Effect of VEGF on endothelial electrical resistance <i>in vitro</i> in bEnd.3 cells..	137
Figure 5.3: Effect of VEGF on tight junction protein expression <i>in vitro</i> in bEnd.3 cells.....	138
Figure 5.4: Dynamic FA profiling <i>in vivo</i> in C57BL/6J mice at 8 AM versus 8 PM.....	140
Figure 5.5: The iBRB permeability <i>in vivo</i> in C57BL/6J mice at 8 AM versus 8 PM.....	141
Figure 5.6: Partial dynamic FA profiles <i>in vivo</i> in age-stratified C57BL/6J mice at 8 AM and 8 PM.....	142
Figure 5.7: The iBRB permeability <i>in vivo</i> in age-stratified C57BL/6J mice at 8 AM.....	143
Figure 5.8: The iBRB permeability <i>in vivo</i> in age-stratified C57BL/6J mice at 8 PM.....	144
Figure 5.9: Partial dynamic FA profiles <i>in vivo</i> in 129 mice at 8 AM versus 8 PM .....	145
Figure 5.10: The iBRB permeability <i>in vivo</i> in 129 mice at 8 AM versus 8 PM .....	146
Figure 5.11: Partial dynamic FA profiles <i>in vivo</i> in CD1 mice at 8 AM versus 8 PM.....	147
Figure 5.12: The iBRB permeability <i>in vivo</i> in CD1 mice at 8 AM versus 8 PM.....	148
Figure 5.13: Partial dynamic FA profiles <i>in vivo</i> in <i>Il18</i> <sup>-/-</sup> mice at 8 AM versus 8 PM ....	149
Figure 5.14: The iBRB permeability <i>in vivo</i> in <i>Il18</i> <sup>-/-</sup> mice at 8 AM versus 8 PM .....	150
Figure 5.15: Effect of IL-18 on the iBRB permeability <i>in vivo</i> at 8 AM .....	151
Figure 5.16: Effect of IL-18 on the iBRB permeability <i>in vivo</i> at 8 PM.....	152
Figure 5.17: Partial dynamic FA profiles <i>in vivo</i> in <i>Bmal1</i> <sup>fl/fl</sup> Tie2-Cre <sup>+</sup> mice at 8 AM and 8 PM.....	154
Figure 5.18: The iBRB permeability <i>in vivo</i> in <i>Bmal1</i> <sup>fl/fl</sup> Tie2-Cre <sup>+</sup> mice at 8 AM versus 8 PM.....	155

Figure 5.19: Partial dynamic FA profiles *in vivo* in *Bmal1*<sup>wt/fl</sup> Tie2-Cre<sup>+</sup> mice at 8 AM and 8 PM..... 156

Figure 5.20: The iBRB permeability *in vivo* in *Bmal1*<sup>wt/fl</sup> Tie2-Cre<sup>+</sup> mice at 8 AM versus 8 PM..... 157

Figure 5.21: Effect of *Bmal1* gene copy number on iBRB permeability *in vivo* at 8 AM..... 158

Figure 5.22: Effect of *Bmal1* gene copy number on iBRB permeability *in vivo* at 8 PM ..... 159

## LIST OF TABLES

---

Table 1.1: Structural and functional differences between retinal rods and cones .....	6
Table 2.1: Preparation of protein standards in the BCA assay protocol.....	57
Table 2.2: SDS-PAGE resolving (separating) and stacking gel composition (per 1 gel)....	58
Table 2.3: Antibodies used for Western blotting .....	61
Table 2.4: Specifications of the ELISA kits' component reagents .....	63
Table 2.5: Mouse and human RT <sup>2</sup> Profiler PCR autophagy array genes.....	68
Table 2.6: Mouse RT <sup>2</sup> Profiler PCR inflammasome array genes .....	69
Table 2.7: Tissue processing treatments during paraffin-embedding of mouse eyes .....	70
Table 2.8: Antibodies used for immunofluorescence and immunohistochemistry.....	72
Table 4.1: Autophagy gene expression in the RPE <i>in vivo</i> at 8 PM relative to 8 AM .....	116
Table 4.2: Inflammasome gene expression in the RPE <i>in vivo</i> at 8 PM relative to 8 AM .....	119
Table 4.3: Autophagy gene expression in response to POS treatment <i>in vitro</i> in hRPE cells .....	123

## LIST OF ABBREVIATIONS

---

4-PL	four-parameter logistic
A2E	<i>N</i> -retinylidene- <i>N</i> -retinylethanolamine
AAV	adeno-associated virus
ABC	avidin biotin complex
ABCA4	ATP-binding cassette subfamily A member 4
AIM2	absent in melanoma 2
AMD	age-related macular degeneration
AMPA	$\alpha$ -amino-3-hydroxy-5-methyl-4-isoxazolepropionic acid
Ang-1	angiopoietin-1
ANOVA	analysis of variance
AP-1	activator protein 1
APS	ammonium persulphate
ARVO	Association for Research in Vision and Ophthalmology
ASC	apoptosis-associated speck-like protein containing a CARD
ATCC	American Type Culture Collection
ATP	adenosine triphosphate
BBB	blood-brain barrier
BCA	bicinchoninic acid
bEnd.3	mouse brain endothelial cell line
bFGF	basic fibroblast growth factor
bPOS	bovine photoreceptor outer segment
BRB	blood-retina barrier
BSA	bovine serum albumin
cGMP	cyclic guanosine monophosphate
CARD	caspase recruitment domain
CC	choriocapillaris
CD	cluster of differentiation
CEP	carboxyethyl pyrrole
CFH	complement factor H
CNS	central nervous system
CNTF	ciliary neurotrophic factor
CNV	choroidal neovascularisation
CRALBP	cellular retinal-binding protein

CRBP	cellular retinol-binding protein
DAMP	danger/damage-associated molecular pattern
DMEM	Dulbecco's modified Eagle medium
DNA	deoxyribonucleic acid
DPBS	Dulbecco's phosphate-buffered saline
DTT	dithiothreitol
ECL	enhanced chemiluminescence
EDTA	ethylenediaminetetraacetic acid
ELISA	enzyme-linked immunosorbent assay
ELM	external limiting membrane
ERG	electroretinography
FA	fluorescein angiography
FAK	focal adhesion kinase
FAZ	foveal avascular zone
FasL	Fas ligand
FBS	foetal bovine serum
FGF	fibroblast growth factor
FMB	flat midget bipolar
G <sub>β5L</sub>	long splice variant of the type 5 G protein β subunit
GA	geographic atrophy
GABA	γ-aminobutyric acid
GAP	GTPase-activating protein, GTPase-accelerating protein
GC	guanylate cyclase
GCAP	GC-activating protein
GCL	ganglion cell layer
GDNF	glial-derived neurotrophic factor
GDP	guanosine diphosphate
GMP	guanosine monophosphate
GPCR	G protein-coupled receptor
GRK1	GPCR kinase 1
GS-IB <sub>4</sub>	Griffonia-simplicifolia-IB <sub>4</sub>
GSK	GlaxoSmithKline
GTP	guanosine triphosphate
H&E	haematoxylin and eosin
hfRPE	human foetal RPE

HRP	horseradish peroxidase
HSA	human serum albumin
iBRB	inner blood-retina barrier
IGF-1	insulin-like growth factor 1
IgG	immunoglobulin G
iGluR	ionotropic glutamate receptor
IL	interleukin
IL-18BP	IL-18-binding protein
ILM	internal (inner) limiting membrane
IMB	invaginating midget bipolar
INL	inner nuclear layer
INS	inner segment
i.p.	intraperitoneal, intraperitoneally
IPC	interplexiform cell
IPL	inner plexiform layer
ipRGC	intrinsically photosensitive retinal ganglion cell
IRAK	interleukin-1 receptor associated kinase
IRBP	interphotoreceptor retinol-binding protein
IRF	interferon regulatory factor
JAM	junctional adhesion molecule
LAP	LC3-associated phagocytosis
LGN	lateral geniculate nucleus
LPS	lipopolysaccharide
LRAT	lecithin retinol acyltransferase
LRR	leucine-rich repeat
MAC	membrane attack complex
MAPK	mitogen-activated protein kinase
MEM- $\alpha$	minimum essential medium Eagle, alpha modification
MerTK	proto-oncogene tyrosine-protein kinase MER
MFG-E8	milk fat globule-EGF factor 8
mGluR	metabotropic glutamate receptor
mRNA	messenger ribonucleic acid
MSA	mouse serum albumin
MyD88	myeloid differentiation primary response 88
NACHT	NAIP, CIITA, HET-E and TP1 domain (nucleotide-binding domain)



NADP	nicotinamide adenine dinucleotide
NADPH	nicotinamide adenine dinucleotide phosphate
NF- $\kappa$ B	nuclear factor kappa-light-chain-enhancer of activated B cells
NFL	nerve fibre layer
NGS	normal goat serum
NLR	NOD-like receptor
NLRP	NACHT, LRR and PYD domains-containing protein
NMDA	<i>N</i> -methyl-D-aspartate
NOD	nucleotide-binding oligomerisation domain
NRV2	neoretinal vascularisation 2
NVU	neurovascular unit
oBRB	outer blood-retina barrier
OLM	outer limiting membrane
ON	optic nerve head
ONL	outer nuclear layer
OPL	outer plexiform layer
OPN	olivary pretectal nucleus
OS	outer segment
PACAP	pituitary adenylate cyclase-activating polypeptide
PAGE	polyacrylamide gel electrophoresis
PAMP	pathogen-associated molecular pattern
PBS	phosphate-buffered saline
PBS-T	PBS containing 0.05% (v/v) Triton <sup>TM</sup> X-100
PCR	polymerase chain reaction
PDE	phosphodiesterase
PDGF	platelet-derived growth factor
PEDF	pigment epithelium-derived factor
PFA	paraformaldehyde
POS	photoreceptor outer segment
PR	photoreceptors
PVDF	polyvinylidene difluoride
PYD	pyrin domain
PRR	pattern recognition receptor
R9AP	RGS9-1 anchor protein
RDH	retinol dehydrogenase

RGS	regulator of G protein signalling
RHT	retinohypothalamic tract
RIPA	radioimmunoprecipitation assay
RIPK	receptor-interacting serine/threonine-protein kinase
RNA	ribonucleic acid
RNAi	RNA interference
ROS	reactive oxygen species
RPE	retinal pigment epithelium
RPE65	RPE-specific 65 kDa protein
rpm	revolutions per minute
S1P1	sphingosine-1-phosphate-1
s.c.	subcutaneous, subcutaneously
SC	superior colliculus
SCN	suprachiasmatic nucleus
SDS	sodium dodecyl sulphate
SEM	standard error of the mean
siRNA	short interfering RNA
SNP	single nucleotide polymorphism
SPF	specific pathogen-free
TBS	Tris-buffered saline
TBS-T	TBS containing Tween <sup>®</sup> 20
TCD	Trinity College Dublin
TEER	transendothelial electrical resistance
TEMED	<i>N,N,N',N'</i> -tetramethylethylenediamine
TGF- $\beta$	transforming growth factor beta
TIMP	tissue inhibitor of metalloproteinases
TLR	toll-like receptor
TMB	3,3',5,5'-tetramethylbenzidine
TRP	transient receptor potential
VEGF	vascular endothelial growth factor
VEGFR	VEGF receptor
WHO	World Health Organisation
ZO	zonula occludens

## Chapter 1

### **General introduction**

# 1 GENERAL INTRODUCTION

---

## 1.1 Anatomy and physiology of the retina

The retina is a multilayered light-sensitive structure at the back of the eye capable of detecting light stimuli and converting them into electrical signals that are transmitted into the visual centre of the brain, where the information is processed and a visual image is formed. Being a part of the central nervous system (CNS), it originates from the neural tube during embryonic development (similar to other CNS regions) and as such represents the only part of the CNS that is easily accessible to examination and can be visualised non-invasively (Kolb, 2005a; Hildebrand and Fielder, 2011). The human retina is a circular disc of 30-40 mm in diameter and has an area of approximately 1100 mm<sup>2</sup> (Kolb, 2005b; Kolb, 2005c).

A highly specialised, oval-shaped region near the centre of the retina is referred to as the macula. It is approximately 4.5-6 mm in diameter, making up less than 4% of the entire retina (Hildebrand and Fielder, 2011), and is unique to humans and primates. This central area is characterised by an increased density of cone photoreceptors compared to the peripheral retina, thus being responsible for the central, high-resolution, colour vision. In addition, it is histologically distinct from the peripheral retina by comprising more than a single layer of ganglion cells (Forrester et al., 2008, p.42). The presence of carotenoid pigments, xanthophylls and carotenes, gives the macula its characteristic yellowish appearance and is therefore commonly known as the "yellow spot".

The number of cone photoreceptors increases towards the centre of the macula and the rod-cone ratio is reduced. The area of central depression, known as the fovea, is entirely cone-dominated, with the cone photoreceptors being more closely spaced and the rods fewer in number (Kolb, 2005b). The fovea is approximately 1.5 mm in diameter and is located around 3 mm temporal to the optic disc edge (Kolb, 2005c; Forrester et al., 2008, p.42; Hildebrand and Fielder, 2011). A flat depression in its centre, known as the foveola (or the foveal pit), is an area of about 0.35 mm in diameter populated almost entirely by cone photoreceptors (and some Müller cells), with the exclusion of rods and other cell types (Gass, 1999; Forrester et al., 2008, p.42; Hildebrand and Fielder, 2011). The foveolar cones are arranged at their most efficient packing density (a hexagonal mosaic) and become narrowed and elongated to further enhance light detection (Curcio et al., 1990; Kolb, 2005b). Thus, this area represents the retinal site of maximum visual acuity under photopic (bright light) conditions, while the absence of rods renders it functionally blind under extreme scotopic (dim light) conditions.

Due to functional differences in various parts of the retina, the overall retinal thickness is region-dependent and ranges from 150-200  $\mu\text{m}$  in the foveola to 320-400  $\mu\text{m}$  at the edge of the fovea, with a rapid gradual thinning towards the periphery and thickness of only 80-120  $\mu\text{m}$  in the far periphery (Kolb, 2005b; Kolb 2005c).

### *1.1.1 Cellular and histological organisation of the retina*

The mammalian retina consists of more than 50 different cell types, each having various specific functions (Masland, 2001). These are arranged in a highly organised manner, giving the retina its characteristic multilayered laminar architecture (Figure 1.1). The functional synapses between cells are formed almost exclusively in two plexiform layers, while the cell bodies (perikarya) containing nuclei are distributed in three nuclear layers. Underlying the neurosensory retina is the retinal pigment epithelium (RPE) that serves multiple important supportive roles to maintain functionality of the neuronal cells.

#### 1.1.1.1 Photoreceptor layer

The photoreceptor layer contains the inner and outer segments of photoreceptors and is the only light-sensitive part of the retina, with all other retinal layers collectively serving to process and transmit signals from this layer. It is the site of visual phototransduction, a process by which light is biologically converted into an electrical signal in photoreceptors. The retina contains two main types of photoreceptor cells, namely rods and cones, that share a common general structure (Table 1.1). On average, there are approximately 4.6-6.5 million cones and 92-115 million rods in the human retina (Osterberg, 1935; Curcio et al., 1990). As already alluded to, the density of rods and cones varies in different regions of the retina, the periphery being rod-dominated, while the cone density increases in the macula, with the foveola consisting exclusively of cones. Rods are generally longer (100-120  $\mu\text{m}$ ) and more slender than cones which are shorter (60-75  $\mu\text{m}$ ) and wider. Rods function best under scotopic conditions, confer achromatic (black-and-white) and peripheral vision, are important for sensing contrast, brightness and motion, and are responsible for night vision, their loss resulting in night blindness. On the other hand, cones are used mainly under photopic conditions, support perception of colour and central vision, are responsible for fine and spatial resolution, and their loss is associated with legal blindness (Forrester et al., 2008, p.43-47; Hildebrand and Fielder, 2011).

Each photoreceptor consists of an outer segment and an inner segment connected by a modified non-motile cilium, a cell body containing the nucleus, an inner fibre (analogous to an axon) and a synaptic terminal (rod spherule or cone pedicle).

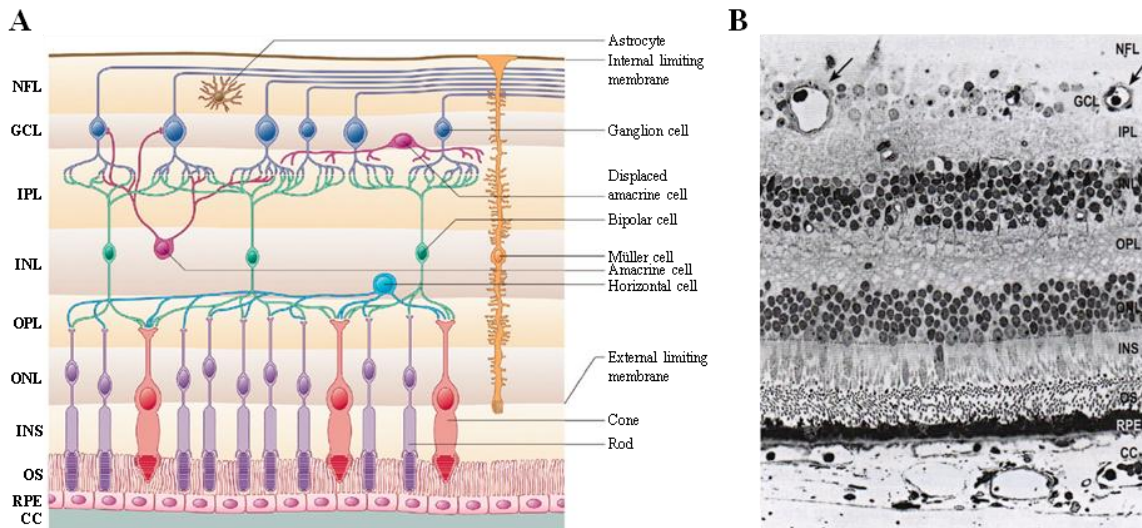


**Figure 1.1:** Cellular and histological organisation of the retina.

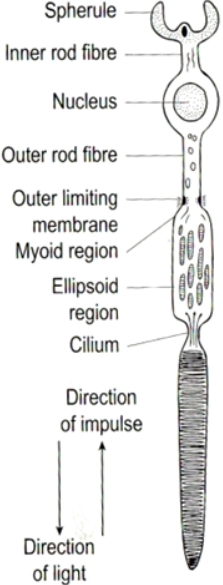
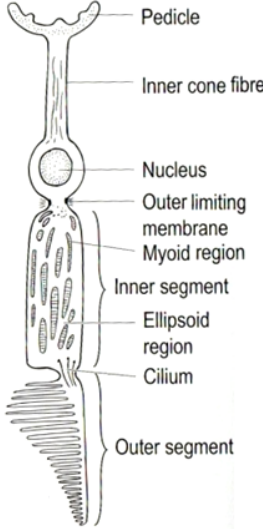
**A.** A diagrammatic representation of the general retinal anatomy, highlighting the characteristic architecture of the retina with the main cellular components arranged in an organised manner into several distinct layers. *From Hildebrand and Fielder (2011).* **B.** A low-power micrograph of the human retina (wax histology), showing the distinct multilayered organisation of cells in the retina, including retinal blood vessels (arrows). Magnification, 150x. *From Forrester et al. (2008), p.41.*

CC, choriocapillaris; RPE, retinal pigment epithelium; OS, outer segment; INS, inner segment; ONL, outer nuclear layer; OPL, outer plexiform layer; INL, inner nuclear layer; IPL, inner plexiform layer; GCL, ganglion cell layer; NFL, nerve fibre layer.

The photoreceptor outer segments (POSs) are structures densely filled with discs of folded double membranes that contain the light-sensitive visual pigment molecules responsible for absorption of light and initiation of the neuroelectrical impulse. The outer segment discs originate from outpouching of the plasma membrane at the base of the cilium (Young, 1967; Steinberg et al., 1980) and their main function is to increase the effective surface area of light detection by photopigments. In rods, these expanding membranes become detached as free floating discs enclosed by the outer segment plasma membrane. In cones, however, the discs remain attached to the plasma membrane throughout the extent of the outer segment and thus are in free communication with the extracellular space, allowing a rapid flux of substances between the outer segment and the interphotoreceptor matrix. Structurally, cone outer segments are shorter than rods and more conical, with a wider base and tapering shape. Although the photoreceptor cells do not divide, their outer segment

discs are constantly renewed. The newly formed discs mature with their distal migration along the length of the outer segment, with the oldest discs shed at the distal tips, phagocytosed by the apical processes of the RPE and subsequently degraded inside the RPE (Young, 1967; Young and Bok, 1969). The process of photoreceptor renewal is similar in rods and cones and occurs in a diurnal manner, controlled by opposing actions of endogenous dopamine and melatonin as light and dark signals, respectively (Nguyen-Legros and Hicks, 2000). A burst of rod disc shedding is observed at light onset in the morning, accompanied by an increased number of phagosomes in the RPE shortly after. Interestingly, cone outer segment discs are phagocytosed at a different time in the diurnal cycle compared with rods, peaking at light offset in the evening. The complete replacement of a rod outer segment takes about 9-10 days, while cone outer segments are much more stable and have a greater life span (Young, 1971; LaVail, 1976; Young, 1976; Steinberg et al., 1977; Besharse, 1982). The visual pigment molecules embedded within the outer segment disc membranes are composed of a light-sensitive chromophore 11-*cis* retinal (a vitamin A derivative), covalently linked to an integral transmembrane protein opsin that anchors the complex in the disc membrane. Rods are characterised by the presence of a single type of opsin, known as rhodopsin, sensitive to blue-green light of maximal spectral sensitivity at 496 nm. Cones, on the other hand, contain three types of spectrally distinct photopsins (also called cone opsins). Based on their sensitivity, three types of cones are generally distinguished in humans and are referred to as blue, green and red (or the short, medium and long wavelength-sensitive) cones, with maximum absorption in humans at 419 nm, 531 nm and 558 nm, respectively. Among the three cone photoreceptors, L-cones (63% or 2.9 million) are generally more common than M-cones (32% or 1.4 million) and S-cones (5% or 0.2 million), although their relative proportion is subject to a significant individual variability (Kolb, 2005d; Forrester et al., 2008, p.47 and p.241-242; Hildebrand and Fielder, 2011).

The photoreceptor inner segments contain the cellular machinery necessary to meet the high metabolic demands of the photoreceptor cells associated with phototransduction. The outer portion of an inner segment (ellipsoid) is packed with long thin mitochondria producing ATP by oxidative phosphorylation, while the inner portion (myoid) contains smooth and rough endoplasmic reticulum, Golgi apparatus, ribosomes, glycogen and microtubules to facilitate protein synthesis, metabolic activity and intracellular transport. Importantly, a visual pigment component opsin is synthesised in the endoplasmic reticulum and Golgi apparatus of the photoreceptor inner segment and transported in protein-rich vesicles through the connecting cilium, which acts as a conduit for metabolites and lipids

RODS	CONES
More numerous (92-115 million)	Less numerous (4.6-6.5 million)
Long (100-120 $\mu\text{m}$ ) and slender	Shorter (60-75 $\mu\text{m}$ ) and wider
Dominant in the peripheral retina	Dominant in the central retina (macula and fovea)
Not present in the foveola	Concentrated in the foveola
Function best under scotopic (dim light) conditions	Function best under photopic (bright light) conditions
Peripheral vision	Central vision
Achromatic (black-and-white) vision	Colour vision
Loss causes night blindness	Loss causes legal blindness
Plasma membrane-enclosed free floating discs	Discs attached to the plasma membrane
A single type of opsin (rhodopsin)	Three spectrally distinct photopsins (cone opsins)
Very sensitive to light	Less sensitive to light
Slow response time	Fast response time
	

**Table 1.1:** Structural and functional differences between retinal rods and cones.

A table summarising the main anatomical and physiological differences between rods and cones, the two main types of photoreceptor cells found in the retina. Although these photoreceptors share a common general structure, their unique characteristic features are highlighted in the diagrammatic representation of their anatomy. *Adapted from Kandel et al. (2000) and Forrester et al. (2008), p.46.*



between the inner and outer segment, to become integrated in the outer segment disc membrane. Thus, any metabolic disturbances or genetic mutations in the photoreceptors may lead to disturbances in visual pigment assembly or photoreceptor membrane (lipid) synthesis and therefore specific visual abnormalities (Kolb, 2005d; Forrester et al., 2008, p.47; Hildebrand and Fielder, 2011).

Phototransduction refers to a series of intracellular signalling events inside photoreceptor cells triggered by the absorption of light, leading to the generation of an electrochemical response (changes in the membrane potential and neurotransmitter release) carried across the retina into the brain for processing and interpretation. Photoreceptors are unique in that they respond to a light stimulus by hyperpolarisation rather than depolarisation typical for other neuronal cell types<sup>1</sup>. In the absence of light (i.e. in their resting state), photoreceptors exist in a depolarised state mediated by a steady influx of Na<sup>+</sup> and Ca<sup>2+</sup> into the cell via cGMP-gated cation channels in the plasma membrane of the outer segment, maintaining a so-called dark current. Following light absorption, 11-*cis* retinal in the outer segment disc membrane undergoes isomerisation to all-*trans* retinal, this transition being the only light-dependent step during vision. This, in turn, causes a conformational change in the structure of the surrounding opsin molecule, initiating a downstream signal transduction cascade that eventually leads to the closure of cGMP-gated cation channels in the outer segment plasma membrane. Opsin belongs to the family of G protein-coupled receptors (GPCRs) and once activated, it binds to its G protein partner transducin, catalysing the exchange of GDP for cytoplasmic GTP in its  $\alpha$  subunit. This activated, GTP-bound,  $\alpha$  subunit of transducin subsequently dissociates from the  $\beta$  and  $\gamma$  subunits and binds to inhibitory  $\gamma$  subunits of cGMP phosphodiesterase (PDE), preventing them from blocking the catalytic sites on PDE  $\alpha$  and  $\beta$  subunits, thus allowing them to catalyse the conversion (hydrolysis) of cGMP to 5'-GMP. Decreased availability of the intracellular cGMP results in the closure of cGMP-gated cation channels in the outer segment plasma membrane, stopping the inward current of Na<sup>+</sup> and Ca<sup>2+</sup>. This subsequently leads to hyperpolarisation of the photoreceptor and generation of an electrical response. The degree of hyperpolarisation is dependent on the amount of photon absorption per unit time and the intensity of the response is directly proportional to the number of transducin molecules that become activated. Generally, rods are more sensitive and can detect lower light levels than cones. Interestingly, fully dark-adapted rods are capable of detecting a single light photon, unlike cones that need much more light to hyperpolarise and elicit a comparable electrical signal. However, cones are

---

<sup>1</sup> Depolarisation (sometimes referred to as hypopolarisation) is a change in a cell's membrane potential, i.e. a shift in the electric charge distribution between the internal and external environment of the cell, that makes it more positive. Hyperpolarisation, on the other hand, results in a more negative charge inside the cell.

characterised by very fast kinetics of phototransduction, whereas rods are known to have a much slower response time following light stimulation. In addition, the generation of an electrical response after absorption of light is possible thanks to an extensive biochemical amplification of the molecular cascade involved in phototransduction. This amplification is achieved by activation of around 100-300 transducin molecules by a single activated opsin, hydrolysis of approximately 600-1000 cGMP molecules by a single molecule of PDE and a further 3-fold amplification of channel opening by one cGMP molecule (Kolb, 2005d; Forrester et al., 2008, p.244 and p.251-253; Fu, 2010; Hildebrand and Fielder, 2011). Clearly, it is vital that such a potent amplification mechanism can rapidly be switched off so that a photoreceptor can respond to the next phototransduction event and signal rapid changes in illumination. The recovery from light requires an efficient inactivation of each of the activated components in the phototransduction cascade, an efficient regeneration of opsin and a rapid restoration of the intracellular cGMP concentration. Activated opsin is phosphorylated by rhodopsin kinase, also known as GPCR kinase 1 (GRK1), on multiple C-terminal serine/threonine residues, which reduces its binding affinity for transducin, thus partially inhibiting transducin activation and decreasing opsin activity. Furthermore, phosphorylated opsin is rapidly recognised and bound by arrestin (S-antigen), capping its residual catalytic activity, thereby completely deactivating opsin, inhibiting downstream signalling and terminating the phototransduction cascade (Wilden et al., 1986; Kühn and Wilden, 1987). Transducin is inactivated when GTP bound to its  $\alpha$  subunit is hydrolysed to GDP, causing the GDP-bound  $\alpha$  subunit to dissociate from PDE  $\gamma$  subunits, bind once again to transducin  $\beta\gamma$  dimer and re-form the inactive heterotrimeric G protein complex. This allows the PDE  $\gamma$  subunits to re-exert their inhibition on the catalytic  $\alpha$  and  $\beta$  subunits, preventing cGMP hydrolysis. In addition, binding of GDP to the transducin  $\alpha$  subunit increases its affinity for the catalytic  $\alpha$  and  $\beta$  subunits of PDE, leading to a conformational change in the PDE structure that results in the inhibition of its cGMP hydrolytic capacity (Kroll et al., 1989). Although transducin does possess a slow intrinsic GTPase activity, the rate of GTP hydrolysis is substantially increased by a GTPase-accelerating protein (GAP) complex containing the regulator of G protein signalling (RGS) 9-1, the long splice variant of the type 5 G protein  $\beta$  subunit ( $G_{\beta 5L}$ ) and RGS9-1 anchor protein (R9AP) (He et al., 1998; Makino et al., 1999; Hu and Wensel, 2002). Despite RGS9-1 being the only one that directly facilitates GTP hydrolysis, the other two components of the GAP complex are required to provide stability and membrane anchoring (Chen et al., 2000; Chen et al., 2003; Keresztes et al., 2004). Interestingly, increasing the intrinsic GTPase activity of transducin by the R9AP-RGS9-1- $G_{\beta 5L}$  complex is the rate-limiting step in the photoreceptor recovery

response (Krispel et al., 2006) and is further enhanced by  $\gamma$  subunits of the effector enzyme PDE, possibly through its ability to increase the affinity between transducin and RGS9-1 (Angleon and Wensel, 1994; He et al., 1998; Skiba et al., 2000). In fact, an efficient transducin inactivation is dependent on its interaction with the target enzyme PDE (Tsang et al., 1998), meaning that the effector enzyme itself has an important role in the negative regulation and deactivation of the phototransduction signalling cascade. As mentioned before, a complete photoreceptor recovery from light not only requires inactivation of PDE to stop cGMP hydrolysis, but also depends on an effective replenishment of intracellular cGMP. Re-synthesis of cGMP from GTP is facilitated by guanylate cyclase (GC) to restore cGMP concentration inside the cell, which allows the cGMP-gated cation channels, that were closed during phototransduction, to re-open and re-establish the inward flux of  $\text{Na}^+$  and  $\text{Ca}^{2+}$ , thus depolarising the photoreceptor cell to its resting state. Noticeably, many of the events involved in the photoreceptor recovery are regulated by intracellular  $\text{Ca}^{2+}$  levels. Decreased levels of  $\text{Ca}^{2+}$ , resulting from the closure of cGMP-gated cation channels during light response, lead to an activation of several calcium-sensitive proteins that function as important negative regulators of phototransduction cascade. For example, GRK1-mediated phosphorylation of activated opsin is negatively regulated by a calcium-binding protein recoverin (Kawamura, 1992; Kawamura, 1993; Chen et al., 1995; Klenchin et al., 1995). In the absence of light when intracellular  $\text{Ca}^{2+}$  levels are high,  $\text{Ca}^{2+}$ -bound recoverin binds to GRK1, inhibiting its interaction with opsin and its subsequent phosphorylation. However, following light stimulation,  $\text{Ca}^{2+}$  dissociates from recoverin, reducing its affinity for GRK1 and releasing its inhibition of opsin kinase activity. Similarly, GC is under a negative control of calcium-dependent GC-activating protein (GCAP), which normally exists in its  $\text{Ca}^{2+}$ -bound form, inhibiting GC enzymatic activity. When  $\text{Ca}^{2+}$  levels decrease during phototransduction, dissociation of  $\text{Ca}^{2+}$  allows GCAP to activate GC to synthesise cGMP. In addition, low intracellular  $\text{Ca}^{2+}$  levels make the  $\text{Ca}^{2+}$ -calmodulin complex within the cGMP-gated cation channels more sensitive to cGMP, thereby keeping them open even at low cGMP levels (Forrester et al., 2008, p.253; Fu, 2010; Hildebrand and Fielder, 2011).

#### 1.1.1.2 External limiting membrane

The external limiting membrane (ELM), also referred to as the outer limiting membrane (OLM), is a layer that separates the inner segment portions of photoreceptors from their cell bodies. This is not a true membrane, but is formed by junctional complexes (adherens junctions) between adjacent Müller cells, and between Müller cells and photoreceptors. It creates a barrier between the subretinal space, into which the photoreceptor inner and outer

segments project to be in close association with the RPE, and the rest of the neural retina (Kolb, 2005b; Hildebrand and Fielder, 2011).

#### 1.1.1.3 Outer nuclear layer

The outer nuclear layer (ONL) consists of nuclei-containing cell bodies (perikarya) and inner fibres of retinal rods and cones. It reaches its maximum thickness in the foveolar area. The photoreceptor nucleus comprises all non-mitochondrial DNA, while the inner fibre represents the axon of a photoreceptor cell that transmits cell signals to its specialised expanded synaptic terminals (Kolb, 2005b; Hildebrand and Fielder, 2011).

#### 1.1.1.4 Outer plexiform layer

The outer plexiform layer (OPL) represents the retinal site where synaptic connections are formed between photoreceptor cells and second-order association neurons (interneurons), namely vertically-running bipolar cells and horizontally-oriented horizontal cells. These interactions play an important physiological role in the transmission and initial processing of visual information in the retina.

Retinal rods and cones possess specialised synaptic terminals, referred to as spherules and pedicles, respectively, that are filled with many presynaptic vesicles. While there is no apparent contact between rod spherules, cone pedicles have small projections from their sides and bases, connecting them to neighbouring spherules and pedicles by gap junctions. The principal synaptic neurotransmitter of photoreceptor cells, both rods and cones, is glutamate which is released from the photoreceptor terminal via  $\text{Ca}^{2+}$ -mediated exocytosis in response to depolarisation. Thus, depolarised photoreceptors maintain a continuous synaptic release of glutamate in the absence of light. During phototransduction, light-induced hyperpolarisation causes voltage-gated calcium channels at the photoreceptor synaptic terminal to close, preventing inward flux of  $\text{Ca}^{2+}$  into the cell. A decrease in the intracellular  $\text{Ca}^{2+}$  concentration slows down and eventually terminates  $\text{Ca}^{2+}$ -induced exocytosis and subsequent glutamate release at the synaptic junction (Kolb, 2005b; Kolb, 2005d; Forrester et al., 2008, p.47-48; Fu, 2010; Hildebrand and Fielder, 2011).

Bipolar cells are oriented in a radial fashion parallel to photoreceptors and receive input from either rods or cones. There are approximately 35.7 million bipolar cells in the human retina, which can be divided into 9-11 functional and morphological subtypes, one for rods and 8-10 for cones. As the retina is dominated by rods outside the fovea, the rod bipolar cell population outnumbers cone bipolar cells, although the latter are more diverse. On average, each rod bipolar cell collects input from 15-30 rod spherules, but may receive

input from up to 50-100 rods, this summation of stimuli being a crucial factor in the sensitivity of the rod system to low levels of illumination. Rod bipolar dendritic trees (receptive fields) range between 15-30  $\mu\text{m}$  and are generally smaller in the central retina and larger in the peripheral retina. The rod bipolar cell makes a single contact with a rod spherule through a central invaginating ribbon-related dendrite which penetrates deeply into the rod spherule (Kolb, 1970). Cone bipolar cells can be further divided into diffuse bipolar cells and midget bipolar cells, that are distinguished by the number of associated cones, size of their dendritic fields and the type of synaptic contact they make with cone pedicles. 5-7 different types of diffuse cone bipolar cells have been identified in the human retina. They are involved in converging signals from multiple cones and contact clusters of cone pedicles. Some of these are very wide-field in their dendritic spread (70-100  $\mu\text{m}$ ) and associate with as many as 15-20 cone pedicles, however, smaller diffuse bipolar cells are more common that collect information from 5-7 cones in the central retina and from 12-14 cones in the peripheral retina. The synaptic connections they make with cone pedicles vary from flat-contacting non-ribbon-related basal junctions to invaginating ribbon-contacting synapses, or can even possess a mix of these (Hopkins and Boycott, 1995). On the other hand, midget cone bipolar cells, of which there are 3 types in the human retina, participate in contacts with single cones only. While invaginating midget bipolar (IMB) cells connect to cone pedicles through central invaginating dendrites at ribbon synapses, flat midget bipolar (FMB) cells contact cone pedicles by means of semi-invaginating, wide-cleft basal junctions that do not penetrate deeply into the synapse. Noticeably, cones of the fovea output to both, IMB and FMB, cells and some even signal to diffuse bipolar cells as well. This is possibly achieved thanks to the FMB cell not invaginating too deep into the cone pedicle. Interestingly, FMB dendrites usually make two contacts with a cone pedicle, on either side of the central invaginating dendrite from the IMB cell (Kolb, 1970). A special type of midget cone bipolar cells are the blue cone-specific (blue S-cone) bipolar cells, described in primates (Mariani, 1984; Kouyama and Marshak, 1992) and humans (Kolb et al., 1992) as bipolar cells that appeared to make invaginating contacts with only a limited number of cones in their territory, the suggestion being that these were specifically blue cones (Kolb, 2005e; Forrester et al., 2008, p.48; Hildebrand and Fielder, 2011).

Bipolar cells are classified as depolarising ON-centre or hyperpolarising OFF-centre cells, based on the nature of their response to glutamate. The different physiological responses of ON and OFF bipolar cells to the release of glutamate by photoreceptors are determined by the type of glutamate receptor embedded in the postsynaptic terminal membrane. ON cells are defined by the expression of a metabotropic glutamate receptor (mGluR), specifically

mGluR6 (Nomura et al., 1994; Vardi and Morigiwa, 1997), which belongs to the GPCR family. Binding of glutamate to this receptor triggers a G protein signalling cascade to close nonselective cation channels, resulting in hyperpolarisation (Nawy and Jahr, 1990; Shiells and Falk, 1990; Nawy, 1999; Dhingra et al., 2000). OFF cells, on the other hand, are characterised by the expression of ionotropic glutamate receptors (iGluRs), namely the non-NMDA AMPA and kainate receptors, which function as nonselective ligand-gated cation channels that open upon glutamate binding, leading to depolarisation. As a result, reduction of glutamate release in the synaptic cleft between a photoreceptor and a bipolar cell during phototransduction causes ON bipolar cells to depolarise in response to light stimulation, while OFF bipolar cells respond by hyperpolarisation. Interestingly, the type of glutamate receptor expressed by bipolar cells is governed by the type of their synaptic connection with cone pedicles and rod spherules. Bipolar cells that contact photoreceptors as central invaginating ribbon-related dendrites are thought to be ON cells, whereas those using basal junctions are generally considered to be OFF cells. Thus, this property allows one distinct population of bipolar cells to be excited by light and another population to be inhibited, although all photoreceptors show the same hyperpolarising response after light absorption. Hence, it is at this site in the retina where visual signals are split into the ON-centre and OFF-centre pathways, meaning that the status of the signal transmitted through the retina to the brain is essentially determined by the nature of a bipolar cell, which in turn is defined by the type of synapse it makes with a photoreceptor (Kolb, 2005d; Kolb, 2005e; Fu, 2010; Hildebrand and Fielder, 2011). This organisation is required for detecting colour, contrast and edges, as it allows one channel (ON-centre pathway) to provide information concerning brighter-than-background stimuli and the other (OFF-centre pathway), darker-than-background stimuli (Kuffler, 1953).

Horizontal cells are inhibitory interneurons that mediate lateral photoreceptor interactions and horizontal signal integration within the retina. Lateral inhibition refers to the capacity of an excited neuron to reduce the activity of its neighbours. In this way, horizontal cells function to increase the contrast and sharpness in visual response. Their name is derived from the extensive horizontal extensions of their cell processes that help integrate and regulate input from multiple photoreceptor cells. Three types of morphologically distinct horizontal cells have been identified in the human retina, designated HI-HIII. HI cells generally make contacts with 7 cone pedicles near the fovea, 18 cone pedicles further from the fovea and up to 100 rod spherules in the peripheral retina, HII cells are connected with about twice as many cones as HI cells, and HIII cells associate with 9-12 cone pedicles in the fovea, 20-25 cone pedicles in the peripheral retina and are also suspected to make

contacts with rod spherules (Kolb, 2005e; Forrester et al., 2008, p.50; Hildebrand and Fielder, 2011). There is evidence that some colour-specific wiring for the three types of horizontal cells might exist in the human retina, with each cell type showing preference for a particular cone type. HI cells seem to make contacts primarily with M-cones (green) and L-cones (red), with a small number of connections to S-cones (blue) in their dendritic field. HII cells appear to be specific for S-cones (blue), contacting only a limited number of M-cones (green) and L-cones (red), with their axons being connected exclusively to S-cones (blue). HIII cells, similar to HI cells, associate with M-cones (green) and L-cones (red), completely avoiding S-cones (blue) in their dendritic tree (Ahnelt and Kolb, 1994a; Ahnelt and Kolb, 1994b). Apparently, there is a considerable degree of overlap between horizontal cells throughout the retina and any one area may be served by up to 20 horizontal cells. Each rod has connections with at least two horizontal cells and each cone is associated with three or four horizontal cells of each type. Similar to OFF bipolar cells, horizontal cells express iGluRs in their postsynaptic terminal membrane and become depolarised by the release of glutamate from photoreceptors in the absence of light. In turn, decreased glutamate levels following light stimulation result in horizontal cell hyperpolarisation. Interestingly, depolarisation of a horizontal cell causes it to hyperpolarise photoreceptors in the surrounding area and conversely, its hyperpolarisation leads to depolarisation of nearby photoreceptor cells. Thus, horizontal cells provide a negative feedback to photoreceptors, which sums information from a network of horizontal cells connected over a wide spatial area and modulates the photoreceptor response to include signals coming from a surround region of the retina (Kolb, 2005e; Forrester et al., 2008, p.51). Although the details of this inhibitory interaction between horizontal cells and photoreceptors are not fully understood, several mechanisms have been proposed that influence the presynaptic voltage-gated  $\text{Ca}^{2+}$  channel activity in the photoreceptor terminal membrane to alter glutamate release. These include the secretion of inhibitory neurotransmitters, mainly  $\gamma$ -aminobutyric acid (GABA), a shift in the  $\text{Ca}^{2+}$  current activation range to more negative potentials, a fast hemichannel-mediated ephaptic transmission<sup>2</sup> and pH changes mediated by pannexin1-dependent ATP release and its subsequent extracellular hydrolysis in the synaptic cleft (Schwartz, 1982; Kaneko and Tachibana, 1986; Verweij et al., 1996; Picaud et al., 1998; Kamermans et al., 2001; Hirasawa and Kaneko, 2003; Verweij et al., 2003; Vessey et al., 2005; Davenport et al., 2008; Thoreson and Mangel, 2012; Vroman et al., 2014).

---

<sup>2</sup> Ephaptic transmission is a form of cell-cell communication within the nervous system, distinct from direct communication pathways, such as electrical and chemical synapses, in which electric fields generated by a specific neuron alter the excitability of neighbouring neurons as a result of their anatomical and electrical proximity. It also refers to the coupling of adjacent neurons caused by a fast exchange of ions between them.

In addition, the outer plexiform layer also contains synaptic terminals of interplexiform cells (IPCs), a special type of GABAergic interneurons that link the two plexiform layers of the retina, having synaptic output upon OPL neurons. Their processes make numerous conventional synapses with cell bodies and dendrites of bipolar cells, are connected to other IPCs and touch cone pedicles, making rather unspecialised junctions at this site (Kolb and West, 1977; Nakamura et al., 1980; Kolb, 2005f; Hildebrand and Fielder, 2011).

#### 1.1.1.5 Inner nuclear layer

The inner nuclear layer (INL) is composed of the nuclei and their surrounding cell bodies (perikarya) of at least 5 different cell types, including horizontal cells, bipolar cells, Müller cells, interplexiform cells and amacrine cells. The cell bodies of horizontal cells are located primarily along the outer limit of the INL facing the OPL, the amacrine cell bodies lie predominantly in the inner part of the INL, while the perikarya of bipolar, interplexiform and Müller cells take up intermediate positions (Kolb, 2005b; Forrester et al., 2008, p.51; Hildebrand and Fielder, 2011).

#### 1.1.1.6 Inner plexiform layer

The inner plexiform layer (IPL) represents the second site of neural processing within the retina, where synaptic connections are established to transmit the vertically-carried visual information from bipolar cells to retinal ganglion cells, these signals being modulated and integrated by complex networks of interacting, horizontally-directed amacrine cells. The processing power of the retina is highlighted by IPL stratification into five laminae, thus enabling parallel transmission and processing of signals from the same photoreceptor to generate multiple, functionally different retinal maps in the various IPL sublayers, all in response to the same light stimulation (Kolb, 2005b; Hildebrand and Fielder, 2011).

Bipolar cells connect the outer and inner retina and are directly responsible for relaying the visual information from photoreceptors, modified by horizontal cells, to ganglion cells. Interestingly, while cone bipolar cells make direct synapses with ganglion cell dendrites, rod bipolar cells are rarely in a direct contact with ganglion cells. Rather, they connect to ganglion cells indirectly via amacrine cells which subsequently associate with cone bipolar cells to join the rod and cone pathways. Like photoreceptors, bipolar cells utilise glutamate as their neurotransmitter. As already discussed, ON bipolar cells become hyperpolarised in the absence of light, which prevents glutamate release from their presynaptic terminal due to the closure of voltage-gated  $\text{Ca}^{2+}$  channels and subsequent inhibition of  $\text{Ca}^{2+}$ -mediated exocytosis. Following light stimulation, however, they depolarise to release glutamate at



the bipolar cell-ganglion cell synapse. Conversely, OFF bipolar cells exist in a depolarised state in the absence of light, secreting glutamate from their synaptic terminal, and respond to light by hyperpolarisation, blocking the neurotransmitter release into the synaptic cleft. As the ribbon synapse between the bipolar and ganglion cell is considered to be excitatory, the type of ganglion cell signal is essentially determined by the nature of the bipolar cell contacting it (Kolb, 2005d; Kolb, 2005e; Fu, 2010; Hildebrand and Fielder, 2011).

Ganglion cells are the final output neurons of the retina that collect the processed visual information from the retina and carry it to the visual centres of the brain for interpretation. They receive input from bipolar and amacrine cells, responding to all common excitatory and inhibitory retinal neurotransmitters. There are approximately 1.2 million ganglion cells in the human retina. Although functionally and morphologically diverse, they share some general structural features, including a large cell body, abundant Nissl substance (arrays of rough endoplasmic reticulum), a large Golgi apparatus and a long axon. Ganglion cells can be classified on the basis of their cell body size, dendritic tree spread (field size), branching patterns (dendritic morphology) and branching level(s) of the five IPL strata in which they synapse with bipolar and amacrine cells. The dendritic field span of each ganglion cell type generally increases with eccentricity from the fovea and may be up to ten times larger in the periphery compared to the central retina (Boycott and Wässle, 1974; Kolb et al., 1981). Therefore, any ganglion cell classification has to always consider their foveal distance and compare cells in similar retinal locations to ensure that they are indeed different cell types. At least 18 morphologically distinct ganglion cell types have been described in the human retina. The two most common types are midget and diffuse ganglion cells, which represent about 80% of the ganglion cell population (Rodieck et al., 1985; Kolb et al., 1992; Dacey, 1993). Midget ganglion cells are more numerous, with relatively small dendritic tree size, making synaptic contacts exclusively with amacrine cells and a single midget bipolar cell. Having slow conduction velocity, they respond to changes in colour, but react weakly to changes in contrast. In comparison, diffuse (parasol) ganglion cells are less numerous, with considerably larger dendritic fields, receiving input from all types of bipolar cells except the midget bipolar cells. Having fast conduction velocity, they can respond to low-contrast stimuli, but are not very sensitive to changes in colour (Kolb, 2001a; Forrester et al., 2008, p.49-50; Hildebrand and Fielder, 2011).

Recently, a small subset ( $\approx 1\%$ ) of ganglion cell population was found to be intrinsically photosensitive, representing a third class of retinal photoreceptors, that differed markedly in their response to light from rods and cones (Berson et al., 2002). These intrinsically photosensitive retinal ganglion cells (ipRGCs) contribute little or nothing to vision, but

instead signal ambient luminance to provide basis for the mostly subconscious non-image-forming visual responses, involving pupillary constriction, neuroendocrine regulation and circadian photoentrainment, i.e. synchronisation of the daily physiological rhythms to the light/dark cycle. Their light sensitivity is dependent on the expression of a characteristic photopigment melanopsin, present in the plasma membrane of cell bodies, dendrites and proximal axon segments. Although sparsely spread, these melanopsin-expressing ganglion cells have large overlapping dendritic fields, forming an extensive photoreceptive network throughout the retina (Provencio et al., 1998; Provencio et al., 2000; Hattar et al., 2002; Provencio et al., 2002). Deletion of the melanopsin gene in melanopsin knock-out mice results in the loss of intrinsic photosensitivity in ipRGCs, so they can no longer respond to light, although their number, morphology and projections remain preserved. Furthermore, animals lacking melanopsin show deficits in multiple visual responses, including pupillary light reflex and circadian photoentrainment (Panda et al., 2002; Ruby et al., 2002; Lucas et al., 2003). Conversely, expression of melanopsin confers photosensitivity to normally non-photoreceptive cell types, leading to robust light responses in such cells (Melyan et al., 2005; Panda et al., 2005; Qiu et al., 2005). Like all other animal opsins, melanopsin is an integral transmembrane protein which belongs to the GPCR family. Similar to classical photopigments found in retinal rods and cones (i.e. rhodopsin and photopsins), melanopsin also utilises 11-*cis* retinal as its light-absorbing chromophore, with maximum sensitivity to blue light at around 480 nm (Lucas et al., 2001), and light-induced isomerisation of 11-*cis* retinal to all-*trans* retinal as the initial step in the phototransduction process. However, its amino acid sequence and downstream signalling cascade resemble those of invertebrate opsins. Thus, activated melanopsin triggers a G protein-coupled, membrane-associated, phosphoinositide pathway, involving the effector enzyme phospholipase C, breakdown of the membrane lipid component phosphatidylinositol bisphosphate and subsequent opening of transient receptor potential (TRP) cation channels, leading to membrane depolarisation (Panda et al., 2005; Qiu et al., 2005; Graham et al., 2008; Xue et al., 2011). Also consistent with some invertebrate photopigments, melanopsin is a bistable molecule, functioning as a photopigment with intrinsic photoisomerase activity for its own regeneration which is spectrally shifted to longer wavelengths (Fu et al., 2005; Melyan et al., 2005; Mure et al., 2007). In addition to being directly light-responsive, ipRGCs express membrane receptors for the neurotransmitters glutamate, glycine and GABA to receive synaptic inputs, both excitatory and inhibitory, from bipolar and amacrine cells (Belenky et al., 2003; Dacey et al., 2005; Perez-Leon et al., 2006; Wong et al., 2007). There seems to be a certain degree of functional redundancy between the melanopsin-dependent pathway and the classical

rod-cone system in the ipRGCs as evident from the studies of melanopsin knock-out mice. Although ipRGCs were found to lose their intrinsic photosensitivity in these animals, their non-image-forming visual responses were only partially impaired, rather than completely ablated (Panda et al., 2002; Ruby et al., 2002; Lucas et al., 2003), suggesting that ipRGCs could be activated via an alternative, melanopsin-independent, mechanism. Interestingly, melanopsin deficiency, coupled with rod and cone dysfunction, results in a complete loss of circadian photoentrainment, pupillary light reflex and other non-image-forming visual functions (Hattar et al., 2003; Panda et al., 2003). Thus, the melanopsin-associated and the classical rod-cone systems have complementary functions, i.e. ipRGCs can respond to light via both an intrinsic melanopsin-based signalling cascade and a synaptic pathway driven by classical rod and cone photoreceptors, to mediate all major accessory visual responses. Moreover, there is evidence that the classical rod and cone photoreceptors are important regulators of melanopsin expression in the retina, as their degeneration decreases levels of melanopsin mRNA (Sakamoto et al., 2004). In addition, while mice lacking ipRGCs retain pattern vision and exhibit normal function of the outer retina, their non-image-forming visual responses become completely abolished, indicating that ipRGCs act as the principal conduits of the photic input for the non-image-forming vision (Göz et al., 2008; Güler et al., 2008; Hatori et al., 2008).

Similar to horizontal cells of the OPL, amacrine cells are inhibitory interneurons involved in lateral interactions within the IPL. Thus far, about 40 different morphological subtypes have been described, though the precise functional significance of all of them is still not fully understood. Like ganglion cells, amacrine cells can be classified according to the size of their dendritic tree, branching pattern and the stratification of their dendrites within the five IPL laminae in which they make synaptic connections with bipolar, ganglion and other amacrine cells (Mariani, 1990; Kolb et al., 1992). Horizontally, their dendritic field span is highly variable, ranging from less than 100  $\mu\text{m}$  to greater than 500  $\mu\text{m}$  (Kolb et al., 1981), and increases with eccentricity from the fovea. Therefore, much the same as ganglion cells, the foveal distance always has to be taken into account when classifying amacrine cells into various morphological subtypes. In addition to their structural diversity, amacrine cells release a number of different neurotransmitters and neuromodulators, including GABA, glycine, acetylcholine and dopamine. Their main function is to facilitate the horizontal and vertical communication within and between the different IPL strata, respectively. In this way, they contribute to the detection of directional motion, modulate light adaptation and circadian rhythm, link rod bipolar cells to the cone bipolar system and allow adjustment of visual sensitivity. The most common amacrine cell type in the retina is the narrow-field

bistratified glycinergic AII amacrine cell which plays a crucial role in the rod pathway and scotopic vision. It acts as the major carrier of rod signals to ganglion cells, by joining the rod and cone bipolar systems (as mentioned before, rod bipolar cells are rarely in a direct contact with ganglion cell dendrites). Another example is the wide-field starburst amacrine cell that uses GABA and acetylcholine as its neurotransmitters and functions in directional selectivity, motion detection, optokinetic eye movement and probably retinal development (Masland and Tauchi, 1986). Several wide-field diffuse GABAergic amacrine cell types (such as A4, A13, A17 and A19) are characterised by making reciprocal feedback synapses with bipolar cells from which they receive input, rather than contacting ganglion cells or other amacrine cells. Thus, they converge signals from large areas of the retina and amplify them at low light intensities (Nelson and Kolb, 1985). In addition, wide-field dopaminergic A18 cells modulate functional outputs of other amacrine cell types, mainly AII, A8, A13 and A17, as well as ganglion cells (Pourcho, 1982; Voigt and Wässle, 1987; Kolb et al., 1990). Importantly, dopamine controls melanopsin mRNA expression in ipRGCs, regulates their sensitivity and alters their responses to affect the non-image-forming visual system (Sakamoto et al., 2005; Van Hook et al., 2012). Furthermore, dopaminergic amacrine cells send GABA-mediated inhibitory signals to ipRGCs. Thus, A18 amacrine cells are involved in modulating the circadian rhythm and light adaptation process in the retina (Pourcho and Goebel, 1983; Pourcho and Goebel, 1985; Crooks and Kolb, 1992; Kalloniatis et al., 1996; Kolb, 2005f; Kolb, 2005g; Hildebrand and Fielder, 2011).

In addition, the inner plexiform layer also provides synaptic input to interplexiform cells which receive signals mostly from the dopaminergic amacrine cells to transmit feedback information from the inner retina to the OPL (Kolb and West, 1977; Nakamura et al., 1980; Kolb, 2005f; Hildebrand and Fielder, 2011).

#### 1.1.1.7 Ganglion cell layer

The ganglion cell layer (GCL) contains nuclei and cell bodies (perikarya) of ganglion cells, as well as several other cell types, including displaced amacrine cells, astrocytes, pericytes and endothelial cells. Interestingly, cell bodies of the midget ganglion cells are generally smaller than perikarya of the diffuse ganglion cells. The layer thickness varies throughout the retina and is used to histologically distinguish the macula from the peripheral retina. Normally, there are up to 8-10 rows of cell bodies (60-80  $\mu\text{m}$ ) in the central retina, as few as a single row of nuclei (10-20  $\mu\text{m}$ ) outside the macula in the peripheral retina, and the GCL is completely absent from the foveola itself (Kolb, 2005b; Forrester et al., 2008, p.48; Hildebrand and Fielder, 2011).

#### 1.1.1.8 Nerve fibre layer

The nerve fibre layer (NFL) is formed by ganglion cell axons that integrate all the image-forming and non-image-forming visual information from the retina and carry it along the optic nerve to specific visual centres of the brain for interpretation. Thus, on their way to ganglion cell axons, the visual signals detected by photoreceptors in the outer retina are transmitted and modulated by bipolar, horizontal and amacrine cells as part of the neural processing in the two plexiform layers of the retina.

The ganglion cell axons are accompanied by astrocytes in the NFL and are separated into bundles by cellular processes of Müller cells and the internal limiting membrane. They are collected at the optic disc to leave the eye and form the optic nerve, in humans consisting of more than one million fibres. Therefore, the NFL thickness typically increases towards the optic nerve head as a result of axon fibre convergence on the optic disc. Upon exiting the eye, ganglion cell axons become myelinated with oligodendrocytes. Due to the long anatomic distance between the retina and the brain, the axon fibres require an effective mechanism for transport of metabolites and organelles away from (anterograde) and back to (retrograde) the ganglion cell nucleus. Axon transport is an active process that consumes large quantities of ATP, supplied by the numerous axonal mitochondria. Retinal ganglion cell axon fibres terminate in several regions of the thalamus, hypothalamus and midbrain, depending on the nature of visual signal they carry (Forrester et al., 2008, p.48; Hildebrand and Fielder, 2011).

The ganglion cell axons transmitting the image-forming visual information target primarily the lateral geniculate nucleus (LGN) of the thalamus and the superior colliculus (SC) of the midbrain, which represent the central connection for the optic nerve to the primary visual cortex located in the occipital lobe and the principal integrating centre for eye movements, respectively. Generally, midget ganglion cell axons terminate in the parvocellular layers of the LGN and are therefore also referred to as P-cells. On the other hand, diffuse (parasol) ganglion cells project to the magnocellular layers of the LGN and thus are also known as M-cells. Once reaching the brain, both ganglion cell types make excitatory synapses with cells in their target area, using glutamate as the major neurotransmitter, to relay the visual information they carry (Forrester et al., 2008, p.48-50 and p.259; Hildebrand and Fielder, 2011).

Melanopsin-expressing ipRGCs transmit non-image-forming visual information, projecting primarily via the retinohypothalamic tract (RHT) to the suprachiasmatic nucleus (SCN) of the hypothalamus and to the olivary pretectal nucleus (OPN) of the midbrain, to control the circadian photoentrainment and mediate the pupillary light reflex, respectively (Provencio

et al., 2000; Gooley et al., 2001; Hannibal et al., 2002; Hattar et al., 2002; Provencio et al., 2002). Recently, additional targets of ipRGC axons have been identified in the thalamus, hypothalamus, midbrain and several other regions, that could contribute to the regulation of circadian rhythms, sleep/wake cycles, body temperature and hormone production, such as the intergeniculate leaflet, lateral nucleus, peri-supraoptic nucleus, subparaventricular zone, lateral and ventrolateral preoptic areas, posterior limitans nucleus, periaqueductal grey, medial amygdala and margin of the lateral habenula (Hattar et al., 2006). In addition, ipRGC axon fibres were also found to terminate in the LGN and SC, indicating that the melanopsin-dependent non-image-forming photoreception merged with the conventional image-forming retinal pathway and the melanopsin-based visual system might thus support conscious visual perception (Dacey et al., 2005; Hattar et al., 2006; Hannibal et al., 2014). Besides utilising glutamate as a neurotransmitter, ipRGCs also influence their target cells by releasing the pituitary adenylate cyclase-activating polypeptide (PACAP) from their synaptic terminals (Hannibal et al., 2002; Hannibal et al., 2004).

#### 1.1.1.9 Internal limiting membrane

The internal (inner) limiting membrane (ILM) represents the inner surface of the retina and thus the boundary between the retina and vitreous humour. It is formed by the basal lamina of laterally-contacting Müller cell end-feet, i.e. proximal cell extensions that enlarge and flatten on the vitreal side. The surface of the Müller cell membrane facing the vitreous is covered with a mucopolysaccharide material, thus forming a true basement membrane and a diffusion barrier between the neural retina and vitreous body (Kolb, 2001b; Kolb, 2005b; Hildebrand and Fielder, 2011).

#### *1.1.2 Glial cells of the retina*

Glial cells are defined as non-neuronal cells that function mostly to maintain homeostasis, regulate communication and provide structural and nutritional support as well as protection to surrounding neurons. The main glial cell types found in the retina include Müller cells, astrocytes and microglia, that each exhibit distinct morphological, developmental and antigenic characteristics.

Müller cells are the predominant type of retinal glia, representing 90% of all glial cells in the retina. They are radially-oriented cells, with nuclei-containing perikarya located in the INL, that traverse the entire neural retina, from the ILM to the ELM. Their lateral cell extensions in the two nuclear layers surround cell bodies of retinal neurons and their cell processes are also found to envelop retinal blood vessels, thus maintaining their structural

and functional stability (Hama et al., 1978; Reichenbach et al., 1988; Reichenbach et al., 1989; Dreher et al., 1992). The cytoplasm contains abundant endoplasmic reticulum, with varying amounts of glycogen granules, and microtubules, reflecting the role of these cells in protein synthesis, intracellular transport and secretion. Large numbers of mitochondria and intermediate filaments are normally present in the inner half of the cells and at their end-feet. Müller cells are essential to maintain the local environment, allowing the visual process to function optimally. Most importantly, they are responsible for uptake of excess glutamate neurotransmitter released by photoreceptors, which is subsequently converted to glutamine by the enzyme glutamine synthetase, thereby protecting retinal neurons from glutamate-induced excitotoxicity. Furthermore, they also regulate removal of neural waste products (such as ammonia and CO<sub>2</sub>), facilitate phagocytosis of neuronal debris, control extracellular pH and K<sup>+</sup> levels, mediate electrical insulation of neurons and photoreceptors, provide physical support of the neural retina, act as mechanosensors responding to changes in mechanical forces, participate in the intraretinal lipid transport, have an important role in water homeostasis and are capable of secreting cytokines (e.g. IL-8 and IL-6). In addition, they modulate neuronal activity by regulating the concentration of neuroactive substances (including GABA, taurine and dopamine) in the extracellular space and may function in retinal development by synthesising retinoic acid from retinol. Interestingly, Müller cells metabolise glucose (stored as glycogen) anaerobically into lactate for their energy supply, with excess lactate being secreted to fuel oxidative phosphorylation in neurons, especially the photoreceptors (Poitry-Yamate et al., 1995). In this way, they may help to nourish and maintain the outer retina which lacks a direct blood supply (Kolb, 2001b; Forrester et al., 2008, p.51 and p.240; Hildebrand and Fielder, 2011; Vecino et al., 2016). Moreover, it has been suggested that these glial cells might act as light-collecting elements that guide light through the inner retinal layers towards photoreceptors, in order to minimise intraretinal light scattering, thus ensuring that high intensity light reaches the individual rods and cones (Franze et al., 2007; Labin and Ribak, 2010). Finally, recent studies provide evidence that Müller cells might have an important role in regeneration of retinal neurons by their ability to de-differentiate under right circumstances into multipotent neuronal progenitor cells that can proliferate and give rise to a number of retinal cell types including ganglion cells, glia and photoreceptors. Hence, this regenerative potential makes Müller cells ideal candidates for cell replacement therapy to treat retinal degenerative diseases (Fischer and Reh, 2001; Ooto et al., 2004; Das et al., 2006; Bernardos et al., 2007; Singhal et al., 2012; Jayaram et al., 2014).

Astrocytes are characterised by a distinct morphology of a flattened cell body and a fibrous series of radiating processes, filled with intermediate filaments. Their structure typically varies throughout the retina, from being extremely elongated near the optic nerve head to a symmetrical star-shaped form in the periphery. Neighbouring cells are connected by gap junctions to allow rapid communication via  $\text{Ca}^{2+}$  wave propagation and extracellular ATP signalling. It is generally believed that retinal astrocytes do not originate from the retinal embryonic epithelium, but rather move into the developing retina from the brain, migrating along the optic nerve and entering the eye together with blood vessels (Stone and Dreher, 1987; Watanabe and Raff, 1988). Astrocyte cell bodies and processes are almost entirely restricted to the NFL, where they ensheath ganglion cell axon bundles coursing towards the optic disc. Similarly, superficial blood vessels running in and among these bundles are also covered with astrocytes. Thus, sending projections to both nerve fibres and blood vessels, astrocytes link neurons to a blood supply. Interestingly, the numbers and distribution of retinal astrocytes depend on the density of nerve fibres that they associate with and are correlated with the presence and distribution of retinal blood vessels (Stone and Dreher, 1987; Watanabe and Raff, 1988; Rungger-Brändle et al., 1993). Astrocytes maintain the extracellular chemical environment in the retina by controlling ion homeostasis, especially the  $\text{K}^+$  levels, and recycling neurotransmitters released during synaptic transmission. They contain abundant glycogen stores and thus may provide nutritional support to neurons. In addition, they have an important role in regulating water homeostasis, extracellular space volume, waste clearance, cell migration and  $\text{Ca}^{2+}$  signalling, participate in tissue repair and scarring following an injury, and are required for synaptic pruning<sup>3</sup> (Kolb, 2001b; Forrester et al., 2008, p.51; Hildebrand and Fielder, 2011; Vecino et al., 2016).

Microglia represent a specialised subpopulation of the mononuclear phagocyte system that resides in the CNS. Although their origin is controversial, they are thought to arise from primitive myeloid progenitors in the yolk sac, rather than the bone marrow, and their continuity during adulthood is ensured by a population of local precursors, thus the local expansion and maintenance of microglia are entirely dependent on the resident cell self-renewal capacity (Ajami et al., 2007; Ginhoux et al., 2010; Schulz et al., 2012). Moreover, unlike blood monocytes and macrophages, microglia have a relatively long lifespan. They are found at variable densities in different retinal layers and being mobile, they can reach virtually any part of the retina. In healthy conditions, however, they typically extend only as far as the ELM. Microglia are an extremely plastic cell type, exhibiting considerable

---

<sup>3</sup> Synaptic pruning is a natural process of synapse elimination that reduces and remodels excess synaptic contacts to obtain functional neuronal circuits. It takes place mainly during development, but can also occur in a mature brain.



morphological diversity based on the local conditions and specific chemical signals they detect. This level of plasticity makes it difficult to define the various functional phenotypes of microglia, but is required to fulfill the variety of functions that these cells perform. Most importantly, it gives them the ability to defend the retina on extremely short notice without causing substantial immunological disturbance. As resident phagocytic cells, they provide the first and main form of active immune defence against infection or tissue damage. Once activated, microglia function as immune effectors, secreting cytokines and chemokines, to promote inflammation and facilitate tissue repair. They contribute to the maintenance of retinal homeostasis, by constantly scavenging for infectious agents and foreign material as well as damaged, dying or unnecessary cells. Being very sensitive to even small changes in the extracellular environment, each cell physically surveys its domain on a regular basis. Although most of their activity is related to immune responses, microglia also participate in the development and maintenance of neural networks. They are involved in synaptic pruning and thus contribute to remodelling of neuronal circuits, modifying the number of synapses by direct elimination of specific synaptic contacts in a process suggested to occur via the complement system. In addition, they control synaptic activity by releasing factors that can influence both neurotransmission and synaptic plasticity (Kolb, 2001b; Forrester et al., 2008, p.52-54; Hildebrand and Fielder, 2011; Vecino et al., 2016).

### *1.1.3 Retinal pigment epithelium*

The retinal pigment epithelium is formed by a single continuous layer of highly polarised, pigmented epithelial cells that underlies the neurosensory retina and separates it from the choroid. A healthy human retina contains around 3.5-6.1 million RPE cells, their density generally decreasing from the fovea towards the periphery. The RPE is characterised by a limited regenerative capacity and the cells are normally non-dividing or have a very slow proliferation rate. Interestingly, the RPE cell density was found to decrease by about 0.3% per year with increasing age (Panda-Jonas et al., 1996). The cells have a typical hexagonal morphology, though their size and shape vary depending on age and location, being more columnar (14  $\mu\text{m}$  tall, 10  $\mu\text{m}$  wide) in the central retina and more flattened (10-14  $\mu\text{m}$  tall, 60  $\mu\text{m}$  wide) in the peripheral retina. Infoldings in the basal and apical membranes increase the overall surface area of the cell monolayer. RPE cells are closely associated with retinal photoreceptors. While their basal aspect sits on the Bruch's membrane, the apical processes envelop the rod and cone outer segments. A single RPE cell can be in contact with up to 30 cones and 22-28 rods (Rapaport et al., 1995; Kolb, 2005c; Kolb, 2005d; Forrester et al., 2008, p.43; Hildebrand and Fielder, 2011). The RPE serves many important roles in order

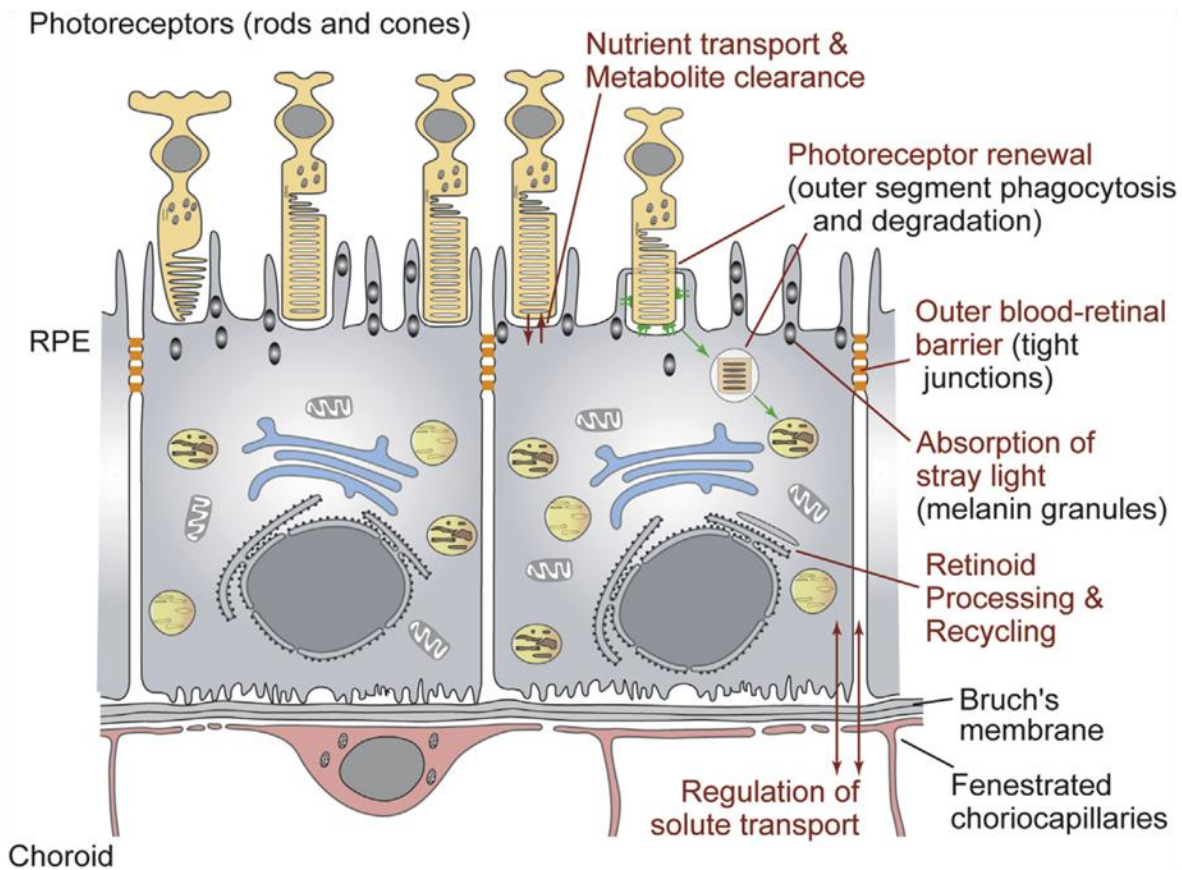


**Figure 1.2:** Support functions of the retinal pigment epithelium (RPE).

The RPE is metabolically a highly active tissue that serves many important roles in order to maintain a healthy ocular microenvironment and retinal homeostasis. Most importantly, the proper visual function of retinal photoreceptor cells (both rods and cones) is critically dependent on the support provided by a healthy RPE layer. *From Lehmann et al. (2014).*

to maintain a healthy ocular microenvironment and retinal homeostasis (Figure 1.2). Most importantly, a functional interaction between the RPE and light-sensing photoreceptor cells is indispensable for normal vision (Strauss, 2005; Forrester et al., 2008, p.43 and p.247-250; Strauss, 2011).

RPE cells are responsible for the upkeep of photoreceptors through phagocytosis of shed POSs and subsequent degradation of this ingested material on daily basis. This process is essential to maintain photoreceptor functionality and survival, as without the regular POS replacement photoreceptor cells can degenerate and die. As previously alluded to, during the process of photoreceptor renewal the distal tips of outer segment discs are shed in a diurnal manner and removed by the apical processes of RPE cells in a short burst of phagocytic activity triggered by light (Young, 1967; Young and Bok, 1969; Young, 1971;

LaVail, 1976; Young, 1976; Besharse et al., 1977; Steinberg et al., 1977; Besharse and Hollyfield, 1979; LaVail, 1980; Besharse, 1982). The uptake of shed POS tips by the RPE is a regulated and coordinated process, starting with POS binding to  $\alpha_v\beta_5$  integrin receptor expressed on the apical side of the RPE plasma membrane (Finnemann et al., 1997; Lin and Clegg, 1998). This in turn leads to phosphorylation and mobilisation of focal adhesion kinase (FAK), which subsequently activates proto-oncogene tyrosine-protein kinase MER (MerTK), a transmembrane protein of the receptor tyrosine kinase family that triggers the engulfment and ingestion of the integrin-bound POSs (D'Cruz et al., 2000; Gal et al., 2000; Vollrath et al., 2001; Feng et al., 2002; Finnemann, 2003). Moreover, MerTK provides a feedback mechanism that limits the POS binding activity of  $\alpha_v\beta_5$  integrin receptors in RPE cells (Nandrot et al., 2012). In addition, binding of shed POSs to  $\alpha_v\beta_5$  integrin is regulated by its soluble glycoprotein ligand milk fat globule-EGF factor 8 (MFG-E8) secreted by the RPE (Nandrot et al., 2007; Nandrot and Finnemann, 2008). Furthermore, internalisation (but not initial binding) of the POS- $\alpha_v\beta_5$  complex depends on cluster of differentiation 36 (CD36), a transmembrane scavenger receptor previously described on haematopoietic cells (such as macrophages) as a receptor for apoptotic neutrophils and oxidised low-density lipoprotein, which is now known to recognise oxidised phosphatidylcholine, a product of aged outer segment tips (Ryeom et al., 1996; Finnemann and Silverstein, 2001). There is also evidence of an interaction between CD36 and toll-like receptor 4 (TLR4), adapting the RPE cell metabolism to handle ingested POSs (Kindzelskii et al., 2004). Interestingly, RPE cells are phagocytically the most active cells in the body, with up to 10% of the POS length being taken up by the RPE each day. It is estimated that a single RPE cell can phagocytose around 2000-4000 POS discs per day. To cope with this enormous phagocytic load, RPE cells possess an extensive phagolysosomal system, comprising a range of enzymes capable of digesting complex lipid-glycoprotein aggregates, that can degrade about 50% of the ingested material within 1-2 hours. Solubilised waste material is subsequently transported across the basal infoldings in the RPE plasma membrane into the systemic circulation via choriocapillaris (Bok, 1993; Strauss, 2005; Forrester et al., 2008, p.249 and p.254-255). It was recently reported that the POS phagocytosis and degradation might proceed via a non-canonical autophagy pathway<sup>4</sup>, termed LC3-associated phagocytosis (LAP), and could depend on proteins classically involved in autophagy that associated with single-membrane phagosomes containing engulfed POSs (Kim et al., 2013). Importantly, the phagocytosis of POSs by the RPE decreases with aging and diminished phagocytic capacity of RPE cells

---

<sup>4</sup> Canonical autophagy can be defined as a natural self-degradative mechanism used by cells to disassemble and recycle any unnecessary or dysfunctional cellular components in a regulated manner intracellularly in double-membrane autophagosomes.

has been associated with several degenerative diseases of the retina (Travis et al., 2007; Kevany and Palczewski, 2010).

The RPE plays an essential role in vitamin A metabolism and visual cycle. As mentioned before, the phototransduction cascade starts with 11-*cis* retinal isomerisation in the POS disc membrane to all-*trans* retinal, which then reacts with phosphatidylethanolamine to produce *N*-retinylidene-phosphatidylethanolamine that is released from the opsin molecule and transferred to the POS cytosolic compartment in a process mediated by an ATP-driven flippase ATP-binding cassette sub-family A member 4 (ABCA4). All-*trans* retinal gets reduced by retinol dehydrogenase 12 (RDH12) to all-*trans* retinol, which is subsequently delivered to the subretinal space, loaded onto a carrier protein interphotoreceptor retinol-binding protein (IRBP) and transported to the RPE. After uptake by an RPE cell, all-*trans* retinol binds to cellular retinol-binding protein (CRBP) and is carried to a protein complex of several enzymes for chemical processing. First, it becomes esterified by lecithin retinol acyltransferase (LRAT) to all-*trans* retinyl esters, then is re-isomerised to 11-*cis* retinol by RPE-specific 65 kDa protein (RPE65) using the energy from ester hydrolysis, and finally gets oxidised back to 11-*cis* retinal by RDH5. The latter reaction is accelerated by cellular retinal-binding protein (CRALBP), which is also part of the enzyme complex and to which 11-*cis* retinal is immediately transferred for delivery to the plasma membrane. There, 11-*cis* retinal is loaded onto IRBP and shuttled back to the POS to recombine with opsin in the disc membrane and recommence the visual cycle. In this way, the RPE serves an important role to ensure a constant chromophore regeneration in the photoreceptors (Strauss, 2005; Forrester et al., 2008, p.252; Strauss, 2011).

In addition, the RPE absorbs scattered light thanks to the presence of melanin pigment granules, thereby improving the quality of the eye's optical system and image resolution, it supplies essential nutrients (mainly glucose, retinol and fatty acids) to the photoreceptors to maintain their proper function, mediates clearance of metabolites from the retina, as well as regulates fluid and ion balance. In order to communicate with their surrounding tissues, RPE cells secrete growth factors, cytokines and signalling molecules, including ATP, Fas ligand (FasL), interleukins (ILs), vascular endothelial growth factor (VEGF), transforming growth factor beta (TGF- $\beta$ ), ciliary neurotrophic factor (CNTF), fibroblast growth factor (FGF), platelet-derived growth factor (PDGF), pigment epithelium-derived factor (PEDF), insulin-like growth factor 1 (IGF-1) and tissue inhibitor of metalloproteinases (TIMP) (Bok, 1993; Strauss, 2005; Hildebrand and Fielder, 2011; Strauss, 2011).

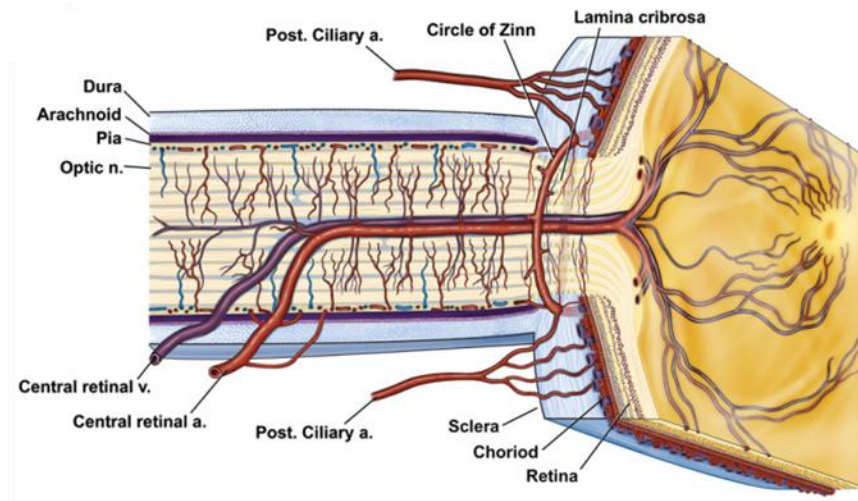
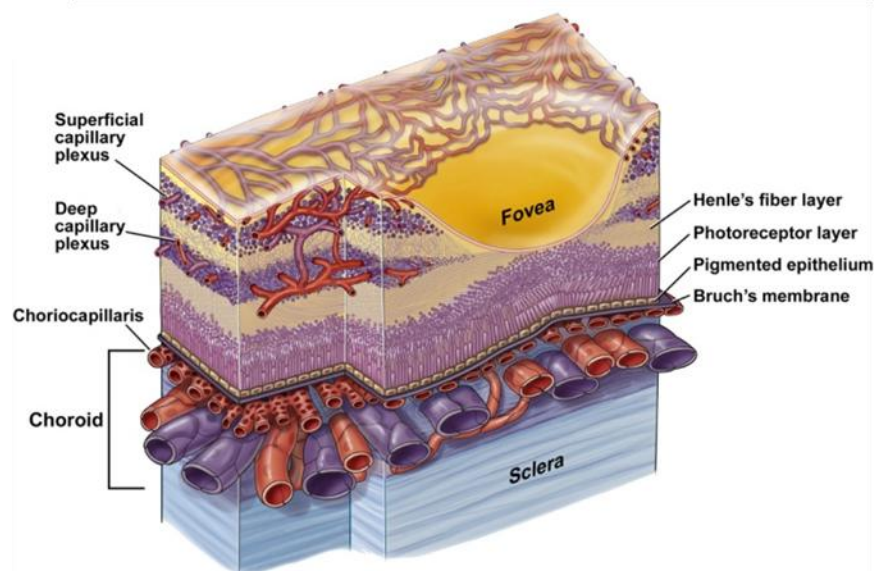
Noticeably, the highly metabolically active RPE is predisposed to chronic oxidative stress due to its substantial oxygen consumption, exposure to lipid peroxidation products derived

from the ingested POSs and almost constant presence of light stimuli (Winkler et al., 1999; Beatty et al., 2000). Therefore, to be protected from the oxidative damage, RPE cells use a number of antioxidants, such as superoxide dismutase, catalase, glutathione, melanin and ascorbate (Boulton and Dayhaw-Barker, 2001).

#### *1.1.4 Blood supply of the retina*

The retina consumes approximately 8% of the basal metabolic rate (Howard et al., 1987; Niven and Laughlin, 2008) and thus belongs to the highest energy-demanding systems in the body, similar to the brain. In addition, it is also considered one of the highest oxygen-consuming tissues (per weight), with an oxygen demand exceeding even that of the brain (Anderson and Saltzman, 1964; Ames et al., 1992; Yu and Cringle, 2001). Because of its relative thickness (approx. 200-250  $\mu\text{m}$ ), the blood supply to the retina is provided via two routes that branch off the ophthalmic artery, the first major branch of the internal carotid artery (Figure 1.3). This facilitates oxygen and nutrient supply to all layers of the retina and allows rapid diffusion of molecules in order to meet the unique metabolic requirements of the different retinal cell types, most importantly the ganglion cells, directly responsible for transmitting visual information from the retina to the brain, and the light-sensitive photoreceptor cells.

The central retinal artery enters the eye through the optic nerve to branch into an extensive network of terminal capillaries supplying the inner retinal layers. They penetrate as deep as the external border of the INL and form two distinct capillary beds, namely the superficial capillary plexus of the GCL and the deep capillary plexus of the INL, leaving the outer retina, containing the photoreceptors, and the adjacent RPE avascular. The density of this capillary network is highest in the macula and decreases towards the peripheral retina. Interestingly, retinal blood vessels do not cross the central fovea, but arc around it, creating a capillary-free region of about 500-600  $\mu\text{m}$  in diameter, referred to as the foveal avascular zone (FAZ). Its main purpose is to allow maximum light detection without scattering due to blood vessels, thereby facilitating high acuity vision. On the other hand, posterior ciliary arteries feed the choroidal circulation, branching into a dense vascular network terminating with the fenestrated choriocapillaris adjacent to the Bruch's membrane, surrounded by a network of collagen fibrils that provides a structural supportive framework. The primary function of the choriocapillaris is to supply oxygen and nutrients to the outer retinal layers, most importantly the photoreceptors, and its loss can result in atrophy of the overlying retina (Provis, 2001; Saint-Geniez and D'Amore, 2004; Forrester et al., 2008, p.56; Anand-Apte and Hollyfield, 2010; Hildebrand and Fielder, 2011).

**A****B**

**Figure 1.3:** Blood supply of the retina.

**A.** A cutaway drawing along the superior–inferior axis of a left human eye through the optic nerve, showing details of the vascular supply in this location. The central retinal artery enters the eye through the optic nerve and gives rise to the inner retinal circulation supplying inner retinal layers. Posterior ciliary arteries feed the choroidal circulation to provide oxygen and nutrients to outer layers of the retina. **B.** A diagram showing details of the retinal and choroidal vasculature. The inner retinal circulation forms an extensive network of terminal capillaries that penetrate as deep as the external border of the inner nuclear layer and create two distinct capillary beds (superficial and deep capillary plexus), leaving the outer retina avascular. The choroidal circulation branches into a dense vascular network terminating with the fenestrated choriocapillaris next to the Bruch's membrane. *Drawings by Dave Schumick from Anand-Apte and Hollyfield (2010).*

Interestingly, the choroid receives about 80-85% of all blood entering the eye, compared with 4-5% supplied to the inner retina. At the same time, the choroidal circulation has one of the highest flow rates in the body, though this comes at the expense of a low oxygen exchange. By contrast, the blood flow through the inner retinal vessels is approximately 6-times slower, but with a high oxygen exchange. Lacking autonomic innervation, the retinal circulation is controlled by autoregulation. This refers to the intrinsic capacity of a tissue to maintain its blood flow constant despite variations of the perfusion pressure. Alternatively, it can also be defined as the ability of a tissue to optimise the blood supply in accordance with its nutritional requirements. Thus, the retinal blood flow is regulated by metabolism through the action of local factors that can modulate the retinal arterial tone. These factors are released by the vascular endothelium itself or the surrounding neural tissue and glial cells. They may be either ionic or molecular, related to arterial blood gas modifications or visual stimulation, and include for example pH level, temperature, partial O<sub>2</sub> and/or CO<sub>2</sub> pressure, light/dark transition, flicker and various endothelial vasoactive agents, such as nitric oxide, lactate, adenosine, angiotensin, endothelin and arachidonic acid metabolites (e.g. prostaglandins). Contrary to the inner retinal vasculature, the choroidal circulation is controlled primarily by extrinsic autonomic innervation, with little or no autoregulation. Importantly, disruptions of normal retinal and choroidal blood flow have been associated with several eye diseases, including diabetic retinopathy, age-related macular degeneration and glaucoma (Forrester et al., 2008, p.54, p.61 and p.241; Pournaras et al., 2008; Anand-Apte and Hollyfield, 2010; Hildebrand and Fielder, 2011; Kur et al., 2012; Purnyn, 2013).

## **1.2 Blood-retina barrier**

The blood-retina barrier (BRB) represents the interface between the vascular system and the retina. It has evolved in order to regulate transport of substances to the retina, thereby protecting the sensitive retinal neurons and photoreceptors from potentially harmful blood-borne agents, such as bacteria, viruses, toxins, immune cells and some plasma proteins. In this way, the BRB maintains a healthy ocular microenvironment and retinal homeostasis.

The existence of a permeability barrier in the retina was recognised through a series of experiments similar to those that led Paul Ehrlich and others to the discovery of the blood-brain barrier (BBB) (Ribatti et al., 2006). In 1885, Ehrlich was the first to observe that various water-soluble dyes injected into the systemic circulation stained all organs except the brain and spinal cord. Much alike this early work, Schnaudigel (1913), Palm (1947) and Ashton (1965) demonstrated that intravenously-injected trypan blue dye stained all organs of rabbits with the exception of the CNS, including the retina. These observations

were recapitulated using fluorescent dyes, colloidal carbon and silver deposition (Wislocki and Ladman, 1955; Rodriguez-Peralta, 1962; Cunha-Vaz et al., 1966) and were further supported at the ultrastructural level, providing the final evidence for the BRB existence and tight junction formation (Cunha-Vaz et al., 1966; Shakib and Cunha-Vaz, 1966).

The BRB has two distinct structural components, the inner and outer blood-retina barriers respectively, reflecting the two routes of blood supply to the retina (Figure 1.4). The inner blood-retina barrier (iBRB) consists of a single layer of non-fenestrated endothelial cells of the inner retinal microvasculature that express tight junctions to seal the intercellular space between neighbouring cells. Importantly, loss of the iBRB integrity causes retinal vascular leakage and subsequent formation of extracellular oedema in the retina that contribute to the pathophysiology of multiple blinding retinal conditions, including diabetic retinopathy, retinal vein occlusions and uveitis (Frey and Antonetti, 2011; Klaassen et al., 2013). The outer blood-retina barrier (oBRB) is formed by the RPE and its barrier properties are also maintained through the expression of tight junctions between adjacent cells that selectively regulate the paracellular movement of substances between the fenestrated blood vessels of choriocapillaris and the subretinal space. Noticeably, epithelial tight junctions are localised specifically at the most apical side of the polarised lateral membrane and appear as contact points of close apposition ("kissing points"), where the two phospholipid bilayers become indistinguishable (Farquhar and Palade, 1963). On the other hand, in endothelial barriers these contact points are located at several sites along the paracellular space between cells as well as within the cell forming the capillary lumen (Reese and Karnovsky, 1967).

### *1.2.1 Transport across the BRB*

The BRB is a highly selective barrier that controls the movement of ions, water, solutes and cells from the retinal blood vessels to the retina. The passage of molecules through the barrier is mediated by two main routes. The transcellular pathway (transcytosis) can occur via multiple mechanisms. Small gaseous and lipophilic molecules, such as O<sub>2</sub> and CO<sub>2</sub>, are able to passively diffuse through cell membranes. The majority of molecules, however, can only cross the BRB via ATP-dependent pathways. Small ions and water are transported through ion channels. Essential polar molecules, such as glucose, amino acids, nucleosides and organic ions, are shuttled across cell membranes using carrier-mediated transporters. Large solutes, such as proteins and peptides, are transported across the BRB by receptor-mediated or adsorption-mediated endocytosis. Moreover, active efflux pumps return many unwanted molecules back to the circulation. Importantly, the expression of all channels, transporters, receptors and vesicle mediators involved in the transcellular transport across



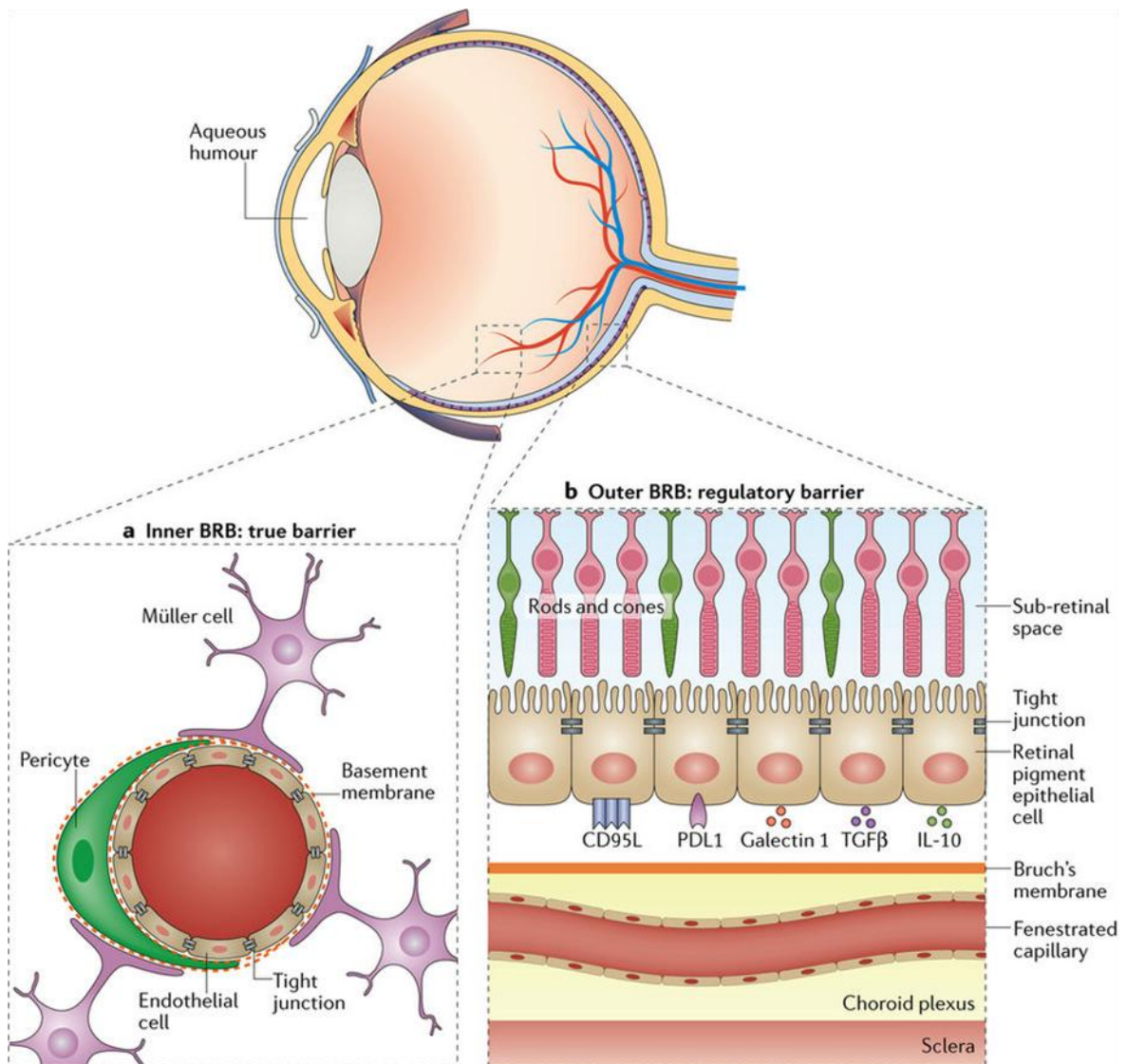


**Figure 1.4:** Components of the blood-retina barrier.

The blood-retina barrier (BRB) represents the interface between the vascular system and the retina. Structurally, it reflects the two routes of blood supply to the retina and consists of the inner BRB formed by endothelial cells of the inner retinal microvasculature and the outer BRB consisting of the retinal pigment epithelium. *From Spadoni et al. (2017).*

the BRB is tightly regulated and is generally quite low (Sagaties et al., 1987), combined with a high expression of efflux pumps. In addition, the BRB has a relatively low content of intracellular vesicles, indicating a low level of vesicle-related transport, and a highly polarised distribution of specific membrane receptors and transporters. Interestingly, the rate of transcytosis increases in pathological conditions (Lightman and Greenwood, 1992; Gardiner et al., 1995). The paracellular transport, which occurs through the intercellular

space, is regulated by tight junctions, restricting the passage of molecules greater than 20-30 kDa (Forrester et al., 2008, p.240-241; Díaz-Coránguez et al., 2017).

### *1.2.2 Tight junctions*

Tight junctions represent a series of more than 40 interacting proteins that can be divided into 1) transmembrane proteins, comprising claudins, occludin, tricellulin and junctional adhesion molecules (JAMs), and 2) cytoplasmic scaffold (adaptor) proteins, for example zonula occludens (ZO) (Díaz-Coránguez et al., 2017). Assembly of a functional tight junction complex involves homotypic and/or heterotypic interactions between extracellular domains of transmembrane proteins expressed on neighbouring cells that are linked to the actin cytoskeleton via their intracellular partners. Tight junctions have evolved for the specific purpose of protecting neural tissues from potential blood-borne toxicity and maintaining proper neural homeostasis by regulating the paracellular transport. In addition, they confer cell polarity by preventing movement of lipids and proteins between the apical and basolateral aspects of the plasma membrane (van Meer and Simons, 1986; Mandel et al., 1993) and have also been implicated in a number of cell-signalling processes, including proliferation, gene expression and differentiation (Takano, 2014; Osanai, 2017). However, tight junctions of the BRB represent a significant impediment to successful drug delivery to the retina and developing therapies for retinal diseases. In fact, it has been estimated that about 95-98% of clinically validated drugs cannot easily diffuse across the paracellular pathway (Pardridge, 2005). Interestingly, RNA interference (RNAi)-mediated approaches to downregulate expression of tight junction proteins allow for a controlled, localised, transient and reversible modulation of the BRB that renders the barrier permeable to low molecular weight compounds (up to 1 kDa), while at the same time excluding larger, potentially harmful, substances. The use of this safe and minimally invasive barrier modulation strategy in tandem with systemic drug administration was shown to enhance drug delivery to the retina and was highly efficient in preventing retinal degeneration and neovascularisation in several mouse models (Campbell et al., 2009; Campbell et al., 2011).

### *1.2.3 The neurovascular unit*

Maintenance of the iBRB integrity is dependent on the support provided by additional cell types, including neurons, glia (especially astrocytes and Müller cells) and pericytes, that together with endothelial cells form a neurovascular unit (NVU), the major structural and functional building block of the iBRB. These cells express specific factors that promote tight junction assembly at cell contacts and regulate the iBRB permeability. Interactions

between pericytes and endothelial cells are important for the maturation, remodelling, stabilisation and maintenance of retinal capillary vasculature (Fisher, 2009; Anand-Apte and Hollyfield, 2010). Furthermore, pericytes secrete growth factors, including TGF- $\beta$ , angiopoietin-1 (Ang-1) and sphingosine-1-phosphate-1 (S1P1), that control endothelial cell functions, such as growth, proliferation, differentiation and migration (Antonelli-Orlidge et al., 1989; Murphy-Ulrich and Poczatek, 2000; Jain and Booth, 2003; Garcia et al., 2004), or promote glial interactions (Armulik et al., 2010). They also regulate capillary blood flow as well as the clearance and phagocytosis of cellular debris. Loss of pericytes results in locally reduced retinal blood flow, followed by damage to the blood vessels, increased permeability, deposition of plasma proteins and barrier breakdown (Armulik et al., 2010; Bell et al., 2010; Daneman et al., 2010). Glial cells (astrocytes and Müller cells) support the iBRB in a structural (mechanical) way by making physical contacts with endothelial cells as well as mediate active communication between neural and vascular cells through intercellular signalling. They also modulate expression and polarisation of transporters, promote specialised enzyme systems and secrete growth factors known to enhance tight junction formation and barrier characteristics in endothelial cells, such as glial-derived neurotrophic factor (GDNF), basic fibroblast growth factor (bFGF) and Ang-1 (DeBault and Cancilla, 1980; Janzer and Raff, 1987; Abbott, 2002; Lee et al., 2003; Haseloff et al., 2005; Abbott et al., 2006). They maintain the local microenvironment by absorbing fluid from the retinal tissue and regulating the uptake of neurotransmitters from nerve terminals, the uptake of nutrients and the disposal of waste products (Tout et al., 1993; Distler and Dreher, 1996; Nagelhus et al., 1999; Reichenbach et al., 2007; Goodyear et al., 2009). In addition, they might control local blood flow in response to changes in neuronal activity (Paulson and Newman, 1987). Abnormalities in glial cell function are associated with neuronal dysfunction and death, retinal swelling and iBRB breakdown (Dyer and Cepko, 2000; Bringmann et al., 2006).

### **1.3 Age-related macular degeneration**

Age-related macular degeneration (AMD) is a degenerative retinal condition that results from the progressive loss of photoreceptors in the macula. This causes central vision loss and, if untreated, may lead to complete blindness. Although the first descriptions of AMD appeared as early as 1850s, it took over 150 years until a clearer concept of the disease was formulated and its high prevalence and impact on the quality of life were appreciated (de Jong, 2016). Some of the early signs and symptoms of AMD include central visual field defects, such as reduced ability to distinguish contrasts, distortion of straight lines, colour

vision impairment and loss of fine central vision, resulting in blurred images and scotomas (central dark spots). Despite sufficient peripheral vision being usually preserved in AMD, especially in its early stages, patients typically lose their ability to read, drive and recognise faces as the disease progresses.

### *1.3.1 Prevalence and epidemiology of AMD*

According to the World Health Organisation (WHO), AMD accounts for 1% of all cases of visual impairment and ranks third as a cause of blindness worldwide, being responsible for approximately 5% of cases. More importantly, it is the leading cause of central vision loss and blindness in the elderly and the primary cause of visual impairment in industrialised countries (Pascolini and Mariotti, 2012). In addition, AMD is the only disease among the main causes of visual impairment that WHO classifies as non-avoidable, i.e. it cannot be prevented or cured if diagnosed and treated early.

In 2010, the economic burden associated with AMD was estimated as 33 million cases and \$343 billion, including \$255 billion in direct health care costs (Access Economics, 2010). The global prevalence of the disease, including its very early stages, was calculated to be 8.7% in people over the age of 45. The prevalence consistently increased with age in all ethnic groups and geographic regions and globally, approximately 1 in 5 people in the age group 70-79 suffered from some form of the disease. The risk of AMD development was even more pronounced in the age group 80-84, with every fourth person being an AMD patient. The number of elderly people worldwide currently living with AMD is similar to that of people diagnosed with the most prevalent types of invasive cancer and is expected to reach 196 million by 2020. Furthermore, as the life expectancy increases globally, the number of people affected by AMD is predicted to rise to 288 million by 2040 (Bright Focus Foundation; Wong et al., 2014).

AMD also remains the leading cause of blindness in Ireland, accounting for 23.44% of all cases. The overall prevalence of any AMD is estimated to be 7.2% in the population aged 50 years or older and, similar to other countries, it increases with age. While it accounts for only 1% and 3% of blindness in the age groups 20-44 and 45-59, respectively, it is the primary cause of blindness for those aged 60 years or older, with 35% of blind people being AMD sufferers. In addition, AMD is also expected to be responsible for 28,000 cases of mild or moderate visual impairment by 2020. The economic costs associated with the expenditure on AMD drugs were approximately €5.8 million in 2010 and are expected to increase in the future (National Council for the Blind of Ireland, 2011; National Council for the Blind of Ireland, 2012; Akuffo et al., 2015).

### *1.3.2 End-stage forms of AMD*

Advanced (late) AMD occurs in two clinical forms. Non-neovascular, also known as non-exudative or "dry", AMD is characterised by geographic atrophy (GA) extending to the centre of the macula, involving a gradual loss of the RPE and photoreceptors due to cell death. This form of the disease affects the majority of AMD patients (approx. 85-90%), but is considered less severe, with a chronic vision deterioration over a longer period of time. On the other hand, neovascular AMD, also called exudative or "wet" AMD, is associated with choroidal neovascularisation (CNV), involving abnormal growth of choroidal blood vessels through the Bruch's membrane and RPE. Unlike normal blood vessels, these CNVs are permeable to blood components, resulting in leakage into the subretinal space. Hence, additional manifestations of this AMD form might include subretinal fluid accumulation, lipid deposition, haemorrhage, RPE detachment and inevitably fibrotic scarring. Although this form is less common among AMD patients (approx. 10-15%), it is much more severe and leads to an acute (rapid) vision loss (Jager et al., 2008). Interestingly, not all patients suffering from the non-neovascular form of the disease will necessarily progress to develop the more severe neovascular AMD.

### *1.3.3 Risk factors in AMD*

AMD is a complex, multifactorial disease. Although the exact causes are still not fully understood, a number of genetic and environmental risk factors have been implicated in its development and progression. A recent meta-analysis of genome-wide association studies identified 19 genetic loci, including 7 previously unreported, that associated with increased susceptibility to AMD. These comprised genes involved in the regulation of complement activity, lipid metabolism, extracellular matrix remodelling and angiogenesis (AMD Gene Consortium, 2013). Factors, such as advanced age, gender, race, smoking and oxidative stress, are now well established within the field that lead to a substantially increased risk of AMD. Additional factors may also contribute to disease development, including prolonged exposure to sunlight and many cardiovascular-related risk factors, such as hypertension, obesity, arteriosclerosis and unhealthy diet, especially high dietary intake of vegetable fat and cholesterol and low dietary intake of antioxidants, minerals and vitamins (Age-Related Eye Disease Study Research Group, 2000; Clemons et al., 2005; Jager et al., 2008; Parekh et al., 2009; Dasari et al., 2011; Millen et al., 2011; Sui et al., 2013).

### *1.3.4 Clinical hallmarks of AMD*

The AMD-associated loss of photoreceptors in the macula is thought to occur secondary to

the progressive degeneration and subsequent death of the RPE. Clinically, AMD manifests by the extracellular deposition of drusen at the Bruch's membrane, i.e. between the RPE and the underlying choroid, and the intracellular accumulation of lipofuscin inside RPE cells. Importantly, the presence of drusen in the macula, the density of the deposits and the area covered by drusen together represent an important diagnostic indicator of early AMD development. In addition, drusen deposition and lipofuscin accumulation are well known to increase the risk for progression of AMD and individuals with drusen and lipofuscin are considered at risk for developing the end-stage blinding forms of the disease. Therefore, extracellular drusen deposits and accumulated intracellular lipofuscin are thought to play a central role in the pathology of AMD (Sarks et al., 1980; Bressler et al., 1990; Pauleikhoff et al., 1990; Vinding, 1990; Holz et al., 1999; Holz et al., 2007).

#### 1.3.4.1 Drusen deposition

Proteomic and immunohistochemical analyses have shown that drusen consist primarily of the glycoprotein vitronectin, serum amyloid P component, apolipoprotein E, coagulation factor X (thrombokinase), immunoglobulin light chains, serum albumin, proteins of the complement cascade, Alzheimer's A $\beta$ -peptide, TIMP3, clusterin (apolipoprotein J) and a number of crystallins synthesised in response to stress (Mullins et al., 2000; Johnson et al., 2002; Anderson et al., 2004; Luibl et al., 2006). Interestingly, these constituents are not unique to AMD drusen composition, but are also found in extracellular deposits associated with several other diseases, such as atherosclerosis, elastosis, dense deposit disease and amyloidosis (Mullins et al., 2000). Moreover, up to 65% of proteins found in drusen are present in drusen isolated from both AMD and non-diseased donors. However, products of lipid oxidation (e.g. carboxyethyl pyrrole (CEP), 4-hydroxynonenal and malondialdehyde), oxidative protein modifications (including abnormal protein cross-links) and advanced glycation end products are more abundant in drusen and serum of AMD patients compared to healthy controls (Crabb et al., 2002; Gu et al., 2003; Zarbin, 2004; Wang et al., 2009; Lin et al., 2011). In addition, at least 40% of drusen are composed of lipids, especially esterified cholesterol and phosphatidylcholine (Wang et al., 2010). Accumulation of drusen deposits at the Bruch's membrane causes gradual separation of the RPE from underlying choroidal vascular bed which supplies oxygen and nutrients to the outer retinal layers. As these deposits increase in number and size, the proper functions of the RPE and choroid are progressively impaired and fail to provide the essential support to photoreceptors, which subsequently leads to their degeneration and death.

#### 1.3.4.2 Lipofuscin accumulation

Lipofuscin is a complex aggregate of pigmented material that results from an incomplete lysosomal degradation of phagocytosed POSs. Although its exact composition is not clear, one of its major known constituents is a fluorophore A2E, which is a byproduct of visual cycle (Sparrow and Boulton, 2005). Importantly, components of lipofuscin (especially the A2E fluorophore) cause irreversible inhibition of lysosomal degradative functions, mainly the cathepsin activity, and act as auto-oxidants, increasing oxidative stress within the RPE (Holz et al., 1999; Schütt et al., 2000; Finnemann et al., 2002; Bergmann et al., 2004; Hammer et al., 2006). Long-term oxidative stress causes damage to mitochondrial DNA, contributes to mitochondrial stress and subsequently leads to generation of reactive oxygen species (ROS). In line with this, increased mitochondrial stress and dysfunction have been observed clinically in the RPE of AMD patients (Feher et al., 2006; Nordgaard et al., 2008; Karunadharma et al., 2010; Lin et al., 2011). Furthermore, mitochondrial dysfunction and lipofuscin components act in synergy to reduce the RPE metabolic capacity (Vives-Bauza et al., 2008).

#### 1.3.4.3 RPE cell death

There is increasing evidence that long-term oxidative stress and cumulative oxidative damage inside the RPE have a negative effect on POS phagocytosis and autophagy, while at the same time they promote protein aggregation and drusen formation, thus contributing to AMD pathogenesis (Winkler et al., 1999; Beatty et al., 2000; Kaarniranta et al., 2011; Jarrett and Boulton, 2012; Plafker et al., 2012). In addition, impaired autophagy flux contributes to lipofuscinogenesis and protein aggregation as well as prevents the selective removal of oxidatively-damaged mitochondria, resulting in increased ROS production (Kaarniranta, 2010; Krohne et al., 2010; Yang and Klionsky, 2010; Mizushima and Komatsu, 2011; Mitter et al., 2012). Moreover, the reduced ability to absorb scattered light can further enhance the photooxidative damage. This leads to a vicious cycle of oxidative damage, impaired metabolic function, increased lipofuscinogenesis and drusen deposition, accumulation of damaged and dysfunctional mitochondria, combined with the failure to effectively clear these damaged organelles and protein aggregates, all of which contribute to a gradual degeneration and death of RPE cells, followed by the death of photoreceptors, as observed in AMD (Kaarniranta et al., 2013; Klettner et al., 2013).

Although the exact mechanism of RPE cell death in AMD remains unclear, a number of different pathways have been proposed. Pyroptosis can be defined as a caspase-1-mediated type of programmed cell death that has evolved as an innate immune effector mechanism

against intracellular bacteria (Miao et al., 2010). It is characterised by pore formation in the plasma membrane, which disrupts cellular ionic gradients, causing an increase in osmotic pressure, water influx, cell swelling and subsequent membrane rupture, followed by release of pro-inflammatory intracellular contents. DNA cleavage and nuclear condensation also occur during pyroptosis, however, these are distinct from the DNA laddering observed in apoptosis. Caspase-1-dependent RPE cell death has been detected in response to lysosomal destabilisation and cathepsin release (Tseng et al., 2013). Apoptosis represents a form of programmed cell death that is mechanistically defined by the requirement for particular caspases (mainly caspase-2, -3, -6, -7, -8, -9 and -10), which mediate an orchestrated cell disassembly. It is fundamentally an anti-inflammatory type of cell death, with its main role to limit the inflammatory response. Other characteristic features include cytoplasmic and nuclear condensation and DNA cleavage (distinct from those associated with pyroptosis), maintenance of an intact plasma membrane, loss of mitochondrial integrity and release of cytochrome-c. It was proposed that the cytotoxic effects of *Alu* RNA accumulation in the RPE might be mediated by caspase-3-dependent apoptosis (Kaneko et al., 2011; Tarallo et al., 2012), however, there was no evidence of this type of cell death in response to a drusen component A $\beta$ -peptide 1-40 in a different experimental model (Liu et al., 2013). Yet another line of evidence suggested that RPE cell death observed in AMD could occur via necroptosis (programmed necrosis), controlled by the receptor-interacting serine/threonine-protein kinase 3 (RIPK3), and that necrotic cell death mechanisms may be the essential part of the cell death modality contributing to the pathology in human subjects (Holler et al., 2000; Vandenabeele et al., 2010; Murakami et al., 2014).

### *1.3.5 Current therapies for AMD*

Currently, there is no standard treatment for dry AMD. Dietary supplementation with vitamins, antioxidants and certain dietary lipids has been beneficial in some cases and associates with a decreased risk of progression to neovascular AMD. The current therapies for wet AMD involve the use of antibodies (ranibizumab, bevacizumab) or recombinant inhibitors (aflibercept) that target VEGF bioactivity and thus suppress CNV development. However, this treatment requires direct and regular intravitreal injections that can be accompanied by retinal detachment, haemorrhage and infection (CATT Research Group et al., 2011). Therefore, new preventive and non-invasive therapeutic alternatives for AMD would be preferable in the future.



## **1.4 Sterile inflammation in AMD pathology**

Inflammation represents a part of an innate immune response and generally refers to the recruitment and activation of immune cells to the site of infection in order to facilitate clearance of pathogens, initiate tissue repair and restore homeostasis. The inflammatory response is triggered by pattern recognition receptors (PRRs), recognising common motifs broadly shared by groups of related pathogens, known as pathogen-associated molecular patterns (PAMPs). PRRs are in turn linked to intracellular signal transduction pathways that activate various cellular responses, mostly involved in the production of inflammatory mediators (cytokines and chemokines), cytoprotection and tissue repair, often through the activation of transcription factors nuclear factor kappa-light-chain-enhancer of activated B cells (NF- $\kappa$ B), activator protein 1 (AP-1) or interferon regulatory factor (IRF). In addition, PRRs also detect products of stressed, injured or dying cells, referred to as danger/damage-associated molecular patterns (DAMPs), leading to sterile inflammation in the absence of an infectious pathogen, to facilitate tissue repair. In recent years, AMD has been associated with a state of chronic local low-grade inflammation, termed para-inflammation, of the retina, accompanied by the activation of resident immune cells and the complement system, production of a number of inflammatory mediators and infiltration of peripheral immune cells to the site of retinal damage (Medzhitov, 2008; Xu et al., 2009; Whitcup et al., 2013; Nita et al., 2014; Chen and Xu, 2015).

### *1.4.1 Immune privilege of the eye*

Immune privilege can be defined as the ability of a tissue or organ to tolerate introduction of antigens without eliciting a systemic inflammatory immune response. It is believed to be an evolutionary adaptation to protect vital structures with a limited regenerative capacity from the potential inflammation-mediated damage. Especially in the case of the retina, any (even minor) structural perturbations to its fine architecture and/or functional dysregulation of its cellular components may lead to severe visual impairment or vision loss.

Immune privilege of the eye is maintained via multiple mechanisms that together prevent over-reactive systemic immune responses to antigens. The presence of the BRB along with the lack of direct lymphatic drainage provide a physical barrier, limiting free entry and exit of cells and molecules into and out of the eye, thus sequestering any antigens within the intraocular compartment where they are unlikely to be recognised by the immune system, a process known as immunological ignorance. Moreover, the local microenvironment within the eye comprises a number of immunomodulatory factors, both soluble and cell surface-bound, including TGF- $\beta$ , neuropeptides (such as  $\alpha$ -melanocyte-stimulating hormone and

vasoactive intestinal peptide), CD86, FasL, thrombospondin and galectins, that can inhibit activation of immune cells and the complement system, promote anti-inflammatory cell phenotypes (especially regulatory T<sub>reg</sub> cells) and cytokine production, or induce apoptosis of infiltrating lymphocytes. In addition, the eye can dynamically interact with immune organs (spleen and lymph nodes) to regulate systemic immune cell responses and induce immune tolerance to foreign antigens. Clearly, this has important implications in relation to tissue transplantation, as tissue grafts can survive for extended periods of time in immune privileged sites without rejection occurring, reflected by a high acceptance rate of corneal transplants, even in the absence of a subsequent immunosuppressive therapy, provided the ocular immune privilege has not been previously compromised. On the other hand, the physical isolation of immune privileged sites from the immune system renders them more susceptible to autoimmunity, resulting from the lack of self-antigen presentation during immune cell development. Hence, if such self-antigens enter the blood stream, either by chance or following a trauma, and are presented to circulating immune cells, they trigger an inflammatory response against the normally immune privileged tissue from which these antigens are derived, as observed in sympathetic ophthalmia or uveitis. Similarly, damage to the physical barriers and/or changes in the local microenvironment caused by exogenous or endogenous factors, for example injury, infection and advanced age, may compromise the ocular immune privilege and lead to systemic inflammation promoting further tissue dysfunction (Streilein, 2003; Taylor, 2009; Zhou and Caspi, 2010).

#### *1.4.2 Para-inflammation in the aging retina*

A number of physiological changes have been described to occur in the retina as part of normal healthy aging. In general, these are associated with a long-term accumulation of oxidative and metabolic stress, and include a steady loss of photoreceptors, Bruch's membrane thickening, choroid thinning, hard drusen formation and breakdown of the BRB (Ardeljan and Chan, 2013). To this end, para-inflammation, an intermediate state between basal homeostatic conditions and a true inflammatory response, exists to adapt the different retinal cells to the persistent low levels of local stress in order to maintain and/or restore their adequate functionality. For example, innate immune cells, in particular microglia, undergo low levels of activation during the aging process, accompanied by an increase in their number and migration into the subretinal space. Importantly, para-inflammation in the retina can be beneficial if it is well controlled or detrimental if it becomes dysregulated, either due to genetic predisposition or environmental factors enhancing the oxidative and metabolic stress, thus exacerbating the inflammatory responses, and might progress to

chronic pathological inflammation contributing to AMD development (Medzhitov, 2008; Xu et al., 2009; Whitcup et al., 2013; Nita et al., 2014; Chen and Xu, 2015).

#### *1.4.3 The complement system*

The complement system can be defined as a series of serum and cell surface proteins that interact, in a highly regulated manner, with one another and with other molecules of the immune system to generate important effectors of innate and adaptive immune responses. There are three major pathways of complement activation: 1) the classical pathway, which is activated by certain isotypes of antibodies bound to antigens, 2) the alternative pathway, activated on microbial surfaces in the absence of an antibody, and 3) the lectin pathway, which is activated by a plasma lectin that binds to mannose residues on microbes. All of these consist of a cascade of proteolytic enzymes that generate inflammatory mediators to promote inflammation, opsonins to enhance phagocytosis and lead to the formation of a common terminal complex causing cell lysis, referred to as the membrane attack complex (MAC) (Abbas et al., 2010, p.329-339 and p.494).

With regards to AMD pathology, virtually all complement proteins have been identified in drusen. Sequence variants associated with disease susceptibility have been characterised in several genes that are involved in the regulation of complement activity. Most importantly, single nucleotide polymorphisms (SNPs) in the gene encoding complement factor H (CFH) show the strongest association and confer major susceptibility to or protection from AMD (Edwards, et al., 2005; Hageman et al., 2005; Haines et al., 2005; Klein et al., 2005). CFH is the principal soluble inhibitor of the alternative complement pathway. Individuals who possess a single copy of the risk-conferring CFH haplotype have 2-4-fold increased risk of developing AMD during their lifetime, while the risk is 5-7-fold higher in those with two copies, highlighting the crucial role of the complement system in AMD pathology.

#### *1.4.4 The NLRP3 inflammasome*

Inflammasomes are large multimeric protein complexes that constitute an important part of the innate immune response. They function as platforms for the complete maturation and secretion of pro-inflammatory cytokines IL-1 $\beta$  and IL-18, by providing molecular scaffold for the activation of caspase-1 (Schroder and Tschopp, 2010; Dowling and O'Neill, 2012). The NACHT, LRR and PYD domains-containing protein 3 (NLRP3) inflammasome, one member of the inflammasome-forming nucleotide-binding oligomerisation domain (NOD)-like receptors, has previously been implicated in several inflammatory and autoimmune disorders, including rheumatoid arthritis, atherosclerosis, type 2 diabetes, obesity, gout and

neurodegenerative diseases, such as Alzheimer's disease, Parkinson's disease and multiple sclerosis (Martinon et al., 2006; Halle et al., 2008; Duewell et al., 2010; Strowig et al., 2012; Guo et al., 2015).

#### 1.4.4.1 Structure and assembly of the inflammasome complex

NLRP3, also called NALP3 or cryopyrin, is a member of the NOD-like receptor (NLR) family. NLRs are cytosolic PRRs sharing a common structure comprised of three structural domains. The central nucleotide-binding domain (NACHT) mediates ATP-dependent self-oligomerisation. It is flanked by C-terminal leucine-rich repeats (LRRs), which sense the presence of ligand, and a variable N-terminal domain responsible for homotypic protein-protein interactions. This can be either a caspase recruitment domain (CARD), a pyrin domain (PYD), an acidic transactivating domain or a baculovirus inhibitor repeat. NLRP3 can assemble into a large oligomeric structure of the inflammasome by recruitment of an adaptor protein apoptosis-associated speck-like protein containing a CARD (ASC; also known as PYCARD), via a homotypic interaction of their PYD domains, and pro-caspase-1 which interacts through its CARD domain with the CARD domain of ASC. In this way, the assembled inflammasome complex provides a scaffold for autocatalytic cleavage of the inactive pro-caspase-1 into its active p10/p20 tetramer which can cleave pro-IL-1 $\beta$  and pro-IL-18 into their biologically active mature forms that are secreted (Figure 1.5).

#### 1.4.4.2 Activation of the inflammasome complex

Canonical inflammasome activation is a two-step process requiring two signals to produce mature IL-1 $\beta$  and IL-18. The first step, referred to as the inflammasome priming, involves NF- $\kappa$ B-mediated upregulation of inflammasome components (Bauernfeind et al., 2009). Subsequently, a second signal is required to induce oligomerisation, caspase-1 activation and cytokine processing. The NLRP3 inflammasome is activated in response to a wide range of stimuli, including both infectious stimuli as well as sterile danger signals caused by cellular stress, such as high concentration of extracellular ATP and hyaluronan released from dying cells, increased extracellular glucose, a decrease in extracellular osmolarity or pH,  $\beta$ -amyloid fibres associated with Alzheimer's disease, crystals of monosodium urate or cholesterol, extracellular matrix components, aluminium vaccine adjuvants, environmental and industrial particles, such as silica and asbestos, or nanoparticles (Mariathasan et al., 2006; Martinon et al., 2006; Dostert et al., 2008; Eisenbarth et al., 2008; Halle et al., 2008; Hornung et al., 2008; Babelova et al., 2009; Yamasaki et al., 2009; Duewell et al., 2010; Yazdi et al., 2010; Zhou et al., 2010; Compan et al., 2012; Rajamäki et al., 2013). It has

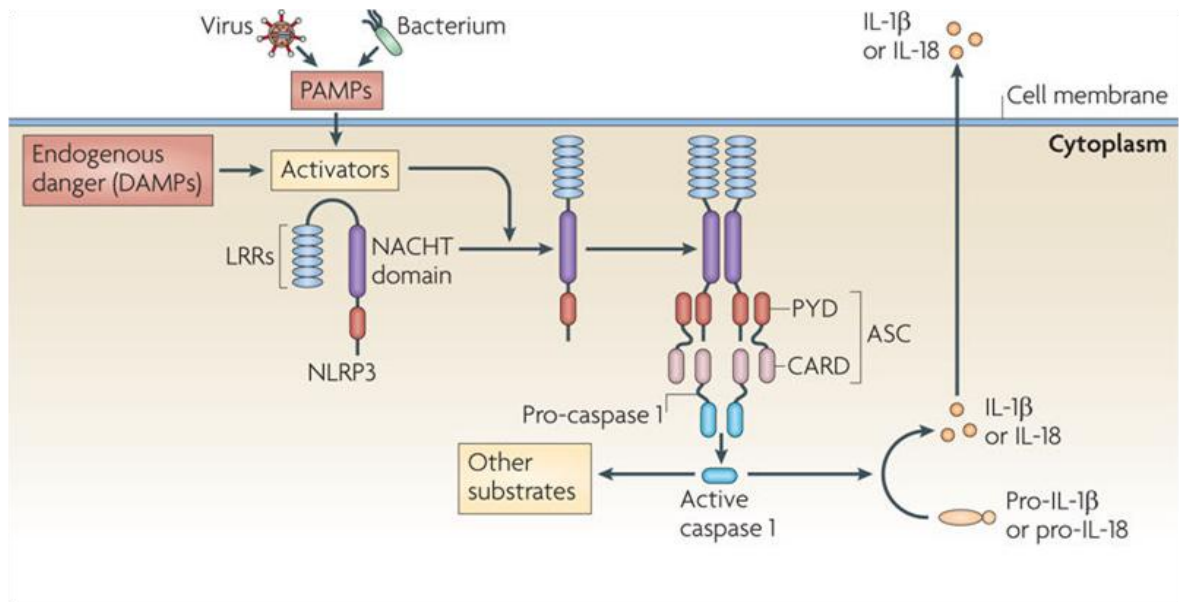


**Figure 1.5:** Mechanism of the NLRP3 inflammasome complex formation.

Upon inflammasome activation, NLRP3 oligomerises and recruits pro-caspase-1 through the adaptor protein ASC. The complex assembly is mediated via homotypic interactions of PYD domains of NLRP3 and ASC, and CARD domains of ASC and pro-caspase-1, respectively. Close proximity of pro-caspase-1 units triggers their autocatalytic cleavage and activation. The active caspase-1 subsequently cleaves precursor forms of IL-1 $\beta$  and IL-18 into their biologically active mature forms that are secreted. Other cytoplasmic proteins, such as enzymes of the glycolytic pathway, are also substrates of active caspase-1.

PAMPs, pathogen-associated molecular patterns; DAMPs, danger-associated molecular patterns; LRRs, leucine-rich repeats; NACHT domain, NAIP, CIITA, HET-E and TP1 domain; NLRP3, NACHT, LRR and PYD domains-containing protein 3; PYD, pyrin domain; ASC, apoptosis-associated speck-like protein containing a CARD; IL, interleukin; CARD, caspase recruitment domain. *From Tschopp and Schroder (2010).*

been suggested that all PAMPs and DAMPs might activate the inflammasome through a common general pathway. Even though this mechanism has not yet been identified, several different models have been proposed, including increased K<sup>+</sup> efflux, Ca<sup>2+</sup> signalling, damage to the phagolysosomal membrane and the activity of protein-degrading enzymes cathepsins, ROS generation and the release of oxidised DNA from mitochondria, TAK1 activation or NLRP3 deubiquitination, which also indicates that NLRP3 is more a sensor of cellular stress rather than a true receptor (Kahlenberg and Dubyak, 2004; Cruz et al., 2007; Pétrilli et al., 2007; Dostert et al., 2008; Halle et al., 2008; Hornung et al., 2008; Zhou et

al., 2010; Hoegen et al., 2011; Compan et al., 2012; Murakami et al., 2012; Shimada et al., 2012; Lopez-Castejon et al., 2013; Muñoz-Planillo et al., 2013).

#### 1.4.4.3 Role in AMD pathology

In 2012, our lab was the first to implicate the NLRP3 inflammasome in AMD development (Doyle et al., 2012). The idea came from the realisation that drusen are extracellular and particulate in nature, which are the main characteristics of typical inflammasome activators associated with other diseases. It was observed that drusen isolated from AMD donor eyes could induce ASC oligomerisation and caspase-1 cleavage *in vitro* in lipopolysaccharide (LPS)-primed peripheral myeloid cells, leading to IL-1 $\beta$  and IL-18 secretion. Furthermore, NLRP3-deficient (*Nlrp3*<sup>-/-</sup>) cells were unable to promote the production of mature IL-1 $\beta$  in response to drusen activation, directly implicating NLRP3 as the sensor for drusen-induced inflammasome formation. Interestingly, drusen alone seemed to be sufficient to cause ASC oligomerisation without a need for the priming step, even though there was no detectable IL-1 $\beta$  secreted in this case. Moreover, it was found that drusen components CEP and C1Q alone were capable of priming and activating the NLRP3 inflammasome, respectively. CEP-adducted human serum albumin (CEP-HSA) could prime the NLRP3 inflammasome to secrete IL-1 $\beta$  *in vitro* in peripheral myeloid cells, while priming with HSA alone had no effect on IL-1 $\beta$  production. In addition, the inflammasome priming by CEP-HSA was shown to be mediated specifically by TLR2 ligation as the levels of secreted IL-1 $\beta$  were decreased in *Tlr2*<sup>-/-</sup> cells primed with CEP-HSA, but not with LPS. Similarly, cells isolated from C3H/HeJ<sup>5</sup> mice produced IL-1 $\beta$  when primed with CEP-HSA, but not with LPS, while cells isolated from C3H/HeN mice secreted comparable levels of IL-1 $\beta$  under either priming conditions. This further confirms CEP to be a specific TLR2 ligand and implicates CEP-adducted proteins in drusen as previously unidentified inflammasome priming agents. Further *in vitro* studies showed that complement factor C1Q induced ASC oligomerisation, caspase-1 cleavage and subsequent production of IL-1 $\beta$  in primed peripheral myeloid cells, which was dependent on the presence of NLRP3. Moreover, all C1Q, either isolated from blood or found in drusen, had a tendency to aggregate. Based on this, it was suggested that a drusen component C1Q could act as a danger signal that is sensed by the NLRP3 inflammasome and that its aggregation is the key factor in the process. Noticeably, the C1Q-induced production of IL-1 $\beta$  and IL-18 not only required active caspase-1, but was also dependent on lysosomal acidification and cathepsin B, while at the same time it did

---

<sup>5</sup> C3H/HeJ mice carry a mutation in their *Tlr4* gene that renders them unresponsive to LPS. C3H/HeN mice do not have this mutation (Poltorak et al., 1998).

not rely on the production of ROS. Modelling the pathology of dry AMD *in vivo* by immunising mice with CEP-adducted mouse serum albumin (CEP-MSA) revealed that cleaved caspase-1 and NLRP3 were present in activated macrophages surrounding the drusen-like lesions in the eyes of these animals. Using a common mouse model of wet AMD it was found that NLRP3 was protective against laser-induced CNV lesion formation as the lesion development and volume were significantly exacerbated in *Nlrp3*<sup>-/-</sup> animals. Surprisingly, NLRP3 was not only present in immune cells, but was also detected in RPE cells *in vitro*, although the levels of secreted IL-1 $\beta$  were found to be very low.

Shortly after these initial studies, another report was published suggesting that the NLRP3 inflammasome was activated in GA in response to repetitive transposable elements of non-coding RNA, termed *Alu* RNA, that accumulated in the RPE due to a loss of a microRNA-processing enzyme DICER1 (Tarallo et al., 2012). The *Alu* RNA-mediated RPE toxicity occurred independently of TLRs or other canonical RNA sensors, but was dependent on the adaptor protein myeloid differentiation primary response 88 (MyD88). Moreover, *Alu* RNA was suggested to act as both a priming agent and an activator of the inflammasome. Up-regulation of *Nlrp3* and *Il18* mRNA in response to *Alu* RNA occurred through the production of ROS by mitochondria independently of MyD88. *Alu* RNA was also required for oligomerisation of NLRP3 and recruitment of ASC to subsequently activate caspase-1 in the inflammasome complex. Interestingly, MyD88 appeared to function downstream of the inflammasome, since MyD88 inhibition did not prevent *Alu* RNA-induced caspase-1 activation, whereas caspase-1 inhibition reduced *Alu* RNA-induced phosphorylation of interleukin-1 receptor associated kinase 1/4 (IRAK1/4), molecules downstream of MyD88. Clinically, RPE of human patients suffering from GA showed high abundance of *Nlrp3*, *Il18* and *Il1 $\beta$*  mRNA compared to healthy eyes, which was accompanied by an increase at protein level of NLRP3, ASC, caspase-1 p20 and phosphorylated forms of IRAK1 and IRAK 4. The authors of this study therefore proposed that DICER1 was an important negative regulator of the NLRP3 inflammasome activation in the RPE and that genetic or pharmacological inhibition of inflammasome components or MyD88 might prevent RPE degeneration due to DICER1 loss or *Alu* RNA exposure in dry AMD.

Results of the two above-mentioned studies, describing dichotomous effects of the NLRP3 inflammasome activation in the development of wet and dry AMD, respectively, prompted a lot of debate over the past few years about the exact involvement of the inflammasome and/or its components in AMD pathology (Figure 1.6). Since then, the assembly of the inflammasome complex and subsequent caspase-1 activation, accompanied by secretion of mature IL-1 $\beta$  and IL-18, have been observed in the RPE in response to oxidative stress,

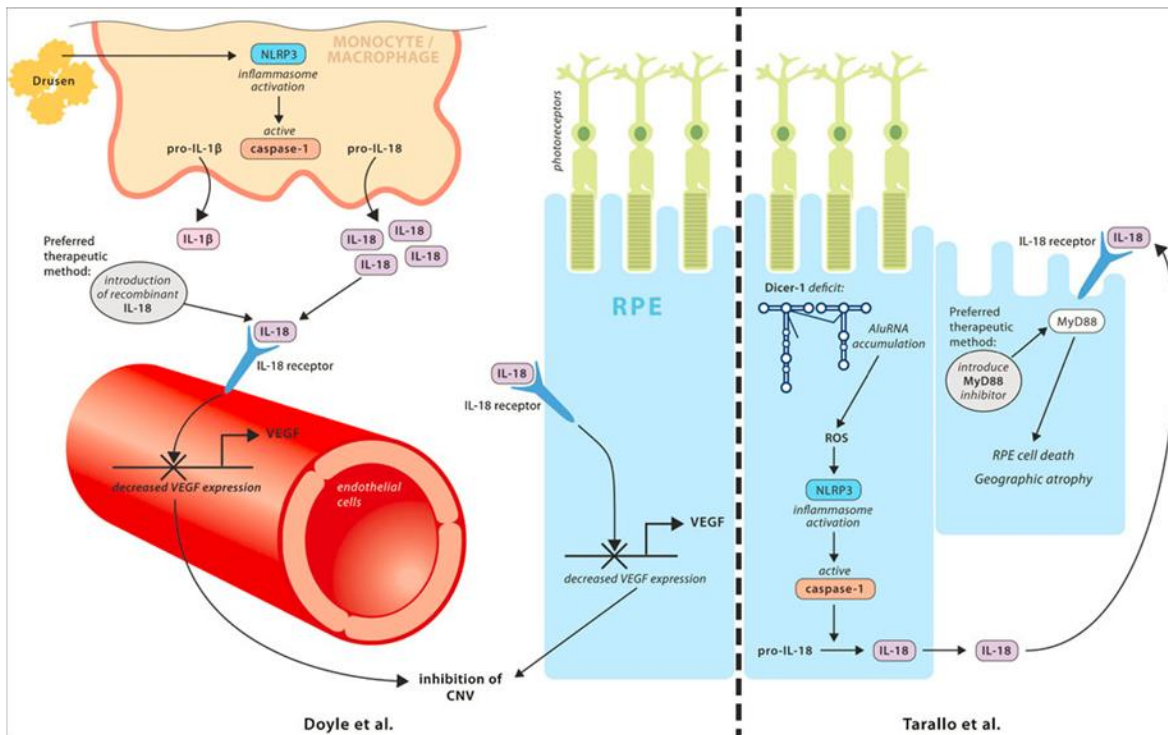


**Figure 1.6:** The NLRP3 inflammasome controversy in AMD pathology.

A diagram highlighting the dichotomous effects of the NLRP3 inflammasome activation in AMD development. Doyle et al. (2012) proposed that drusen isolated from AMD donor eyes could induce the inflammasome complex assembly followed by caspase-1 activation in peripheral myeloid cells, leading to secretion of IL-1 $\beta$  and IL-18. The mature IL-18 could subsequently activate IL-18 receptors on choroidal endothelial cells and RPE cells to inhibit the production of VEGF and prevent CNV development in a mouse model of wet AMD. Tarallo et al. (2012) suggested that the NLRP3 inflammasome was activated in dry AMD in response to *Alu* RNA that accumulated in the RPE due to DICER1 deficiency and that this activation occurred through the production of ROS by mitochondria. Mature IL-18 produced by the assembled inflammasome subsequently activated MyD88 in an autocrine manner through IL-18 receptor to cause RPE cell degeneration and death via apoptosis. NLRP3, NACHT, LRR and PYD domains-containing protein 3; IL, interleukin; VEGF, vascular endothelial growth factor; RPE, retinal pigment epithelium; CNV, choroidal neovascularisation; ROS, reactive oxygen species. *From Campbell and Doyle (2013).*

lysosomal destabilisation and cathepsin release, drusen components such as A $\beta$ -peptide 1-40, lipofuscin component A2E, increased VEGF levels, decline in cellular clearance mechanisms, including proteasome and autophagy, oxidised cholesterol and lipoproteins,



light, mitochondrial DNA and high extracellular NaCl (Kauppinen et al., 2012; Anderson et al., 2013; Liu et al., 2013; Marneros, 2013; Tseng et al., 2013; Liu et al., 2014; Piippo et al., 2014; Brandstetter et al., 2015; Dib et al., 2015; Shi et al., 2015; Gnanaguru et al., 2016; Prager et al., 2016; Wang et al., 2016; Wang et al., 2017). Despite the controversy, it is now widely accepted that the NLRP3 inflammasome components are present in and around the RPE of patients with both dry and wet AMD, although the exact role of this immune complex in AMD development and progression remains unclear. This concept, however, has recently been challenged by Kosmidou et al. (2017) who argued specificity of key reagents used to study NLRP3 in the RPE, questioning the interpretation of results reporting NLRP3 expression and upregulation in AMD. They suggested that RPE may not contain meaningful amounts of NLRP3 to contribute to diseased states and if NLRP3 is implicated in AMD, it is more likely to be related to resident or infiltrating immune cells.

#### *1.4.5 Interleukin-18*

IL-18 is a member of the IL-1 cytokine family. As discussed above, it is synthesised as an inactive precursor pro-IL-18 that requires cleavage by caspase-1 to produce a mature, biologically active cytokine. Mature IL-18 has the capacity to stimulate both Th1 and Th2 responses depending on the local microenvironment (Nakanishi et al., 2001a; Nakanishi et al., 2001b) and its activity is balanced by a naturally occurring high-affinity IL-18-binding protein (IL-18BP). A role for IL-18 has been implicated in a number of inflammatory conditions, whereas other disease models have shown protective effects of IL-18 (Boraschi and Dinarello, 2006; Dinarello et al., 2013). This highlights a dichotomous role for IL-18 that can be either protective or pro-inflammatory, depending on the immunological status of the cell or the type or phase of the inflammatory process (Bamias et al., 2012).

##### 1.4.5.1 Role in AMD pathology

Initial studies from our lab showed that NLRP3 conferred its protection against laser-induced CNV lesion formation in an IL-1 $\beta$ -independent manner through the induction of IL-18, as the lesion development was exacerbated in *Il18*<sup>-/-</sup> mice (similar to *Nlrp3*<sup>-/-</sup> mice), but not in *Il1r1*<sup>-/-</sup> animals. Furthermore, intravitreal administration of IL-18-neutralising antibodies following the introduction of laser-induced CNVs also resulted in significantly increased lesion formation, thus implicating IL-18 as a key regulator of pathological CNV development. In addition, IL-18 was found to significantly decrease the levels of VEGF secretion *in vitro* and it was suggested that the protective effects of IL-18 were mediated by controlling VEGF synthesis (Doyle et al., 2012). Moreover, exogenous administration

of mature recombinant IL-18, both intravitreal and systemic, attenuated laser-induced CNV lesion formation in mice. At the same time, IL-18 had no effect on the RPE cell viability or RPE barrier integrity, while remaining biologically active and stimulating NF- $\kappa$ B and p38 MAPK pathways. Although the IL-18 treatment was shown to work effectively alone, it was more potent in combination with anti-VEGF therapies currently used in the treatment of AMD (Doyle et al., 2014). This suggested that IL-18 might represent a novel therapeutic alternative and may be particularly beneficial for AMD patients who become unresponsive to anti-VEGF treatment. IL-18 also functions as an anti-angiogenic and anti-permeability factor. It was found to block VEGF-induced leakage and barrier breakdown, inhibit retinal and subretinal neovascularisation and prevent VEGF-induced suppression of vascular tight junctions in the retina (Shen et al., 2014). Noticeably, *Alu* RNA accumulation caused by DICER1 deficiency was shown to increase the secretion of IL-18, but not IL-1 $\beta$ , in human RPE cells after NLRP3 inflammasome activation, suggesting that IL-18 was the effector molecule in *Alu* RNA-mediated RPE cytotoxicity. In addition, neutralising IL-18, but not IL-1 $\beta$ , reversed *Alu* RNA-induced RPE degeneration and administration of a recombinant IL-18 induced RPE cell death independently of caspase-1. Hence, a model was proposed whereby IL-18 produced by the assembled inflammasome in the RPE in response to *Alu* RNA activated MyD88 in an autocrine manner through the IL-18 receptor to cause RPE cell degeneration via IRAK1/4-mediated apoptosis (Tarallo et al., 2012). Taken together, studies performed thus far suggest dichotomous effects of IL-18 in models of wet and dry AMD, although the precise role of IL-18 (similar to the NLRP3 inflammasome) in AMD pathology remains to be clarified.

### **1.5 Objectives**

Previous work in our lab demonstrated that IL-18 represented a potential new therapeutic strategy in the treatment of neovascular AMD, either as a stand-alone therapy which could be of a particular benefit to patients who do not respond to the classic treatment, or as a combination therapy with the currently used anti-VEGFs (Doyle et al., 2014). To further evaluate its therapeutic potential, the efficacy of IL-18 administration was investigated in a novel genetic mouse model of spontaneous neovascularisation, the JR5558 mouse strain. In addition, it was observed that IL-18 had potent anti-angiogenic and anti-permeability functions in the retina and it was suggested that these effects could be mediated by its regulation of VEGF synthesis (Doyle et al., 2012; Shen et al., 2014). The mechanism of IL-18 action was therefore examined *in vivo* and *in vitro*.

The NLRP3 inflammasome and its effector cytokine IL-18 have been shown to exhibit

dichotomous effects in the development and progression of wet and dry AMD (Doyle et al., 2012; Tarallo et al., 2012). Although it is now widely accepted that the inflammasome components are present in and around the RPE of AMD patients, their exact roles in AMD pathology remain unclear. Importantly, association of these factors with the diseased tissue might not automatically imply a causative role, even though the function (if any) of the inflammasome complex and IL-18 in normal retinal homeostasis is unknown. As already mentioned, the RPE plays an important role in POS renewal by phagocytically clearing their shed tips every morning. Therefore, activation of the inflammasome complex was studied with respect to the POS phagocytosis to establish its function in RPE homeostasis. The iBRB is autoregulated to optimise its blood supply in order to meet the metabolic requirements of all retinal neurons. Factors that modify the iBRB permeability have been extensively described with respect to disease pathology, however, the control mechanisms in retinal homeostasis are less characterised. Hence, the question of the iBRB permeability regulation in normal retinal physiology was addressed.

In summary, the main objectives of the present study were as follows:

- to evaluate IL-18 efficacy in a mouse model of spontaneous neovascularisation
- to examine changes in the RPE activity and the presence of inflammasome components in the RPE during the phagocytically active period at 8 AM compared to 8 PM
- to investigate effects of the diurnal changes in the RPE on the iBRB permeability

## Chapter 2

### **Materials and methods**

## 2 MATERIALS AND METHODS

---

### 2.1 Buffer compositions

Phosphate-buffered saline (PBS): 137 mM NaCl, 2.7 mM KCl, 1.5 mM KH<sub>2</sub>PO<sub>4</sub>, 8.1 mM Na<sub>2</sub>HPO<sub>4</sub> (pH 7.2-7.4)

Radioimmunoprecipitation assay (RIPA) lysis buffer: 50 mM Tris (pH 8.0), 1% (v/v) IGEPAL<sup>®</sup> CA-630, 150 mM NaCl, 0.5% (w/v) sodium deoxycholate, 0.1% (w/v) sodium dodecyl sulphate (SDS)

Resolving (separating) buffer: 1.5 M Tris (pH 8.8)

Stacking buffer: 0.5 M Tris (pH 6.8)

Running buffer: 192 mM glycine, 25 mM Tris, 0.1% (w/v) SDS (pH 8.6)

Transfer buffer: 192 mM glycine, 25 mM Tris, 20% (v/v) methanol (pH 8.3)

Tris-buffered saline (TBS): 50 mM Tris, 150 mM NaCl (pH 7.4)

TBS containing Tween<sup>®</sup> 20 (TBS-T): 50 mM Tris, 150 mM NaCl, 0.05% (v/v) Tween<sup>®</sup> 20 (pH 7.4)

DuoSet<sup>®</sup> ELISA wash buffer: 0.05% (v/v) Tween<sup>®</sup> 20 in PBS

DuoSet<sup>®</sup> ELISA reagent diluent: 1% (w/v) bovine serum albumin (BSA) in PBS

IL-18 ELISA wash buffer: 10 mM Tris, 150 mM NaCl, 0.1% (v/v) Tween<sup>®</sup> 20 (pH 7.5)

IL-18 ELISA reagent diluent: 1% (w/v) BSA, 10 mM Tris, 150 mM NaCl, 0.1% (v/v) Tween<sup>®</sup> 20 (pH 7.5)

Davidson's fixative: 8% (v/v) formaldehyde, 11% (v/v) acetic acid, 32% (v/v) ethanol

All chemicals used to make up buffers were from Sigma-Aldrich.

### 2.2 Animal studies

JR5558 mice were bred at GlaxoSmithKline (GSK; Stevenage, UK) and were shipped to Trinity College Dublin (TCD) for experimentation. C57BL/6J, 129, CD1 and *Il18*<sup>-/-</sup> mice were obtained from our in-house colony. *Bmal1*<sup>fl/fl</sup> animals were crossed with endothelial cell-specific Cre recombinase-expressing (Tie2-Cre) animals on C57BL/6J background to generate *Bmal1*<sup>fl/fl</sup> Tie2-Cre<sup>+</sup> mice and their corresponding littermate controls. All animals were genotyped before use in an experiment. *Bmal1*<sup>fl/fl</sup> Tie2-Cre<sup>+</sup> and *Bmal1*<sup>wt/fl</sup> Tie2-Cre<sup>+</sup> animals were used in the present study. Genotyping of experimental animals was carried out by Dr. Natalie Hudson.

All animals were housed in a specific pathogen-free (SPF) environment, were allowed free access to food and water and were maintained on a 12-hour light/dark cycle, with lights turned on at 8 AM and turned off at 8 PM. All animal experiments were assessed and

approved by an internal ethics committee at TCD. All studies adhered to the Association for Research in Vision and Ophthalmology (ARVO) statement for the use of animals in ophthalmic and vision research.

### *2.2.1 IL-18 administration in JR5558 mice*

Mouse IL-18 (SB-528775; GSK, Stevenage, UK) was injected intraperitoneally (i.p.) into JR5558 mice on four consecutive days. Two doses of IL-18 (diluted in saline), 100 or 1000 µg/kg body weight, were administered to examine any dose-dependent effects. An age-matched cohort of saline-injected animals was used as a negative control. Animals at 3-4 weeks of age were used to assess the effect on the progression of developing neovascular lesions. Animals older than 8 weeks (typically 9-13 weeks) were used in regression studies to assess the effect on established neovascular lesions.

## **2.3 Cell culture and *in vitro* experiments**

All cells were maintained in a humidified incubator at 37°C in 5% CO<sub>2</sub>, 95% air. All cell culture procedures were carried out under sterile conditions in a laminar flow cabinet.

Primary human foetal RPE (hFRPE) cells were isolated from human donor eyes and were generally cultured in minimum essential medium Eagle, alpha modification (MEM-α; Lonza), supplemented with 5% (v/v) foetal bovine serum (FBS; Sigma-Aldrich), 1% (v/v) L-glutamine (Gibco) and 1% (v/v) penicillin-streptomycin (Gibco). Cells, provided by Dr. Arvydas Maminishkis (National Eye Institute, USA), were received at the Ocular Genetics Unit as a confluent monolayer at passage 0 and were designated with a unique reference number that related to each donor. Cells were maintained as monolayers in flasks they arrived in, with three media changes per week, until they were used in experiments. All experimental procedures were carried out using cells at passage 1. To passage the cells, these were first washed twice with Dulbecco's phosphate-buffered saline (DPBS; Gibco) by filling the whole flask (≈ 50 ml) with buffer and removing it. The cell monolayer was subsequently incubated with 5 ml of 0.25% (w/v) trypsin-EDTA (Gibco) for 15 minutes at 37°C. Attached cells were stream-washed using a 2 ml syringe fitted with an 18G (pink) needle and the cell suspension was collected into a plastic tube containing ≈ 7 ml of cell culture medium supplemented with 15% (v/v) FBS. The trypsinisation step was repeated for further 5-10 minutes. After all cells have been dislodged from the flask surface, they were collected by centrifuging at 1000 rpm for 5 minutes and then resuspended in 7 ml of fresh growth medium supplemented with 15% (v/v) FBS. To minimise cell clumping and obtain a single cell suspension, the cells were thoroughly vortexed and passed through a

pipette several times. They were counted and seeded onto appropriate plates as required by the type of an experiment. One T25 flask usually yielded  $1.2-1.5 \times 10^7$  hFRPE cells. The typical seeding density used in most experiments was  $1.0-1.2 \times 10^5$  cells/cm<sup>2</sup>. Cells were cultured for at least 4 weeks before they were used in an experiment, with three media changes per week.

Mouse brain endothelial (bEnd.3) cell line (American Type Culture Collection, ATCC<sup>®</sup> CRL-2299<sup>™</sup>) was generally cultured in Dulbecco's modified Eagle medium (DMEM; Gibco), containing 25 mM glucose and GlutaMAX<sup>™</sup>, supplemented with 1 mM sodium pyruvate (Gibco) and 10% (v/v) FBS. The cells were routinely maintained by passaging once a week, with three media changes per week. To passage the cells, they were first washed with DPBS to remove all traces of serum which contains trypsin inhibitor. The cell monolayer was subsequently incubated with 0.25% (w/v) trypsin-EDTA for approximately 5 minutes at 37°C until the cells became completely detached from the flask surface. The trypsin was inactivated by adding complete cell culture medium supplemented with FBS. All cells were collected and centrifuged at 1000 rpm for 5 minutes. The cell pellet was resuspended in an appropriate volume of fresh growth medium and the cell suspension was split between 2-3 new flasks for routine subculturing. Cells were incubated at 37°C until they reached confluency, i.e. approximately 7 days, and then passaged again to maintain the line. Alternatively, they were counted and seeded onto suitable plates to be used in experimental procedures. The number of cells obtained was dependent on the surface area of the flask they were cultured in. The usual yield was  $\approx 4.0-5.0 \times 10^4$  cells harvested from 1 cm<sup>2</sup> of a cell culture flask. The typical seeding density used in most experiments was  $1.0 \times 10^4$  cells/cm<sup>2</sup> and the cells were cultured for at least one week before they were used in an experiment, with three media changes per week.

### *2.3.1 Cell counting procedure*

Cells were counted using the Luna<sup>™</sup> automated cell counter (Logos Biosystems) as per manufacturer's instructions. A thoroughly resuspended cell suspension was necessary to ensure accurate counting results. A 10 µl aliquot of cell suspension was mixed with 10 µl of 0.4% (w/v) trypan blue (Sigma-Aldrich). Duplicate samples were prepared. Then, 10-12 µl of the mixture were loaded into a chamber port on a counting slide and inserted into the cell counter. The image was focused to optimise it for analysis, so that live cells had bright centres and dark edges and dead cells had uniform blue colour throughout the cell with no bright centres, and the cells were counted. Only the number of live cells was considered in subsequent calculations.

### 2.3.2 *IL-18 treatment*

hfRPE cells were plated at a density of  $1.1 \times 10^5$  cells/cm<sup>2</sup> and allowed to reach confluency for approximately 4 weeks, with a regular medium change every 2-3 days. Cell monolayers were washed once with DPBS and treated with increasing doses (10, 50, 100 or 1000 ng/ml) of human IL-18 (SB-485232; GSK, Stevenage, UK) diluted in complete growth medium for 1, 3, 6, 12, 24, 36, 48 or 72 hours. Medium without IL-18 supplementation (0 ng/ml) was used as a negative control at each time point. Each treatment was carried out in triplicate.

bEnd.3 cells were plated at a seeding density of  $1.0 \times 10^4$  cells/cm<sup>2</sup> and allowed to reach confluency for 7 days, with a regular medium renewal every 2-3 days. Cell monolayers were washed once with DPBS and subsequently treated with a single dose (50 ng/ml) of mouse IL-18 diluted in complete growth medium for 12, 24 or 48 hours. Cells treated with control medium without IL-18 supplementation (Untreated) for 48 hours were used as a negative control for the experiment. Each treatment was carried out in triplicate.

### 2.3.3 *VEGF treatment*

bEnd.3 cells were seeded on 6.5 mm polyester membrane (pore size 0.4 mm) transwell inserts (Corning<sup>®</sup> Costar) at a density of  $1.5-2.5 \times 10^5$  cells/cm<sup>2</sup> and were allowed to polarise and reach confluency for 5 days, with a regular medium renewal in both chambers every 2-3 days. The cell monolayers were washed once with DPBS on both sides and treated with a single dose (50 ng/ml) of recombinant mouse VEGF (R&D Systems) diluted in complete growth medium, either on the basolateral or apical side, for up to 24 hours. Medium without VEGF supplementation was used as a negative control. Each treatment was carried out in triplicate.

Alternatively, bEnd.3 cells were plated at a seeding density of  $1.0 \times 10^4$  cells/cm<sup>2</sup> and allowed to reach confluency for 7 days, with a regular medium renewal every 2-3 days. Cell monolayers were washed once with DPBS and subsequently treated with a single dose (50 ng/ml) of recombinant mouse VEGF diluted in complete growth medium for 12 or 24 hours. Cells treated with control medium without VEGF supplementation (Untreated) for 48 hours were used as a negative control for the experiment. Each treatment was carried out in triplicate.

### 2.3.4 *Inflammasome activation*

hfRPE cells were plated at a density of  $1.1 \times 10^5$  cells/cm<sup>2</sup> and allowed to reach confluency for approximately 4 weeks, with a regular medium change every 2-3 days. Cell monolayers



were washed once with DPBS and primed with recombinant human IL-1 $\alpha$  (10 ng/ml; R&D Systems) diluted in complete growth medium for 0, 3 or 24 hours. Cell monolayers were washed again with DPBS and activated with ATP (2.5 mM; Sigma-Aldrich) diluted in complete growth medium for 0, 0.5, 1, 3 or 24 hours. Corresponding single treatments with IL-1 $\alpha$  or ATP alone and untreated cells were used as controls. Each treatment was carried out in triplicate.

### *2.3.5 POS treatment*

Isolated bovine POSs (bPOSs) were provided by Dr. Sarah Doyle (School of Medicine) and were stored at -80°C. The suspensions were gently passed through a needle just before use to prevent excessive bPOS aggregation. hFRPE cells were plated at a density of  $1.1 \times 10^5$  cells/cm<sup>2</sup> and allowed to reach confluency for approximately 4 weeks, with a regular medium change every 2-3 days. Cell monolayers were washed once with DPBS and treated with bPOSs diluted in complete growth medium at a ratio of 10 bPOSs per 1 hFRPE cell for 6 or 24 hours. Untreated cells were used as a negative control for the experiment. Each treatment was carried out at least in triplicate.

### *2.3.6 Serum starvation*

hFRPE cells were plated at a density of  $1.1 \times 10^5$  cells/cm<sup>2</sup> and allowed to reach confluency for approximately 4 weeks, with a regular medium change every 2-3 days. bEnd.3 cells were plated at a seeding density of  $1.0 \times 10^4$  cells/cm<sup>2</sup> and allowed to reach confluency for 7 days, with a regular medium renewal every 2-3 days. To serum starve cells, the cell monolayers were washed once with DPBS and treated with their corresponding serum-free growth medium. Cells treated with complete growth medium with serum supplementation appropriate for each cell type were used as a negative control for the experiment. Each treatment was carried out in triplicate.

## **2.4 Protein analysis**

### *2.4.1 Sample preparation and protein extraction*

To isolate tissues from mouse eyes, animals were sacrificed by cervical dislocation or CO<sub>2</sub> asphyxia. Eyes were enucleated, collected in PBS on ice and immediately dissected under a microdissection microscope (Leica Biosystems). The exterior of the eyeball was cleared off excessive muscle tissue, the optic nerve was snipped off and a small incision made at the ora serrata. The anterior parts of the eye (cornea, iris, lens) were dissected out along the circumference around the pars plana. The retina was carefully removed from the posterior

eye cup and lysed in 100-150  $\mu\text{l}$  of RIPA lysis buffer containing protease inhibitors (Roche Molecular Systems). All retinas were thoroughly homogenised by vortexing and repeated passing through a pipette tip. After incubation on ice for 30 minutes with occasional vortexing, tissue lysates were centrifuged at 13000 rpm for 20 minutes. Supernatants containing isolated protein were transferred into fresh tubes and stored at  $-20^{\circ}\text{C}$  until analysis.

For *in vitro* experiments, cell culture media were collected and centrifuged at 300 g for 8 minutes to pellet down any detached cells. The cell-free supernatants were transferred into fresh tubes and stored at  $-20^{\circ}\text{C}$  until analysis. Each cell monolayer was subsequently washed once with ice-cold DPBS and lysed in  $\approx 25\text{-}75 \mu\text{l}/\text{cm}^2$  (depending on the cell type) of RIPA lysis buffer with protease inhibitors. Cell lysates were transferred into eppendorf tubes, incubated on ice for 30 minutes with occasional vortexing and then centrifuged at 12000 g for 20 minutes to remove any unlysed cells, cell debris and insoluble material. Cleared supernatants containing extracted protein were transferred into fresh tubes and stored at  $-20^{\circ}\text{C}$  until analysis.

#### 2.4.2 Bicinchoninic acid (BCA) assay

The total protein concentration in cell and tissue lysates was determined using the Pierce<sup>®</sup> BCA protein assay kit (Thermo Scientific) as per manufacturer's instructions, following the recommended microplate procedure. A set of BSA standards of known concentration was prepared by serial dilutions of the 2 mg/ml BSA stock solution in  $\text{dH}_2\text{O}$  as outlined in Table 2.1. Sufficient volume of BCA working reagent was prepared by mixing 50 parts of BCA Reagent A with 1 part of BCA Reagent B. 10  $\mu\text{l}$  of each BSA standard and unknown protein sample were loaded in duplicate onto a 96-well plate and 200  $\mu\text{l}$  of the working reagent were added. The plate was sealed to prevent reagent evaporation and incubated for 30 minutes at  $37^{\circ}\text{C}$ . A colour change from light green to purple was detected, the degree of colour development being directly proportional to the amount of protein in a sample. The absorbance of each well was measured at 620 nm using the Multiskan<sup>™</sup> FC microplate photometer (Thermo Scientific) and 0  $\mu\text{g}/\text{ml}$  BSA standard solution as a blank. A standard curve was constructed by plotting the mean blank-corrected absorbance measurement of each protein standard against its concentration (in  $\mu\text{g}/\text{ml}$ ). The plotted data were fitted with second-order polynomial (quadratic) non-linear regression and used to determine protein concentration in each unknown sample.

<b>Final BSA concentration in the protein standard</b>	<b>Volume of diluent (dH<sub>2</sub>O)</b>	<b>Volume and source of BSA</b>
<b>2000 µg/ml</b>	0 µl	300 µl of 2 mg/ml BSA stock
<b>1500 µg/ml</b>	125 µl	375 µl of 2 mg/ml BSA stock
<b>1000 µg/ml</b>	300 µl	300 µl of 2 mg/ml BSA stock
<b>750 µg/ml</b>	150 µl	150 µl of 1500 µg/ml BSA solution
<b>500 µg/ml</b>	300 µl	300 µl of 1000 µg/ml BSA solution
<b>250 µg/ml</b>	300 µl	300 µl of 500 µg/ml BSA solution
<b>125 µg/ml</b>	300 µl	300 µl of 250 µg/ml BSA solution
<b>0 µg/ml</b>	300 µl	0 µl

**Table 2.1:** Preparation of protein standards in the BCA assay protocol.

### *2.4.3 Sodium dodecyl sulphate polyacrylamide gel electrophoresis (SDS-PAGE)*

#### 2.4.3.1 Pouring an SDS-PAGE gel

Proteins were separated on the basis of their molecular weight using the AE-6500 dual mini slab electrophoresis system (ATTO Corporation). First, the gel cast was prepared by assembling electrophoretic glass plates that were sealed with a rubber gasket and tightened by clamping on both sides. The resolving (separating) gel solution was prepared by mixing the components listed in Table 2.2 in the order shown (all were from Sigma-Aldrich). The ammonium persulphate (APS) and *N,N,N',N'*-tetramethylethylenediamine (TEMED) were always added last just before pouring the gel as they initiate gel polymerisation. APS forms oxygen free radicals in aqueous solutions by a base-catalysed mechanism. The free radicals subsequently cause polymerisation of acrylamide and bis-acrylamide to form a gel matrix. The percentage (%) of each gel, reflecting the size of gel pores, was selected depending on experimental requirements to achieve the best possible separation of proteins of interest. In general, lower % gels (with larger pores) are suitable for resolving higher molecular weight proteins, whereas the higher % gels (with smaller size of pores) are more appropriate for separating proteins of lower molecular weight. The resolving gel solution ( $\approx$  8 ml) was poured between the assembled glass plates, leaving sufficient space for the stacking gel corresponding to the length of a comb plus 1 cm. The top of the gel was overlaid with isopropanol to prevent it from drying out during polymerisation, to keep air bubbles away (as air would inhibit polymerisation) and to straighten the gel. Once the resolving gel was completely set (approx. 30-40 minutes at room temperature), the isopropanol overlay was

discarded, the top of the gel was washed with dH<sub>2</sub>O and the excess water dried between the plates with a filter paper. The stacking gel solution was prepared as specified in Table 2.2 and poured over the resolving gel until it reached the edge of the glass plates. A comb was inserted to create loading wells, taking caution not to trap any air bubbles in the gel as this would cause lane distortion during electrophoresis, and the gel was allowed to polymerise. If not used immediately, an SDS-PAGE gel could be stored overnight at 4°C, wrapped in wet tissue paper and cling film to keep it hydrated during storage.

Component	Resolving (separating) gel			Stacking gel
	10%	12%	15%	4%
<b>dH<sub>2</sub>O</b>	3.97 ml	3.3 ml	2.3 ml	1.7 ml
<b>Resolving (separating) buffer</b>	2.5 ml	2.5 ml	2.5 ml	-
<b>Stacking buffer</b>	-	-	-	420 µl
<b>Acrylamide/bis-acrylamide</b> 30% solution, 37.5:1	3.33 ml	4 ml	5 ml	330 µl
<b>10% (w/v) SDS (pH 7.2)</b>	100 µl	100 µl	100 µl	25 µl
<b>10% (w/v) APS (prepared fresh)</b>	100 µl	100 µl	100 µl	25 µl
<b>TEMED</b>	10 µl	10 µl	10 µl	2.5 µl
Total volume	10 ml	10 ml	10 ml	2.5 ml

**Table 2.2:** SDS-PAGE resolving (separating) and stacking gel composition (per 1 gel).

#### 2.4.3.2 Preparing protein samples for SDS-PAGE

Before loading onto an SDS-PAGE gel, a desired amount (typically 10 µg) of each protein lysate was adjusted with dH<sub>2</sub>O, so that all samples had equal volume, and diluted with an appropriate volume of 5x Pierce<sup>®</sup> lane marker reducing sample buffer (Thermo Scientific) to achieve the final concentration of 1x reducing sample buffer in each sample, by adding one volume of sample buffer to four volumes of protein lysate. All samples were vortexed to ensure thorough mixing, followed by boiling for 10 minutes at 95°C in a heating block. The samples were cooled to room temperature and pulse centrifuged to bring all liquid to the bottom of the tube before loading them on a gel. The addition of sample buffer ensures that proteins in a complex mixture are separated exclusively on the basis of their molecular weight (size) independent of their amino acid sequence and net charge. It contains excess

amount of SDS which dissociates proteins into their individual polypeptide subunits and confers a uniform negative charge along each denatured polypeptide, masking its intrinsic charge and binding in a constant weight ratio of 1.4 g SDS per 1 g polypeptide irrespective of its amino acid composition. Other constituents include dithiothreitol (DTT), a reducing agent which breaks any disulphide linkages in proteins so that all polypeptide subunits can be analysed separately, glycerol which increases sample density so that it will sink to the bottom of the well and will not diffuse into the buffer solution, and a tracking dye to allow monitoring the progression of an electrophoretic run.

#### 2.4.3.3 Running an SDS-PAGE gel

The electrophoresis chamber was placed on a flat surface and filled with running buffer to the indicated level ( $\approx$  200 ml). The rubber seal gasket and clamping clips were removed from the gel sandwich and it was slowly lowered into one side of the chamber with its notched glass plate facing inwards, while slightly slanting it to avoid trapping air bubbles at its bottom. Once in position, the gel sandwich was tightly fastened with a plastic plate holder. Two gel sandwiches are required to create a functioning assembly. Thus, to close the circuit when running only one gel, empty plates were placed to the opposite side of the electrophoresis chamber with the notched glass plate facing outwards. The inner chamber between two gel sandwiches was subsequently filled with running buffer up to 2-3 mm from the top ( $\approx$  140 ml). The comb(s) were carefully removed and any crooked wells were straightened. Each sample well was washed with running buffer to prevent any unwanted material from obstructing the well. Protein samples were loaded into appropriate wells in the required order, allowing them to settle evenly to the bottom of the well. 5  $\mu$ l of pre-stained protein standards (New England Biolabs) were included to monitor electrophoretic separation and provide molecular weight markers. The assembled electrophoresis chamber was connected to a power supply and the gels were run at constant voltage of 80 V until samples reached the bottom of the stacking gel ( $\approx$  35 minutes). After that, the voltage was increased to 120 V and run until the tracking dye reached the bottom of the gel ( $\approx$  1.5 hours). After electrophoresis was complete, each gel was removed by carefully separating the two glass plates, stacking gel was discarded and resolving gel containing the separated proteins was retrieved.

#### *2.4.4 Western blotting*

##### 2.4.4.1 Semi-dry electrophoretic protein transfer

Once separated by SDS-PAGE, protein samples were transferred electrophoretically onto

methanol-activated polyvinylidene difluoride (PVDF) membranes using the Enduro™ semi-dry blotter (Labnet International). The blotter was placed on a flat surface. One set of Whatman™ cellulose blotting paper (GE Healthcare), with 4 sheets cut to the dimensions of a gel (i.e. 6.5 x 9.5 cm), was soaked in pre-cooled transfer buffer and placed onto the base electrode (anode) plate. A piece of Immobilon®-P 0.45 µm PVDF transfer membrane (Millipore) was activated by incubating for 1 minute in 100% (v/v) methanol, equilibrated in transfer buffer and placed on top of the stacked filter papers. Similarly, the SDS-PAGE gel was equilibrated briefly in transfer buffer and placed on top of the membrane, followed by another set of pre-soaked blotting papers. Importantly, removing any air bubbles which may have formed between the layers of a blot sandwich was crucial to obtain good transfer results. Transfer buffer chilled to 4°C was used in order to improve heat dissipation during transfer. Any excess liquid was wiped away from around the assembled blot sandwich(es), taking care not to disturb them, to prevent overheating. The blotter was closed by securing the lid electrode (cathode) plate, the unit was connected to a power supply and samples were transferred at constant voltage of 12 V for 1.5-2 hours, depending on the size of the protein(s) of interest (generally, the larger the protein, the longer the transfer time). After transfer was complete, each blot sandwich was disassembled, filter papers and the SDS-PAGE gel were discarded and the membrane was retrieved for immunodetection.

#### 2.4.4.2 Immunodetecting proteins of interest

To assess the transfer efficiency and visualise the total protein content, the membrane was stained for 5 minutes at room temperature with a sufficient amount of Ponceau S solution (Sigma-Aldrich). As soon as a protein pattern was clearly visible, the staining solution was recycled and the membrane was rinsed briefly with dH<sub>2</sub>O. The parts of the membrane that did not contain any protein were cut off with a razor blade and the membrane was washed thoroughly (at least 3 x 5 minutes) with TBS-T until all traces of the staining solution were removed. To block non-specific binding sites, the membrane was incubated with 5% (w/v) non-fat dried milk in TBS-T for a minimum of 1 hour at room temperature with shaking. Following 3 washes (5 minutes each) with TBS-T, the membrane was incubated in primary antibody solution targeted specifically against the protein of interest, diluted in 3% (w/v) BSA in TBS-T, overnight at 4°C with gentle rocking. The primary antibody solution was recycled and stored at -20°C for reuse. After 3 more washes (5 minutes each) with TBS-T to remove any unbound antibody, the membrane was incubated in appropriate horseradish peroxidase (HRP)-conjugated secondary antibody solution, diluted in 2% (w/v) non-fat dried milk in TBS-T, for 1-3 hours at room temperature with shaking. The secondary

antibody solution was discarded and the membrane was washed thoroughly 5 x 5 minutes with TBS-T to remove any unbound antibody. In general, 10 ml of each solution were used per a full-size membrane. The details of primary and secondary antibodies that were used in the present study are provided in Table 2.3.

Name	Description	Type	Supplier	Dilution
Claudin-5	rabbit polyclonal	primary	Invitrogen	1:1000
Occludin	rabbit polyclonal	primary	Abcam	1:500
ZO-1	rabbit polyclonal	primary	Invitrogen	1:1000
IL-18*	rabbit polyclonal	primary	Abcam	1:1000
IL-1 $\beta$ *	rabbit polyclonal	primary	Abcam	1:1000
Caspase-1*	rabbit polyclonal	primary	Abcam	1:1000
$\beta$ -actin	rabbit polyclonal	primary	Abcam	1:2000
Anti-rabbit IgG	HRP-conjugated goat polyclonal	secondary	Sigma-Aldrich	1:2000-1:5000

\* These antibodies recognise both the precursor pro-forms and the mature (cleaved) forms of the corresponding proteins.

**Table 2.3:** Antibodies used for Western blotting.

#### 2.4.4.3 Western blot development and analysis

Western blots were developed with the enhanced chemiluminescence (ECL) method using the WesternBright™ ECL Western blotting HRP substrate kit (Advansta) and scanned on the C-DiGit™ chemiluminescence Western blot scanner (LI-COR Biosciences). The HRP substrate working solution was always prepared just before use, by mixing equal parts of the kit's component reagents (luminol/enhancer and peroxide solution). The membrane was incubated with the HRP substrate for 1-2 minutes at room temperature, using 0.1 ml of working solution per cm<sup>2</sup> of membrane (i.e.  $\approx$  6 ml per a full-size membrane). The excess reagent was drained and the wet membrane was placed directly on the C-DiGit™ scanning surface, with the protein side facing down and the top of the membrane facing towards the back of the instrument. All scans were acquired using the high sensitivity setting (a 12-minute scan). At the end of each scan, an optimal image display was selected that gave the best visual appearance. Band intensity was quantified using the publicly available ImageJ

software or the ImageStudio™ Lite software version 4.0 (LI-COR Biosciences). All bands were normalised to an appropriate loading control.

#### 2.4.5 Enzyme-linked immunosorbent assay (ELISA)

VEGF and IL-1 $\beta$  concentration in mouse retinal tissue lysates and/or cell-free supernatants from *in vitro* experiments was determined using commercially available DuoSet® ELISA development systems (R&D Systems), with minor modifications to the manufacturer's recommended general protocol. IL-18 concentration in cell-free supernatants from *in vitro* experiments was analysed using a custom-made protocol as described. The details of the different ELISA kits' component reagents that were used in the present study are provided in Table 2.4.

The capture antibody was diluted to the working concentration in PBS and 50  $\mu$ l per well were used to coat a required number of wells on a 96-well microplate. In the case of IL-18 ELISA, the capture antibody was diluted in 50 mM BupH™ sodium carbonate-bicarbonate buffer (pH 9.4) (Thermo Scientific) and 100  $\mu$ l were used to coat the wells. The plate was sealed and incubated overnight at room temperature or at 4°C for the IL-18 ELISA. Each well was washed 3 times with 200  $\mu$ l of appropriate wash buffer. After the last wash, any remaining wash buffer was removed by inverting the plate and blotting it against clean paper towels. Complete removal of liquid at each step was essential for good performance. Non-specific binding sites on the plate were blocked by adding 200  $\mu$ l of reagent diluent, or SuperBlock™ blocking buffer (Thermo Scientific) for IL-18 ELISA, to each well and incubated for a minimum of 1 hour at room temperature. The wash step was repeated as before. A set of protein standards was prepared by serial 2-fold dilutions, in corresponding reagent diluent, of the supplied standard stock solution and the top standard specified in Table 2.4. 50  $\mu$ l of each unknown sample or standard were added per well. Standards were typically loaded in duplicate or triplicate, while unknown samples were assayed either in triplicate or as single replicates, depending on the available sample amount. The plate was covered and incubated for 2 hours at room temperature. All wells were washed as before and 50  $\mu$ l of detection antibody, diluted to the working concentration in appropriate reagent diluent, were added to each well and incubated for 2 hours at room temperature. In the case of IL-18 ELISA, 100  $\mu$ l of detection antibody per well were used and incubated for 1 hour. The wash step was repeated and 50  $\mu$ l, or 100  $\mu$ l for IL-18 ELISA, of the working dilution (1:200) in corresponding reagent diluent of streptavidin-HRP were added to each well and incubated for 20 minutes at room temperature away from direct light. Sufficient volume of 3,3',5,5'-tetramethylbenzidine (TMB) substrate working solution was prepared by mixing



ELISA kit	Reagent	Stock concentration	Working concentration	Dilution
<b>Mouse VEGF</b>	<b>Capture antibody</b> goat anti-mouse VEGF	72 µg/ml	0.4 µg/ml	1 in 180
	<b>Standard</b> recombinant mouse VEGF	95 ng/ml	1600 pg/ml	1 in 60
	<b>Detection antibody</b> biotinylated goat anti-mouse VEGF	18 µg/ml	100 ng/ml	1 in 180
<b>Human VEGF</b>	<b>Capture antibody</b> mouse anti-human VEGF	180 µg/ml	1 µg/ml	1 in 180
	<b>Standard</b> recombinant human VEGF	110 ng/ml	2000 pg/ml	1 in 55
	<b>Detection antibody</b> biotinylated goat anti-human VEGF	18 µg/ml	100 ng/ml	1 in 180
<b>Human IL-1β</b>	<b>Capture antibody</b> mouse anti-human IL-1β	720 µg/ml	4 µg/ml	1 in 180
	<b>Standard</b> recombinant human IL-1β	75 ng/ml	1500 pg/ml	1 in 50
	<b>Detection antibody</b> biotinylated goat anti-human IL-1β	36 µg/ml	200 ng/ml	1 in 180
<b>Human IL-18</b>	<b>Capture antibody</b> mouse anti-human IL-18	1 mg/ml	500 ng/ml	1 in 2000
	<b>Standard</b> recombinant human IL-18	5 mg/ml	500 pg/ml	1 in 10 <sup>7</sup>
	<b>Detection antibody</b> biotinylated rat anti-human IL-18	500 µg/ml	100 ng/ml	1 in 5000

**Table 2.4:** Specifications of the ELISA kits' component reagents.

equal parts of the Pierce<sup>®</sup> TMB substrate kit's (Thermo Scientific) component reagents (TMB solution and peroxide solution). After 3 washes as before, 50 µl of the substrate working solution were added per well and incubated for 20 minutes at room temperature, protected from direct light. Once oxidised by HRP, this substrate yields a blue product, the amount of colour development being directly proportional to the amount of protein in a sample. Each reaction was terminated by adding 50 µl of stop reagent for TMB substrate (Sigma-Aldrich) per well, denaturing the HRP enzyme and causing a colour shift from blue to yellow. The plate was gently tapped to ensure thorough mixing. The absorbance of each well was measured at 450 nm using the Multiskan<sup>™</sup> FC microplate photometer and the 0 pg/ml protein standard solution as a blank. A standard curve was constructed by plotting the mean blank-corrected absorbance reading of each standard against its concentration (in

pg/ml). Plotted data were fitted with four-parameter logistic (4-PL) non-linear regression and used to interpolate the protein concentration in each unknown sample. The measured VEGF levels in the retinas were expressed as pg amounts of VEGF per mg of total retinal protein as determined by the BCA assay. Where required, the rate of protein secretion was determined from the slope of linear regression fit of secreted protein concentration (in pg/ml) plotted against time (in hours) and expressed in  $\text{pg ml}^{-1} \text{ h}^{-1}$ .

## **2.5 Gene expression analysis**

### *2.5.1 Sample preparation*

To isolate tissues from mouse eyes, animals were sacrificed by  $\text{CO}_2$  asphyxia. Eyes were enucleated, collected in PBS on ice and immediately dissected under a microdissection microscope. The exterior of the eyeball was cleared off excessive muscle tissue, the optic nerve was snipped off and a small incision made at the ora serrata. The anterior parts of the eye (cornea, iris, lens) were dissected out along the circumference around the pars plana. The retina was gently removed from the posterior eye cup and RPE/choroid was carefully scraped off the underlying sclera with a blunt end of a razor blade (size 11).

For *in vitro* experiments, cell culture media were collected and centrifuged at 300 g for 8 minutes to pellet down any detached cells. The cell-free supernatants were transferred into fresh tubes and stored at  $-20^\circ\text{C}$  until analysis. Each cell monolayer was subsequently washed once with ice-cold DPBS.

### *2.5.2 RNA extraction*

RNA from isolated tissue(s) and cell monolayers was extracted using the E.Z.N.A.<sup>®</sup> total RNA kit I (Omega Bio-tek) according to the manufacturer's instructions. Each sample was completely homogenised by repeated pipetting and vortexing in 350  $\mu\text{l}$  of TRK lysis buffer and centrifuged at maximum speed for 5 minutes. The cleared supernatant was thoroughly mixed with one volume of 70% (v/v) ethanol, transferred to a HiBind<sup>®</sup> RNA mini column and centrifuged at 10000 g for 1 minute, discarding the filtrate. The column was washed with 500  $\mu\text{l}$  of wash buffer I and centrifuged at 10000 g for 30 seconds. The filtrate was discarded again and the column was washed twice by adding 500  $\mu\text{l}$  of wash buffer II, followed by centrifugation at 10000 g for 1 minute. The column was completely dried by centrifuging at maximum speed for 2 minutes. RNA was eluted from the column by adding 40  $\mu\text{l}$  of nuclease-free water and centrifugation at maximum speed for 2 minutes. The yield (in  $\text{ng}/\mu\text{l}$ ) and quality ( $A_{260}/A_{280}$ ) of eluted RNA in each sample were assessed using the NanoDrop<sup>™</sup> 1000 spectrophotometer (Thermo Scientific).

### 2.5.3 Polymerase chain reaction (PCR) arrays

The gene expression was analysed with RT<sup>2</sup> Profiler PCR arrays (Qiagen) according to the manufacturer's instructions on LightCycler<sup>®</sup> 480 96-well block system (Roche Molecular Systems) using 115 ng of starting material. The PCR arrays used in the present study were focused on the autophagy and inflammasome pathways and the genes included on the array plates are listed in Table 2.5 and Table 2.6, respectively.

First, cDNA was synthesised using the RT<sup>2</sup> First Strand kit (Qiagen). The genomic DNA elimination mix was prepared for each RNA sample by mixing 115 ng of extracted RNA, 2 µl of buffer GE and an appropriate volume of nuclease-free water to give the total reaction volume of 10 µl in each tube. All samples were incubated for 5 minutes at 42°C and then placed on ice for at least 1 minute. Sufficient amount of the reverse-transcription mix was prepared by mixing, per one reaction, 4 µl of 5x buffer BC3, 1 µl of control P2, 2 µl of RE3 reverse transcriptase mix and 3 µl of nuclease-free water to give the total volume of 10 µl per single reaction. Subsequently, 10 µl of the reverse-transcription mix were added to each tube containing 10 µl of the genomic DNA elimination mix and were mixed gently by pipetting. Samples were incubated for exactly 15 minutes at 42°C and reactions were immediately stopped by incubating for 5 minutes at 95°C. 91 µl of nuclease-free water were added to each tube, mixed by pipetting up and down several times and the reactions were stored at -20°C until PCR was performed.

The PCR components mix was prepared by combining 1350 µl of 2x RT<sup>2</sup> SYBR green mastermix, 102 µl of cDNA synthesis reaction and 1248 µl of nuclease-free water, giving the total volume of 2700 µl. 25 µl of the PCR components mix were dispensed into each well on the RT<sup>2</sup> Profiler PCR array plate. Carefully, the plate was tightly sealed with an optical adhesive film and centrifuged at 1000 g for 1 minute to remove air bubbles. The PCR was carried out using the following cycling conditions: 10 minutes at 95°C (1 cycle), 15 seconds at 95°C and 1 minute at 60°C (45 cycles), 4°C (hold). The ramp rate was adjusted to 1.5°C/s and the dissociation (melting) curve analysis was included to verify PCR specificity. Data analysis was performed using Qiagen's online Data Analysis Center and the comparative C<sub>t</sub> ( $\Delta\Delta C_t$ ) method, with gene expression normalised to an appropriate housekeeping control showing the least variation between time points or treatments.

Position	Refseq (mouse)	Refseq (human)	Gene symbol	Description
A01	NM_009652	NM_005163	Akt1	Thymoma viral proto-oncogene 1
A02	NM_172669	NM_017749	Ambra1	Autophagy/beclin 1 regulator 1
A03	NM_007471	NM_000484	App	Amyloid beta (A4) precursor protein
A04	NM_025770	NM_031482	Atg10	Autophagy-related 10 (yeast)
A05	NM_026217	NM_004707	Atg12	Autophagy-related 12 (yeast)

A06	NM_029846	NM_017974	Atg16l1	Autophagy-related 16-like 1 (yeast)
A07	NM_001111111	NM_033388	Atg16l2	Autophagy related 16 like 2 (S. cerevisiae)
A08	NM_026402	NM_022488	Atg3	Autophagy-related 3 (yeast)
A09	NM_174875	NM_052936	Atg4a	Autophagy-related 4A (yeast)
A10	NM_174874	NM_178326	Atg4b	Autophagy-related 4B (yeast)
A11	NM_175029	NM_178221	Atg4c	Autophagy-related 4C (yeast)
A12	NM_153583	NM_032885	Atg4d	Autophagy-related 4D (yeast)
B01	NM_053069	NM_004849	Atg5	Autophagy-related 5 (yeast)
B02	NM_028835	NM_006395	Atg7	Autophagy-related 7 (yeast)
B03	NM_001003917	NM_024085	Atg9a	Autophagy-related 9A (yeast)
B04	NM_001002897	NM_173681	Atg9b	ATG9 autophagy related 9 homolog B (S. cerevisiae)
B05	NM_007522	NM_004322	Bad	BCL2-associated agonist of cell death
B06	NM_007523	NM_001188	Bak1	BCL2-antagonist/killer 1
B07	NM_007527	NM_004324	Bax	Bcl2-associated X protein
B08	NM_009741	NM_000633	Bcl2	B-cell leukemia/lymphoma 2
B09	NM_009743	NM_138578	Bcl2l1	Bcl2-like 1
B10	NM_019584	NM_003766	Becn1	Beclin 1, autophagy related
B11	NM_007544	NM_001196	Bid	BH3 interacting domain death agonist
B12	NM_009760	NM_004052	Bnip3	BCL2/adenovirus E1B interacting protein 3
C01	NM_009810	NM_004346	Casp3	Caspase 3
C02	NM_009812	NM_001228	Casp8	Caspase 8
C03	NM_009875	NM_004064	Cdkn1b	Cyclin-dependent kinase inhibitor 1B
C04	NM_009877	NM_000077	Cdkn2a	Cyclin-dependent kinase inhibitor 2A
C05	NM_009907	NM_000086	Cln3	Ceroid lipofuscinosis, neuronal 3, juvenile (Batten, Spielmeyer-Vogt disease)
C06	NM_007798	NM_001908	Ctsb	Cathepsin B
C07	NM_009983	NM_001909	Ctsd	Cathepsin D
C08	NM_021281	NM_004079	Ctss	Cathepsin S
C09	NM_009911	NM_003467	Cxcr4	Chemokine (C-X-C motif) receptor 4
C10	NM_029653	NM_004938	Dapk1	Death associated protein kinase 1
C11	NM_027878	NM_018370	Dram1	DNA-damage regulated autophagy modulator 1
C12	NM_026013	NM_178454	Dram2	VDNA-damage regulated autophagy modulator 2
D01	NM_010121	NM_004836	Eif2ak3	Eukaryotic translation initiation factor 2 alpha kinase 3
D02	NM_001005331	NM_182917	Eif4g1	Eukaryotic translation initiation factor 4, gamma 1
D03	NM_007956	NM_000125	Esr1	Estrogen receptor 1 (alpha)
D04	NM_010175	NM_003824	Fadd	Fas (TNFRSF6)-associated via death domain
D05	NM_007987	NM_000043	Fas	Fas (TNF receptor superfamily member 6)
D06	NM_008064	NM_000152	Gaa	Glucosidase, alpha, acid
D07	NM_019749	NM_007278	Gabarap	Gamma-aminobutyric acid receptor associated protein
D08	NM_020590	NM_031412	Gabarap11	Gamma-aminobutyric acid (GABA) A receptor-associated protein-like 1
D09	NM_026693	NM_007285	Gabarap12	Gamma-aminobutyric acid (GABA) A receptor-associated protein-like 2
D10	NM_008228	NM_004964	Hdac1	Histone deacetylase 1
D11	NM_010413	NM_006044	Hdac6	Histone deacetylase 6
D12	NM_008244	NM_004712	Hgs	HGF-regulated tyrosine kinase substrate
E01	NM_010480	NM_001017963	Hsp90aa1	Heat shock protein 90, alpha (cytosolic), class A member 1

E02	NM_031165	NM_006597	Hspa8	Heat shock protein 8
E03	NM_010414	NM_002111	Htt	Huntingtin
E04	NM_008337	NM_000619	Ifng	Interferon gamma
E05	NM_010512	NM_000618	Igf1	Insulin-like growth factor 1
E06	NM_008387	NM_000207	Ins2	Insulin II
E07	NM_008326	NM_001145805	Irgm1	Immunity-related GTPase family M member 1
E08	NM_010684	NM_005561	Lamp1	Lysosomal-associated membrane protein 1
E09	NM_025735	NM_181509	Map1lc3a	Microtubule-associated protein 1 light chain 3 alpha
E10	NM_026160	NM_022818	Map1lc3b	Microtubule-associated protein 1 light chain 3 beta
E11	NM_011951	NM_001315	Mapk14	Mitogen-activated protein kinase 14
E12	NM_016700	NM_002750	Mapk8	Mitogen-activated protein kinase 8
F01	NM_020009	NM_004958	Mtor	Mechanistic target of rapamycin (serine/threonine kinase)
F02	NM_008689	NM_003998	Nfkb1	Nuclear factor of kappa light polypeptide gene enhancer in B-cells 1, p105
F03	NM_008720	NM_000271	Npc1	Niemann Pick type C1
F04	NM_181414	NM_002647	Pik3c3	Phosphoinositide-3-kinase, class 3
F05	NM_020272	NM_002649	Pik3cg	Phosphoinositide-3-kinase, catalytic, gamma polypeptide
F06	NM_001081309	NM_014602	Pik3r4	Phosphatidylinositol 3 kinase, regulatory subunit, polypeptide 4, p150
F07	NM_001013367	NM_006251	Prkaa1	Protein kinase, AMP-activated, alpha 1 catalytic subunit
F08	NM_008960	NM_000314	Pten	Phosphatase and tensin homolog
F09	NM_009000	NM_130781	Rab24	RAB24, member RAS oncogene family
F10	NM_009029	NM_000321	Rb1	Retinoblastoma 1
F11	NM_026446	NM_005873	Rgs19	Regulator of G-protein signaling 19
F12	NM_028259	NM_003161	Rps6kb1	Ribosomal protein S6 kinase, polypeptide 1
G01	NM_009221	NM_000345	SncA	Synuclein, alpha
G02	NM_011018	NM_003900	Sqstm1	Sequestosome 1
G03	NM_011577	NM_000660	Tgfb1	Transforming growth factor, beta 1
G04	NM_009373	NM_004613	Tgm2	Transglutaminase 2, C polypeptide
G05	NM_175502	NM_153015	Tmem74	Transmembrane protein 74
G06	NM_013693	NM_000594	Tnf	Tumor necrosis factor
G07	NM_009425	NM_003810	Tnfsf10	Tumor necrosis factor (ligand) superfamily, member 10
G08	NM_011640	NM_000546	Trp53	Transformation related protein 53
G09	NM_009469	NM_003565	Ulk1	Unc-51 like kinase 1 (C. elegans)
G10	NM_013881	NM_014683	Ulk2	Unc-51 like kinase 2 (C. elegans)
G11	NM_178635	NM_003369	Uvrag	UV radiation resistance associated gene
G12	NM_145940	NM_017983	Wipi1	WD repeat domain, phosphoinositide interacting 1
H01	NM_007393	NM_001101	Actb	Actin, beta
H02	NM_009735	NM_004048	B2m	Beta-2 microglobulin
H03	NM_008084	NM_002046	Gapdh	Glyceraldehyde-3-phosphate dehydrogenase
H04	NM_010368	NM_000194	Gusb	Glucuronidase, beta
H05	NM_008302	NM_001002	Hsp90ab1	Heat shock protein 90 alpha (cytosolic), class B member 1
H06	SA_00106	SA_00105	MGDC	Mouse genomic DNA contamination
H07	SA_00104	SA_00104	RTC	Reverse transcription control

H08	SA_00104	SA_00104	RTC	Reverse transcription control
H09	SA_00104	SA_00104	RTC	Reverse transcription control
H10	SA_00103	SA_00103	PPC	Positive PCR control
H11	SA_00103	SA_00103	PPC	Positive PCR control
H12	SA_00103	SA_00103	PPC	Positive PCR control

**Table 2.5:** Mouse and human RT<sup>2</sup> Profiler PCR autophagy array genes.

Position	Refseq (mouse)	Gene symbol	Description
A01	NM_001013779	Aim2	Absent in melanoma 2
A02	NM_009741	Bcl2	B-cell leukemia/lymphoma 2
A03	NM_009743	Bcl2l1	Bcl2-like 1
A04	NM_007465	Birc2	Baculoviral IAP repeat-containing 2
A05	NM_007464	Birc3	Baculoviral IAP repeat-containing 3
A06	NM_001163138	Card6	Caspase recruitment domain family, member 6
A07	NM_009807	Casp1	Caspase 1
A08	NM_009808	Casp12	Caspase 12
A09	NM_009812	Casp8	Caspase 8
A10	NM_011331	Ccl12	Chemokine (C-C motif) ligand 12
A11	NM_013653	Ccl5	Chemokine (C-C motif) ligand 5
A12	NM_013654	Ccl7	Chemokine (C-C motif) ligand 7
B01	NM_011616	Cd40lg	CD40 ligand
B02	NM_009805	Cflar	CASP8 and FADD-like apoptosis regulator
B03	NM_007700	Chuk	Conserved helix-loop-helix ubiquitous kinase
B04	NM_007575	Ciita	Class II transactivator
B05	NM_007798	Ctsb	Cathepsin B
B06	NM_008176	Cxcl1	Chemokine (C-X-C motif) ligand 1
B07	NM_203320	Cxcl3	Chemokine (C-X-C motif) ligand 3
B08	NM_010175	Fadd	Fas (TNFRSF6)-associated via death domain
B09	NM_010480	Hsp90aa1	Heat shock protein 90, alpha (cytosolic), class A member 1
B10	NM_011631	Hsp90b1	Heat shock protein 90, beta (Grp94), member 1
B11	NM_010510	Ifnb1	Interferon beta 1, fibroblast
B12	NM_008337	Ifng	Interferon gamma
C01	NM_010546	Ikbkb	Inhibitor of kappaB kinase beta
C02	NM_010547	Ikbkg	Inhibitor of kappaB kinase gamma
C03	NM_008351	Il12a	Interleukin 12A
C04	NM_008352	Il12b	Interleukin 12B
C05	NM_008360	Il18	Interleukin 18
C06	NM_008361	Il1b	Interleukin 1 beta
C07	NM_133775	Il33	Interleukin 33
C08	NM_031168	Il6	Interleukin 6
C09	NM_008363	Irak1	Interleukin-1 receptor-associated kinase 1
C10	NM_008390	Irf1	Interferon regulatory factor 1
C11	NM_016849	Irf3	Interferon regulatory factor 3
C12	NM_013674	Irf4	Interferon regulatory factor 4
D01	NM_172688	Map3k7	Mitogen-activated protein kinase kinase kinase 7
D02	NM_011949	Mapk1	Mitogen-activated protein kinase 1
D03	NM_011161	Mapk11	Mitogen-activated protein kinase 11
D04	NM_013871	Mapk12	Mitogen-activated protein kinase 12
D05	NM_011950	Mapk13	Mitogen-activated protein kinase 13
D06	NM_011952	Mapk3	Mitogen-activated protein kinase 3
D07	NM_016700	Mapk8	Mitogen-activated protein kinase 8
D08	NM_016961	Mapk9	Mitogen-activated protein kinase 9
D09	NM_019453	Mefv	Mediterranean fever

D10	NM_010851	Myd88	Myeloid differentiation primary response gene 88
D11	NM_008670	Naip1	NLR family, apoptosis inhibitory protein 1
D12	NM_010870	Naip5	NLR family, apoptosis inhibitory protein 5
E01	NM_008689	Nfkb1	Nuclear factor of kappa light polypeptide gene enhancer in B-cells 1, p105
E02	NM_010907	Nfkbia	Nuclear factor of kappa light polypeptide gene enhancer in B-cells inhibitor, alpha
E03	NM_010908	Nfkbib	Nuclear factor of kappa light polypeptide gene enhancer in B-cells inhibitor, beta
E04	NM_001033367	Nlrc4	NLR family, CARD domain containing 4
E05	NM_001033207	Nlrc5	NLR family, CARD domain containing 5
E06	NM_001033431	Nlrp12	NLR family, pyrin domain containing 12
E07	NM_001004142	Nlrp1a	NLR family, pyrin domain containing 1A
E08	NM_145827	Nlrp3	NLR family, pyrin domain containing 3
E09	NM_172481	Nlrp4b	NLR family, pyrin domain containing 4B
E10	NM_001004194	Nlrp4e	NLR family, pyrin domain containing 4E
E11	NM_011860	Nlrp5	NLR family, pyrin domain containing 5
E12	NM_001081389	Nlrp6	NLR family, pyrin domain containing 6
F01	NM_194058	Nlrp9b	NLR family, pyrin domain containing 9B
F02	NM_178420	NlrX1	NLR family member X1
F03	NM_172729	Nod1	Nucleotide-binding oligomerization domain containing 1
F04	NM_145857	Nod2	Nucleotide-binding oligomerization domain containing 2
F05	NM_011027	P2rx7	Purinergic receptor P2X, ligand-gated ion channel, 7
F06	NM_019482	Panx1	Pannexin 1
F07	NM_011063	Pea15a	Phosphoprotein enriched in astrocytes 15A
F08	NM_011193	Pstpip1	Proline-serine-threonine phosphatase-interacting protein 1
F09	NM_011198	Ptgs2	Prostaglandin-endoperoxide synthase 2
F10	NM_023258	Pycard	PYD and CARD domain containing
F11	NM_009045	Rela	V-rel reticuloendotheliosis viral oncogene homolog A (avian)
F12	NM_138952	Ripk2	Receptor (TNFRSF)-interacting serine-threonine kinase 2
G01	NM_011973	Mok	Serine/threonine kinase 30
G02	NM_026474	Sugt1	SGT1, suppressor of G2 allele of SKP1 (S. cerevisiae)
G03	NM_025609	Tab1	TGF-beta activated kinase 1/MAP3K7 binding protein 1
G04	NM_138667	Tab2	TGF-beta activated kinase 1/MAP3K7 binding protein 2
G05	NM_054096	Tirap	Toll-interleukin 1 receptor (TIR) domain-containing adaptor protein
G06	NM_013693	Tnf	Tumor necrosis factor
G07	NM_011613	Tnfsf11	Tumor necrosis factor (ligand) superfamily, member 11
G08	NM_019418	Tnfsf14	Tumor necrosis factor (ligand) superfamily, member 14
G09	NM_009452	Tnfsf4	Tumor necrosis factor (ligand) superfamily, member 4
G10	NM_009424	Traf6	Tnf receptor-associated factor 6
G11	NM_023719	Txnip	Thioredoxin interacting protein
G12	NM_009688	Xiap	X-linked inhibitor of apoptosis
H01	NM_007393	Actb	Actin, beta
H02	NM_009735	B2m	Beta-2 microglobulin
H03	NM_008084	Gapdh	Glyceraldehyde-3-phosphate dehydrogenase
H04	NM_010368	Gusb	Glucuronidase, beta
H05	NM_008302	Hsp90ab1	Heat shock protein 90 alpha (cytosolic), class B member 1
H06	SA_00106	MGDC	Mouse Genomic DNA Contamination
H07	SA_00104	RTC	Reverse transcription control
H08	SA_00104	RTC	Reverse transcription control
H09	SA_00104	RTC	Reverse transcription control
H10	SA_00103	PPC	Positive PCR control
H11	SA_00103	PPC	Positive PCR control
H12	SA_00103	PPC	Positive PCR control

**Table 2.6:** Mouse RT<sup>2</sup> Profiler PCR inflammasome array genes.

## 2.6 Histology and immunofluorescence staining

### 2.6.1 Paraffin-embedding and sectioning of mouse eyes

Mice were sacrificed by cervical dislocation. Eyes were enucleated and immediately fixed in Davidson's fixative overnight at 4°C. Following 3 washes with PBS, eyes were placed individually into tissue embedding cassettes (Sigma-Aldrich) and submerged in 70% (v/v) ethanol. They were subsequently processed using the TP1020 automated tissue processor (Leica Biosystems) under gentle agitation by successive incubation in different treatment solutions as outlined in Table 2.7. Each eye was then carefully placed into a plastic mould in sagittal orientation, embedded in paraffin using the EG1150 heated paraffin embedding module (Leica Biosystems) and left to cool and solidify on a cold plate for several hours. Paraffin-embedded eyes were stored at room temperature and subsequently sectioned on the RM2235 manual rotary microtome (Leica Biosystems) into 5 µm thick slices, mounted on polylysine adhesion slides in a water bath at 50°C and allowed to dry overnight.

Incubation step	Treatment	Duration	Temperature
1	70% (v/v) ethanol	1 hour	room temperature
2	80% (v/v) ethanol	1 hour	room temperature
3	95% (v/v) ethanol	1 hour	room temperature
4	100% (v/v) ethanol	1 hour	room temperature
5	100% (v/v) ethanol	1 hour	room temperature
6	50% (v/v) ethanol and 50% (v/v) xylene	1 hour	room temperature
7	100% (v/v) xylene	1 hour	room temperature
8	100% (v/v) xylene	1 hour	room temperature
9	paraffin	1 hour	60°C
10	paraffin under vacuum	1 hour	60°C

**Table 2.7:** Tissue processing treatments during paraffin-embedding of mouse eyes.

### 2.6.2 Haematoxylin and eosin (H&E) staining

Paraffin-embedded sections were deparaffinised and rehydrated by sequentially dipping them 10 times in and out of 100% (v/v) xylene, 100% (v/v) ethanol, 90% (v/v) ethanol and 70% (v/v) ethanol. Subsequently, they were submerged into haematoxylin (Sigma-Aldrich) for 6 minutes, rinsed with tap water and incubated in eosin (Sigma-Aldrich) for 2 minutes.



After rinsing with tap water, they were dehydrated and cleared by dipping them in and out of 70% (v/v) ethanol, 90% (v/v) ethanol, 100% (v/v) ethanol and 100% (v/v) xylene as before. Coverslips were mounted using Sub-X<sup>®</sup> mounting medium (Leica Biosystems) and slides were analysed using the BX51 upright microscope (Olympus). All steps were carried out at room temperature.

### *2.6.3 RPE flatmount preparation and staining*

Mice were sacrificed by cervical dislocation or CO<sub>2</sub> asphyxia. Eyes were enucleated, collected in PBS on ice and immediately dissected under a microdissection microscope. The exterior of the eyeball was cleared off excessive muscle tissue, the optic nerve was snipped off and a small incision made at the ora serrata. The anterior parts of the eye (cornea, iris, lens) were dissected out along the circumference around the pars plana and the retina was carefully removed from the posterior eye cup. The resulting RPE/choroid/sclera complex was cut radially 4 times at 90° and fixed in 4% (w/v) paraformaldehyde (PFA; pH 7.4) overnight at 4°C. After 3 washes (15 minutes each) with PBS at room temperature, eye cups were incubated with AlexaFluor<sup>®</sup>488-conjugated phalloidin (1:300 dilution in PBS; Invitrogen) and AlexaFluor<sup>®</sup>568-conjugated Griffonia-simplicifolia-IB<sub>4</sub> (GS-IB<sub>4</sub>) isolectin (1:300 dilution in PBS; Invitrogen) overnight at 4°C, with gentle agitation and protected from light. The eye cups were washed again as before and carefully flattened on polylysine adhesion slides with the RPE side facing upwards. Coverslips were mounted using Aqua Poly/Mount<sup>®</sup> medium (Polysciences).

For antibody staining, the eye cups were blocked in 5% (v/v) normal goat serum (NGS; Sigma-Aldrich) in PBS containing 0.05% (v/v) Triton<sup>™</sup> X-100 (Sigma-Aldrich) (PBS-T) for 1 hour at room temperature, following fixation and subsequent 3 washes (30 minutes each) in PBS-T. After blocking, they were incubated with a primary antibody of interest, diluted in 1% (v/v) NGS in PBS-T, overnight at 4°C. Following 3 washes (15 minutes each) with PBS, eye cups were incubated with an appropriate secondary antibody solution, diluted in 1% (v/v) PBS-T, for 3 hours at room temperature protected from direct light. Optionally, other fluorescent stains could be added at this stage. The eye cups were washed again 3 times (15 minutes each) in PBS and counterstained with the nuclear stain Hoechst 33342 (1:10000 dilution in PBS-T; Sigma-Aldrich) for 1 minute at room temperature away from direct light. After 3 more washes with PBS, they were mounted on polylysine slides as described above. The details of primary and secondary antibodies that were used in the present study are provided in Table 2.8.

All slides were analysed on the LSM710 confocal microscope (Carl Zeiss Microscopy). Volumetric analysis was carried out on 3-D Z-stack images using Imaris<sup>®</sup> 7.0 (Bitplane Scientific Software).

Name	Description	Type	Supplier	Dilution
LC3	rabbit polyclonal	primary	Abcam	1:100
Caspase-1*	rabbit polyclonal	primary	Novus Biologicals	1:50
IL-18*	rabbit polyclonal	primary	Antibodies Online	1:100
NLRP3	mouse monoclonal	primary	Novus Biologicals	1:50
IL-1 $\beta$ *	rabbit polyclonal	primary	Abcam	1:100
NLRP6	rabbit polyclonal	primary	Atlas Antibodies	1:20
Anti-rabbit IgG	Cy2 <sup>®</sup> -conjugated goat polyclonal	secondary	Abcam	1:500
Anti-rabbit IgG	Cy3 <sup>®</sup> -conjugated goat polyclonal	secondary	Abcam	1:500
Anti-mouse IgG	Biotin-conjugated horse polyclonal	secondary	Vector Laboratories	1:100
Anti-rabbit IgG	Biotin-conjugated goat polyclonal	secondary	Vector Laboratories	1:100

\* These antibodies recognise both the precursor pro-forms and the mature (cleaved) forms of the corresponding proteins.

**Table 2.8:** Antibodies used for immunofluorescence and immunohistochemistry.

#### 2.6.4 Immunohistochemistry of human sections

Immunohistochemical staining of human specimens was carried out in the lab of Dr. Rob Mullins (University of Iowa, USA). Frozen cross-sections through the macular region of 5 geographic atrophy patients and 4 age-matched healthy donors were provided.

The sections were stained using the Vector VIP staining kit (Vector Laboratories), with all incubation steps carried out in a humidifying chamber at room temperature. The sections were blocked in the VIP kit's serum (1:100 dilution in PBS) for 15 minutes, using 50  $\mu$ l of blocking solution per section. After the blocking solution was gently tapped off from the slides, 50  $\mu$ l of a primary antibody of interest diluted in blocking buffer, or 50  $\mu$ l of the blocking solution alone for secondary control sections, were applied and incubated for 1 hour. The slides were rinsed 3 times (5 minutes each) in PBS and 50  $\mu$ l of an appropriate secondary antibody diluted in blocking buffer were added to each section and incubated for

30 minutes. The details of primary and secondary antibodies that were used in the present study are provided in Table 2.8. Again, the slides were rinsed 3 times (5 minutes each) in PBS. Avidin biotin complex (ABC) solution was prepared by diluting components A and B from the VIP kit (1:50 dilution in PBS), 50 µl were applied to each section and incubated for 30 minutes. In the meantime, the VIP developer was prepared by adding three drops of each of the four reagents to 5 ml of PBS or one drop per 1.5 ml of PBS. Following 3 more rinses (5 minutes each) in PBS, 50 µl of the VIP developer were added to each section and watched for development under a light microscope. The slides were rinsed with running distilled water in a Koplun jar for 1 minute, placed into a glass staining boat and dehydrated by gently dipping them (10 times) in and out of 80% (v/v) ethanol, 95% (v/v) ethanol, 100% (v/v) ethanol and Clear-Rite-3. They were then placed on a flat surface to dry for 15 minutes, coverslips were mounted with Permount mounting medium (Fisher Scientific) and allowed to dry overnight. Images were acquired using the BX52 upright microscope (Olympus).

## **2.7 Functional *in vitro* measurements**

### *2.7.1 Cell viability assay*

Cell viability was measured using CellTiter 96<sup>®</sup> AQueous One Solution cell proliferation MTS assay (Promega) as per manufacturer's instructions. Cell monolayers were washed once with DPBS and incubated with CellTiter 96<sup>®</sup> AQueous One Solution reagent, using 20 µl of substrate per 100 µl of complete growth medium, for 1-4 hours in a humidified incubator at 37°C and 5% CO<sub>2</sub>, 95% air. The absorbance of each well was measured at 450 nm using the Multiskan<sup>™</sup> FC microplate photometer. The average background absorbance of control wells with no cells was subtracted from each reading to yield blank-corrected absorbance values, directly proportional to the number of metabolically active (living) cells in culture.

### *2.7.2 Wound-healing (scratch) assay*

Cells were seeded onto chamber slides with coverslip-like bottom surface (ibidi), suitable for live cell imaging, and grown until they reached confluency. The cell monolayers were washed once with DPBS and a scratch through the centre of each well was made with a pipette tip immediately before an experimental treatment. Bright-field microscopy images were captured using the FluoView FV1000 confocal microscope (Olympus) equipped with a motorised stage, capable of taking images at the same location over time. Images were acquired at baseline right after an experimental treatment and then at appropriate intervals

(2 hours in the case of hFRPE cells) over the period of 18 hours. The size of the wound at each time point was quantified using publicly available ImageJ software and normalised to the baseline wound area. The wound closure was calculated as the difference between the normalised wound size at a specific time point and the baseline. The rate of wound closure was determined from the slope of linear regression of wound closure (% area at baseline) against time (in hours) and was expressed as % per hour.

### *2.7.3 Transendothelial electrical resistance (TEER) measurement*

Transendothelial electrical resistance (TEER) of cell monolayers cultured on permeable supports was measured using the Millicell<sup>®</sup> ERS-2 electrical resistance system (Millipore Corporation). The electrode was sterilised in 70% (v/v) alcohol before use and between measurements of each well to avoid cross-contamination, followed by a dip in DPBS to remove excess alcohol. The electrode was immersed into each well with the shorter tip in the transwell insert and the longer tip in the outer well. Holding the electrode steady at a 90° angle to the insert, stabilised resistance readings were recorded. Average resistance value of control wells with no cells was subtracted from each reading to obtain true blank-corrected resistance of the cell monolayer. The unit area resistance was calculated by multiplying the blank-corrected resistance by the effective surface area of the filter membrane and expressed in  $\Omega \text{ cm}^2$ .

## **2.8 Functional *in vivo* measurements**

### *2.8.1 Fluorescein angiography (FA) imaging*

Fluorescein angiography (FA) was performed on the Heidelberg Spectralis<sup>®</sup> HRA+OCT imaging platform (Heidelberg Engineering). Pupils were dilated with instillation of 1% (w/v) tropicamide and 2.5% (w/v) phenylephrine. Mice were sedated using a mixture of ketamine and medetomidine and then imaged in the FA mode, following an injection (i.p.) of 2% (w/v) sodium fluorescein. A-scan images (30° field of view, 1536 x 1536 pixels, average of 100 frames) were captured at 3-5 minutes post fluorescein injection using the Heidelberg Eye Explorer software (version 1.7.1.0). The body temperature was maintained during imaging by placing the animal on a flask of hot water. At the end of procedure, animals were injected with atipamezole (Antisedan, Pfizer) and returned to their cages for recovery.

Dynamic FA profiling was carried out using a standard dose of 100 mg/kg body weight of sodium fluorescein and images acquired as above at regular intervals starting at 2 minutes post injection, with an image taken every 30 seconds and 10 minutes chosen arbitrarily as

the assay end-point. Series of images were analysed using the publicly available ImageJ software. To correct for animal movement during procedure, minimum overlapping image area was identified by superimposing all images and selecting the area common to all of them. Raw integrated pixel density (RawIntDen), giving the sum of all pixel values in an image or selection, was subsequently measured in the selected area to quantify the signal intensity of each image and then normalised to the starting point, i.e. the signal intensity at 2 minutes post injection, to account for inter-individual variability. A dynamic FA signal intensity profile was obtained for each animal by plotting the normalised pixel intensity (as % value at 2.0 min) against time (in minutes). Area under this curve, representing leakage of the sodium fluorescein tracer, was calculated using the designated function in GraphPad Prism Software version 5.01. Animals with an incomplete set of captured images or insufficient image quality were excluded from the analysis.

### *2.8.2 Electroretinography (ERG)*

All ERGs were carried out by Dr. Paul Kenna. Mice were dark-adapted overnight and prepared for electroretinography under dim red light. Pupils were dilated with instillation of 1% (w/v) cyclopentolate and 2.5% (w/v) phenylephrine. Animals were anaesthetised by injection (i.p.) of ketamine (2.08 mg per 15 g body weight) and xylazine (0.21 mg per 15 g body weight). Standardised flashes of light were presented to each mouse in a Ganzfeld bowl to ensure uniform retinal illumination. Electrophysiological responses were recorded simultaneously from both eyes by means of gold wire electrodes (Roland Consulting) using Vidisic (Dr. Mann Pharma) as a conducting agent and to maintain corneal hydration. Reference and ground electrodes were positioned subcutaneously (s.c.) at  $\approx 1$  mm from the temporal canthus and anterior to the tail, respectively. Body temperature was maintained at 37°C using a heating device controlled by a rectal temperature probe. Responses were analysed using the RetiScan RetiPort electrophysiology unit (Roland Consulting). The protocol was based on that approved by the International Clinical Standards Committee for human ERG. Rod-isolated responses were recorded using a dim white flash (25 dB maximal intensity, where maximal flash intensity was 3 candelas/m<sup>2</sup>/s) presented in the dark-adapted state. Maximal combined rod-cone response to the maximal intensity flash was then recorded. Cone-isolated responses were recorded by using a white flash of intensity 3 candelas/m<sup>2</sup>/s presented against a rod-suppressing background light of 30 candelas/m<sup>2</sup>, to which previously dark-adapted animals had been exposed for 10 minutes before stimulation. Responses to 48 individual flashes, presented at a frequency of 0.5 Hz,

were computer-averaged. Based on standard conventions, a-waves were measured from the baseline to a-wave trough and b-waves from the a-wave trough to the b-wave peak.

## **2.9 Statistical analysis**

Statistical analysis was performed using GraphPad Prism software (version 5.01). Two treatment groups were compared by two-tailed Student's t test. For multiple comparisons, one-way analysis of variance (ANOVA) with Tukey post test was used. All data were assumed to follow normal distribution with equal variances. In all cases,  $p < 0.05$  was considered significant. Data are presented as mean  $\pm$  SEM.

## Chapter 3

# **IL-18 efficacy in a mouse model of spontaneous retinal neovascularisation and its mechanism of action**

### 3 IL-18 EFFICACY IN A MOUSE MODEL OF SPONTANEOUS RETINAL NEOVASCULARISATION AND ITS MECHANISM OF ACTION

---

*Some of the data presented here have been published in Doyle, S.L., López, F.J., Celkova, L., Brennan, K., Mulfaul, K., Ozaki, E., Kenna, P.F., Kurali, E., Hudson, N., Doggett, T., Ferguson, T.A., Humphries, P., Adamson, P. & Campbell, M. 2015. IL-18 immunotherapy for neovascular AMD: tolerability and efficacy in nonhuman primates. Invest Ophthalmol Vis Sci, 56(9), 5424-5430. See Appendix.*

#### 3.1 Introduction

As mentioned before, previous work in our lab showed that NLRP3 had a protective role in a mouse model of wet AMD and that this effect was mediated by the induction of IL-18 (Doyle et al., 2012). Furthermore, exogenous administration, either systemic or intravitreal, of recombinant IL-18 effectively attenuated experimental CNV development (Doyle et al., 2014). These studies were based on the laser-induced CNV mouse model of neovascular (wet) AMD.

The laser-induced CNV model was first developed in non-human primates (Ryan, 1979; Ryan, 1980; Ryan, 1982) and the technique was later modified for use in mice (Tobe et al., 1998). It represents a robust, relevant model that mimics neovascular AMD. It relies on the application of laser burns to focally disrupt the RPE monolayer and allow development of choroidal leakage and neovascularisation. Inflammatory cells are believed to be potent initiators of the angiogenic process observed after the photocoagulation (Noël et al., 2007). This model has several clear advantages over others that can be used to mimic neovascular AMD, such as sub-retinal injections of pro-angiogenic material (Pennesi et al., 2012). It is relatively rapid to develop and, more importantly, develops on an easily accessible type of tissue. Moreover, it is applicable to a wide range of animals, both wild-type and transgenic, and is readily combined with additional experimental techniques, including administration of drugs, viruses, cells, antibodies, recombinant proteins and other compounds that can be delivered via several routes, thus offering a large degree of flexibility. On the other hand, it is only suitable to study neovascular AMD, not the atrophic form. Key features of AMD, such as drusen and the influence of age, are either absent or not relevant. Furthermore, it requires the use of pigmented animals, a trauma is necessary to induce the CNV and the laser-induced lesions spontaneously regress, limiting the length of time they are available



for experimentation. Nonetheless, it has thus far been the most successful animal model of wet AMD and has been widely used to study the mechanism leading to CNV development as well as to predict therapeutic efficacy of potential new drugs and treatment strategies. Noticeably, it was an invaluable tool in the discovery of anti-VEGFs for the treatment of CNVs. Although this model is commonly used to mimic the pathology of wet AMD, some argue that it is more a model of an acute wound-healing response in the retina, as the laser-induced CNVs are introduced in the context of healthy eyes, and thus represents a very limited model of the chronic disease process associated with neovascular AMD (He and Marneros, 2013). In addition, while it was established as a highly reproducible model in non-human primates, its use in mouse eyes was shown to be susceptible to a relatively high degree of variability (Poor et al., 2014).

The JR5558 mouse strain (also known as neoretinal vascularisation 2, NRV2) represents a novel genetic model of spontaneous neovascularisation. It was discovered at The Jackson Laboratory (Bar Harbor, ME) and carries recessive mutations in unknown genes, which in the homozygous state cause the development of multifocal, bilateral spontaneous CNVs in the centre to mid-periphery of the retina and retinal angiomatous proliferation, eventually leading to retinal-choroidal anastomosis. Moreover, the mice are also known to harbour the *rd8* mutation, but do not manifest a typical *rd8* phenotype, suppressed in the C57BL/6J background of this strain. The early changes are characterised by retinal depigmentation and vascular leakage which, if persistent, can give rise to retinal oedema and local gliosis followed by photoreceptor dysfunction and death. The neovascular lesion development in JR5558 mice typically starts in early postnatal days (between P10 and P15) and gradually regresses. In addition, the phenotype of this mouse model is more than 95% penetrant, with no bias for gender or changes in other organs (Hasegawa et al., 2014; Nagai et al., 2014). Importantly, VEGF overexpression in the retina was found to be an important driver of the pathological changes observed in this mouse strain (Hasegawa et al., 2014; Nagai et al., 2014). Systemic blockade of VEGF with a neutralising antibody showed that the average number and size of spontaneous neovascular lesions were significantly reduced. Moreover, various VEGF functions are mediated by its binding to one of VEGF receptors (VEGFRs). Administration of a VEGFR2 neutralising antibody significantly decreased, in a dose-dependent manner, the number and size of vascular leakage sites (Nagai et al., 2014). By contrast, the levels of soluble VEGFR1, that can sequester VEGF and inhibit its function, were not affected (Hasegawa et al., 2014), suggesting that the VEGF-mediated neovascular lesion development in the JR5558 mice is mediated by VEGFR2 signalling rather than decreased levels of soluble VEGFR1.

The main purpose of experiments presented in this section was to evaluate the therapeutic efficacy of IL-18 administration in the JR5558 mouse model as an alternative to the laser-induced CNV model of wet AMD. The specific aims can be summarised as follows:

- to characterise and confirm the phenotype in JR5558 mice
- to investigate the effect of IL-18 administration on the progression of JR5558 lesions
- to investigate the effect of IL-18 administration on the regression of JR5558 lesions
- to study the potential mechanism of IL-18 action *in vivo* and *in vitro*

## 3.2 Results

### 3.2.1 Spontaneous neovascular lesions disrupt retinal architecture in JR5558 mice

The JR5558 mouse strain is characterised by the spontaneous development of neovascular retinal lesions due to recessive mutations in unknown genes. These lesions were found to markedly disrupt the normal histological organisation of the retina. The most significant changes occurred in the two nuclear layers, causing substantial distortion of the distinct multilayered retinal architecture. The neovascular lesions appeared to originate in the INL and extend through the OPL into the ONL, eventually disrupting the inner and outer segments of photoreceptors. Damage to the RPE was often observed, accompanied by an evident thinning and degradation of the pigmented cell layer underlying the photoreceptor outer segments. No changes in the GCL or IPL were detected (Figure 3.1).

Furthermore, multifocal neovascular chorio-retinal lesions disrupting the RPE, staining positively with a blood vessel marker GS-IB<sub>4</sub> isolectin, were identified on RPE flatmounts. These lesions were concentrated mostly around the optic nerve head in the centre of the flatmount (Figure 3.2). RPE integrity is essential for the maintenance of the oBRB. Thus, RPE disruption and subsequent decrease in barrier properties cause increased permeability of fluids and blood components from the fenestrated choriocapillaris into the subretinal space. Sites of vascular leakage were detected in JR5558 mice as signal-enhancing regions following an injection (i.p.) of a low molecular weight (approx. 300 Da) tracer molecule sodium fluorescein. Again, these lesions were localised predominantly in the central retina and did not seem to extend into the far periphery (Figure 3.3).

In addition, the regions of vascular leakage were detected as early as 3.5 weeks after birth and their number and size developed over time. A spontaneous gradual regression in the lesion number and/or intensity was observed at around 9 weeks of age, leaving only a small number of fluorescein-enhancing areas, usually of larger size and lower intensity (Figure 3.4A). By comparison, age-matched C57BL/6J control mice developed a normal pattern of vascular network, without any obvious aberrations (Figure 3.4B).

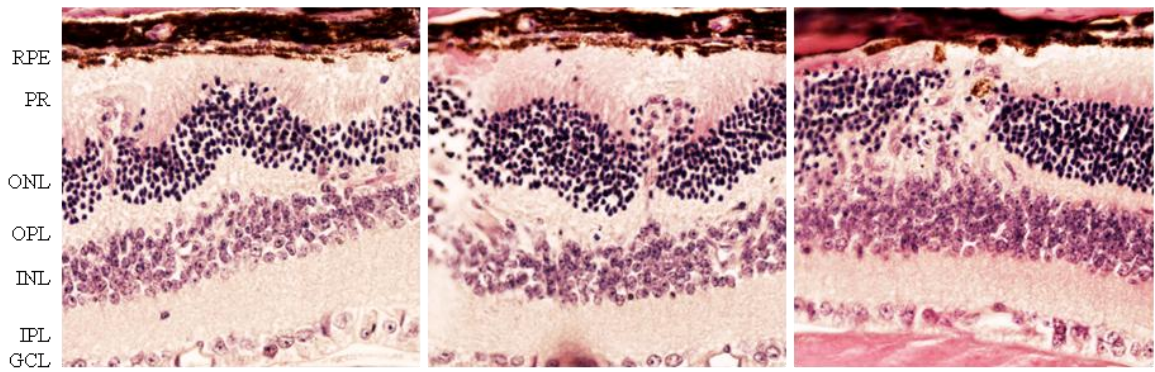


**Figure 3.1:** Effect of spontaneous neovascular lesion development on retinal architecture in JR5558 mice.

Representative haematoxylin and eosin (H&E) staining images of eye cross-sections in a single JR5558 mouse showing histological disorganisation of the distinct multilayered architecture of the retina. Magnification, 40x.

RPE, retinal pigment epithelium; PR, photoreceptors; ONL, outer nuclear layer; OPL, outer plexiform layer; INL, inner nuclear layer; IPL, inner plexiform layer; GCL, ganglion cell layer.

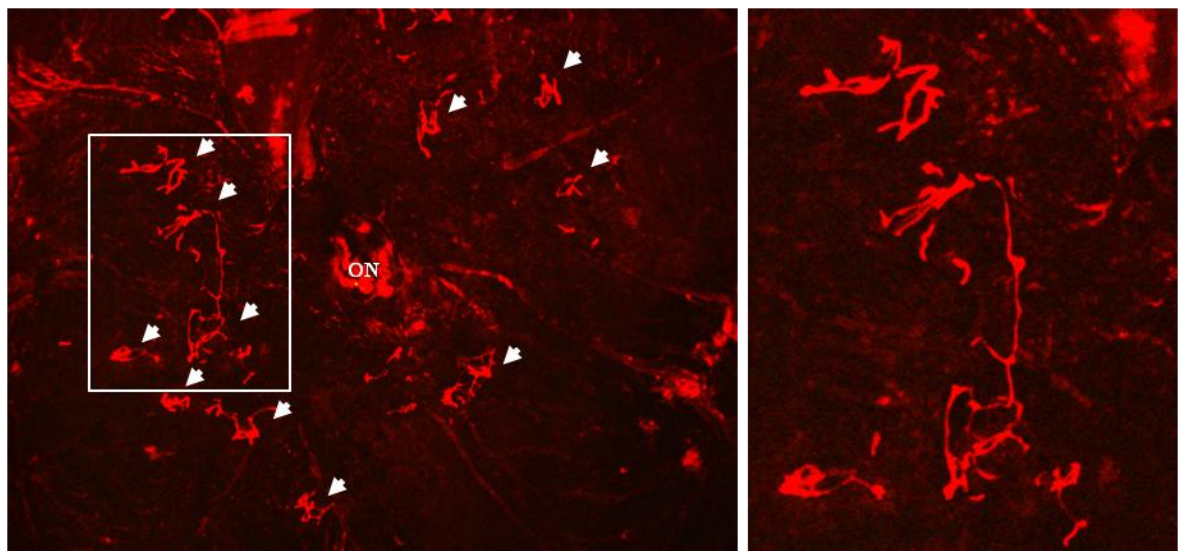


**Figure 3.2:** Detection of spontaneous chorio-retinal lesions in JR5558 mice.

A representative RPE flatmount stained with GS-IB<sub>4</sub> isolectin (blood vessels, *red*) showing neovascular chorio-retinal lesions disrupting the RPE (arrows). Magnification, 5x. *Right panel:* a close-up image of the area in white rectangle.

ON, optic nerve head.

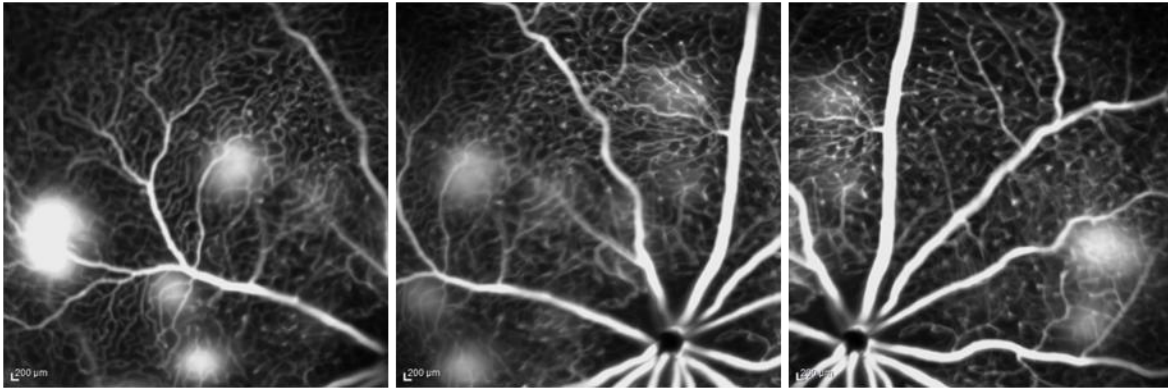


**Figure 3.3:** Detection of vascular leakage sites in JR5558 mice.

Representative fluorescein angiography (FA) images obtained in a single JR5558 mouse, showing signal-enhancing lesions in the left mid-periphery, centre and right mid-periphery of the retina.

Taken together, these described characteristics of the JR5558 mouse strain make it a suitable model to study spontaneous neovascularisation in the mouse retina. Moreover, the model allows to investigate the effect of potential therapeutics on the progression of neovascular lesion development (early stages) as well as the regression of fully established lesions (later stages).

### *3.2.2 IL-18 prevents progression and enhances regression of JR5558 lesions*

As previously suggested, IL-18 could prevent the development of laser-induced CNVs in a mouse model of wet AMD (Doyle et al., 2012; Doyle et al., 2014). To investigate the effect of IL-18 on the spontaneous neovascular lesions in JR5558 mice, repeated injections (i.p.) of IL-18 (100 or 1000 µg/kg body weight) were administered on 4 consecutive days. Progression of developing lesions was studied in 3-week-old animals, whereas regression of fully established lesions was examined in animals over 8 weeks of age.

IL-18 significantly reduced the number of signal-enhancing regions of vascular leakage in 3-week-old animals, as detected by fluorescein angiography, to about half the number seen in saline-injected controls. Both IL-18 doses had comparable effects on the number of developing vascular leakage sites (Figure 3.5). The total number of lesions in both eyes analysed on RPE flatmounts was not significantly different between the treatment groups, although the 100 µg/kg IL-18-treated mice trended towards a decreased number of lesions (Figure 3.6A). Volumetric analysis of lesion size showed a trend towards a dose-dependent decrease in total lesion volume in both eyes of animals injected with IL-18 (Figure 3.6B).

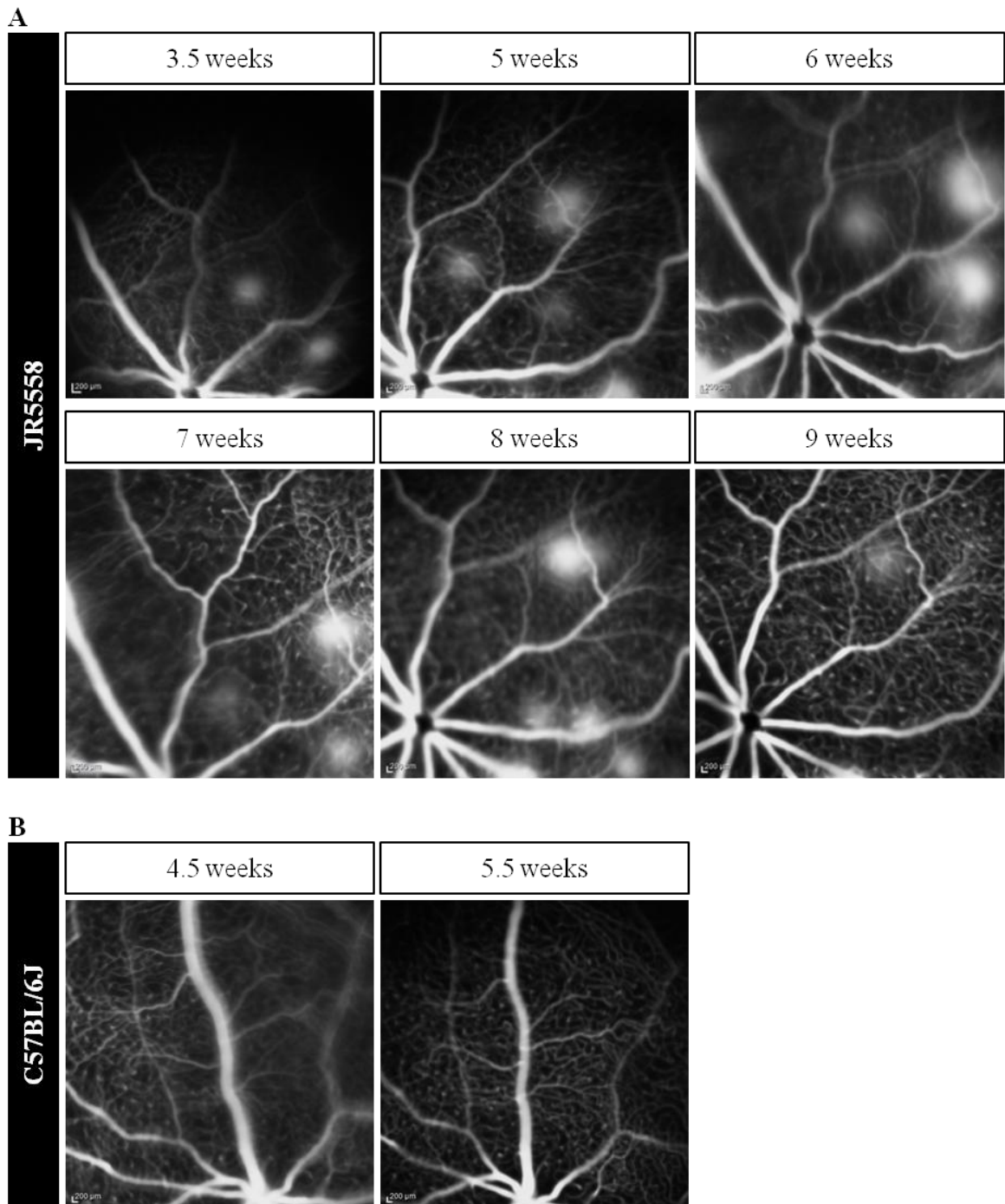


**Figure 3.4:** Development of vascular leakage sites in JR5558 mice over time.

A representative fluorescein angiography (FA) image profile from a single JR5558 mouse at 3.5-9 weeks of age, showing development and subsequent gradual regression of signal-enhancing lesions (A), and from a single C57BL/6J control mouse at 4.5 and 5.5 weeks of age, showing no vascular changes (B).

The average lesion volume per mouse was increased after the injection of the lower (100 µg/kg) IL-18 dose, although this was not significant (Figure 3.6C). A significant decrease in lesion size was observed in the case of lesions treated with the higher (1000 µg/kg) IL-18 dose, if these were analysed individually (Figure 3.6D). Moreover, IL-18 administration also significantly reduced the number of fluorescein-enhancing sites in older (8-14-week-old) mice with fully established neovascular lesions, but only at the lower, 100 µg/kg, dose (Figure 3.7). No significant differences were observed in the total number of lesions, the total lesion volume, average lesion volume or individual lesion size as detected on RPE flatmounts (Figure 3.8A-D). In addition, IL-18 had no effect on the electrophysiology of the retina. Neither dose of IL-18 caused any significant changes in the function of rods, measured by a-wave at the level of photoreceptors (Figure 3.9A,B) or b-wave at the level of interneurons (Figure 3.9C,D), as compared to saline-injected controls. Similarly, the cone responses, both a-wave (Figure 3.10A,B) and b-wave (Figure 3.10C,D), were neither significantly disrupted nor improved after IL-18 treatment.

To summarise, IL-18 administration could effectively reduce vascular permeability and attenuate growth of developing neovascular lesions in the JR5558 mouse model as well as enhance regression of vascular leakage areas at later stages when the neovascular lesions became fully established. These results provide further evidence that IL-18 could indeed represent a novel therapeutic strategy for the treatment of wet AMD.

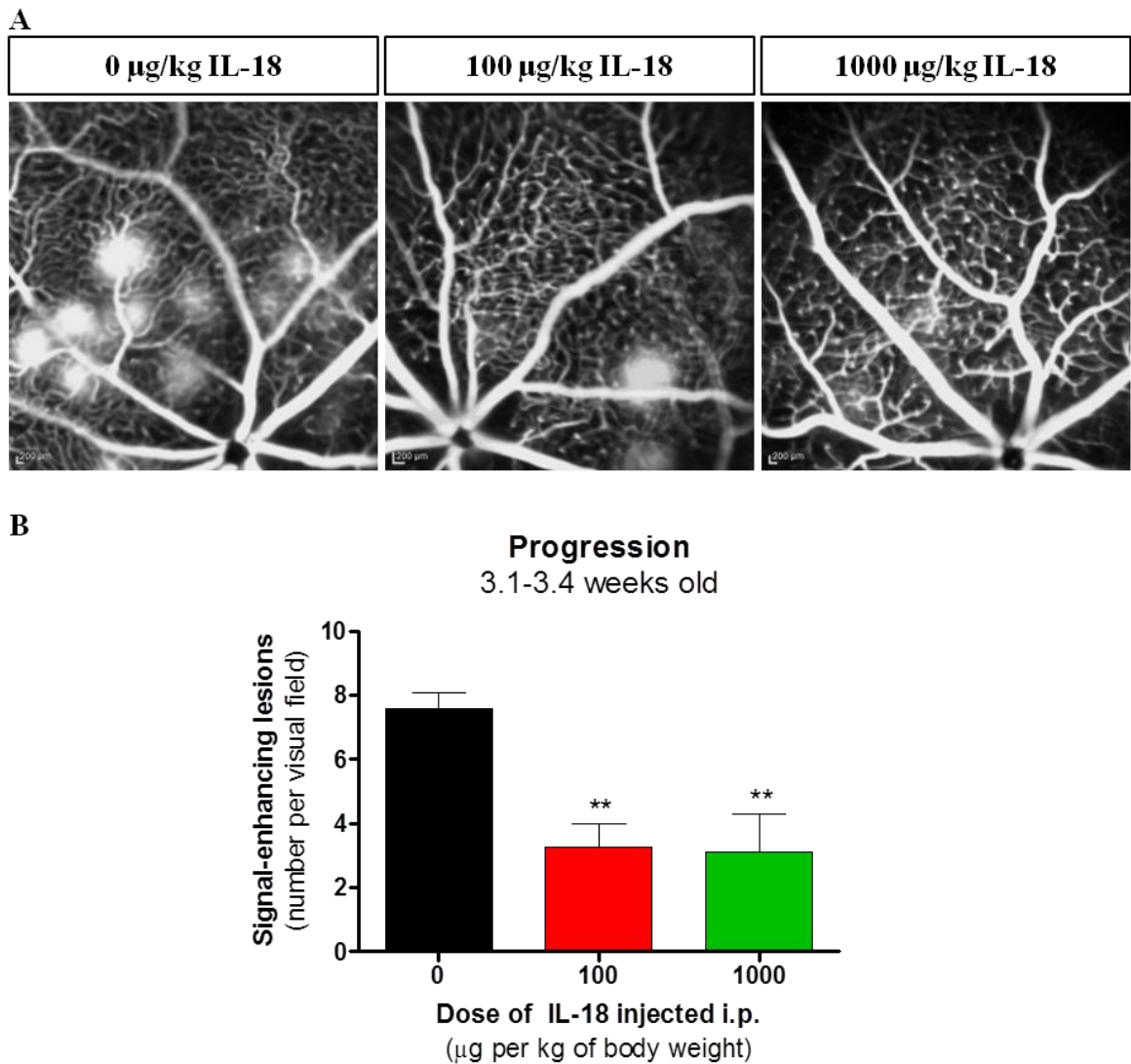


**Figure 3.5:** IL-18 in the progression of developing JR5558 vascular leakage sites. JR5558 mice ( $\approx$  3 weeks old) were injected (i.p.) with saline (0  $\mu\text{g}/\text{kg}$ ) or two different IL-18 doses (100 or 1000  $\mu\text{g}/\text{kg}$ ) on 4 consecutive days (day 1-4). Fluorescein angiography was carried out on day 5. Representative images for each treatment group are shown (A). The number of signal-enhancing lesions in each mouse was quantified per visual field of a fluorescein angiogram (B). Data are presented as mean  $\pm$  SEM (n=7-8 animals per each treatment group). \*\*p<0.01 by one-way ANOVA with Tukey post test compared to saline controls.

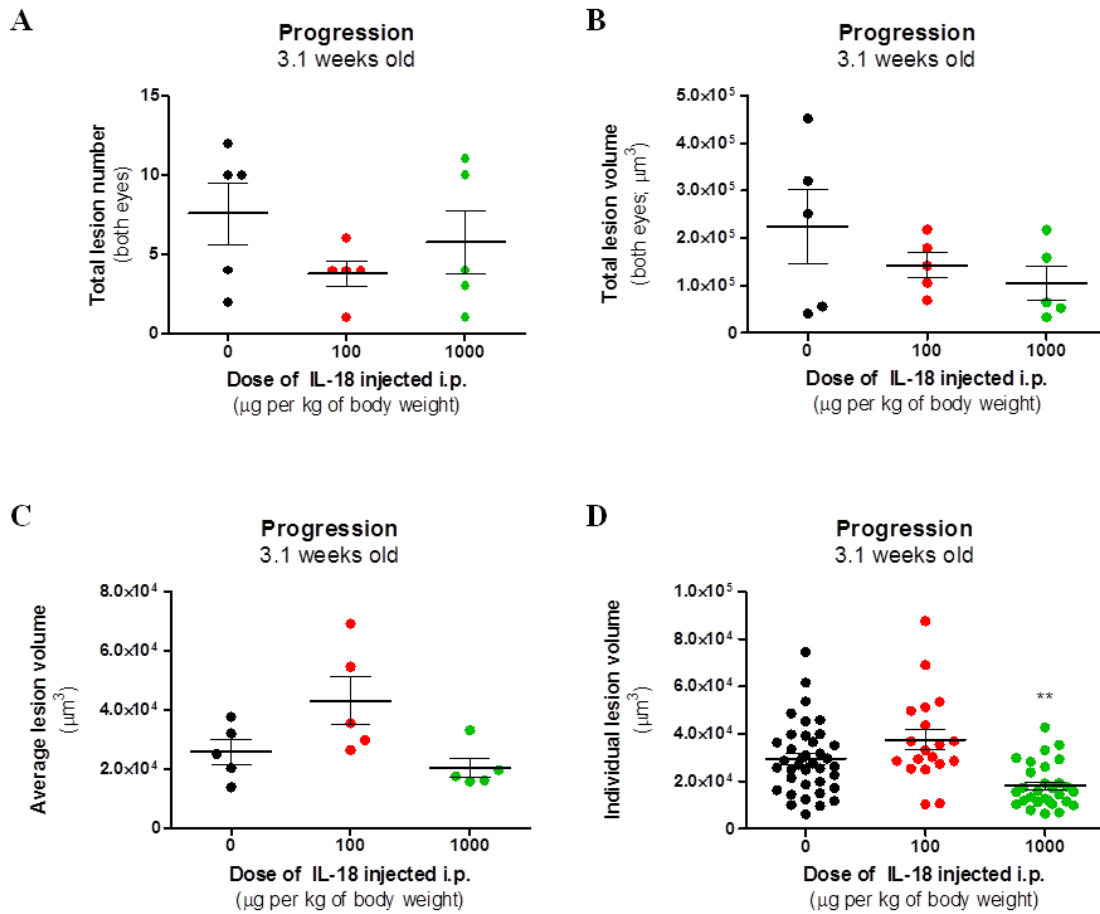
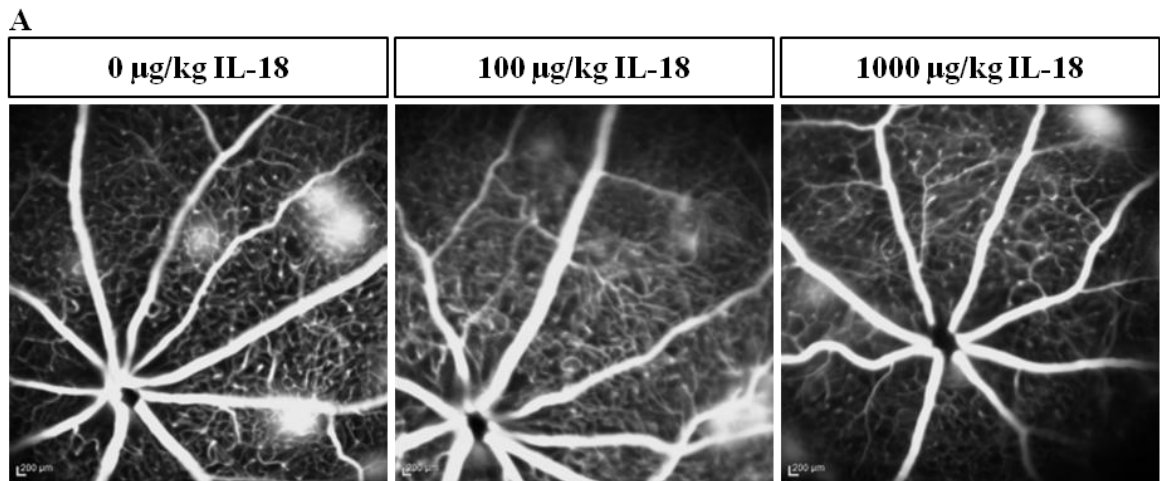


**Figure 3.6:** IL-18 in the progression of developing JR5558 chorio-retinal lesions.

JR5558 mice ( $\approx 3$  weeks old) were injected (i.p.) with saline (0  $\mu\text{g}/\text{kg}$ ) or two different doses of IL-18 (100 or 1000  $\mu\text{g}/\text{kg}$ ) on 4 consecutive days (day 1-4). RPE flatmounts were prepared on day 8 and volumetric analysis of chorio-retinal lesions was performed based on GS-IB<sub>4</sub> isolectin staining. The number of lesions in both eyes (A), total lesion volume in both eyes (B) and average lesion volume (C) per mouse were quantified (n=5 animals per each treatment group). Individual lesion volumes are also shown (n=19-38 per treatment group) (D). Data are presented as mean  $\pm$  SEM. \*\*p<0.01 by one-way ANOVA with Tukey post test compared to saline controls.





**B**

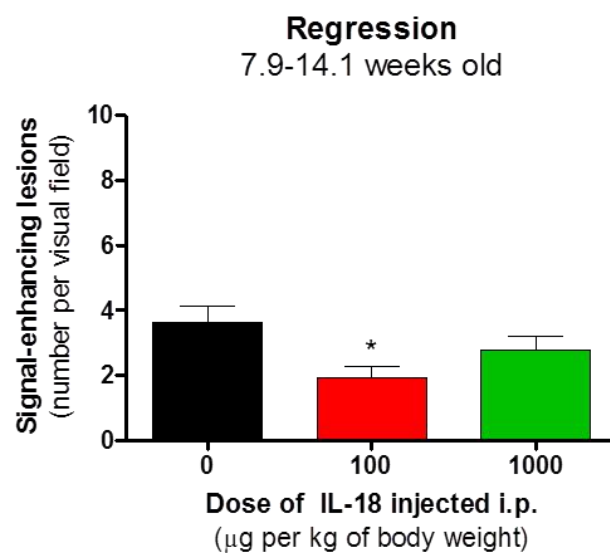


**Figure 3.7:** IL-18 in the regression of established JR5558 vascular leakage sites.

JR5558 mice ( $\approx$  8-14 weeks old) were injected (i.p.) with saline (0  $\mu\text{g/kg}$ ) or two different IL-18 doses (100 or 1000  $\mu\text{g/kg}$ ) on 4 consecutive days (day 1-4). Fluorescein angiography was carried out on day 5. Representative images for each treatment group are shown (A). The number of signal-enhancing lesions in each mouse was quantified per visual field of a fluorescein angiogram (B). Data are presented as mean  $\pm$  SEM (n=15-22 animals per each treatment group). \* $p < 0.05$  by one-way ANOVA with Tukey post test compared to saline controls.

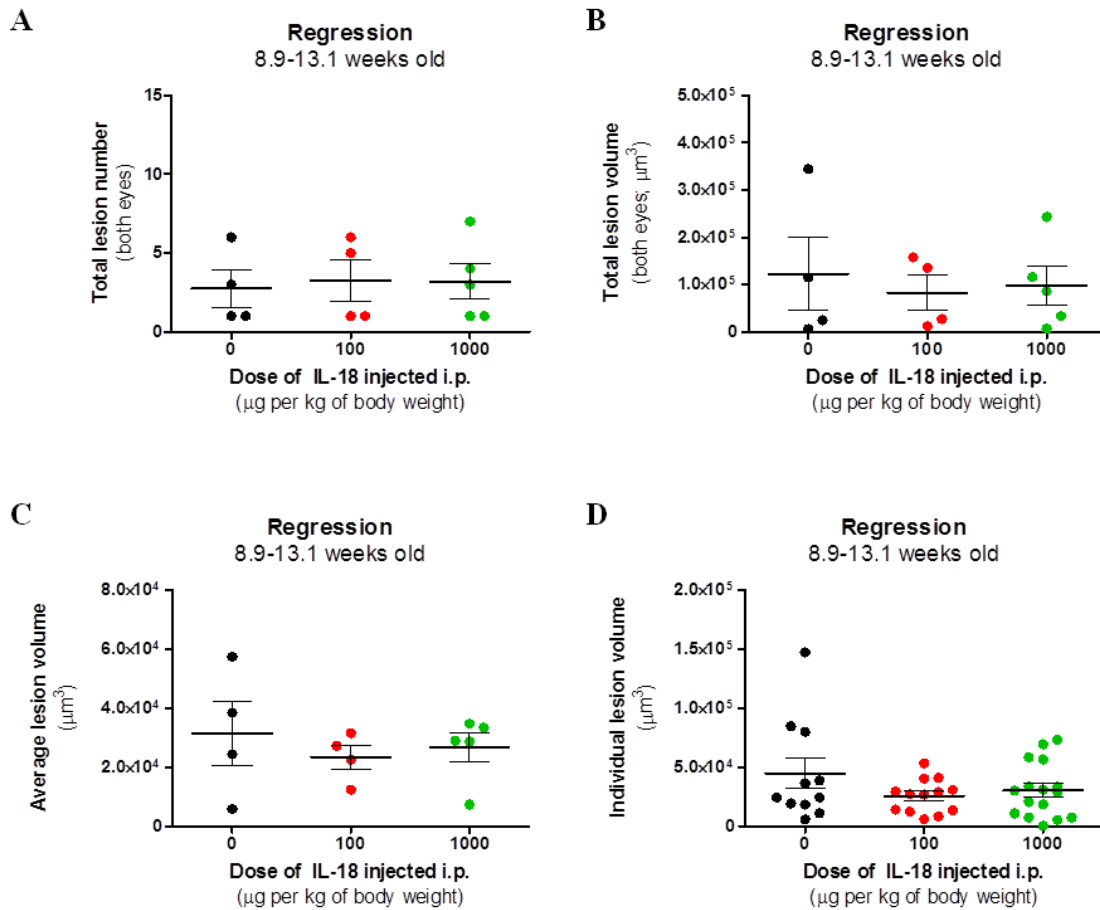


**Figure 3.8:** IL-18 in the regression of established JR5558 chorio-retinal lesions.

JR5558 mice ( $\approx$  9-13 weeks old) were injected (i.p.) with saline (0  $\mu\text{g}/\text{kg}$ ) or two different doses of IL-18 (100 or 1000  $\mu\text{g}/\text{kg}$ ) on 4 consecutive days (day 1-4). RPE flatmounts were prepared on day 8 and volumetric analysis of chorio-retinal lesions was performed based on GS-IB<sub>4</sub> isolectin staining. The number of lesions in both eyes (A), total lesion volume in both eyes (B) and average lesion volume (C) per mouse were quantified (n=4-5 animals per each treatment group). Individual lesion volumes are also shown (n=11-16 per treatment group) (D). Data are presented as mean  $\pm$  SEM. No significant differences between treatment groups by one-way ANOVA with Tukey post test compared to saline controls.

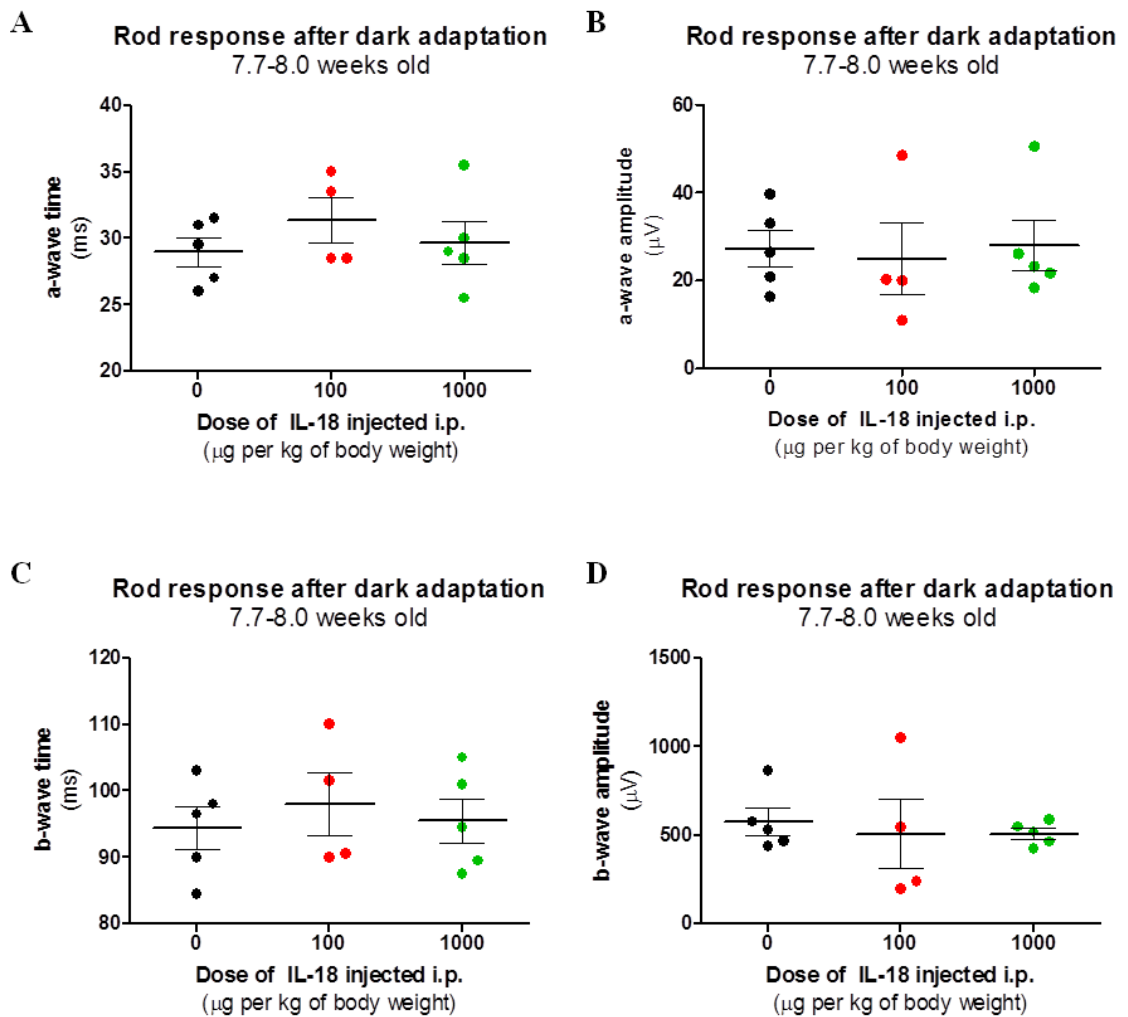


**Figure 3.9:** Effect of IL-18 on rod function in JR5558 mice.

JR5558 mice ( $\approx$  8 weeks old) were injected (i.p.) with saline (0  $\mu\text{g}/\text{kg}$ ) or two different IL-18 doses (100 or 1000  $\mu\text{g}/\text{kg}$ ) on 4 consecutive days (day 1-4). Electroretinography (ERG) was carried out on day 6. Rod-isolated responses were recorded using a dim white flash (25 dB maximal intensity, where maximal flash intensity was 3 candelas/ $\text{m}^2/\text{s}$ ) presented after dark adaptation overnight and assessed by a-wave at the level of photoreceptors (A,B) or b-wave at the level of interneurons (C,D). Time (A,C) and amplitude (B,D) of each response were measured. Physiological responses in the right and left eye were averaged. Data are presented as mean  $\pm$  SEM (n=4-5 animals per treatment group). No significant differences between treatment groups by one-way ANOVA with Tukey post test compared to saline controls.

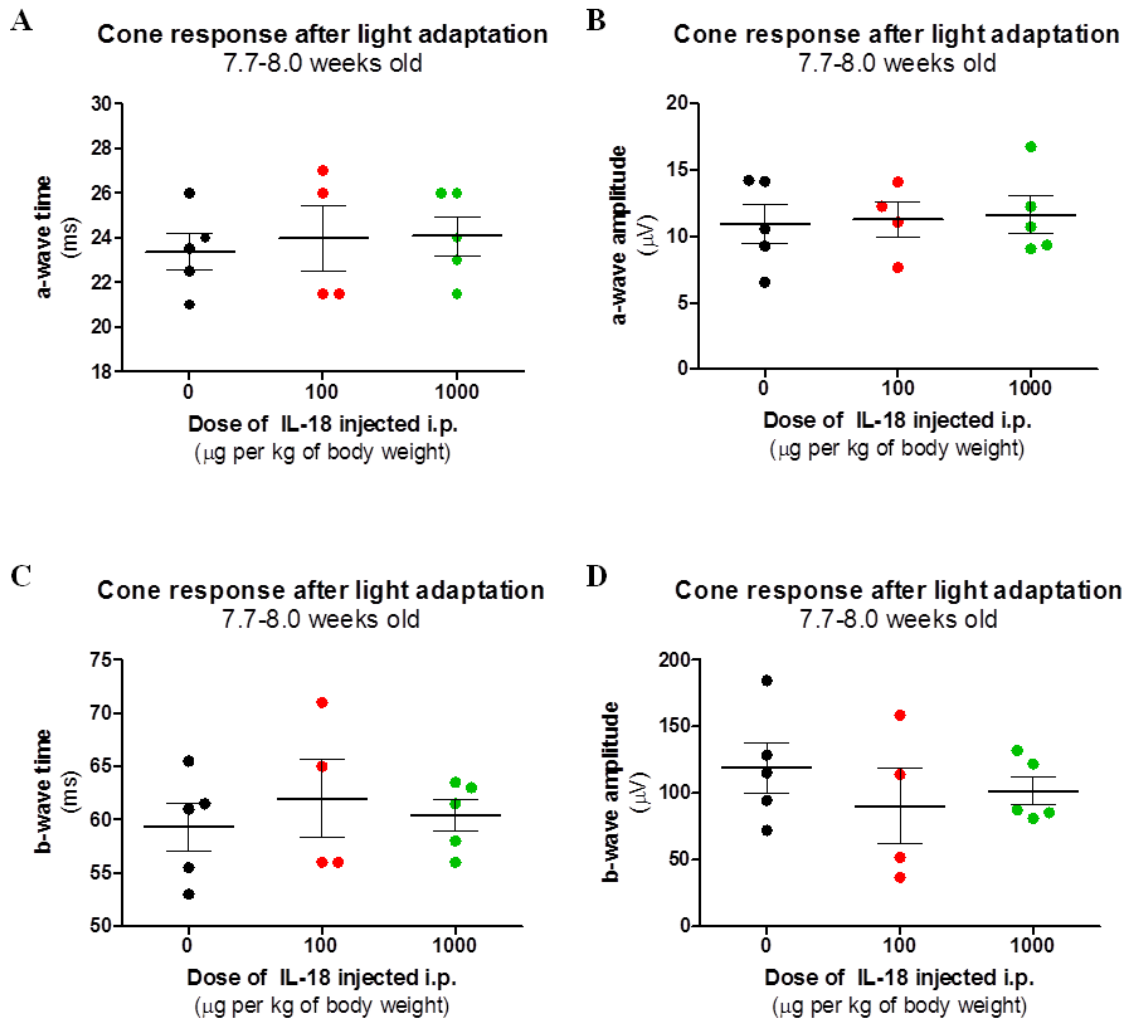


**Figure 3.10:** Effect of IL-18 on cone function in JR5558 mice.

JR5558 mice ( $\approx 8$  weeks old) were injected (i.p.) with saline ( $0 \mu\text{g}/\text{kg}$ ) or two different IL-18 doses ( $100$  or  $1000 \mu\text{g}/\text{kg}$ ) on 4 consecutive days (day 1-4). Electroretinography (ERG) was carried out on day 6. Cone-isolated responses were recorded using a white flash of intensity  $3 \text{ candelas}/\text{m}^2/\text{s}$  presented after light adaptation for 10 minutes to rod-suppressing background light of  $30 \text{ candelas}/\text{m}^2$  and assessed by a-wave at the level of photoreceptors (A,B) or b-wave at the level of interneurons (C,D). Time (A,C) and amplitude (B,D) of each response were measured. Physiological responses in the right and left eye were averaged. Data are presented as mean  $\pm$  SEM ( $n=4-5$  animals per treatment group). No significant differences between treatment groups by one-way ANOVA with Tukey post test compared to saline controls.

### 3.2.3 IL-18 regulates VEGF secretion *in vivo* and *in vitro*

The anti-angiogenic and anti-permeability properties of IL-18 have been suggested to be mediated by its regulation of VEGF synthesis (Doyle et al., 2012; Shen et al., 2014). In addition, VEGF appeared to be an important driver of the phenotypic changes observed in the JR5558 mouse strain (Hasegawa et al., 2014; Nagai et al., 2014). The effect of IL-18 on VEGF production was therefore explored *in vivo* in JR5558 mice and *in vitro* in hRPE cells.

In the retinas of younger animals (3 weeks old), VEGF levels were significantly decreased after treatment with the lower (100 µg/kg) dose of IL-18, but no significant difference was observed at the higher dose (1000 µg/kg) (Figure 3.11A). Similarly, the concentration of VEGF in the retinas of older animals (9-13 weeks old) was not affected by administration of the higher IL-18 dose, however, the effect of the lower dose on the retinal VEGF levels was not analysed in this case (Figure 3.11B). The RPE serves many important support functions in order to maintain retinal homeostasis, one of them being production of growth factors, including VEGF. *In vitro*, the levels of secreted VEGF were found to increase over time in a linear manner, suggesting that VEGF was being constitutively produced by the RPE. Supplementation of the cell culture media with IL-18 (1000 ng/ml) decreased VEGF concentration at (almost) all time points examined (1-72 hours) (Figure 3.12A) and also significantly slowed down the overall rate of VEGF secretion (Figure 3.12B). The cell viability was not negatively affected by treatment with increasing doses of IL-18 (up to 1000 ng/ml) over the period of 72 hours (Figure 3.13), but was in fact significantly higher, especially during the earlier time points (up to 12 hours) (Figure 3.13A-D).

Taken together, these results support previous observations that IL-18 could exert its effect on neovascularisation and vascular permeability by regulating VEGF levels secreted by the RPE, without causing RPE cell degeneration and death.

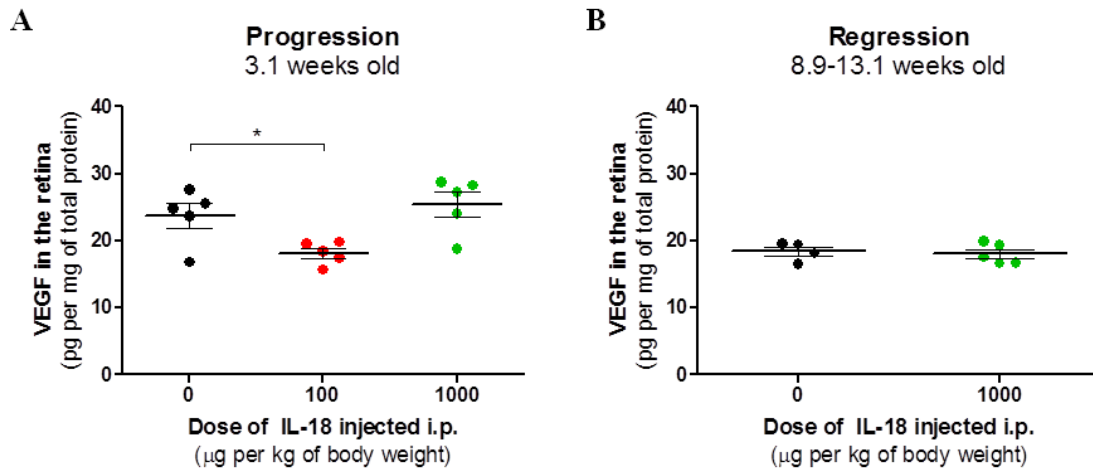


**Figure 3.11:** Effect of IL-18 on VEGF production in the JR5558 retina.

JR5558 mice, either  $\approx$  3 weeks (A) or 9-13 weeks (B) old, were injected (i.p.) with saline (0  $\mu\text{g}/\text{kg}$ ) or two different IL-18 doses (100 or 1000  $\mu\text{g}/\text{kg}$ ) on 4 consecutive days (day 1-4). Retinas were isolated on day 8 and VEGF concentration in protein lysates was determined using an appropriate ELISA. Data are presented as mean  $\pm$  SEM (n=4-5 animals per each treatment group) and expressed as pg of VEGF per mg of total retinal protein as measured by the BCA assay. \* $p < 0.05$  by one-way ANOVA with Tukey post test compared to saline controls.

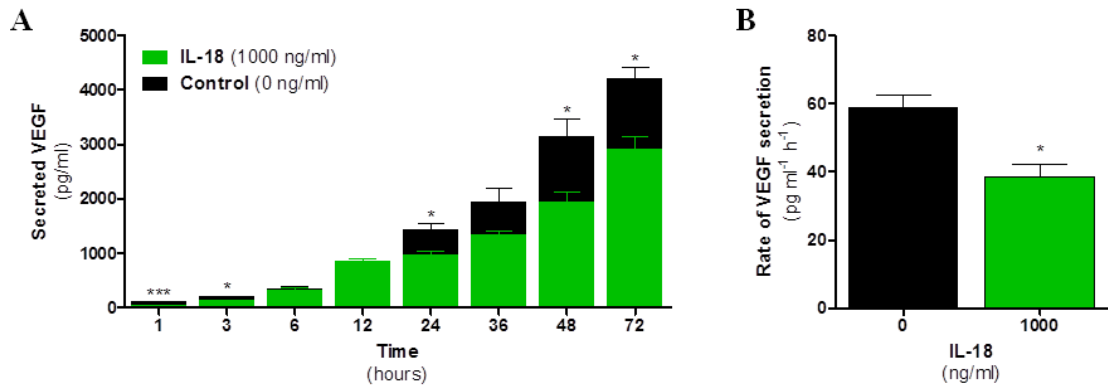


**Figure 3.12:** Effect of IL-18 on VEGF production *in vitro* in hFRPE cells.

Primary human foetal RPE (hFRPE) cells were treated with control medium (0 ng/ml) or a single dose of IL-18 (1000 ng/ml) for 1 to 72 hours. VEGF concentration in the cell-free supernatants was measured at each time point (A). Rate of VEGF secretion was calculated from the slope of linear regression of VEGF concentration (pg/ml) against time (hours) (B). Data are presented as mean  $\pm$  SEM and represent a single experiment carried out in triplicate. \* $p < 0.05$ , \*\*\* $p < 0.001$  by Student's t test compared to control at each time point.

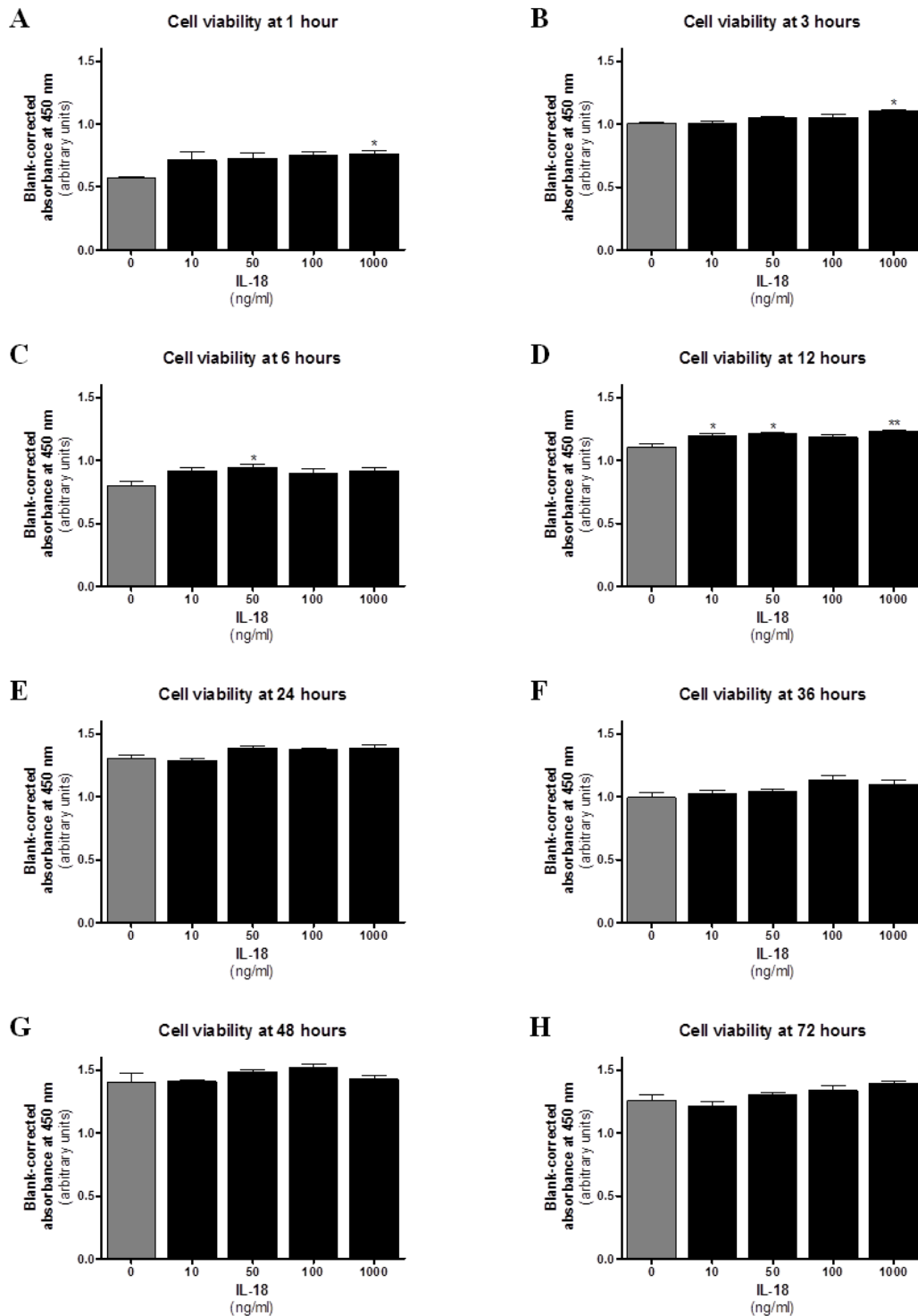


**Figure 3.13:** Effect of IL-18 on RPE cell viability *in vitro*.

Primary human foetal RPE (hFRPE) cells were treated with control medium (0 ng/ml) or increasing doses of IL-18 (10-1000 ng/ml) over the period of 72 hours. Cell viability was measured by an MTS assay at 1 (A), 3 (B), 6 (C), 12 (D), 24 (E), 36 (F), 48 (G) or 72 (H) hours, and is presented as the blank-corrected absorbance at 450 nm. Data are presented as mean  $\pm$  SEM and represent a single experiment carried out in triplicate. \*p<0.05, \*\*p<0.01 by one-way ANOVA with Tukey post test compared to control at each time point.



#### 3.2.4 IL-18 promotes RPE wound-healing *in vitro*

An increase in RPE cell viability observed after IL-18 treatment was rather intriguing. RPE cells are generally non-dividing or have a very slow proliferation rate. Due to the nature of reagents used in the assay, however, it could not be concluded whether the effects of IL-18 on cell viability were caused by active cell proliferation or simply reflected an increase in metabolic activity. A series of wound-healing assays was therefore carried out to address this issue (Figure 3.14).

As expected, the normal rate of wound closure was very slow, with only 4% of the original wound size healed after 18 hours in control cells and an overall rate of wound closure of 0.2% per hour (Figure 3.15, black bars). IL-18 exposure significantly increased the rate of wound-healing to about double the rate observed in control samples, i.e. approximately 0.4% per hour. All IL-18 doses showed comparable effects and an overall wound closure of about 7-8% after 18 hours of treatment. Noticeably, the earliest significant differences between control and IL-18-treated samples were detected at 10-12 hours and continued until 18 hours (Figure 3.15). Based on this, IL-18 acts as an important regulator of the wound-healing process in the RPE.

#### 3.2.5 IL-18 regulates tight junction protein expression in endothelial cells *in vitro*

The vascular permeability and the paracellular transport are controlled by tight junctions that exist between endothelial cells lining the blood vessels. For this reason, the effect of IL-18 treatment on tight junction protein expression in endothelial cells was investigated as yet another potential mechanism of IL-18 action to prevent vascular leakage.

IL-18 was found to cause a transient up-regulation of tight junction proteins claudin-5 and occludin *in vitro* in bEnd.3 cells. Increased levels of these proteins were detected after 12 hours of treatment with IL-18 and returned back to baseline after 24 hours. Interestingly, this increase in claudin-5 and occludin was accompanied by a transient down-regulation of ZO-1, showing minimum expression after 12 hours of treatment and slowly returning back to baseline at 24 and 48 hours (Figure 3.16). Thus, these results point towards an additional regulatory function of IL-18 that could have a direct effect on vascular permeability.

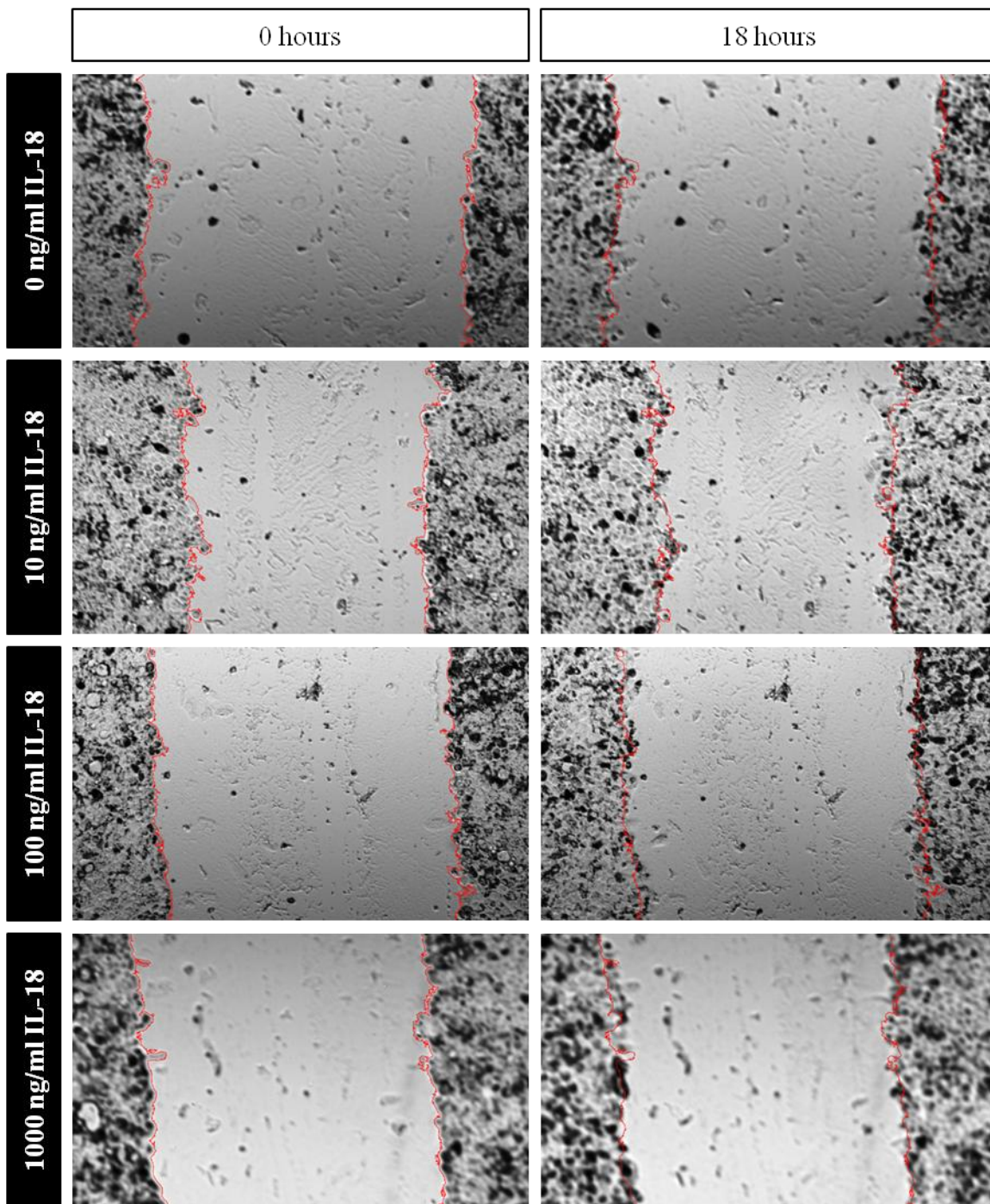


**Figure 3.14:** Effect of IL-18 on RPE wound-healing *in vitro* (representative images).

Primary human foetal RPE (hfRPE) cells were treated with control medium (0 ng/ml) or increasing doses of IL-18 (10-1000 ng/ml) immediately after making a scratch through the centre of the well. Bright-field microscopy images were acquired at the same location at baseline (0 hours) and then every 2 hours until 18 hours. Representative images for each treatment group are shown. The corresponding wound size at baseline is demarcated (*red*). Magnification, 20x.

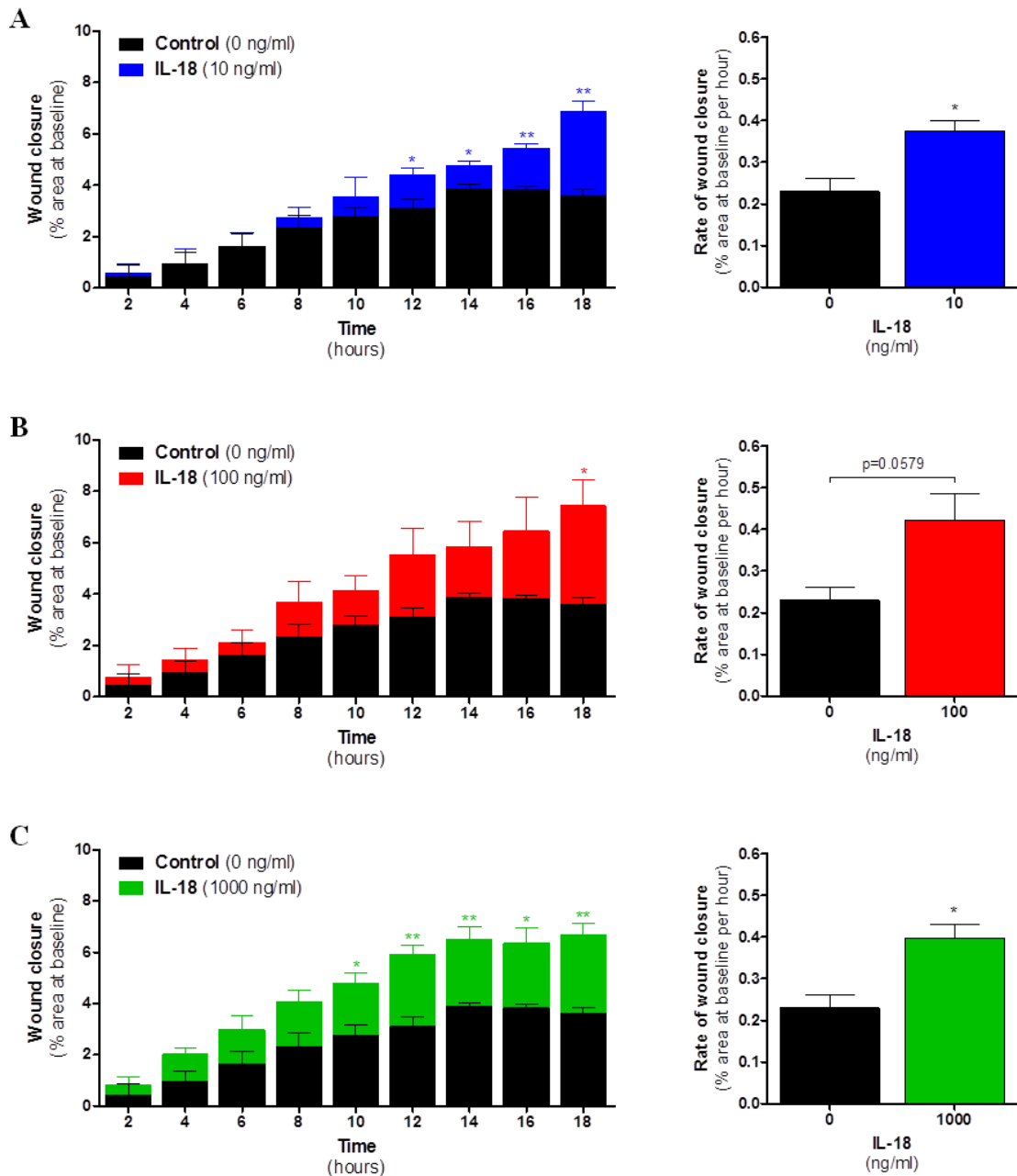


**Figure 3.15:** Effect of IL-18 on RPE wound-healing *in vitro* (quantification).

Primary human foetal RPE (hfRPE) cells were treated with control medium (0 ng/ml) or increasing doses of IL-18 at 10 (A), 100 (B) or 1000 (C) ng/ml immediately after making a scratch through the centre of the well. Bright-field microscopy images were acquired at the same location at baseline (0 hours) and then every 2 hours until 18 hours. The wound size at each time point was quantified in ImageJ. Wound closure is expressed as % area at baseline. Rate of wound closure was calculated from the slope of linear regression of wound closure (% area at baseline) against time (hours). Data are presented as mean  $\pm$  SEM and represent a single experiment carried out in 3-4 replicates. \* $p < 0.05$ , \*\* $p < 0.01$  by Student's t test compared to control at each time point.

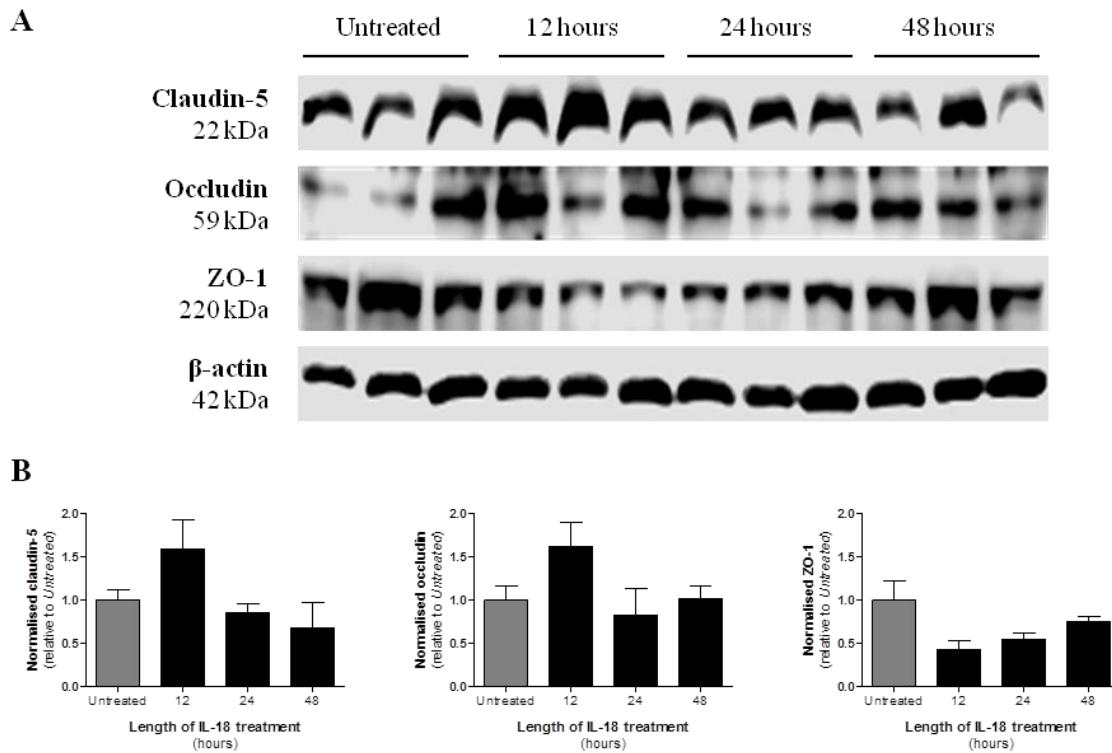


**Figure 3.16:** Effect of IL-18 on tight junction protein expression *in vitro* in bEnd.3 cells. Mouse brain endothelial (bEnd.3) cells were treated with control medium (untreated) or a single dose of IL-18 (50 ng/ml) for 12 to 48 hours. Protein lysates were separated by SDS-PAGE using 10  $\mu$ g of total protein as determined by the BCA assay. Proteins of interest were immunodetected by Western blotting (A). Band intensity was quantified in ImageJ and data normalised to the corresponding  $\beta$ -actin loading control (B). Data are presented as mean  $\pm$  SEM and represent a single experiment carried out in triplicate. No significant differences between treatment groups by one-way ANOVA with Tukey post test compared to untreated control.

### 3.3 Discussion

To further evaluate the efficacy of IL-18 administration as a potential therapeutic strategy for wet AMD, a novel mouse model of spontaneous neovascularisation, the JR5558 mouse, was utilised as an alternative to the previously used laser-induced CNV model. This mouse strain harbours recessive mutations in unknown genes that in the homozygous state result in spontaneous CNV development and retinal angiomatous proliferation, with occasional retinal-choroidal anastomoses (Hasegawa et al., 2014; Nagai et al., 2014). In our hands, the JR5558 mice developed a spontaneous neovascular phenotype consistent with previously published reports (Hasegawa et al., 2014; Nagai et al., 2014). Some of the neovascular

lesions seemed to originate in the deep vascular plexus of the retina, at the outer edge of the INL, and descend into the typically avascular ONL, which is in line with observations by Hasegawa et al. (2014). Other lesions appeared to be of choroidal origin, disrupting the RPE, and were readily detected on RPE flatmounts, similar to descriptions by Nagai et al. (2014). The development of multifocal neovascular lesions was accompanied by increased vascular leakage that manifested as signal-enhancing regions in sodium fluorescein tracer studies. These lesions seemed to localise predominantly in the centre to mid-periphery of the retina around the optic nerve head, as previously suggested (Hasegawa et al., 2014; Nagai et al., 2014). The areas of vascular leakage were found to appear soon after birth and continued to develop over time, with a spontaneous gradual regression observed at around 9 weeks. These signal-enhancing sites of vascular leakage were not part of normal retinal vascular development, as age-matched C57BL/6J control mice developed a normal pattern of retinal vascular network. These observations were consistent with others (Hasegawa et al., 2014; Nagai et al., 2014), who demonstrated that the neovascular lesion development in JR5558 mice started in early postnatal days (between P10 and P15). The areas of vascular leakage initially increased in number and severity (until approx. P25-30) and this was followed by a gradual decline in their number, although the established lesions seemed to be larger in size and were present for at least 3 months (no observations were made beyond this point). As suggested by Hasegawa et al. (2014), the decline in vascular permeability observed at later stages of lesion development might be due to the RPE encapsulating the neovascular lesions and blocking the leakage.

In addition, the early phenotypic changes in JR5558 mice were accompanied by multiple areas of retinal depigmentation that generally localised to the sites of increased vascular permeability and became more diffuse and enlarged over time (Hasegawa et al., 2014). The neovascular lesions were shown to progressively associate with macrophages and their depletion resulted in decreased lesion size, but not number, indicating that macrophages were involved in driving the growth of existing lesions, rather than initiating the sprouting of new blood vessels. Persistent vascular leakage during later stages gave rise to retinal oedema and local gliosis, followed by photoreceptor dysfunction and death (Nagai et al., 2014). The degree of depigmentation, development of retinal oedema and gliosis, function of photoreceptors or the involvement of macrophages, however, were not addressed in the present study.

Administration of IL-18 was found to prevent the progression of developing neovascular lesions in the JR5558 mouse model. A significant decrease in the number of vascular leakage sites was observed using both doses of injected IL-18. The lower (100 µg/kg) IL-

18 dose also seemed to decrease the total number of chorio-retinal lesions detected on RPE flatmounts, even though the remaining lesions appeared to be larger in size, suggesting that it might be highly efficient against the smaller developing lesions, but is not sufficient to decrease the size of larger ones. The higher (1000 µg/kg) dose of IL-18 had no effect on the total lesion number or their average volume. However, if these lesions were analysed individually, the lesion size was found to significantly decrease, indicating that the higher dose of IL-18 might be efficient even against the larger lesions. Overall, a trend towards a dose-dependent decrease in the total volume of chorio-retinal lesions was observed after IL-18 treatment. The major drawback of the volumetric analysis of chorio-retinal lesions on RPE flatmounts was the high degree of variability of lesion sizes within the same animal and even within the same eye. Analysis of individual lesions (rather than analysis per animal) showed to be less susceptible to outliers and appeared to be more appropriate in this case. In summary, these results show that IL-18 administration could effectively reduce vascular leakage and attenuate the growth of developing neovascular lesions in JR5558 mice. Furthermore, IL-18 treatment significantly enhanced regression of vascular leakage associated with established neovascular lesions, but only at the lower, 100 µg/kg, dose. It seems possible that in this case, the increased concentration of IL-18 could induce expression of its own balancing factor IL-18BP, limiting the availability of free, active IL-18, although this question was not addressed in the present study. No significant effects on the chorio-retinal lesion number or size were detected. A considerable degree of variability was once again a major issue, especially in the control mice, prompting a speculation that the spontaneous lesion regression could occur at various rates, possibly depending on the original lesion size and/or the capacity of the RPE to encapsulate it, as mentioned before (Hasegawa et al., 2014). Moreover, IL-18 administration had neither a positive nor a negative effect on electrophysiological function of retinal rods and cones, suggesting that it was not sufficient to reverse the damage that had already occurred in the photoreceptors and at the same time did not enhance retinal degeneration. This is in line with our previous observations that IL-18 had no effect on the RPE cell viability or barrier integrity (Doyle et al., 2014) and contrary to others who proposed that IL-18 induced RPE cell degeneration and death (Tarallo et al., 2012). Taken together, these results reinforce the idea that IL-18 represents a novel therapeutic strategy for the treatment of neovascular AMD. In addition, they provide further evidence for the diverse roles of IL-18 which might depend on the local microenvironment, as it appears that IL-18 could attenuate the vascular leakage and neovascular lesion growth in the JR5558 mouse strain via distinct mechanisms determined by the stage of lesion development.

It was previously suggested that the protective function of IL-18 in models of wet AMD might be mediated by its regulation of VEGF synthesis as IL-18 significantly decreased the levels of VEGF secretion *in vitro* (Doyle et al., 2012). Moreover, IL-18 could efficiently inhibit VEGF-induced changes in the retina, including increased vascular permeability and barrier breakdown, development of retinal and subretinal neovascularisation, and tight junction suppression (Shen et al., 2014). As previously alluded to, the JR5558 phenotype is driven by VEGF overexpression and VEGFR2-mediated signal transduction cascade.

The retinal levels of VEGF were found to be significantly decreased in younger JR5558 mice that were administered the lower dose of IL-18 (100 µg/kg), which correlated with the reduced number of vascular leakage sites in these animals, as already discussed. The VEGF production, however, was not affected by treatment with the higher (1000 µg/kg) IL-18 dose, even though a decreased number of vascular leakage areas and smaller size of individual chorio-retinal lesions were still observed. These results further point towards multiple mechanisms of IL-18 action in attenuating neovascular lesion development and its associated increased vascular permeability in the JR5558 mouse model. It appears that IL-18 not only reduces vascular leakage by decreasing VEGF levels in the retina, but can also affect vascular permeability and chorio-retinal lesion development through a mechanism independent of VEGF regulation. One possibility is that IL-18 can promote encapsulation of neovascular lesions by the RPE, that was previously described (Hasegawa et al., 2014), and/or enhance the barrier properties of this RPE, thus limiting both lesion growth and vascular leakage. In addition, the RPE is one of the key contributors to VEGF production in the retina. VEGF was found to be constitutively secreted by the RPE cells *in vitro* and treatment with IL-18 significantly slowed down the overall rate of VEGF production. At the same time, IL-18 had no effect on RPE cell viability, confirming that the reduction in VEGF production was not due to RPE cell death. On the contrary, the RPE cell viability was significantly increased after IL-18 exposure, especially during earlier time points (up to 12 hours), which could be explained by a relatively short half-life of IL-18 (approx. 16 hours). Noticeably, the cell viability assay used in this study relies on the bioreduction of the MTS tetrazolium substrate into formazan product that is accomplished by NADPH or NADH produced by dehydrogenase enzymes in metabolically active cells. Therefore, to address the question whether IL-18 could increase the proliferation rate of RPE cells or just affected their metabolic capacity without increasing the actual cell number, a series of *in vitro* wound-healing (scratch) assays was carried out. Most importantly, IL-18 was found to promote the wound-healing process in the RPE by increasing the rate of wound closure. Interestingly, the first significant effects of IL-18 on the wound size were detected after 10-

12 hours and thus did not correlate with the time points when significant changes in RPE cell viability were observed. This suggests that the increase in cell viability after short-term IL-18 treatment was not associated with cell proliferation, but rather reflected an increase in metabolic activity, possibly to induce cell migration and initiate wound healing. Once this process was triggered, significant changes in the wound size were observed, but the cell viability was no longer affected. In other words, if the early increase in cell viability was caused by active cell proliferation, then the wound would have been closed shortly after IL-18 exposure by proliferating cells, however, this was not the case. In addition, there was no increase in cell viability during later time points, even though the wound size was significantly smaller, indicating that the wound-healing process was mediated by cell migration, rather than cell proliferation, accompanied by an early increase in metabolic activity. This is in line with the fact that RPE cells are generally non-dividing or have a very slow proliferation rate. Thus, these results support the idea of the RPE encapsulating the neovascular lesions in JR5558 mice to limit vascular leakage. Furthermore, IL-18 was found to directly regulate tight junction protein expression in endothelial cells *in vitro*. It induced a transient up-regulation of transmembrane proteins claudin-5 and occludin, while at the same time down-regulating their cytoplasmic partner ZO-1, potentially as a form of compensatory mechanism to maintain equilibrium. However, to elucidate the details of this control pathway would require further investigations. IL-18 could interfere with the tight junction mRNA expression at the transcriptional and/or post-transcriptional level, affect the protein stability by regulating their post-translational modifications known to target them for degradation or influence their transport to the plasma membrane and assembly of a functional tight junction complex. In addition, the functional relevance of the above observation needs to be evaluated by functional assays, such as TEER measurements or flux assay, to confirm that the increase in tight junction protein expression translates into enhanced endothelial barrier properties. Moreover, to investigate whether IL-18 could mediate its effects on vascular leakage and lesion development in JR5558 mice via its control of tight junctions, the mRNA and protein levels of tight junction components would need to be analysed in the retinas and RPE flatmounts of these mice following IL-18 treatment. Nonetheless, these *in vivo* and *in vitro* studies provide further evidence that the anti-angiogenic and anti-permeability roles of IL-18 could be mediated by its regulation of VEGF secretion, RPE wound-healing and/or endothelial tight junction protein expression. Importantly, identifying the specific mutations that underlie the phenotypic changes in the JR5558 mouse strain could provide an invaluable insight into the development of retinal



and choroidal neovascularisation as well as shed more light on the mechanism of IL-18 action to prevent vascular leakage and lesion development in these animals.

The main conclusions inferred from experiments presented in this section are as follows:

- JR5558 mice develop spontaneous neovascular lesions that disrupt normal histological organisation of the retina
  - these lesions disrupt the RPE
  - these lesions are accompanied by vascular leakage
  - these lesions appear soon after birth
  - these lesions spontaneously regress
- IL-18 prevents progression of developing JR5558 neovascular lesions
- IL-18 enhances regression of established JR5558 neovascular lesions
- IL-18 has no effect on retinal electrophysiology in JR5558 mice
- IL-18 decreases VEGF secretion *in vitro* and *in vivo*
- IL-18 has no effect on RPE cell viability
- IL-18 promotes RPE wound-healing *in vitro*
- IL-18 regulates tight junction protein expression in endothelial cells *in vitro*

## Chapter 4

# **Diurnal processing of the NLRP3 inflammasome in RPE homeostasis**

## 4 DIURNAL PROCESSING OF THE NLRP3 INFLAMMASOME IN RPE HOMEOSTASIS

---

### 4.1 Introduction

The RPE serves many important roles in order to support the proper visual function of retinal photoreceptors. Importantly, it is responsible for the phagocytosis and degradation of shed POS discs on daily basis. As recently reported, this process occurs through a non-canonical autophagy pathway (LAP) and depends on proteins of the classical autophagy machinery (Kim et al., 2013). Furthermore, components of the NLRP3 inflammasome, a large oligomeric complex of the innate immunity, and its effector cytokines IL-1 $\beta$  and IL-18 have been observed to associate with the RPE of patients with both dry and wet AMD. In addition, several types of cell death mechanisms have been suggested to mediate RPE degeneration, including apoptosis, pyroptosis and necroptosis. Noticeably, none of these cellular processes function in isolation, but rather seem to interact in complex crosstalk networks that are now slowly being realised and currently become extensively reported in the literature.

Autophagy has been shown to regulate endogenous inflammasome activators and function as a key modulator of IL-1 $\beta$  and IL-18 transcription, processing and release (Harris, 2013; Jones et al., 2013). Inhibition of autophagy was found to cause accumulation of damaged mitochondria producing ROS, which in turn lead to the NLRP3 inflammasome activation (Nakahira et al., 2011; Zhou et al., 2011). Autophagy could also control IL-1 $\beta$  secretion by targeting pro-IL-1 $\beta$  for lysosomal degradation and by regulating inflammasome assembly. Stimulating autophagy *in vivo* significantly decreased serum levels of IL-1 $\beta$  in response to LPS challenge (Harris et al., 2011). Interestingly, activation of the inflammasome was also found to induce autophagy. Blocking autophagy increased the inflammasome activation, whereas induction of autophagy limited it, suggesting that autophagy might be a negative regulator of inflammasome activity. Assembled inflammasomes were ubiquitinated, which targeted them for delivery to autophagosome, leading to their subsequent degradation. This demonstrated that autophagy could function to limit excessive inflammation by directly eliminating active inflammasome complexes (Shi et al., 2012). In line with these findings, autophagy was shown to protect against caspase-1-dependent pyroptosis. When autophagy was suppressed, pyroptosis occurred more frequently, potentially because of a sustained inflammasome activation (Byrne et al., 2013). Moreover, the RPE cell swelling observed after over-expression of pro-IL-1 $\beta$  and pro-IL-18 was abrogated by inducing autophagy, possibly due to sequestration and subsequent degradation of excessive cytokine precursors

in autophagosome (Doyle et al., 2014). Surprisingly, caspase-8, classically characterised as one of the pro-apoptotic caspases, has recently been described to serve as a direct effector and regulator of the NLRP3 as well as the absent in melanoma 2 (AIM2) inflammasomes to cleave IL-1 $\beta$  in a process independent of caspase-1 without the induction of pyroptosis. It was found to form an integral part of the inflammasome complex by binding directly to the pyrin domain of the adaptor protein ASC and localised to ASC inflammasome specks (Sagulenko et al., 2013; Antonopoulos et al., 2015). Interestingly, caspases also seem to be at the heart of the complex interplay between apoptosis and autophagy. Activated caspases were found to degrade autophagy proteins, shutting down the autophagic responses. In addition, they have the capacity to convert pro-autophagic proteins into pro-apoptotic ones to trigger cell death (Wu et al., 2014). It is clear that these complex crosstalk mechanisms allow an interaction between the inflammasome, autophagy and apoptosis to fine tune the cell function(s) and/or type of cell death depending on local conditions. Hence, elucidating the details of these complex networks in the RPE might contribute to understanding of AMD development.

The main purpose of experiments presented in this section was to study the role of the NLRP3 inflammasome in RPE homeostasis, i.e. in relation to the daily POS phagocytosis. The specific aims can be summarised as follows:

- to confirm the presence of inflammasome components in the RPE of AMD patients
- to establish a platform for inflammasome detection in the RPE *in vitro*
- to examine changes in the RPE activity and the presence of inflammasome components in the RPE in response to POS phagocytosis *in vivo* and *in vitro*
- to study the effect of autophagy induction on VEGF production *in vitro*

## 4.2 Results

### 4.2.1 Inflammasome components are present in human AMD tissue samples

To confirm that the NLRP3 inflammasome components and its effector cytokines IL-1 $\beta$  and IL-18 associate with the RPE of AMD patients, human sections of the macular region from healthy and GA donors were stained for the presence of NLRP3, caspase-1, NLRP6, IL-1 $\beta$  and IL-18.

NLRP3 was found to show a very weak staining pattern in both healthy controls and GA eyes. In both groups, its expression in the retina was localised mainly in the photoreceptor layer (especially in cones) and OPL. It was also detected in the choroid, staining primarily along the blood vessels. Although its presence in the RPE of healthy controls was difficult

to discern, in GA it seemed to accumulate specifically between the basal aspect of the RPE and Bruch's membrane (Figure 4.1, top panel). By contrast, a strong caspase-1 staining was observed in the retina of healthy controls, spanning more-less all retinal layers, localising mostly to photoreceptors (specifically the cones) and OPL. Its expression was also detected in the choroid, mainly around the blood vessels, however, its presence inside the RPE was once again difficult to make out in healthy controls. A similar general pattern of caspase-1 staining, although much weaker and more diffuse, was demonstrated in the GA samples. Moreover, the choroidal staining appeared to be stronger in this case, particularly around the blood vessels, and caspase-1 seemed to accumulate between the RPE and Bruch's membrane, sometimes found to completely surround the RPE (Figure 4.1, middle panel). The expression of NLRP6, an alternative inflammasome-forming member of the NLR family, was not detected in the retina, choroid or RPE of either healthy or GA-affected eyes (Figure 4.1, bottom panel). The general staining patterns of inflammasome effector cytokines IL-1 $\beta$  and IL-18 were comparable to that of caspase-1. They were detected in both healthy controls and GA patients, concentrating predominantly in the photoreceptor layer (especially in the cones and tips of the outer segments) and OPL, though in GA the staining appeared weaker and less regular. Their expression was increased in the choroid, especially around blood vessels, and they were also detected on the basolateral side of the RPE, even in healthy controls. In GA, the choroidal staining for IL-18 seemed stronger, particularly around blood vessels, but weaker in the case of IL-1 $\beta$ . Both cytokines were found to deposit between the RPE and Bruch's membrane as well as entirely surround the RPE (Figure 4.2). In addition, swelling, depigmentation, severe degeneration and bursting of the RPE were associated with GA. Some disturbances, although not as dramatic, of the RPE monolayer were also observed in healthy controls, possibly due to advanced age. No signs of apoptotic or blebbing cells were detected (Figure 4.1 and 4.2).

Taken together, these results support previous observations that components of the NLRP3 inflammasome complex as well as its effector cytokines can be detected in the RPE and retina of GA patients, but are also present in age-matched healthy controls, even though with slightly varying expression patterns. Moreover, they provide further evidence of a necrotic, rather than apoptotic, type of cell death in GA.

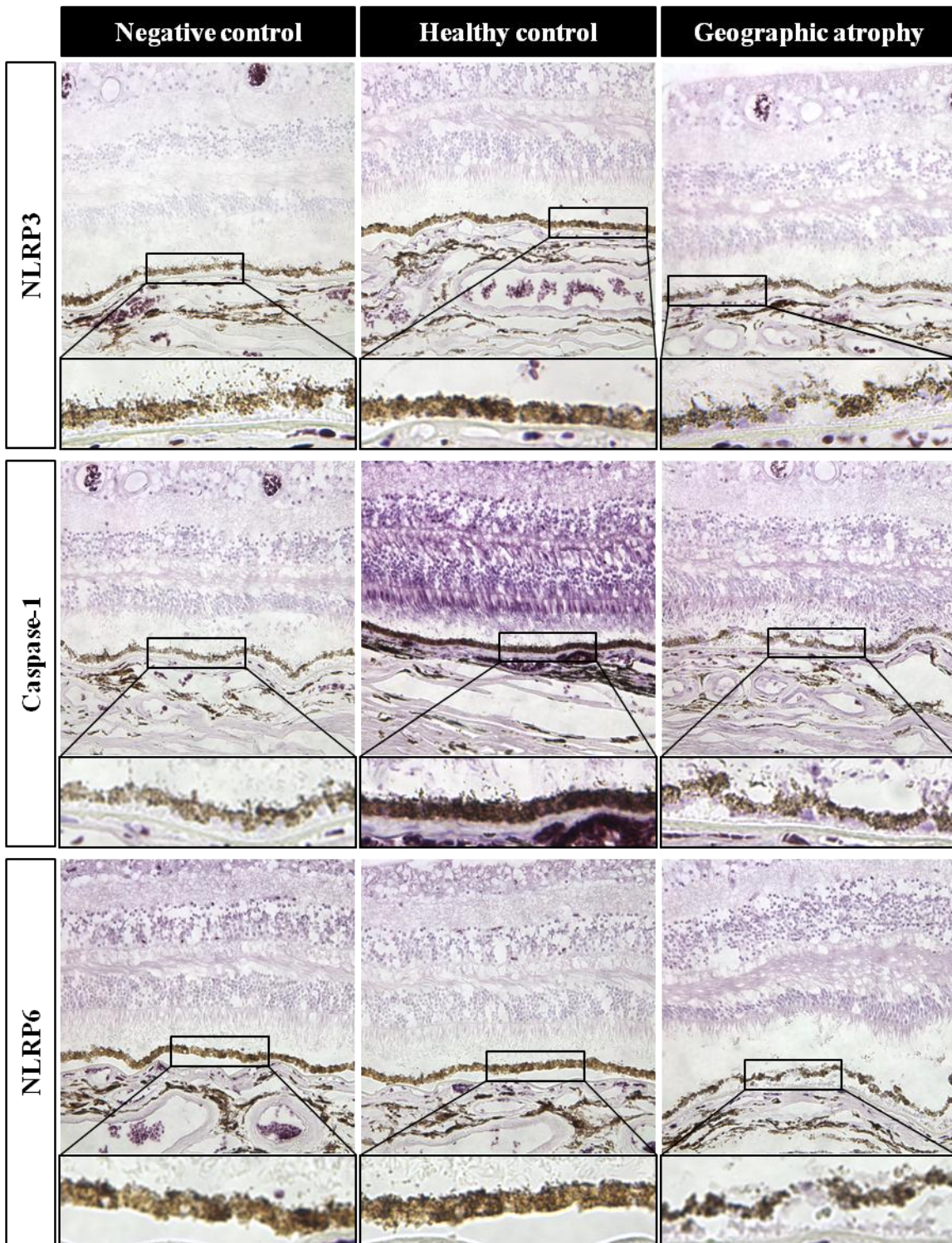


**Figure 4.1:** Inflammasome components in healthy and GA-affected human maculae. Representative images of eye cross-sections from the macular region of a single human GA donor and an age-matched healthy control, stained immunohistochemically for NLRP3 (*top*), caspase-1 (*middle*) and NLRP6 (*bottom*). Corresponding negative controls for each antibody are provided. Antibody against caspase-1 recognises both the precursor pro-form and the activated (cleaved) forms of caspase-1. Close-up images of the RPE area bound by the black rectangle are presented underneath each image. Magnification, 20x.

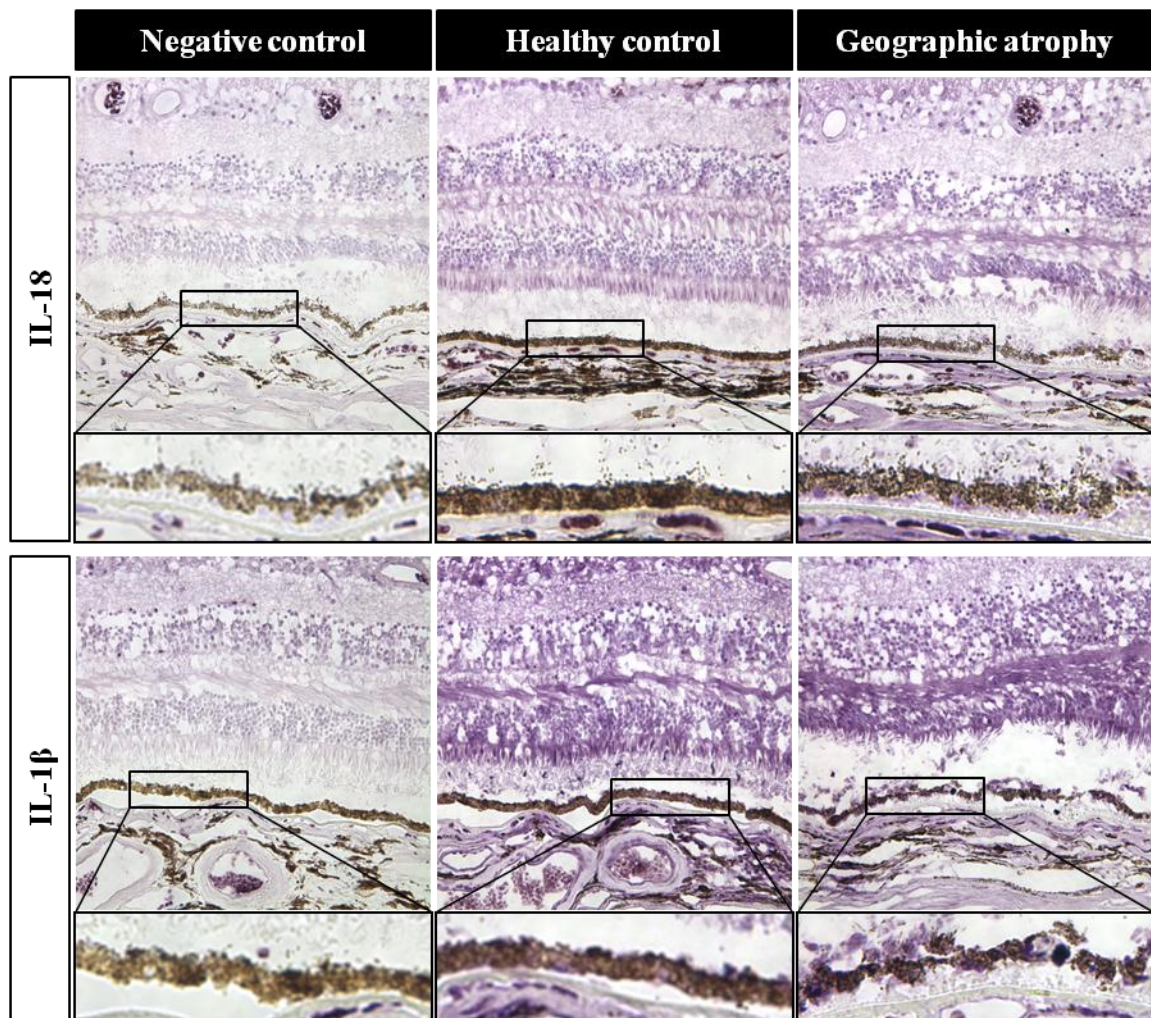


**Figure 4.2:** Inflammasome effector cytokines in healthy and GA-affected human maculae. Representative images of eye cross-sections from the macular region of a single human GA donor and an age-matched healthy control, stained immunohistochemically for IL-18 (*top*) and IL-1 $\beta$  (*bottom*). Corresponding negative controls for each antibody are provided. Antibodies recognise both the precursor pro-forms and the mature (cleaved) forms of IL-18 and IL-1 $\beta$ . Close-up images of the RPE area bound by the black rectangle are presented underneath each image. Magnification, 20x.

#### 4.2.2 Detection of inflammasome activation in the RPE *in vitro*

To provide an experimental platform for studying the role of inflammasome in the RPE *in vitro*, a reliable method for detecting inflammasome activation had first to be established. The levels of secreted cytokines and the intracellular expression of inflammasome proteins were therefore analysed in IL-1 $\alpha$ -primed hRPE cells following treatment with ATP. Standard conditions of inflammasome priming for 3 hours and activation for 30 minutes,

typically used in immune cell studies, yielded significantly increased levels of IL-18 in response to the combined IL-1 $\alpha$  and ATP treatment compared to untreated control (Figure 4.3A), with no detectable production of IL-1 $\beta$  and no significant differences in VEGF secretion (Figure 4.3B). Moreover, pro-IL-18, pro-IL-1 $\beta$  and pro-caspase-1 were detected intracellularly in protein lysates, with pro-IL-1 $\beta$  and pro-caspase-1 expression being relatively stable and unresponsive to any of the treatment conditions, either individual or in combination, whereas pro-IL-18 levels were significantly increased following treatment with ATP alone and even more when combined with IL-1 $\alpha$  (Figure 4.4). Interestingly, extended IL-1 $\alpha$  priming (24 hours) and/or ATP activation (up to 24 hours) had no negative effects on cell viability, as is normally the case of immune cells, but rather promoted RPE metabolic health, with the longest priming and activation showing the most significant change (Figure 4.5).

In summary, these results suggest that measuring levels of secreted IL-18 represents the best method for detecting the inflammasome activation in RPE cells *in vitro*, with extended priming and activation conditions potentially giving the best cellular responses.

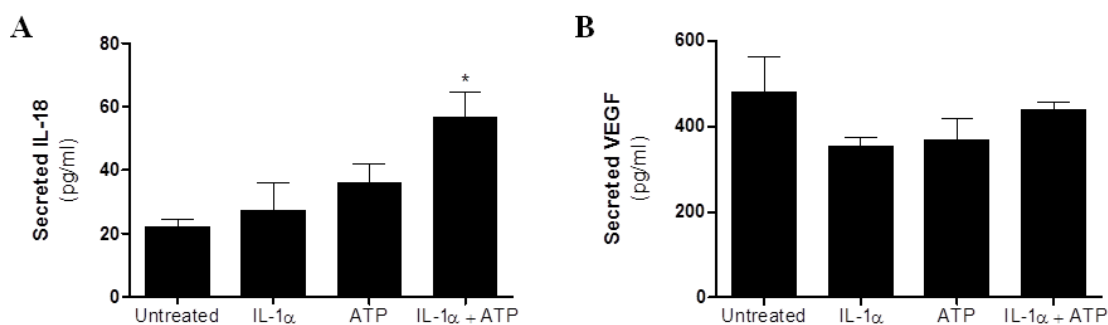


**Figure 4.3:** Effect of standard inflammasome activation on RPE protein secretion *in vitro*. Primary human foetal RPE (hFRPE) cells were primed with IL-1 $\alpha$  (10 ng/ml) for 3 hours, followed by ATP treatment (2.5 mM) for 30 minutes to activate the inflammasome. Cells treated with IL-1 $\alpha$  or ATP alone as well as untreated cells were used as controls. IL-18 (A) and VEGF (B) concentrations in cell-free supernatants were measured. Data are presented as mean  $\pm$  SEM and represent a single experiment carried out in triplicate. \* $p$ <0.05 by one-way ANOVA with Tukey post test compared to untreated control.



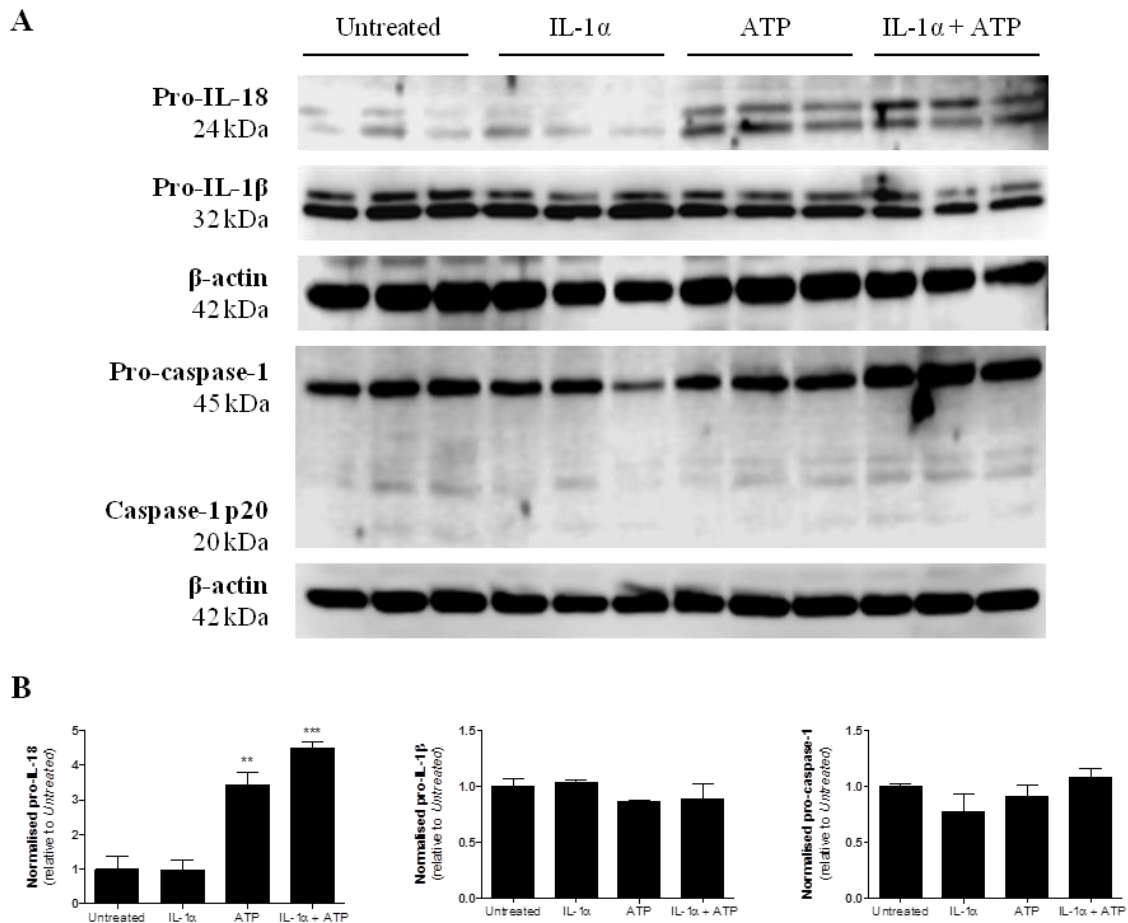


**Figure 4.4:** Detection of inflammasome components intracellularly *in vitro* in hFRPE cells. Primary human foetal RPE (hFRPE) cells were primed with IL-1 $\alpha$  (10 ng/ml) for 3 hours, followed by ATP treatment (2.5 mM) for 30 minutes to activate the inflammasome. Cells treated with IL-1 $\alpha$  or ATP alone as well as untreated cells were used as controls. Protein lysates were separated by SDS-PAGE using 10  $\mu$ g of total protein as determined by the BCA assay. Proteins of interest were immunodetected by Western blotting (A). Band intensity was quantified in ImageJ and data normalised to the corresponding  $\beta$ -actin loading control (B). Data are presented as mean  $\pm$  SEM and represent a single experiment carried out in triplicate. \*\* $p$ <0.01, \*\*\* $p$ <0.001 by one-way ANOVA with Tukey post test compared to untreated control.

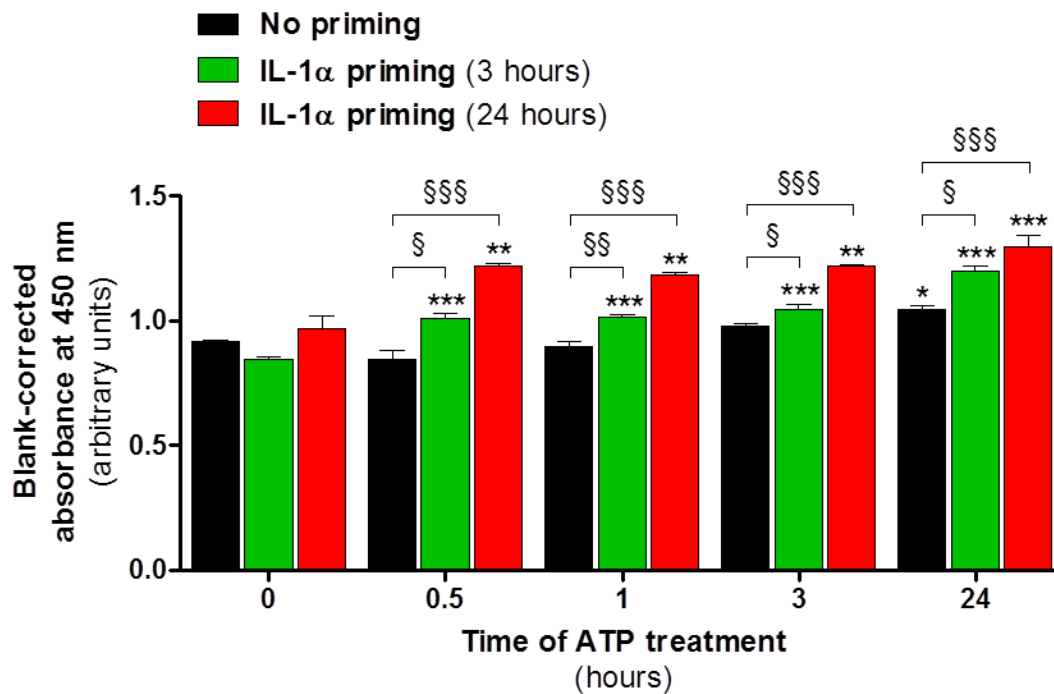


**Figure 4.5:** Effect of extended inflammasome activation on RPE cell viability *in vitro*.

Primary human foetal RPE (hfRPE) cells were primed with IL-1 $\alpha$  (10 ng/ml) for 0, 3 or 24 hours, followed by ATP treatment (2.5 mM) for 0, 0.5, 1, 3 or 24 hours to activate the inflammasome. Cell viability was measured by an MTS assay in each case and is presented as the blank-corrected absorbance at 450 nm. Data are presented as mean  $\pm$  SEM and represent a single experiment carried out in triplicate. \* $p$ <0.05, \*\* $p$ <0.01, \*\*\* $p$ <0.001 by one-way ANOVA with Tukey post test compared to 0 hour ATP treatment for each priming condition. § $p$ <0.05, §§ $p$ <0.01, §§§ $p$ <0.001 by one-way ANOVA with Tukey post test compared to no priming control.

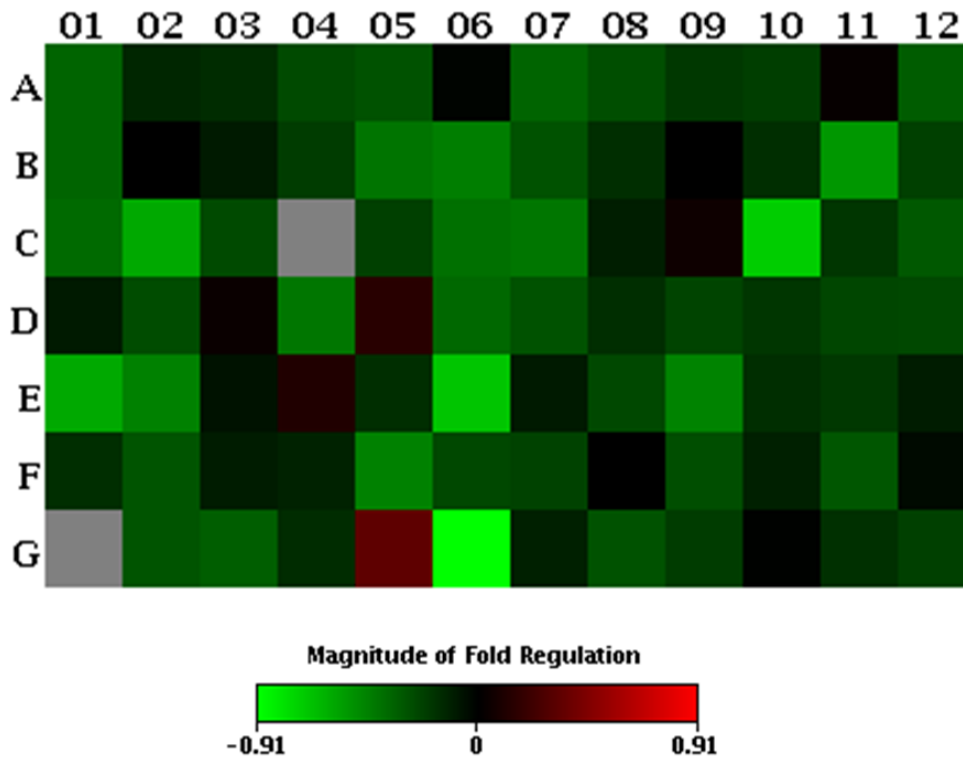
#### 4.2.3 Molecular response of the RPE to POS phagocytosis *in vivo* and *in vitro*

As already shown in line with previous reports, components of the inflammasome complex and its effector cytokines can be detected in and around the RPE of patients with AMD. However, their physiological role in RPE homeostasis is unknown. On daily basis, the RPE is involved in maintenance of photoreceptors by phagocytosing their shed outer segment tips. Hence, to establish the function of the inflammasome complex in RPE homeostasis, expression of its components was analysed in the RPE *in vivo* during the phagocytically active period at 8 AM compared to 8 PM. This scenario was subsequently mimicked *in vitro* by treatment of hRPE cells with isolated bPOSs.

A number of autophagy-related genes were down-regulated at 8 PM compared to 8 AM, with 15 genes reaching statistical significance (Figure 4.6 and Table 4.1). These included genes classically encoding autophagy machinery components, involved in the formation of autophagic vacuole (*Gabarapl2*, *Gabarap*, *Atg12*, *Rgs19*), vacuole targeting (*Gabarap*), protein transport (*Gabarapl2*, *Gabarap*) and autophagosome-lysosome linkage (*Gabarap*), as well as co-regulators of autophagy and apoptosis (*caspase-8*, *Bak1*, *Nfkb1*, *Bad*), co-regulators of autophagy and the cell cycle (*p27Kip1*), regulators of chaperone-mediated autophagy (*Hsp90aa1*, *Hsc70*) and regulators in response to other intracellular signals (*Gaa*, *Dram2*, *Ctsd*). Simultaneously, expression of 17 inflammasome-related genes was significantly down-regulated in the same samples at 8 PM compared to 8 AM (Figure 4.7 and Table 4.2), comprising genes typically considered to serve as negative inflammasome regulators (*Hsp90aa1*, *Tnf*, *Sugt1*, *Ctsb*), signal transduction molecules downstream of inflammasomes (*Panx1*, *Il1b*, *Il18*, *Irak1*) and signalling molecules downstream of NOD-like receptors (*Pea15a*, *Tak1*, *Tnf*, *Erk2*, *Sugt1*, *Jnk2*, *Nfkb1*, *Ikk1*, *caspase-8*, *Mal*, *Rela*). Furthermore, IL-18 and caspase-1 specks were more readily detected on RPE flatmounts at 8 AM compared to 8 PM (Figure 4.8).

Correlating with these observations, 38 autophagy-related genes were significantly down-regulated *in vitro* in control samples, corresponding to the 8 PM time point, compared to the bPOS-treated cells equivalent to the 8 AM time point (Figure 4.9 and Table 4.3). At the same time, the levels of secreted IL-18 were significantly increased in response to bPOS stimulation at 24 hours (Figure 4.10B), trending towards a significant increase as early as 6 hours after treatment (Figure 4.10A).

To conclude, these findings link, for the first time, the phagocytosis of POSs with the expression of inflammasome components and in this way provide a novel insight into the function of the inflammasome complex in RPE homeostasis.



	01	02	03	04	05	06	07	08	09	10	11	12
<b>A</b>	Akt1	Ambra1	App	Atg10	Atg12	Atg16l1	Atg16l2	Atg3	Atg4a	Atg4b	Atg4c	Atg4d
<b>B</b>	Atg5	Atg7	Atg9a	Atg9b	Bad	Bak1	Bax	Bcl2	Bcl2l1	Becn1	Bid	Bnip3
<b>C</b>	Casp3	Casp8	Cdkn1b	Cdkn2a	Cln3	Ctsb	Ctsd	Ctss	Cxcr4	Dapk1	Dram1	Dram2
<b>D</b>	Eif2ak3	Eif4g1	Esr1	Fadd	Fas	Gaa	Gabarap	Gabarap1	Gabarap2	Hdac1	Hdac6	Hgs
<b>E</b>	Hsp90aa1	Hspa8	Htt	Ifng <sup>b</sup>	Igf1	Ins2	Irgm1	Lamp1	Map11c3a	Map11c3b	Mapk14	Mapk3
<b>F</b>	Mtor	Nfkb1	Npc1	Pik3c3	Pik3cg	Pik3r4	Prkaa1	Pten	Rab24	Rb1	Rgs19	Rps6kb1
<b>G</b>	Snca	Sqstm1	Tgfb1	Tgm2	Tmem74	Tnf	Tnfsf10	Trp53	Ulk1	Ulk2	Uvrag	Wipi1

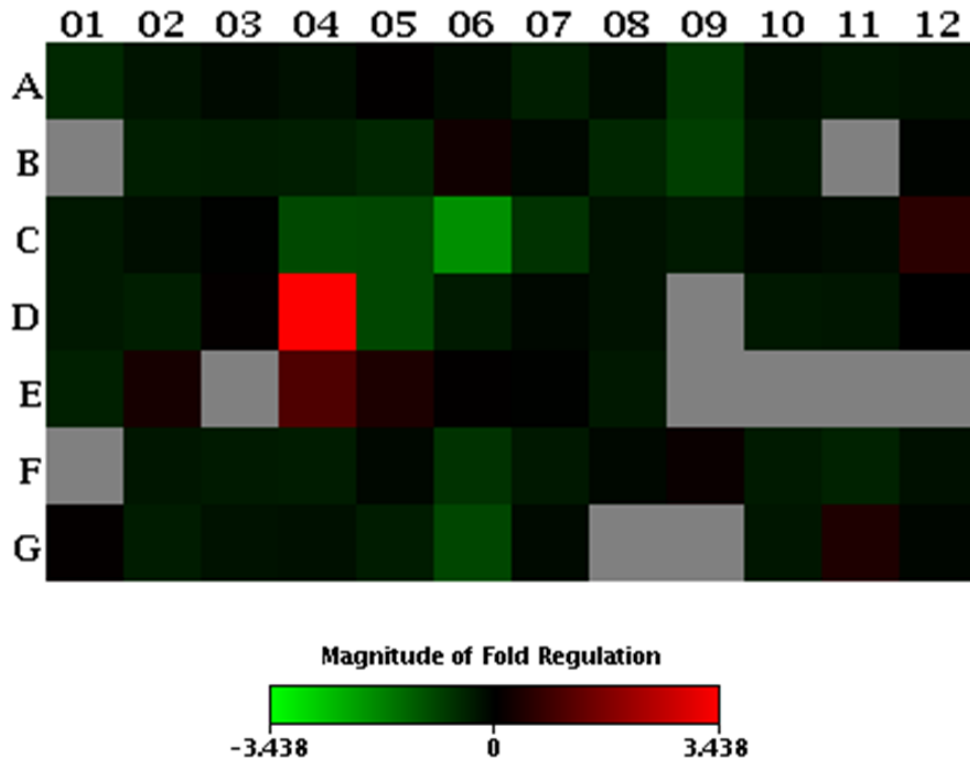
**Figure 4.6:** Autophagy gene expression in the RPE *in vivo* at 8 PM relative to 8 AM. C57BL/6J mice (3 months old) were sacrificed at either 8 AM, just after the light onset, or 8 PM, after the light offset. Autophagy gene expression in the RPE/choroid was analysed using a standard autophagy PCR array. At 8 PM, all procedures were carried out under dim red light and exposure of tissue to light was minimised. Heat map shows the magnitude of fold regulation of 8 PM samples compared to the 8 AM time point. Table provides the layout of the PCR array plate. Genes that reached statistical significance of differential expression are highlighted in red.

<b>Gene</b>	<b>Average Ct</b>	<b>Fold change at 8 PM (relative to 8 AM)</b>	<b>Standard deviation (of the fold change)</b>	<b>Significance (p value)</b>
Casp8	29,503	0,629	0,118	0,00883**
Hsp90aa1	22,832	0,624	0,052	0,01227*
Gabarap12	25,078	0,805	0,067	0,01523*
Bak1	28,943	0,699	0,125	0,01754*
Hspa8	22,827	0,688	0,080	0,01954*
Nfkb1	27,878	0,773	0,075	0,02323*
Gaa	25,753	0,736	0,115	0,03051*
Bad	28,888	0,714	0,104	0,03376*
Dram2	27,682	0,762	0,076	0,03789*
Cdkn1b	25,745	0,794	0,074	0,03959*
Gabarap	24,337	0,780	0,100	0,04072*
Ctsd	22,212	0,718	0,157	0,04495*
Atg12	26,865	0,775	0,058	0,04534*
Rgs19	30,935	0,769	0,077	0,04941*
Atg5	28,045	0,743	0,104	0,04978*
Hgs	28,890	0,802	0,108	0,05275
Prkaa1	28,707	0,813	0,097	0,05378
Dapk1	28,942	0,604	0,208	0,05416
Eif4g1	26,158	0,792	0,091	0,05521
Map1lc3a	26,315	0,689	0,140	0,06095
Bid	32,163	0,665	0,181	0,06218
Sqstm1	24,937	0,773	0,105	0,06804
Casp3	29,472	0,736	0,147	0,07044
Pik3cg	32,102	0,697	0,160	0,07193
Wipi1	27,907	0,813	0,028	0,07438
Ctsb	23,982	0,724	0,134	0,08110
Atg10	30,167	0,797	0,126	0,08488
Bax	27,633	0,777	0,111	0,08541
Atg3	27,347	0,794	0,155	0,08711
Tnf	32,017	0,540	0,163	0,08820
Ins2	29,578	0,619	0,232	0,09073
Rab24	27,598	0,790	0,139	0,09386
Fadd	28,652	0,720	0,206	0,10535
Tgfb1	27,187	0,751	0,091	0,11460
Trp53	29,793	0,780	0,129	0,11668
Lamp1	24,673	0,806	0,140	0,13613
Map1lc3b	24,898	0,867	0,127	0,17710
Akt1	26,482	0,758	0,215	0,18885
Atg4a	29,680	0,839	0,094	0,19287
Pik3r4	29,243	0,816	0,204	0,21438
Hdac6	28,993	0,816	0,182	0,22185
Gabarap11	25,102	0,865	0,104	0,22254
Bcl2	28,658	0,867	0,158	0,24566
Atg4b	28,167	0,839	0,206	0,25120
Eif2ak3	28,778	0,918	0,106	0,25346
Igf1	27,630	0,863	0,112	0,25919
Ulk1	27,940	0,840	0,191	0,26730
Atg16l2	30,577	0,761	0,219	0,27794
Mapk14	28,333	0,848	0,178	0,28714
Dram1	31,682	0,846	0,112	0,34556
Hdac1	27,225	0,850	0,186	0,36659
Atg4d	30,680	0,801	0,314	0,38217
Cln3	28,813	0,846	0,259	0,38231
Bnip3	27,157	0,843	0,243	0,38244
Mtor	28,408	0,877	0,217	0,40117

Ambra1	28,988	0,894	0,181	0,40304
Uvrag	28,552	0,873	0,220	0,41762
Becn1	27,655	0,880	0,227	0,42063
Fas	29,325	1,170	0,291	0,44739
Tnfsf10	29,347	0,903	0,142	0,44785
Pik3c3	28,723	0,901	0,163	0,45170
Ifng	34,878	1,140	0,276	0,46625
Tmem74	33,863	1,415	0,604	0,50909
Npc1	27,435	0,922	0,183	0,53943
App	23,262	0,888	0,254	0,55959
Tgm2	26,710	0,893	0,280	0,57097
Atg9a	28,982	0,936	0,215	0,65658
Mapk8	28,177	0,930	0,253	0,66293
Rb1	28,360	0,927	0,276	0,68139
Cxcr4	29,433	1,098	0,362	0,71219
Atg4c	28,812	1,079	0,458	0,78504
Ctss	24,685	0,950	0,344	0,80635
Cdkn2a	35,000	0,969	0,296	0,85945
Snca	35,000	0,969	0,296	0,85945
Rps6kb1	27,748	0,983	0,225	0,88582
Bcl2l1	26,673	1,028	0,295	0,88914
Pten	26,568	1,018	0,245	0,91240
Irgm1	27,117	1,052	0,699	0,91262
Atg7	29,790	1,017	0,237	0,92581
Esr1	31,612	1,055	0,259	0,93314
Atg16l1	28,858	1,017	0,307	0,94558
Htt	29,235	1,017	0,479	0,95780
Ulk2	28,387	1,001	0,133	0,98502
Atg9b	32,675	1,037	0,729	0,99900

**Table 4.1:** Autophagy gene expression in the RPE *in vivo* at 8 PM relative to 8 AM.

C57BL/6J mice (3 months old) were sacrificed at either 8 AM, just after the light onset, or 8 PM, after the light offset. Autophagy gene expression in the RPE/choroid was analysed using a standard autophagy PCR array. At 8 PM, all procedures were carried out under dim red light and exposure of tissue to light was minimised. Data analysis was performed using the comparative  $C_t$  ( $\Delta\Delta C_t$ ) method. The average  $C_t$  value for each gene, mean fold change of 8 PM samples relative to the 8 AM time point and standard deviation of this fold change are presented (n=3 animals per time point). \* $p < 0.05$ , \*\* $p < 0.01$  by Student's t test compared to 8 AM.



	01	02	03	04	05	06	07	08	09	10	11	12
A	Aim2	Bcl2	Bcl2l1	Birc2	Birc3	Card6	Casp1	Casp12	Casp8	Ccl12	Ccl5	Ccl7
B	Cd40lg	Cflar	Chuk	Ciita	Ctsb	Cxcl1	Cxcl3	Fadd	Hsp90aal	Hsp90b1	Ifnb1	Ifng
C	Ikbkb	Ikbkg	Il12a	Il12b	Il18	Il1b	Il33	Il6	Irak1	Irf1	Irf3	Irf4
D	Map3k7	Mapk1	Mapk11	Mapk12	Mapk13	Mapk3	Mapk8	Mapk9	Mefv	Myd88	Naip1	Naip5
E	Nfkb1	Nfkbia	Nfkbib	Nlrc4	Nlrc5	Nlrp12	Nlrp1a	Nlrp3	Nlrp4b	Nlrp4e	Nlrp5	Nlrp6
F	Nlrp9b	Nlrz1	Nod1	Nod2	P2rx7	Panx	Pea15a	Pstpip1	Ptgs2	Pycard	Rela	Ripk2
G	Mok	Sugt1	Tab1	Tab2	Tirap	Tnf	Tnfsf11	Tnfsf14	Tnfsf4	Traf6	Txnip	Xiap

**Figure 4.7:** Inflammasome gene expression in the RPE *in vivo* at 8 PM relative to 8 AM. C57BL/6J mice (3 months old) were sacrificed at either 8 AM, just after the light onset, or 8 PM, after the light offset. Inflammasome gene expression in RPE/choroid was analysed using a standard inflammasome PCR array. At 8 PM, all procedures were carried out under dim red light and exposure of tissue to light was minimised. Heat map shows the magnitude of fold regulation of 8 PM samples compared to the 8 AM time point. Table provides the layout of the PCR array plate. Genes that reached statistical significance of differential expression are highlighted in red.

Gene	Average Ct	Fold change at 8 PM (relative to 8 AM)	Standard deviation (of the fold change)	Significance (p value)
Panx1	31,357	0,599	0,077	0,00121**
Pea15a	25,913	0,751	0,033	0,00248**
Hsp90aa1	22,900	0,546	0,089	0,00375**
Map3k7	27,917	0,763	0,063	0,00452**
Il1b	28,898	0,344	0,046	0,00833**
Tnf	32,078	0,534	0,156	0,01314*
Mapk1	26,362	0,716	0,122	0,01627*
Sugt1	27,338	0,735	0,113	0,02243*
Ctsb	24,500	0,670	0,154	0,02345*
Mapk9	27,675	0,810	0,007	0,02388*
Nfkb1	27,943	0,699	0,058	0,02746*
Chuk	27,923	0,734	0,097	0,03091*
Il18	28,525	0,555	0,235	0,03268*
Casp8	29,733	0,592	0,156	0,03957*
Tirap	30,652	0,738	0,147	0,04070*
Rela	29,123	0,692	0,089	0,04447*
Irak1	28,828	0,752	0,145	0,04584*
Cflar	26,640	0,722	0,172	0,05057
Nod1	30,720	0,756	0,147	0,05123
Pycard	29,547	0,747	0,116	0,05244
Aim2	32,528	0,647	0,038	0,05323
Myd88	32,968	0,753	0,031	0,05374
Fadd	28,775	0,678	0,200	0,05389
Irf3	27,787	0,859	0,034	0,05530
Mapk12	31,422	4,657	1,606	0,06944
Hsp90b1	24,940	0,776	0,158	0,07702
Ikbkb	28,828	0,765	0,108	0,07731
Mapk3	26,362	0,758	0,161	0,08247
Casp1	31,902	0,714	0,106	0,08777
Bcl2	28,855	0,797	0,108	0,08927
Ccl5	31,070	0,789	0,157	0,10560
Tab1	30,868	0,805	0,122	0,12691
Txnip	26,378	1,434	0,375	0,13861
Traf6	29,362	0,783	0,203	0,14940
Ciita	33,428	0,737	0,220	0,15942
Irf4	33,868	1,597	0,308	0,16452
Nod2	32,010	0,730	0,141	0,18218
Nfkbia	26,463	1,316	0,337	0,18887
Nlrc4	34,068	2,273	1,352	0,19628
Mapk13	32,340	0,590	0,386	0,19992
Birc2	28,483	0,833	0,071	0,21759
Tab2	27,665	0,838	0,172	0,24227
Casp12	30,280	0,872	0,050	0,24343
Mapk8	28,380	0,903	0,103	0,25586
Ripk2	30,683	0,837	0,126	0,27910
Xiap	26,892	0,917	0,100	0,28102
Card6	31,173	0,867	0,154	0,32093
Cxcl1	28,385	1,277	0,458	0,36129
Il12b	32,117	0,681	0,539	0,36739
Ccl7	28,767	0,839	0,302	0,42259
Ptgs2	25,555	1,139	0,106	0,45864
Ikbkg	29,703	0,859	0,257	0,46656
P2rx7	31,118	0,899	0,128	0,47005
Nlrc5	31,795	1,465	0,602	0,49059
Nlrx1	30,512	0,835	0,377	0,49403



Naip1	34,247	0,812	0,315	0,52243
Tnfsf11	34,878	0,893	0,198	0,54462
Bcl2l1	26,775	0,911	0,241	0,56102
Cxcl3	34,895	0,914	0,203	0,57119
Il33	26,932	0,788	0,666	0,58340
Nlrp3	32,055	0,847	0,526	0,61693
Ccl12	30,125	0,910	0,466	0,72712
Cd40lg	35,000	1,057	0,235	0,73407
Ifnb1	35,000	1,057	0,235	0,73407
Mefv	35,000	1,057	0,235	0,73407
Nfkbib	35,000	1,057	0,235	0,73407
Nlrp4b	35,000	1,057	0,235	0,73407
Nlrp4e	35,000	1,057	0,235	0,73407
Nlrp5	35,000	1,057	0,235	0,73407
Nlrp6	35,000	1,057	0,235	0,73407
Nlrp9b	35,000	1,057	0,235	0,73407
Tnfsf14	35,000	1,057	0,235	0,73407
Tnfsf4	35,000	1,057	0,235	0,73407
Mok	32,558	1,082	0,358	0,74288
Mapk11	31,983	1,126	0,452	0,76044
Birc3	29,138	1,077	0,367	0,76094
Ifng	34,932	0,961	0,214	0,77518
Pstpip1	31,635	0,950	0,316	0,78701
Il12a	34,722	0,980	0,049	0,80399
Nlrp12	33,622	1,063	0,263	0,81438
Il6	29,040	0,941	0,675	0,88147
Irf1	26,070	0,966	0,421	0,88606
Naip5	33,790	1,087	0,497	0,97058
Nlrp1a	34,963	1,004	0,223	0,98839

**Table 4.2:** Inflammasome gene expression in the RPE *in vivo* at 8 PM relative to 8 AM. C57BL/6J mice (3 months old) were sacrificed at either 8 AM, just after the light onset, or 8 PM, after the light offset. Inflammasome gene expression in RPE/choroid was analysed using a standard inflammasome PCR array. At 8 PM, all procedures were carried out under dim red light and exposure of tissue to light was minimised. Data analysis was performed using the comparative  $C_t$  ( $\Delta\Delta C_t$ ) method. The average  $C_t$  value for each gene, mean fold change of 8 PM samples relative to the 8 AM time point and standard deviation of this fold change are presented (n=3 animals per time point). \* $p < 0.05$ , \*\* $p < 0.01$  by Student's t test compared to 8 AM.

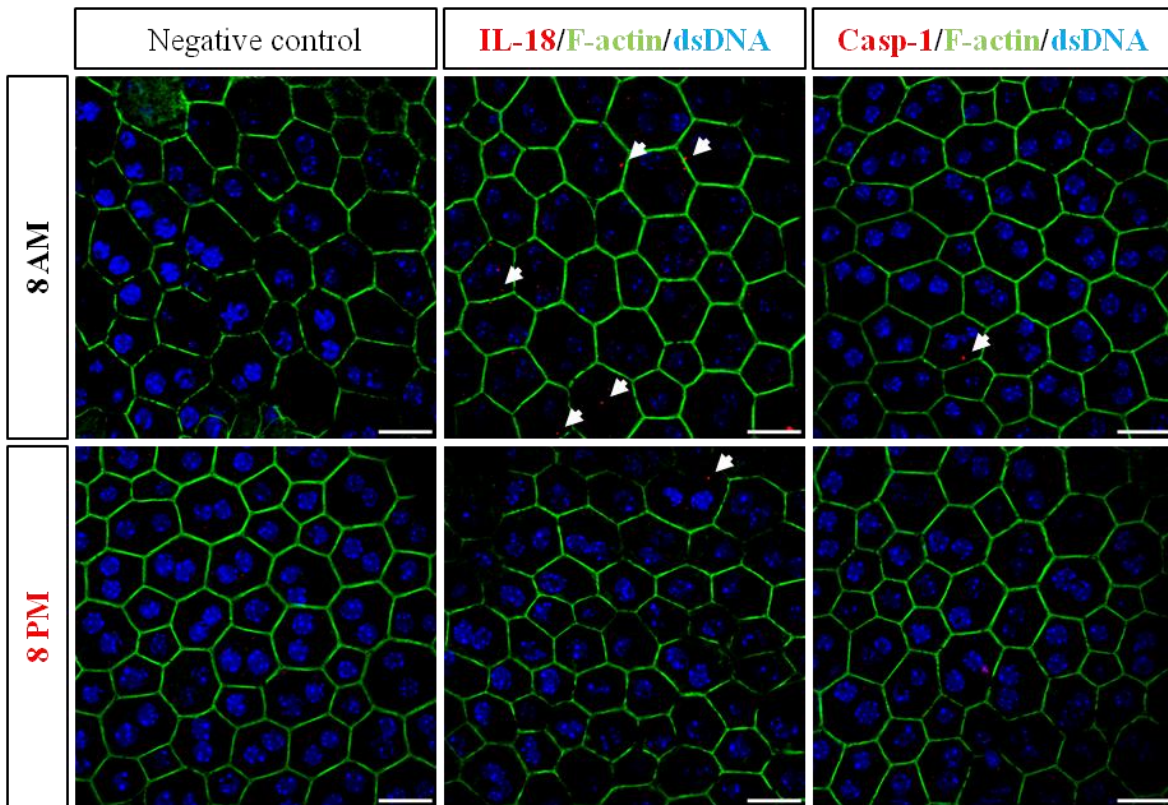
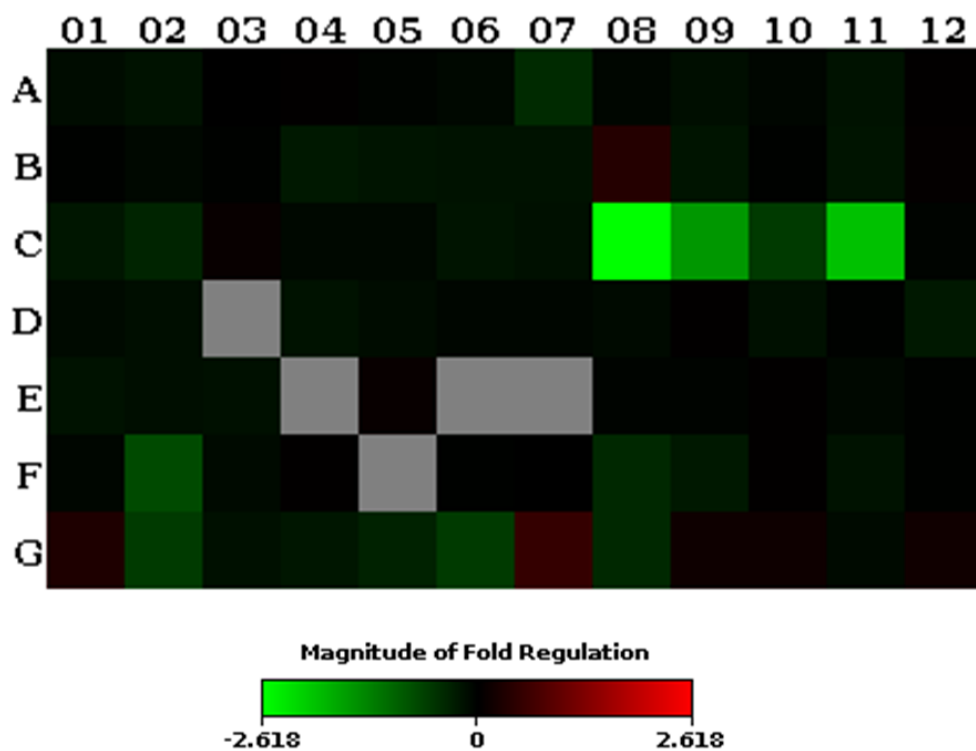


**Figure 4.8:** Patterns of IL-18 and caspase-1 expression in the RPE *in vivo* at 8 AM and 8 PM.

Representative RPE flatmounts prepared at 8 AM and 8 PM, respectively, stained with inflammasome-related IL-18 or caspase-1 (*red*), F-actin (*green*) and counterstained with a nuclear stain Hoechst 33342 (*blue*). Corresponding negative controls at each time point are provided. Antibodies against IL-18 and caspase-1 recognise both the precursor pro-forms and the mature (cleaved) forms of the corresponding proteins. Arrows pointing to IL-18 or caspase-1 specks. Scale bar, 20  $\mu\text{m}$ .



	01	02	03	04	05	06	07	08	09	10	11	12
<b>A</b>	Akt1	Ambra1	App	Atg10	Atg12	Atg1611	Atg1612	Atg3	Atg4a	Atg4b	Atg4c	Atg4d
<b>B</b>	Atg5	Atg7	Atg9a	Atg9b	Bad	Bak1	Bax	Bcl2	Bcl211	Becn1	Bid	Enip3
<b>C</b>	Casp3	Casp8	Cdkn1b	Cdkn2a	Cln3	Ctsb	Ctsd	Ctss	Cxcr4	Dapk1	Dram1	Dram2
<b>D</b>	Eif2ak3	Eif4g1	Esr1	Fadd	Fas	Gaa	Gabarap	Gabarap1	Gabarap2	Hdac1	Hdac6	Hgs
<b>E</b>	Hsp90aal	Hspa8	Htt	Ifng <sup>b</sup>	Igf1	Ins2	Irgm1	Lamp1	Map11c3a	Map11c3b	Mapk14	Mapk8
<b>F</b>	Mtor	Nfkb1	Npc1	Pik3c3	Pik3cg	Pik3r4	Prkaa1	Pten	Rab24	Rb1	Rgs19	Rps6kb1
<b>G</b>	Snca	Sqstm1	Tgfb1	Tgm2	Tmem74	Tnf	Tnfsf10	Tp53	Ulk1	Ulk2	Uvrag	Wipi1

**Figure 4.9:** Autophagy gene expression in response to POS treatment *in vitro* in hRPE cells.

Primary human foetal RPE (hRPE) cells were treated with control medium or isolated bovine photoreceptor outer segments (bPOSs), at the ratio of 10 bPOSs per 1 cell, for 6 hours. Autophagy gene expression was analysed using a standard autophagy PCR array. Heat map shows the magnitude of fold regulation of control samples compared to the bPOS-treated cells. Table provides the layout of the PCR array plate. Genes that reached statistical significance of differential expression are highlighted in red.

Gene	Average Ct	Fold change of control (relative to bPOS-treated)	Standard deviation (of the fold change)	Significance (p value)
Dram1	22,743	0,335	0,045	0,00002***
Tp53	23,345	0,710	0,028	0,00007***
Nfkb1	26,197	0,571	0,040	0,00017***
Hsp90aa1	20,087	0,848	0,016	0,00023***
Sqstm1	19,850	0,631	0,031	0,00040***
Dapk1	30,077	0,633	0,063	0,00073***
Atg4c	26,668	0,850	0,018	0,00082***
Cxcr4	25,493	0,392	0,048	0,00156**
Npc1	23,783	0,900	0,024	0,00221**
Atg16l2	28,293	0,704	0,072	0,00271**
Bcl2	29,200	1,367	0,098	0,00301**
BID	24,825	0,834	0,009	0,00352**
Tgfb1	21,512	0,866	0,011	0,00442**
Ulk2	25,663	1,134	0,014	0,00546**
Casp8	28,072	0,733	0,012	0,00617**
Ctsb	21,587	0,830	0,058	0,00873**
Hspa8	18,737	0,872	0,042	0,00909**
Bad	24,447	0,829	0,019	0,01022*
Hdac1	25,097	0,852	0,017	0,01155*
Pten	23,503	0,711	0,021	0,01300*
Tmem74	31,202	0,747	0,025	0,01332*
Ambra1	25,818	0,846	0,034	0,01385*
Bak1	26,082	0,847	0,049	0,01720*
Rab24	28,617	0,800	0,065	0,01797*
Atg4a	26,280	0,872	0,029	0,02174*
Snca	23,635	1,316	0,123	0,02308*
Ctsd	19,307	0,852	0,038	0,02463*
Atg3	24,163	0,943	0,023	0,02516*
Bax	23,153	0,844	0,022	0,02838*
Ctss	31,728	0,284	0,074	0,03229*
Bcl2l1	23,943	0,829	0,026	0,03388*
Fas	24,757	0,885	0,053	0,03569*
Atg7	26,042	0,923	0,017	0,03609*
Uvrag	27,708	0,903	0,044	0,04058*
Wipi1	24,050	1,173	0,085	0,04066*
Casp3	24,257	0,820	0,089	0,04084*
Gabarap	21,058	0,936	0,018	0,04579*
Tnfsf10	32,670	1,544	0,231	0,04984*
Htt	26,247	0,865	0,058	0,05432
Eif4g1	22,772	0,874	0,029	0,06187
Fadd	24,575	0,842	0,029	0,06680
Cln3	24,938	0,920	0,046	0,06688
Rgs19	28,098	0,847	0,057	0,07378
Hgs	26,990	0,806	0,027	0,08091
Atg9b	28,768	0,814	0,133	0,08337
Akt1	23,390	0,888	0,020	0,11537
Cdkn2a	23,300	0,921	0,014	0,12378
Ulk1	26,227	1,155	0,133	0,12619
Eif2ak3	25,475	0,912	0,050	0,13576
Tgm2	20,647	0,821	0,041	0,14277
Gabarap1	23,542	0,907	0,052	0,16953
Cdkn1b	24,832	1,094	0,101	0,19454
Pik3c3	24,323	1,025	0,020	0,25966
Mtor	24,725	0,943	0,075	0,28027
Gaa	24,788	0,941	0,031	0,29125

Tnf	34,650	0,629	0,094	0,31177
Mapk14	24,448	0,933	0,041	0,33444
Atg16l1	25,668	0,926	0,077	0,38765
Atg12	24,558	0,964	0,057	0,40663
Map1lc3a	24,535	0,954	0,017	0,44646
Atg4b	25,235	0,946	0,051	0,44713
Igf1	28,862	1,099	0,172	0,49473
Gabarapl2	21,458	1,018	0,011	0,49529
Dram2	24,388	0,967	0,025	0,53647
Lamp1	21,672	0,967	0,036	0,57663
Map1lc3b	22,072	1,018	0,013	0,58255
App	19,903	0,992	0,022	0,60803
Bnip3	21,502	1,035	0,102	0,61434
Atg5	24,927	0,983	0,039	0,62334
Rb1	24,950	1,021	0,069	0,64742
Becn1	24,350	0,979	0,053	0,67378
Pik3r4	25,965	0,986	0,043	0,69039
Atg9a	24,960	0,974	0,043	0,69288
Mapk8	24,910	0,984	0,058	0,70275
Rps6kb1	24,827	0,985	0,074	0,74473
Atg10	29,005	1,019	0,064	0,76009
Atg4d	25,928	1,024	0,066	0,76342
Hdac6	25,368	0,990	0,009	0,80381
Esr1	35,000	1,022	0,153	0,83474
Ifng	35,000	1,022	0,153	0,83474
Ins	35,000	1,022	0,153	0,83474
Irgm	35,000	1,022	0,153	0,83474
Pik3cg	35,000	1,022	0,153	0,83474
Prkaa1	24,340	0,997	0,020	0,91170

**Table 4.3:** Autophagy gene expression in response to POS treatment *in vitro* in hFRPE cells.

Primary human foetal RPE (hFRPE) cells were treated with control medium or isolated bovine photoreceptor outer segments (bPOSs), at the ratio of 10 bPOSs per 1 cell, for 6 hours. Autophagy gene expression was analysed using a standard autophagy PCR array. Data analysis was performed using the comparative  $C_t$  ( $\Delta\Delta C_t$ ) method. The average  $C_t$  value for each gene, mean fold change of control samples relative to the bPOS-treated cells and standard deviation of the fold change are presented. Data represent a single experiment carried out in triplicate. \* $p < 0.05$ , \*\* $p < 0.01$ , \*\*\* $p < 0.001$  by Student's t test compared to bPOS-treated samples.

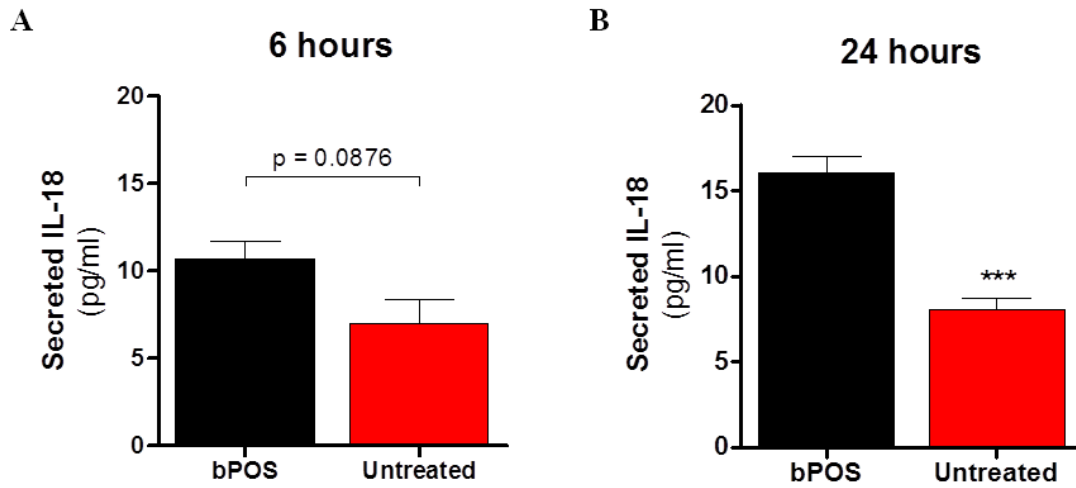


**Figure 4.10:** IL-18 secretion in response to POS treatment *in vitro* in hfRPE cells.

Primary human foetal RPE (hfRPE) cells were treated with control medium or isolated bovine photoreceptor outer segments (bPOSs), at the ratio of 10 bPOSs per 1 cell, for 6 (A) or 24 (B) hours. IL-18 concentration in the cell-free supernatants was measured in each case. Data are presented as mean  $\pm$  SEM and represent a single experiment carried out in 3-7 replicates. \*\*\* $p < 0.001$  by Student's t test compared to bPOS-treated samples.

#### 4.2.4 Serum starvation regulates VEGF production by the RPE *in vitro*

Nutrient deprivation due to serum starvation is a widely-used tool to induce autophagy *in vitro* in cell culture experiments. Previous results linked autophagy with the inflammasome activation and IL-18 secretion in the RPE. As shown already, IL-18 can regulate VEGF secretion *in vitro* and *in vivo*. In addition, the inflammasome formation alone has been suggested to be sufficient to decrease VEGF production by the RPE (Mohr et al., 2015). Therefore, VEGF levels were examined in response to serum starvation in hRPE cells *in vitro*.

It was observed that the induction of autophagy *in vitro* by serum starvation significantly reduced VEGF levels at all time points examined, i.e. 1 to 72 hours (Figure 4.11A), and significantly decreased the overall rate of VEGF secretion (Figure 4.11B), without any negative effects on cell viability (Figure 4.12). On the contrary, the cell viability was increased after short-term serum starvation (Figure 4.12A-C), most significantly at 1 hour (Figure 4.12A). In comparison, it caused significant cell death in endothelial cells (Figure 4.13), with only 30% of them surviving after 72 hours (Figure 4.13C), thus suggesting that the RPE might be unique in its response to serum starvation, withstanding even prolonged periods of nutrient deprivation, with autophagy induction being an important regulator of VEGF secretion.

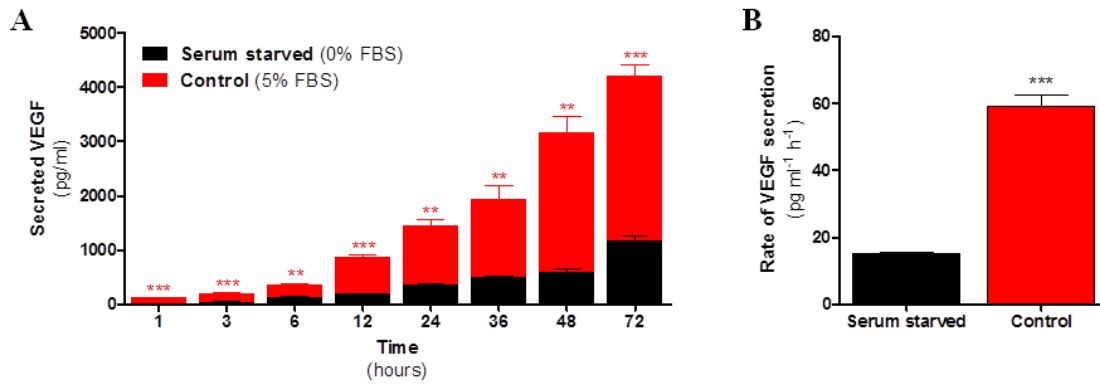


**Figure 4.11:** Effect of serum starvation on VEGF production *in vitro* in hFRPE cells.

Primary human foetal RPE (hFRPE) cells were treated with complete serum-supplemented medium (5% FBS) or serum-free medium (0% FBS) for 1-72 hours. VEGF concentration in the cell-free supernatants was measured at each time point (A). Rate of VEGF secretion was calculated from the slope of linear regression of VEGF concentration (pg/ml) against time (hours) (B). Data are presented as mean  $\pm$  SEM and represent a single experiment carried out in triplicate. \*\*p<0.01, \*\*\*p<0.001 by Student's t test compared to serum starved at each time point.



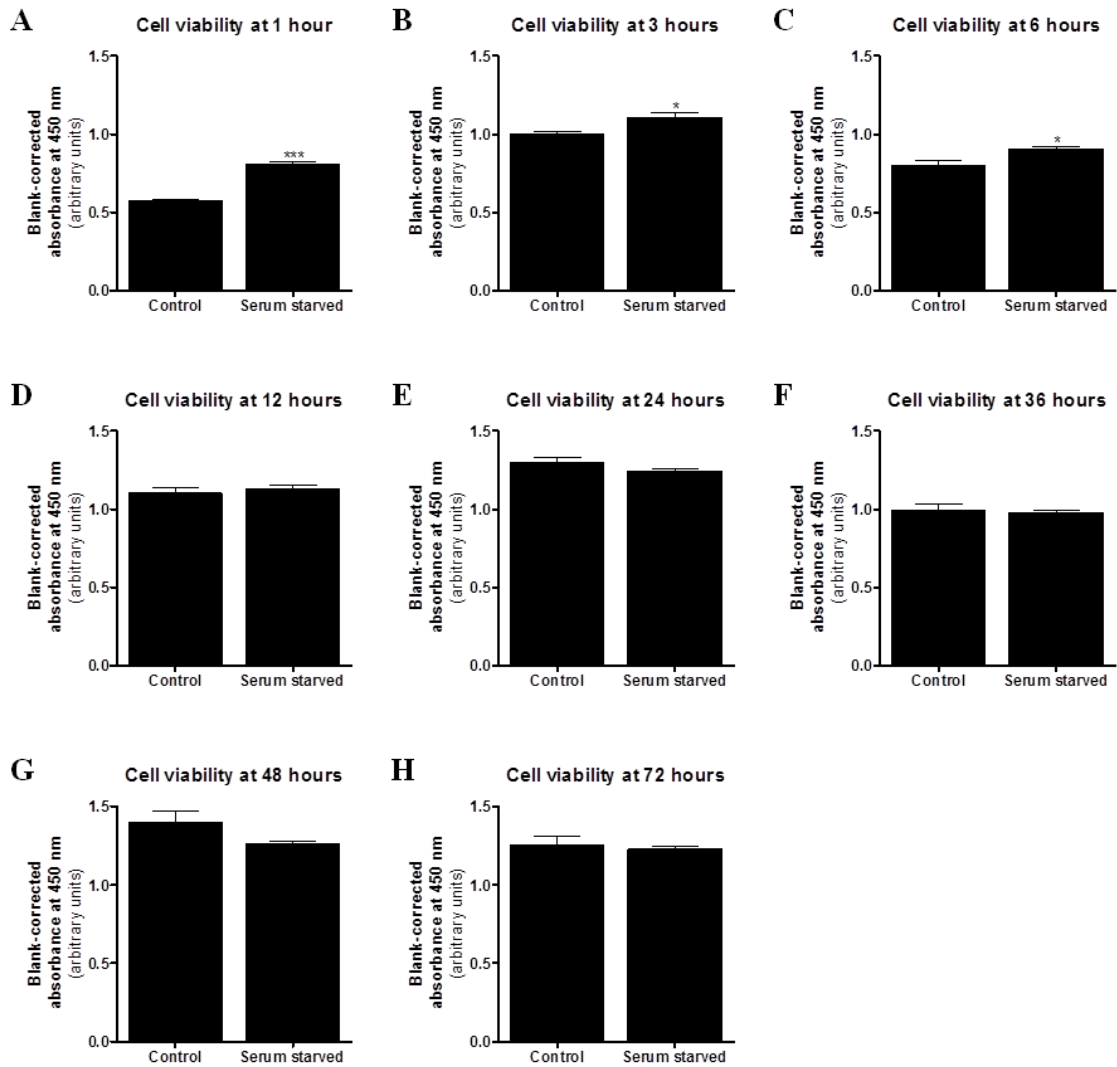


**Figure 4.12:** Effect of serum starvation on RPE cell viability *in vitro*.

Primary human foetal RPE (hFRPE) cells were treated with complete serum-supplemented medium (5% FBS) or serum-free medium (0% FBS) for 1-72 hours. Cell viability was measured by an MTS assay at 1 (A), 3 (B), 6 (C), 12 (D), 24 (E), 36 (F), 48 (G) or 72 (H) hours, and is presented as the blank-corrected absorbance at 450 nm. Data are presented as mean  $\pm$  SEM and represent a single experiment carried out in triplicate. \* $p < 0.05$ , \*\*\* $p < 0.001$  by Student's t test compared to control at each time point.

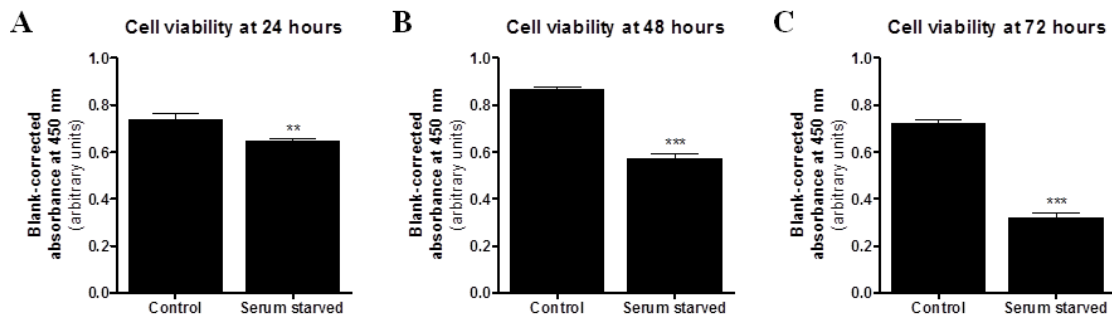


**Figure 4.13:** Effect of serum starvation on endothelial cell viability *in vitro*.

Mouse brain endothelial (bEnd.3) cells were treated with complete serum-supplemented medium (10% FBS) or serum-free medium (0% FBS) for 24 (A), 48 (B) or 72 (C) hours. Cell viability was measured by an MTS assay at each time point and is presented as the blank-corrected absorbance at 450 nm. Data are presented as mean  $\pm$  SEM and represent a single experiment carried out in four replicates. \*\* $p < 0.01$ , \*\*\* $p < 0.001$  by Student's t test compared to control at each time point.

### 4.3 Discussion

Dichotomous effects of the NLRP3 inflammasome complex and its effector cytokine IL-18 in AMD development have been described and prompted a lot of debate over the past years (Doyle et al., 2012; Tarallo et al., 2012). Although it is now widely accepted that the inflammasome components are present in and around the RPE of AMD patients, their exact role(s) in retinal homeostasis and AMD pathology are still unclear.

In line with previous observations, the presence of the inflammasome components NLRP3 and caspase-1 was detected in the maculae of human AMD patients diagnosed with GA. Similarly, the inflammasome effector cytokines IL-18 and IL-1 $\beta$  were also found to be expressed in the retinas and RPE of both GA-affected as well as healthy human donors. The staining patterns, however, appeared to be slightly different between the healthy and GA eyes. While the expression of inflammasome components seemed to be more localised in healthy controls, the staining pattern was more diffuse in GA. In general, the RPE staining was quite difficult to discern due to its pigmentation. Only when the RPE was disrupted, which was typically accompanied by its depigmentation as observed in dry AMD, it was possible to detect the presence of inflammasome components between the RPE and Bruch's membrane. In line with a recent report by Kosmidou et al. (2017), the NLRP3 staining was quite weak, arguing the specificity of the antibody used in the

staining protocol and/or suggesting that the RPE might not contain meaningful amounts of NLRP3. In addition, further evidence was provided for a necrotic, rather than apoptotic, type of cell death being responsible for the RPE degeneration in GA patients.

The inflammasome component pro-caspase-1 and the precursor forms of IL-1 $\beta$  and IL-18 were also detected intracellularly in hfRPE cells *in vitro*. Interestingly, the standard conditions of inflammasome priming and activation had no effect on pro-caspase-1 and pro-IL-1 $\beta$  expression levels, even though the priming step is well known to increase the mRNA and protein expression of inflammasome components in immune cells, which was also observed in ARPE-19 cell line (Tseng et al., 2013). The relatively high levels of pro-caspase-1 and pro-IL-1 $\beta$  in untreated samples were quite surprising, as this is unlike any previously published observations. Whether these were caused by cell culture conditions or some other mechanism would need to be revisited. Similarly, pro-IL-18 levels were not affected by priming alone, however, its expression was increased after activation with ATP, even without the need for priming, although this further up-regulated pro-IL-18 expression. Its low baseline levels were once again unexpected, as pro-IL-18 is normally expressed in cells without the requirement for induction. At the same time, inflammasome activation in the RPE was associated with IL-18 secretion, but no IL-1 $\beta$  release (despite pro-IL-1 $\beta$  being readily detected), which is consistent with previously published reports (Doyle et al., 2012; Shi et al., 2015). Noticeably, IL-1 $\alpha$  was selected as an inflammasome priming agent in these studies, based on the report by Tseng et al. (2013) who directly compared three different priming strategies, namely LPS, IL-1 $\alpha$  and TNF- $\alpha$ , under various experimental conditions, demonstrating that IL-1 $\alpha$  exhibited the best priming capabilities in RPE cells *in vitro*. Interestingly, extended inflammasome priming and activation did not kill RPE cells, as is normally observed in immune cells, but in fact promoted the RPE metabolic health. However, as mentioned before, the cell viability assay used in this case relies on the bioreduction of its substrate in metabolically active cells and thus cannot truly discriminate between actively proliferating cells and an improved metabolic capacity. A series of wound-healing assays similar to those already described would be required to address this matter. In addition, levels of secreted IL-18 would need to be analysed to confirm the formation of an active inflammasome. Furthermore, it might be interesting to evaluate the VEGF levels under these experimental conditions, as it was reported that the inflammasome formation itself might be sufficient to decrease VEGF production in the RPE (Mohr et al., 2015).

The RPE supports retinal function in several different ways. On daily basis, it is involved in the phagocytic clearance of shed POSs, a process now known to be dependent on the

components of autophagy pathway (Kim et al., 2013). Expression of autophagy-related components was found to be differentially regulated between 8 AM and 8 PM, highlighting the changes in the RPE activity during the day. Moreover, components of the autophagy pathway were up-regulated in the morning compared to the evening, corresponding to the reported increase in the RPE phagocytic activity. Concomitantly, many inflammasome-related genes were also up-regulated in the morning, including *Il1b* and *Il18*. In addition, the rate of VEGF secretion in RPE cells was markedly reduced in response to autophagy induction by serum starvation *in vitro* and this was not associated with a decrease in RPE cell viability. In fact, the short-term serum starvation (up to 6 hours) had a positive effect on the RPE metabolic health. Taken together, these findings, for the first time, established a link between the POS phagocytosis and expression of inflammasome components in the RPE. In addition, they suggested that these processes might have an important role in the regulation of VEGF synthesis.

The main conclusions inferred from experiments presented in this section are as follows:

- the NLRP3 inflammasome components and its effector cytokines are present in the RPE and retinas of patients with GA as well as in age-matched healthy controls, with varying patterns of expression
- RPE cells secrete IL-18, but not IL-1 $\beta$ , *in vitro*
- inflammasome components can be detected in the RPE *in vitro*
- prolonged inflammasome activation has no effect on RPE cell viability *in vitro*
- expression of autophagy-related genes increases in response to POS phagocytosis *in vivo* and *in vitro*
- expression of inflammasome-related genes increases in response to POS phagocytosis *in vivo*
- IL-18 is secreted in response to POS phagocytosis *in vitro*
- serum starvation decreases VEGF secretion by the RPE *in vitro*
- serum starvation has no effect on RPE cell viability *in vitro*
- serum starvation causes endothelial cell death *in vitro*

## Chapter 5

# **Regulation of the inner blood-retina barrier in retinal homeostasis**

## 5 REGULATION OF THE INNER BLOOD-RETINA BARRIER IN RETINAL HOMEOSTASIS

---

### 5.1 Introduction

As already described, the retina comprises two structurally and functionally different light-detection systems. The image-forming visual system processes detailed information about the surrounding environment with high spatial and temporal resolution, culminating in the ability to distinguish shapes, depths, colour and motion. It is facilitated by retinal rods and cones and relies on the support provided by the RPE. Thus, any changes in activity and/or damage to either photoreceptors themselves or the RPE affect the output of this system.

By contrast, there are a number of visual functions concerned with the detection of ambient light levels rather than the visual image itself, including the entrainment (synchronisation) of the circadian pacemaker, the pupillary light reflex and some other aspects of behaviour and neurophysiology. Interestingly, this non-image-forming vision is independent of the classical photoreceptors and remains functional even in the complete absence of rods and cones or if these are seriously damaged (Keeler, 1927; Keeler et al., 1928; Czeisler et al., 1995; Freedman et al., 1999; Lucas et al., 1999; Lucas and Foster, 1999; Zaidi et al., 2007). Still, ocular photoreception is required for its proper function as these visual responses are abolished following bilateral enucleation (Freedman et al., 1999; Lucas and Foster, 1999; Yamazaki et al., 1999). The non-image-forming visual system is mediated by melanopsin-expressing retinal ganglion cells which are intrinsically photosensitive and project mostly into the SCN of the hypothalamus, the primary circadian oscillator responsible for setting, maintaining and coordinating circadian rhythms throughout the body (Provencio et al., 2000; Hattar et al., 2002; Provencio et al., 2002). These ipRGCs were shown to directly respond to light even when they were pharmacologically or physically dissociated from the rest of the retina (Berson et al., 2002). Furthermore, they were preserved in retinas of blind patients with severe degeneration of the outer and/or inner retinal layers (Hannibal et al., 2004). In addition, some of the ipRGC axons were found to terminate in the LGN and SC and recent research suggested that these cells might contribute to rudimentary conscious visual perception in humans, including brightness discrimination and contrast detection, independently of retinal rods and cones (Dacey et al., 2005; Zaidi et al., 2007; Brown et al., 2012). Noticeably, the melanopsin-dependent photoreception is the earliest visual function detected in the mammalian retina (Sekaran et al., 2005). Unlike rods and cones, ipRGCs do not rely on the support of the RPE and remain directly light-sensitive even when the key RPE enzymes involved in the visual cycle are genetically or pharmacologically inhibited

(Doyle et al., 2006; Tu et al., 2006), owing to the bistable nature of melanopsin which not only acts as a photopigment, but also possesses an intrinsic photoisomerase activity for its own regeneration (Fu et al., 2005; Melyan et al., 2005; Mure et al., 2007).

Circadian rhythms are biological processes displaying endogenous, entrainable oscillations of approximately 24 hours. Although they are endogenous, i.e. self-sustained, they require synchronisation (entrainment) to the local environment by external cues, called zeitgebers, which include light, temperature and redox cycles. Circadian rhythms regulate a number of physiological and behavioural functions, such as sleep and wakefulness, body temperature, blood pressure, hormone production, digestive secretion and immune activity. In this way, they allow organisms to anticipate regular environmental changes, enabling them to better capitalise on environmental resources (e.g. light and food) compared to those that cannot predict such availability. Disruption of circadian rhythms in humans has been associated with insomnia, jet lag, stomach ailments, coronary heart attacks, depression and is common among cancer patients. Circadian rhythms are driven by an internal timing machine, known as the circadian clock (circadian oscillator), which can sustain biological rhythms of about 24 hours in the absence of external cues. The clock is reset when it receives sufficient daily corrective signals from the environment, with light being the most powerful circadian synchroniser among all environmental time cues. The anatomy of the mammalian circadian clock consists of three major components: 1) a central biochemical oscillator (pacemaker) located in the SCN with a period of about 24 hours that keeps time, 2) a series of input pathways to this central pacemaker that transmit information from environmental cues and allow entrainment of the clock, and 3) a series of output pathways converting instructions from the central pacemaker into daily oscillations of various biochemical, physiological and behavioural processes throughout an organism. At the molecular level, the circadian clockwork is operated by positive and negative autoregulatory transcription-translation feedback loops of the core circadian genes in the central pacemaker as well as in most peripheral tissues (Figure 5.1). Core circadian genes are defined as genes whose protein products are necessary components for the generation and regulation of circadian rhythms and include *Clock*, *CK1ε*, *Cry1*, *Cry2*, *Per1*, *Per2*, *Per3* and *Bmal1*. Circadian oscillators are ubiquitous in tissues of the body where they are synchronised by both endogenous and external signals to regulate transcriptional activity throughout the day in a tissue-specific manner (Fu and Lee, 2003).

The iBRB has evolved in order to protect the retina from potential blood-borne toxicity and maintain the local microenvironment and homeostasis. The barrier properties are regulated by the formation of tight junctions between adjacent endothelial cells of the inner retinal

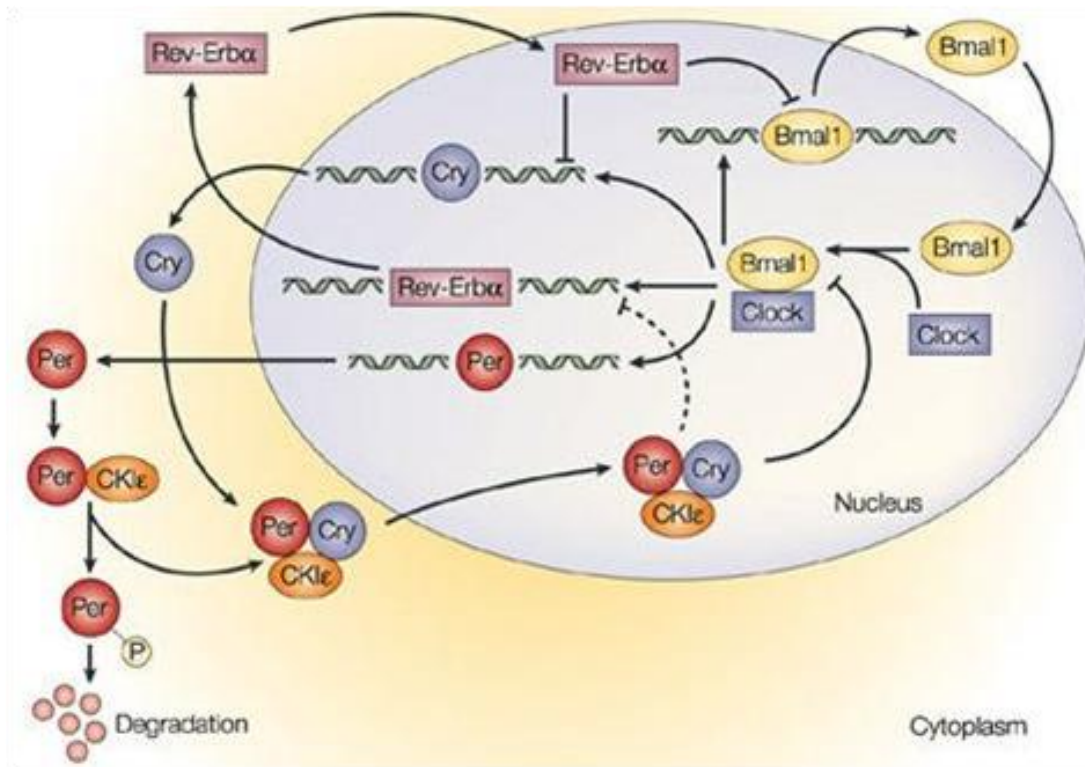


**Figure 5.1:** Feedback loops of the mammalian core circadian genes.

Mammalian circadian rhythms are generated by feedback loops of the core circadian genes in the central pacemaker, the suprachiasmatic nucleus (SCN), as well as in most peripheral tissues. The intracellular levels of Clock protein remain stable over the 24-hour period. The high expression levels of Bmal1 at the beginning of a subjective day promote the formation of Bmal1-Clock heterodimers which translocate into the nucleus where they bind to E-box sequences in the promoters of *Cry*, *Per* and *Rev-Erba* genes to initiate their transcription. After transcription and translation, the Rev-Erba protein re-enters the nucleus to suppress transcription of *Bmal1* and *Cry* genes. As the Per protein accumulates in the cytoplasm, it becomes phosphorylated by CKIε, rendering it unstable and targeting it for ubiquitination and subsequent proteasomal degradation. Late in the subjective day, cytoplasmic levels of the Cry protein increase, promoting the formation of stable CKIε-Per-Cry complexes that enter the nucleus at the beginning of a subjective night. Once in the nucleus, Cry disrupts Bmal1-Clock heterodimers to suppress their activity, resulting in the inhibition of *Cry*, *Per* and *Rev-Erba* transcription and derepression (stimulation) of *Bmal1* transcription. Thus, these interacting positive and negative feedback loops of circadian genes ensure low levels of Per and Cry and a high level of Bmal1 at the beginning of a new circadian day.

Clock, circadian locomotor output cycles kaput; Cry, cryptochrome; Per, period; CKIε, casein kinase Iε. *From Fu and Lee (2003).*



vasculature that effectively seal off the intercellular spaces and thus control the paracellular movement of substances. Furthermore, the maintenance of the iBRB integrity relies on the support provided by other components of the NVU, i.e. pericytes, glial cells and neurons. Importantly, the barrier permeability can be influenced by multiple additional factors and processes that might occur in the retina, including growth factors, shear stress, oxidised phospholipids, advanced glycation end products, inflammatory mediators (cytokines and chemokines), oxidative stress, hyperglycaemia and hypoxia. The mechanisms by which these factors could modify the barrier properties have been proposed to involve a dynamic modulation of tight junction protein expression and/or the assembly of a functional tight junction complex through phosphorylation of junctional molecules and their subsequent ubiquitination, internalisation and degradation, disruption of adherens junctions, increased transcellular vesicular transport, endothelial cell death or structural damage, pericyte loss or dysfunction causing their migration and detachment from endothelial cells, abnormal glial cell functions and loss or impairment of the endothelial glycocalyx<sup>6</sup> (Klaassen et al., 2013). Thus far, the modulation of the iBRB permeability has been studied primarily in relation to disease pathology, however, its role in normal retinal homeostasis is still poorly understood.

The main purpose of experiments presented in this section was to explore the physiological regulation of the iBRB permeability. The specific aims can be summarised as follows:

- to investigate the effect of VEGF treatment on endothelial barrier properties *in vitro*
- to study the iBRB permeability at 8 AM and 8 PM *in vivo*
- to examine the potential mechanism(s) of the iBRB regulation *in vivo*

## 5.2 Results

### 5.2.1 VEGF regulates endothelial barrier properties *in vitro*

Having observed that the RPE undergoes periodic changes in its activity that could affect VEGF secretion, the effect of VEGF on endothelial barrier properties was first examined *in vitro*.

Adding VEGF (50 ng/ml) to either the basolateral or apical surface of bEnd.3 cells grown on permeable membrane supports and subsequently monitoring TEER of cell monolayers over the period of 24 hours (Figure 5.2A), it was found that VEGF significantly decreased electrical resistance at 12 and 24 hours after treatment (Figure 5.2D,E), with no changes

---

<sup>6</sup> Glycocalyx, also referred to as the pericellular matrix, is a network of membrane-bound proteoglycans, glycoproteins and glycolipids at the apical (luminal) side of vascular endothelial cells, which constitutes the first permeability barrier for plasma proteins and adhering leukocytes.

detected at 3 or 6 hours (Figure 5.2B,C) and both the basolateral (Figure 5.2, red bars) and apical (Figure 5.2, green bars) VEGF administration having comparable effects on barrier properties. This reduction in electrical resistance was accompanied by decreased levels of tight junction proteins claudin-5 and ZO-1 observed at both time points, although in the case of claudin-5 they were not significant. The levels of occludin protein expression were not affected by VEGF treatment under these experimental conditions (Figure 5.3). Taken together, these results demonstrate that VEGF can regulate endothelial barrier properties by modulating the expression of tight junction proteins.

### *5.2.2 Functional changes in the iBRB permeability at 8 AM and 8 PM in vivo*

As already shown, injection of a low molecular weight tracer molecule sodium fluorescein allows efficient visualisation of the inner retinal microvasculature and detection of vascular leakage. A burst of POS disc shedding followed by their phagocytosis and degradation in the RPE is known to occur every morning, which changes metabolic requirements of the retinal cells and leads to a production of various local factors. For this reason, the iBRB permeability was investigated just after the light onset at 8 AM and compared to 8 PM to determine whether its barrier properties could be modulated periodically to maintain retinal homeostasis.

Dynamic FA profiles obtained at 2-10 minutes after sodium fluorescein injection showed different patterns of signal enhancement at 8 AM and 8 PM in wild-type C57BL/6J mice (Figure 5.4). Quantification of these FA profiles revealed a peak of signal intensity at 3.5 minutes after fluorescein injection in mice assessed at 8 AM, followed by a gradual decline as the fluorescent tracer was cleared from the systemic circulation. In comparison, the peak of signal intensity was shifted to a later time point (4.5 minutes) at 8 PM. Furthermore, the signal intensity between 2.5 and 7.5 minutes post fluorescein injection was significantly increased at 8 PM compared to 8 AM (Figure 5.5A). Area under the curve of the signal intensity profile, representing the iBRB permeability, was also significantly higher at 8 PM than at 8 AM, by approximately 20% (Figure 5.5B). As these initial studies examined the vascular leakage in C57BL/6J mice of various ages, ranging from 4 to almost 20 months, any potential effect(s) of age on the observed permeability changes were investigated by stratifying animals on the basis of their age into two separate groups, with 6 months being the threshold to classify them as either "young" or "old". Dynamic FA profiles revealed similar patterns of signal enhancement in both age groups at 8 AM as well as at 8 PM (Figure 5.6). When quantified, there were no significant differences between young and old animals at 8 AM (Figure 5.7) or at 8 PM (Figure 5.8). At both time points, the signal

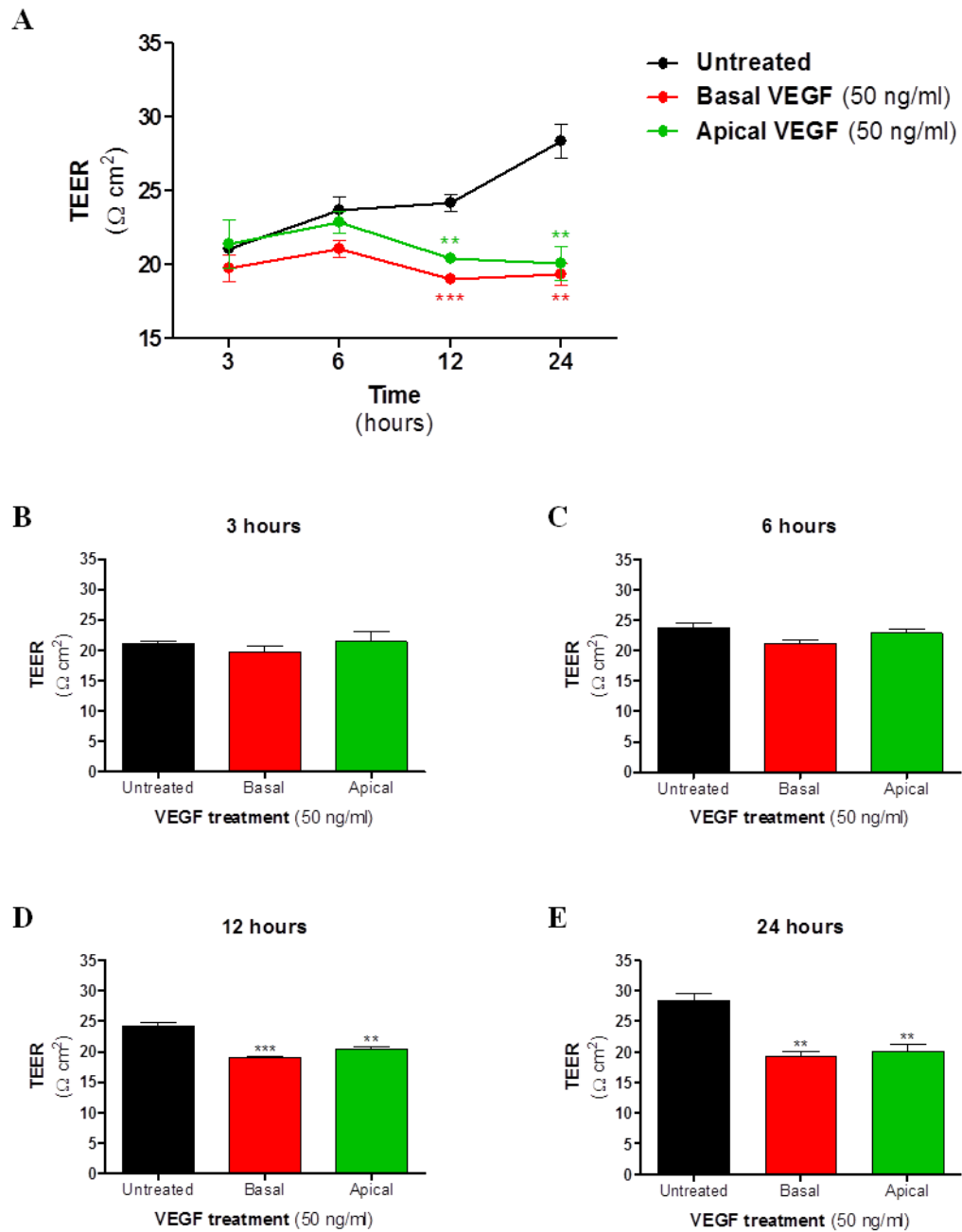


**Figure 5.2:** Effect of VEGF on endothelial electrical resistance *in vitro* in bEnd.3 cells.

Mouse brain endothelial (bEnd.3) cells were grown as confluent monolayers on permeable membrane supports. On day 5 post seeding, the cells were treated with control medium (untreated, *black*) or a single dose of VEGF (50 ng/ml), either on the basolateral (*red*) or apical (*green*) side of the monolayer. Transendothelial electrical resistance (TEER) was monitored over 24 hours (A), with measurements taken at 3 (B), 6 (C), 12 (D) and 24 (E) hours after treatment. TEER values are expressed as blank-corrected unit area resistance in  $\Omega \text{ cm}^2$ . Data are presented as mean  $\pm$  SEM and represent a single experiment carried out in triplicate. \*\* $p < 0.01$ , \*\*\* $p < 0.001$  by one-way ANOVA with Tukey post test compared to untreated control at each time point.

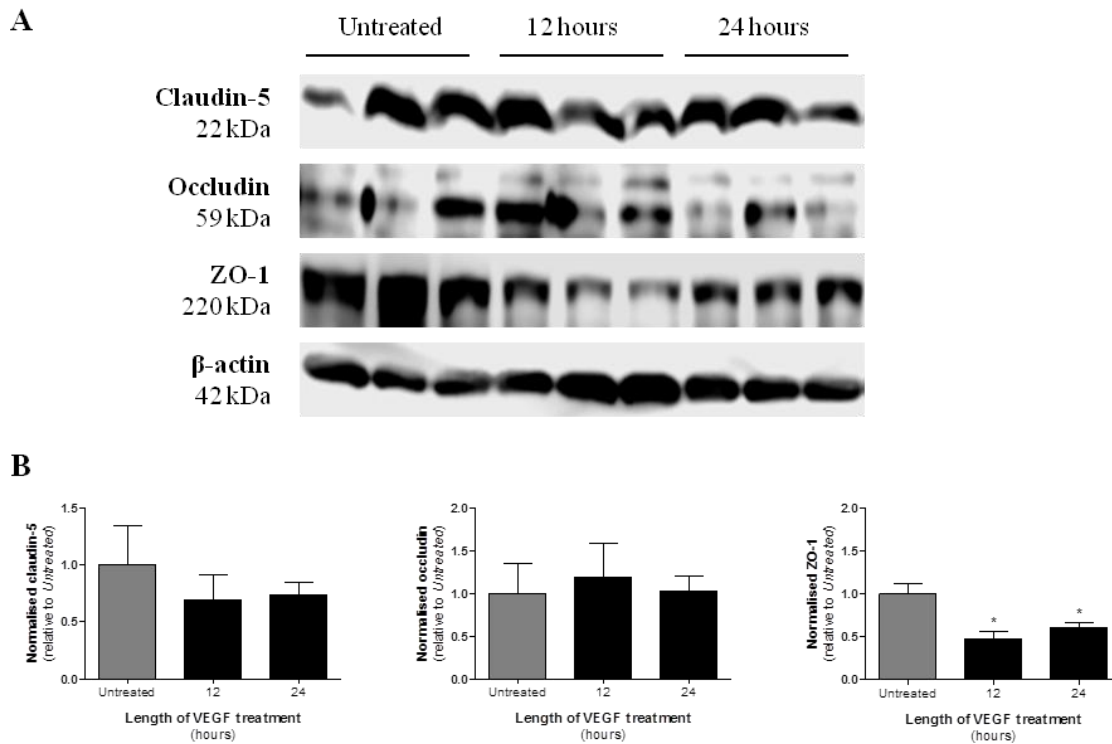


**Figure 5.3:** Effect of VEGF on tight junction protein expression *in vitro* in bEnd.3 cells.

Mouse brain endothelial (bEnd.3) cells were treated with control medium (untreated) or a single dose of VEGF (50 ng/ml) for 12 or 24 hours. Protein lysates were separated by SDS-PAGE using 10 µg of total protein as determined by the BCA assay. Proteins of interest were immunodetected by Western blotting (A). Band intensity was quantified in ImageJ and data normalised to the corresponding β-actin loading control (B). Data are presented as mean ± SEM and represent a single experiment carried out in triplicate. \*p<0.05 by one-way ANOVA with Tukey post test compared to untreated control.

intensity profile plots were fairly overlapping, with comparable areas under the respective curves.

To establish whether these permeability changes were unique to C57BL/6J mice or applied universally to other strains, similar studies were carried out in 129 and CD1 (albino) mice. As was the case of C57BL/6J strain, dynamic FA profiling revealed different patterns of signal enhancement at 8 AM and 8 PM also in 129 mice (Figure 5.9). The quantified 129 profiles closely resembled those observed in C57BL/6J strain, although the peaks of signal intensity were slightly shifted compared to C57BL/6J mice at both 8 AM and 8 PM and occurred at 4.0 and 5.5 minutes post fluorescein injection, respectively. Unlike C57BL/6J, 129 mice showed significantly increased signal intensity at 8 PM at all time points after

fluorescein injection (Figure 5.10A) and the area under the curve was increased by almost 50% at 8 PM in these animals (Figure 5.10B). On the other hand, CD1 mice demonstrated much less pronounced differences in the signal enhancement patterns of their dynamic FA profiles acquired at 8 AM and 8 PM (Figure 5.11). Despite there being a similar general trend, quantified signal intensity profiles were less separated, with significant differences only between 3.0 and 5.5 minutes post fluorescein administration (Figure 5.12A), and a non-significant increase in vascular leakage of 15% at 8 PM (Figure 5.12B). Nonetheless, these results suggest that the iBRB is a dynamic structure that undergoes periodic changes in its permeability during the day as part of normal retinal physiology. In addition, these changes represent a universal phenomenon, as they were found to be independent of the animal age or strain.

### 5.2.3 IL-18 regulates the iBRB permeability *in vivo*

As previous results suggested, the phagocytically active period of the RPE in the morning was associated with inflammasome formation, leading to IL-18 secretion. Moreover, IL-18 was shown to regulate VEGF production *in vivo* and *in vitro* as well as have a direct effect on tight junction protein expression in endothelial cells. To assess the role of IL-18 in the observed periodic iBRB permeability changes, the vascular leakage was examined in *Il18*<sup>-/-</sup> mice at 8 AM and 8 PM.

The different patterns of signal enhancement at 8 AM and 8 PM were preserved in *Il18*<sup>-/-</sup> mice (Figure 5.13). Similarly, quantification of the dynamic FA profiles revealed the same trend as demonstrated in wild-type mice. The peaks of signal intensity at 8 AM and 8 PM were detected at 5.0 and 6.5 minutes after fluorescein injection, respectively, and the signal intensity was generally higher (although not significant) at 8 PM than at 8 AM at all time points post injection (Figure 5.14A). Area under the curve was increased non-significantly by 44% at 8 PM (Figure 5.14B). Furthermore, the overall signal intensity appeared to be higher at both times in *Il18*<sup>-/-</sup> mice compared to the wild-type strains. Because *Il18*<sup>-/-</sup> mice were raised on the C57BL/6J background, the signal intensity profiles at 8 AM (Figure 5.15A) and 8 PM (Figure 5.16A) were directly compared between the two mouse strains. The vascular leakage was increased in *Il18*<sup>-/-</sup> mice compared to age-matched C57BL/6J controls by approximately 32% at 8 AM (Figure 5.15B) and 63% at 8 PM (Figure 5.16B). Taken together, these results suggest that IL-18 can regulate the iBRB permeability *in vivo*, but has no effect on its periodic cycling.

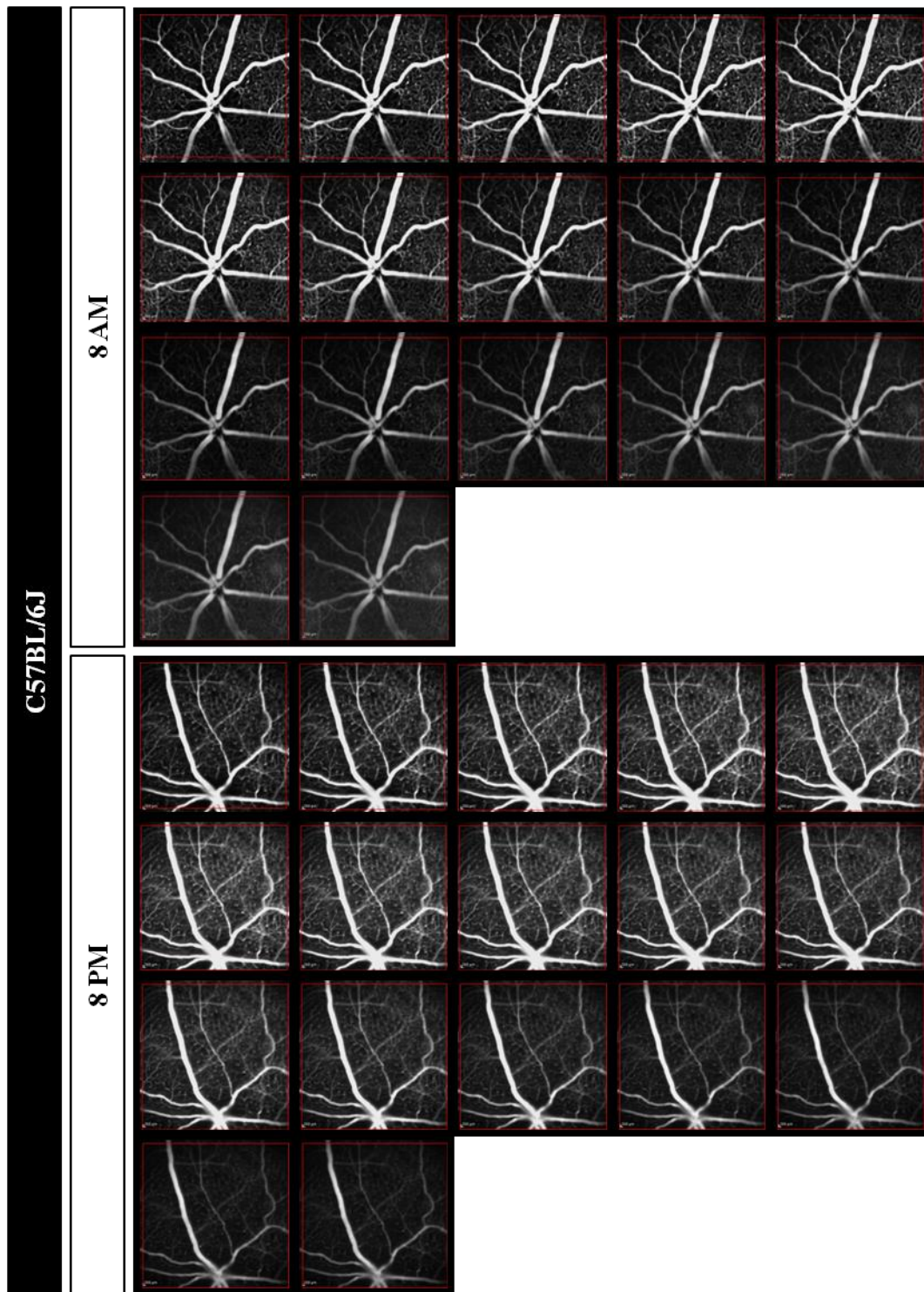


**Figure 5.4:** Dynamic FA profiling *in vivo* in C57BL/6J mice at 8 AM versus 8 PM. Representative dynamic FA profiles of two wild-type C57BL/6J mice obtained at 8 AM and 8 PM, respectively, are presented. Mice were injected (i.p.) with sodium fluorescein (100 mg/kg body weight) and FA images acquired at regular intervals (every 30 seconds) at 2-10 minutes post injection. To correct for small animal movements during procedure, the minimum overlapping area was identified in ImageJ and is highlighted in red rectangle in each image.

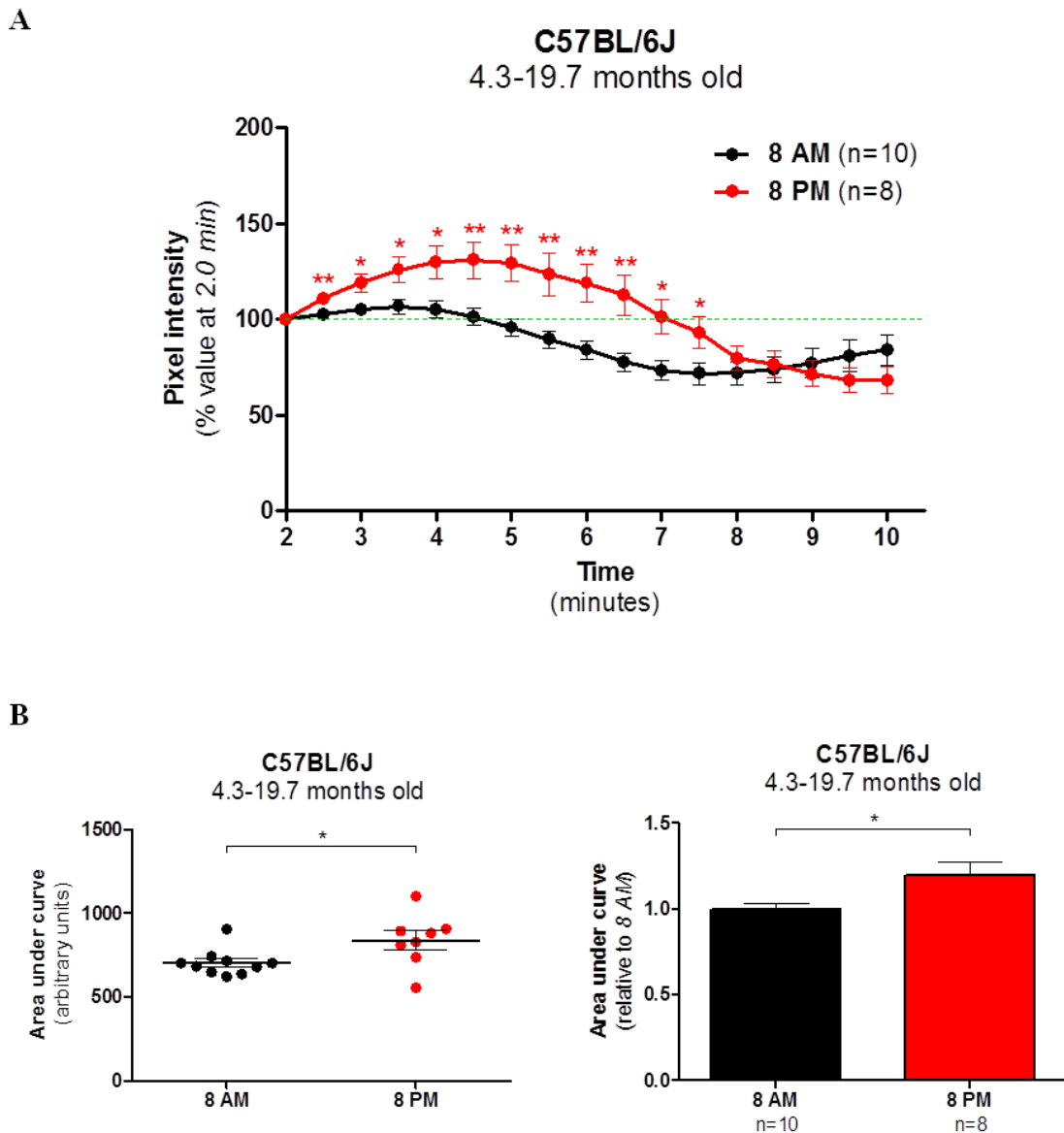


**Figure 5.5:** The iBRB permeability *in vivo* in C57BL/6J mice at 8 AM versus 8 PM.

Dynamic FA profiles were acquired in wild-type C57BL/6J mice at 8 AM or 8 PM. The minimum overlapping image area was identified in each case. The signal intensity in the selected region was measured in ImageJ, each value normalised to the starting point and expressed as % value at 2.0 min. Profile plot was obtained by plotting normalised pixel intensity against time (in minutes) (A). Area under this curve was quantified to represent leakage of the sodium fluorescein tracer (B). Data are presented as mean  $\pm$  SEM (n=8-10 animals per each time point). \* $p < 0.05$ , \*\* $p < 0.01$  by Student's t test compared to 8 AM.

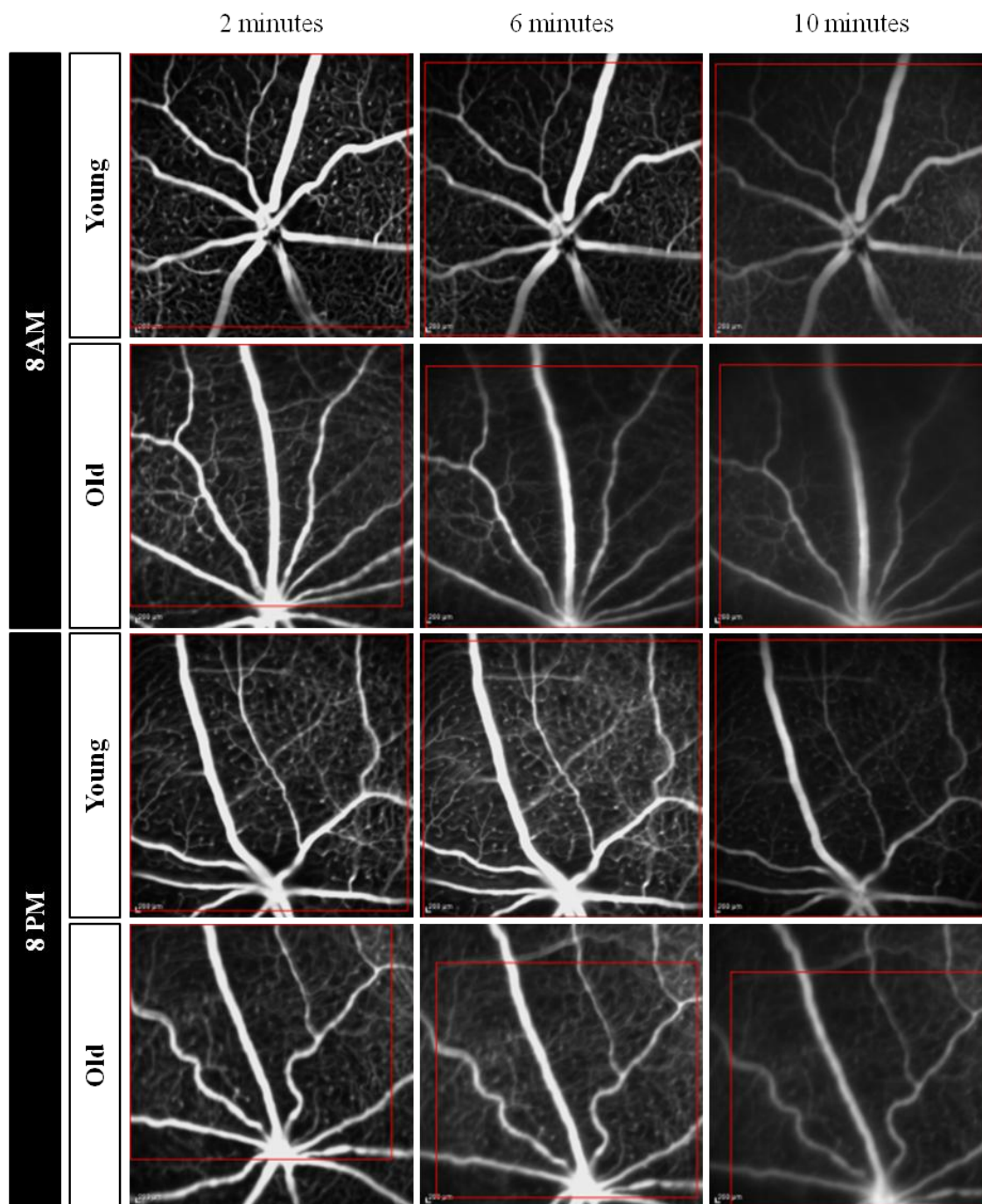


**Figure 5.6:** Partial dynamic FA profiles *in vivo* in age-stratified C57BL/6J mice at 8 AM and 8 PM.

Representative partial dynamic FA profiles of wild-type C57BL/6J mice, stratified on the basis of their age, obtained at 8 AM and 8 PM are presented. Mice were injected (i.p.) with sodium fluorescein (100 mg/kg body weight) and FA images acquired at regular intervals (every 30 seconds) at 2-10 minutes post injection. Images captured at 2, 6 and 10 minutes after the injection are shown. To correct for small animal movements during procedure, the minimum overlapping area was identified in ImageJ and is highlighted in red rectangle in each image.



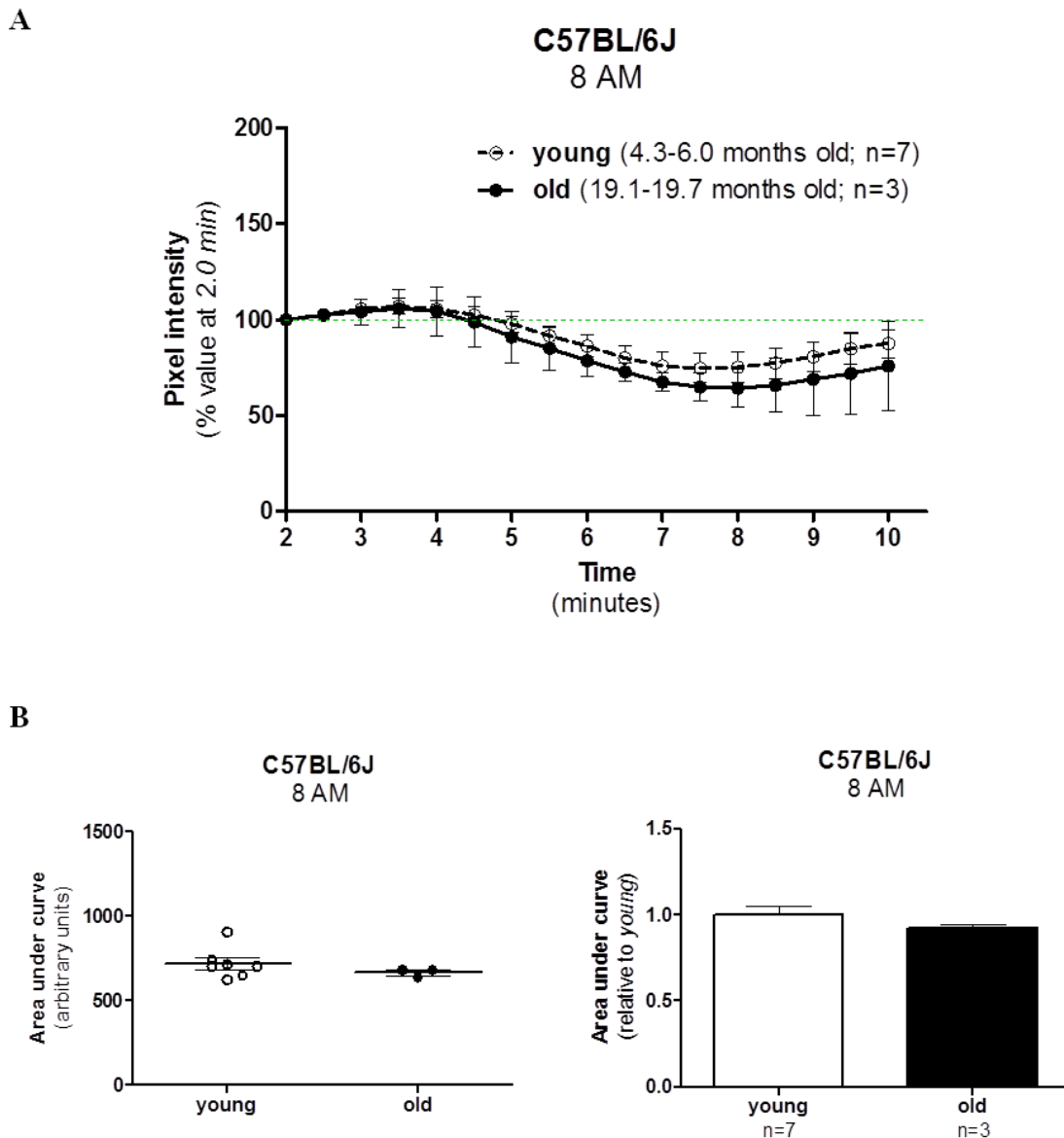
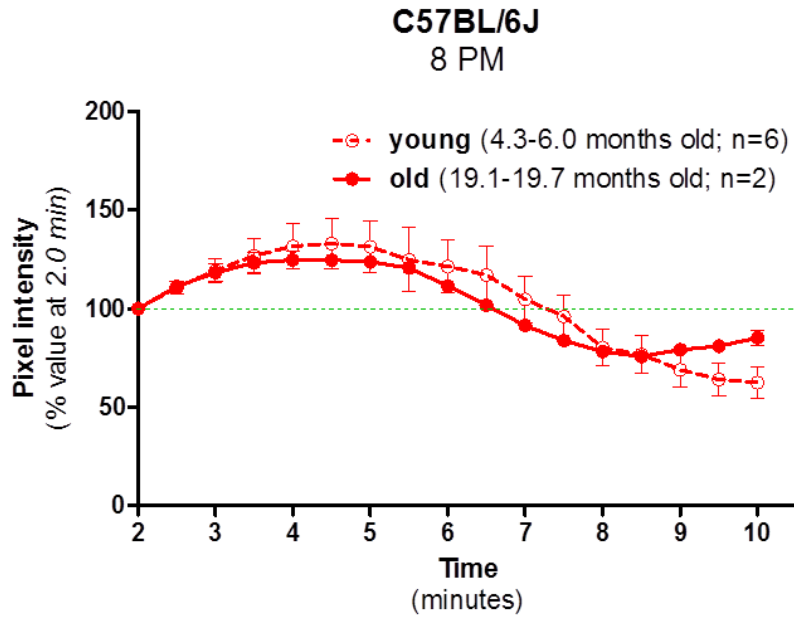


**Figure 5.7:** The iBRB permeability *in vivo* in age-stratified C57BL/6J mice at 8 AM.

Dynamic FA profiles were acquired in wild-type C57BL/6J mice at 8 AM. Animals were classified as "young" if they were  $\leq 6$  months old or as "old" if they were  $> 6$  months of age. The minimum overlapping image area was identified in each case. The signal intensity in the selected region was measured in ImageJ, each value normalised to the starting point and expressed as % value at 2.0 min. Profile plot was obtained by plotting normalised pixel intensity against time (in minutes) (A). Area under this curve was quantified to represent leakage of the sodium fluorescein tracer (B). Data are presented as mean  $\pm$  SEM (n=3-7 animals per each age group). No significant differences between age groups by Student's t test.

A



B

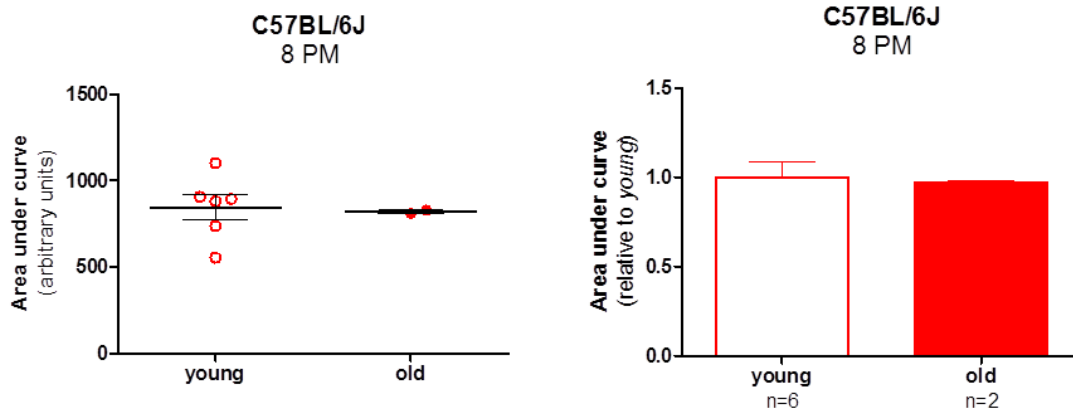


**Figure 5.8:** The iBRB permeability *in vivo* in age-stratified C57BL/6J mice at 8 PM.

Dynamic FA profiles were acquired in wild-type C57BL/6J mice at 8 PM. Animals were classified as "young" if they were  $\leq 6$  months old or as "old" if they were  $> 6$  months of age. The minimum overlapping image area was identified in each case. The signal intensity in the selected region was measured in ImageJ, each value normalised to the starting point and expressed as % value at 2.0 min. Profile plot was obtained by plotting normalised pixel intensity against time (in minutes) (A). Area under this curve was quantified to represent leakage of the sodium fluorescein tracer (B). Data are presented as mean  $\pm$  SEM (n=2-6 animals per each age group). No significant differences between age groups by Student's t test.

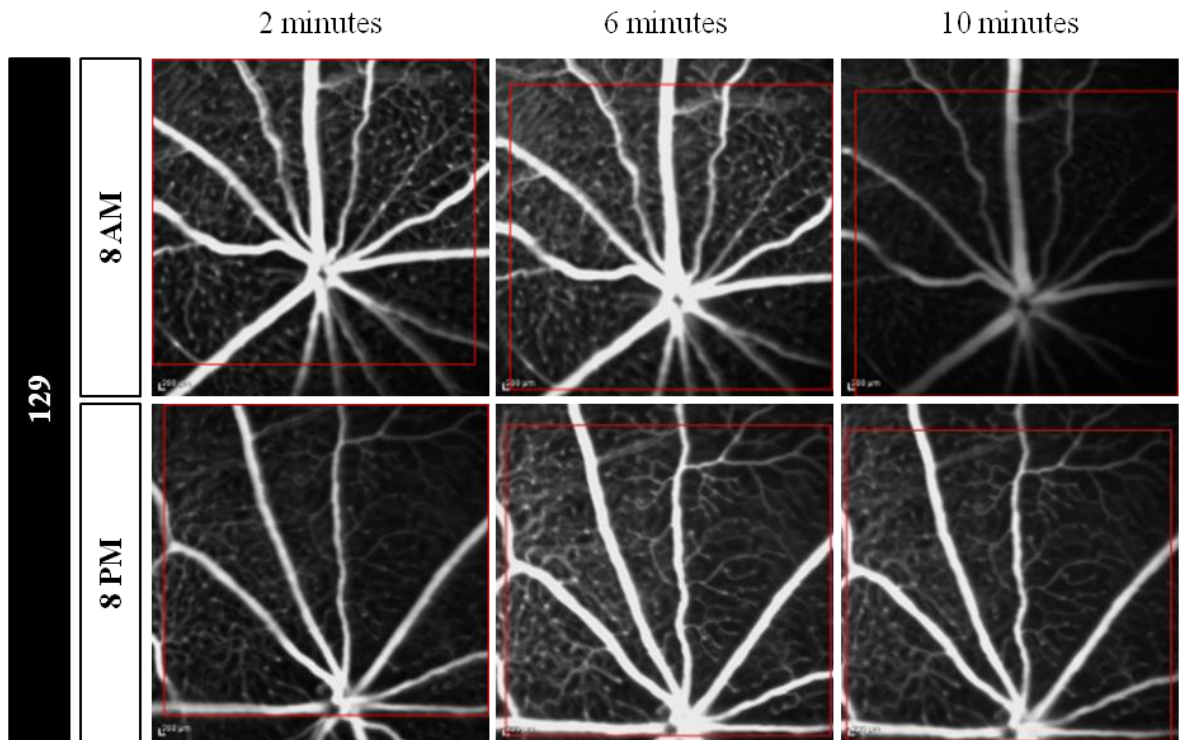
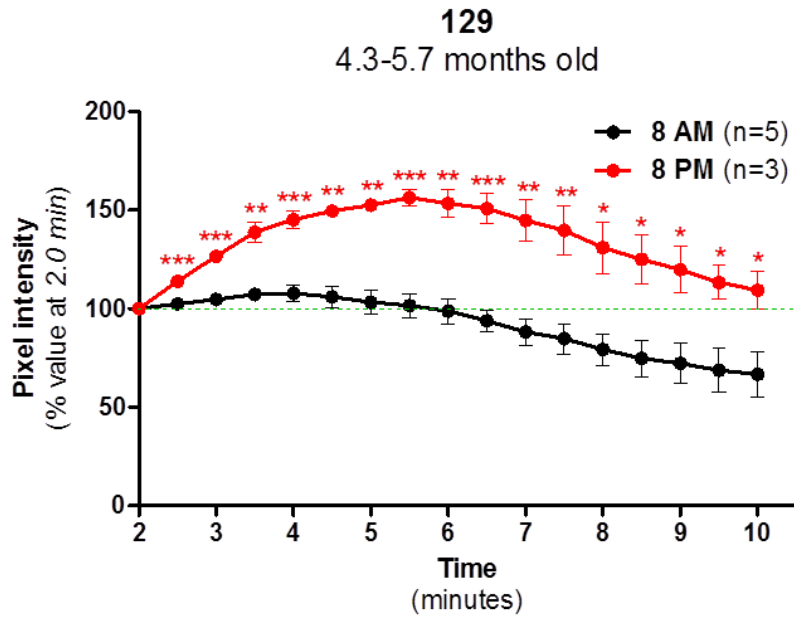


**Figure 5.9:** Partial dynamic FA profiles *in vivo* in 129 mice at 8 AM versus 8 PM.

Representative partial dynamic FA profiles of two wild-type 129 mice obtained at 8 AM and 8 PM, respectively, are presented. Mice were injected (i.p.) with sodium fluorescein (100 mg/kg body weight) and FA images acquired at regular intervals (every 30 seconds) at 2-10 minutes post injection. Images at 2, 6 and 10 minutes after the injection are shown. To correct for small animal movements during procedure, the minimum overlapping area was identified in ImageJ and is highlighted in red rectangle in each image.

A



B

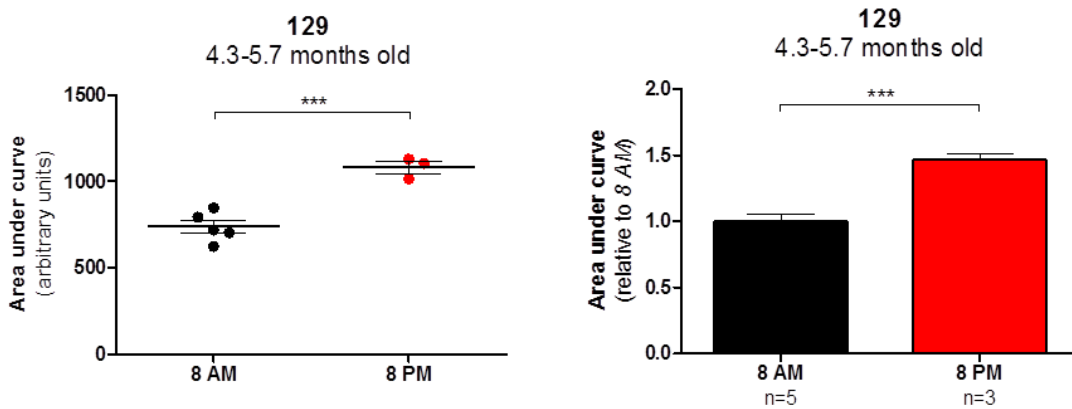


**Figure 5.10:** The iBRB permeability *in vivo* in 129 mice at 8 AM versus 8 PM.

Dynamic FA profiles were acquired in wild-type 129 mice at either 8 AM or 8 PM. The minimum overlapping image area was identified in each case. The signal intensity in the selected region was measured in ImageJ, each value normalised to the starting point and expressed as % value at 2.0 min. Profile plot was obtained by plotting normalised pixel intensity against time (in minutes) (A). Area under this curve was quantified to represent leakage of the sodium fluorescein tracer (B). Data are presented as mean  $\pm$  SEM (n=3-5 animals per each time point). \* $p < 0.05$ , \*\* $p < 0.01$ , \*\*\* $p < 0.001$  by Student's t test compared to 8 AM.

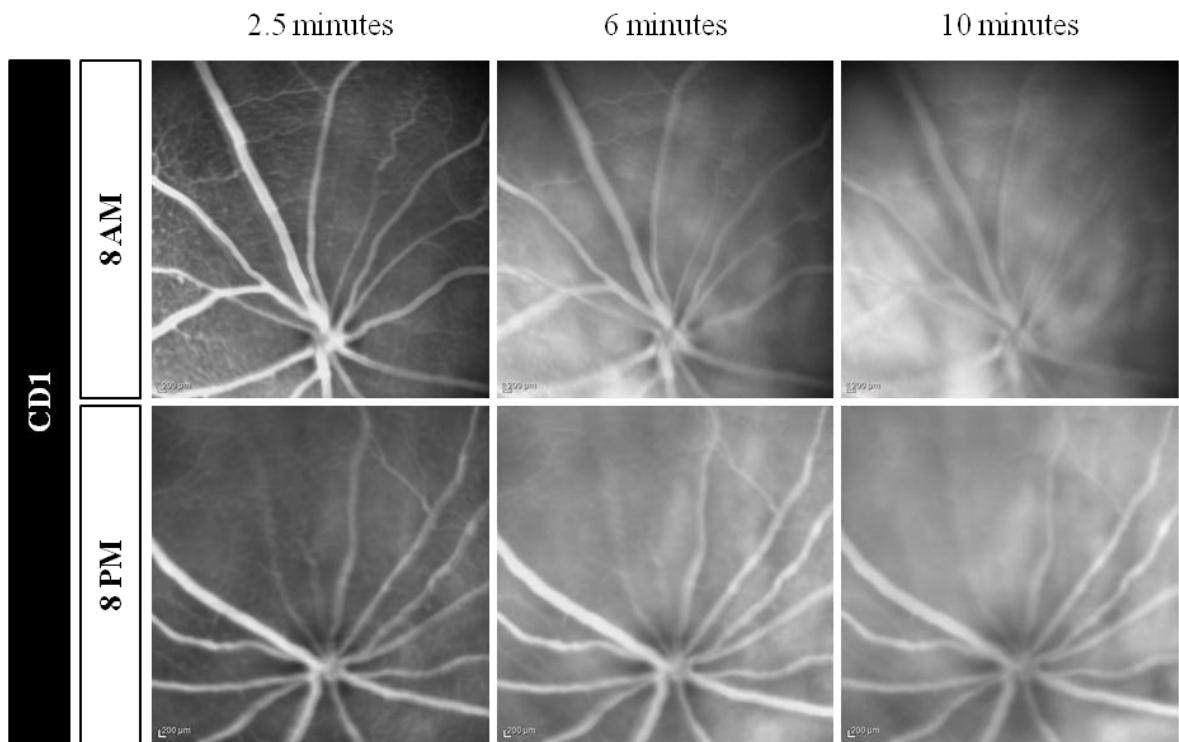
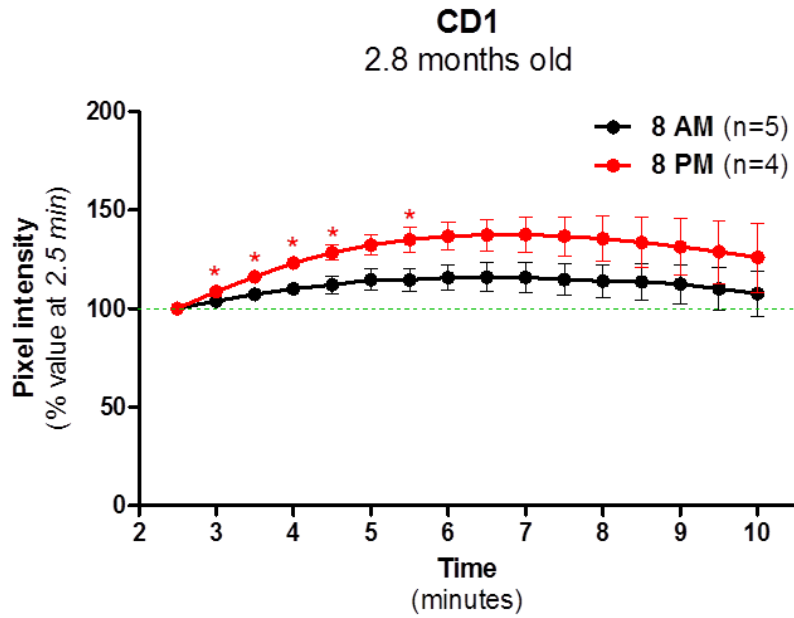


**Figure 5.11:** Partial dynamic FA profiles *in vivo* in CD1 mice at 8 AM versus 8 PM.

Representative partial dynamic FA profiles of two wild-type CD1 mice obtained at 8 AM and 8 PM, respectively, are presented. Mice were injected (i.p.) with sodium fluorescein (100 mg/kg body weight) and FA images acquired at regular intervals (every 30 seconds) at 2.5-10 minutes post injection. Images captured at 2.5, 6 and 10 minutes after injection are shown.

A



B

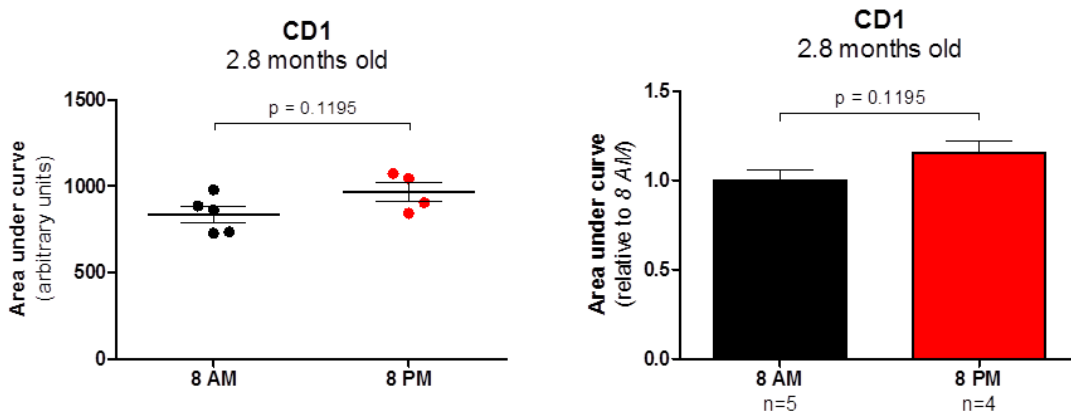


**Figure 5.12:** The iBRB permeability *in vivo* in CD1 mice at 8 AM versus 8 PM.

Dynamic FA profiles were acquired in wild-type CD1 mice at either 8 AM or 8 PM. The minimum overlapping image area was identified in each case. The signal intensity in the selected region was measured in ImageJ, each value normalised to the starting point and expressed as % value at 2.5 min. Profile plot was obtained by plotting normalised pixel intensity against time (in minutes) (A). Area under this curve was quantified to represent leakage of the sodium fluorescein tracer (B). Data are presented as mean  $\pm$  SEM (n=4-5 animals per each time point). \* $p < 0.05$  by Student's t test compared to 8 AM.

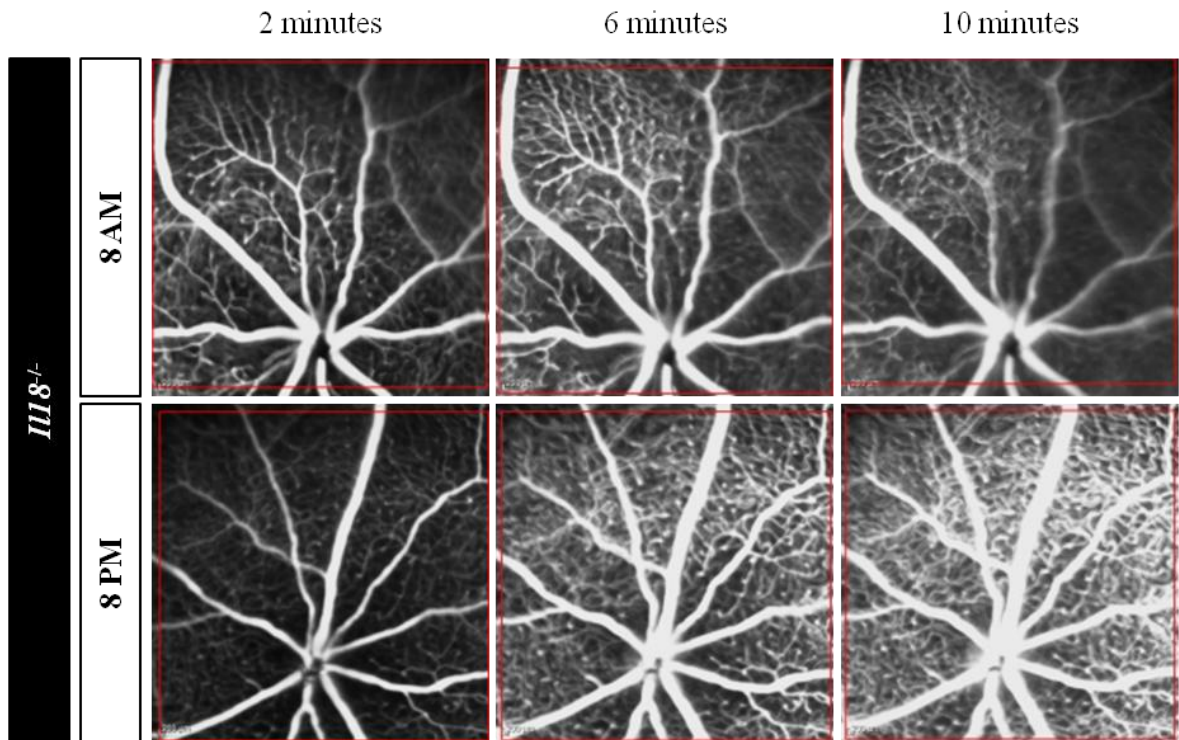
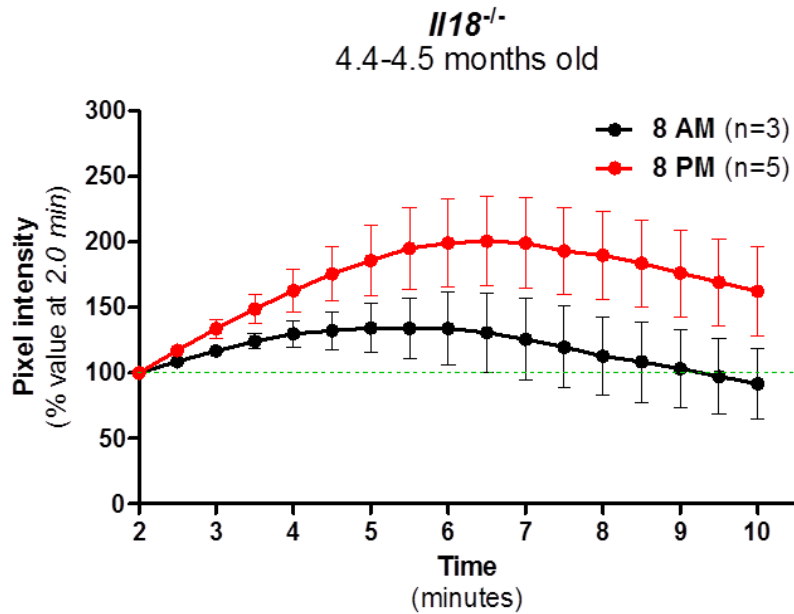


**Figure 5.13:** Partial dynamic FA profiles *in vivo* in *Il18<sup>-/-</sup>* mice at 8 AM versus 8 PM. Representative partial dynamic FA profiles of two *Il18<sup>-/-</sup>* mice obtained at 8 AM and 8 PM, respectively, are presented. Mice were injected (i.p.) with sodium fluorescein (100 mg/kg body weight) and FA images were acquired at regular intervals (every 30 seconds) at 2-10 minutes post injection. Images captured at 2, 6 and 10 minutes after injection are shown. To correct for small animal movements during procedure, the minimum overlapping area was identified in ImageJ and is highlighted in red rectangle in each image.

A



B

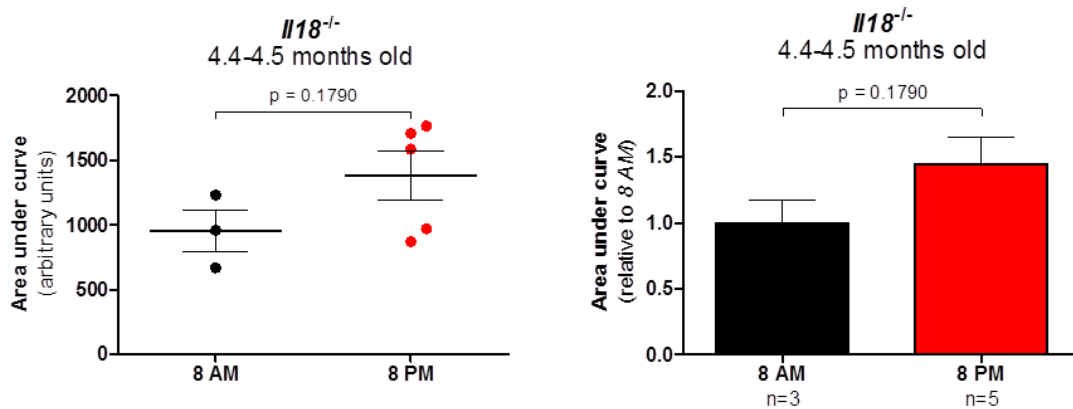
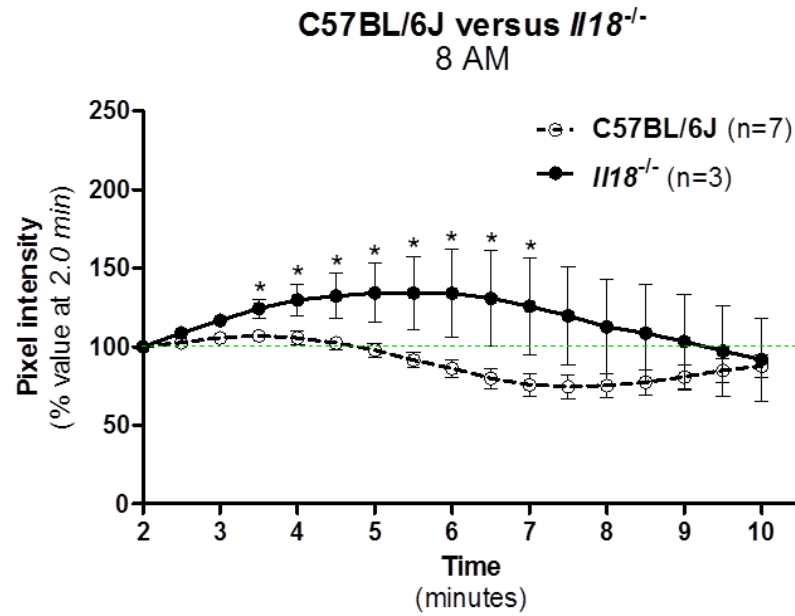


**Figure 5.14:** The iBRB permeability *in vivo* in *II18<sup>-/-</sup>* mice at 8 AM versus 8 PM.

Dynamic FA profiles were acquired in *II18<sup>-/-</sup>* mice at either 8 AM or 8 PM. The minimum overlapping image area was identified in each case. The signal intensity in the selected region was measured in ImageJ, each value normalised to the starting point and expressed as % value at 2.0 min. Profile plot was obtained by plotting normalised pixel intensity against time (in minutes) (A). Area under this curve was quantified to represent leakage of the sodium fluorescein tracer (B). Data are presented as mean  $\pm$  SEM (n=3-5 animals per each time point). No significant differences between time points by Student's t test.



A



B

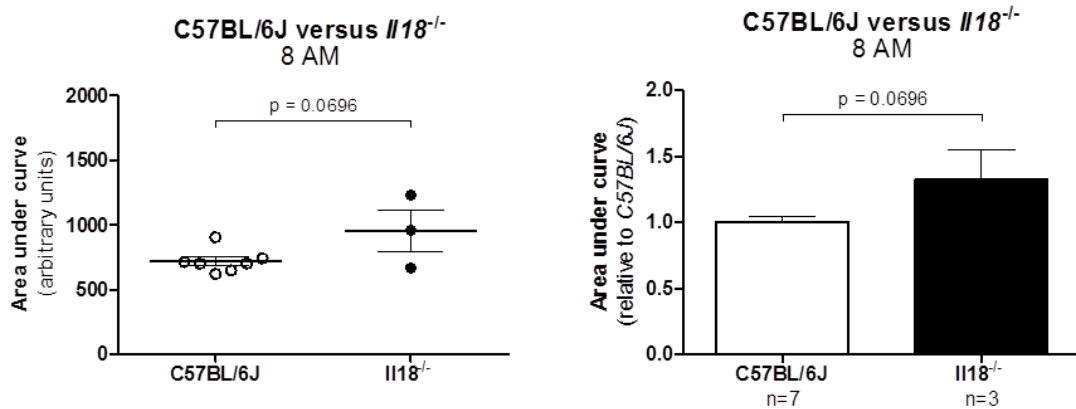
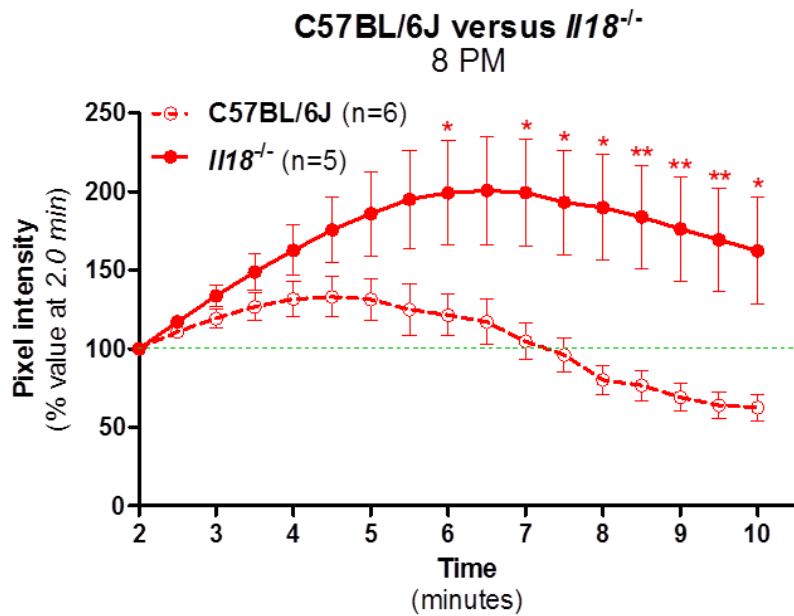


**Figure 5.15:** Effect of IL-18 on the iBRB permeability *in vivo* at 8 AM.

Dynamic FA profiles were acquired in *Il18*<sup>-/-</sup> mice or age-matched wild-type C57BL/6J mice at 8 AM. The minimum overlapping image area was identified in each case. Signal intensity in the selected region was measured in ImageJ, each value was normalised to the starting point and expressed as % value at 2.0 min. Profile plot was obtained by plotting the normalised pixel intensity against time (in minutes) (A). Area under this curve was quantified to represent leakage of the sodium fluorescein tracer (B). Data are presented as mean  $\pm$  SEM (n=3-7 animals per each strain). \*p<0.05 by Student's t test compared to C57BL/6J.

A



B

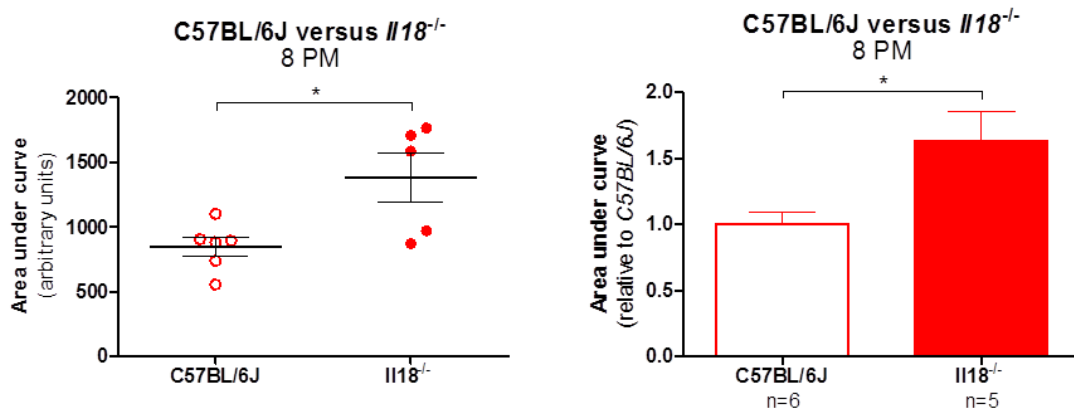


**Figure 5.16:** Effect of IL-18 on the iBRB permeability *in vivo* at 8 PM.

Dynamic FA profiles were acquired in *Il18*<sup>-/-</sup> mice or age-matched wild-type C57BL/6J mice at 8 PM. The minimum overlapping image area was identified in each case. Signal intensity in the selected region was measured in ImageJ, each value was normalised to the starting point and expressed as % value at 2.0 min. Profile plot was obtained by plotting the normalised pixel intensity against time (in minutes) (A). Area under this curve was quantified to represent leakage of the sodium fluorescein tracer (B). Data are presented as mean  $\pm$  SEM (n=5-6 animals per each strain). \*p<0.05, \*\*p<0.01 by Student's t test compared to C57BL/6J.

#### 5.2.4 The iBRB permeability cycling is under circadian control

It was reported that the tight junction protein claudin-5 contained three E-box sequences in its promoter region (Burek and Förster, 2009). As mentioned before, an E-box sequence represents a binding site for the Bmal1-Clock heterodimers as part of the core circadian gene feedback loops. To elucidate the potential role of circadian regulation in the cyclic iBRB permeability changes, the vascular leakage was investigated in *Bmal1<sup>fl/fl</sup>* Tie2-Cre<sup>+</sup> and *Bmal1<sup>wt/fl</sup>* Tie2-Cre<sup>+</sup> mice, lacking either both or only a single copy of the *Bmal1* gene, respectively, specifically in their endothelial cells.

Interestingly, the dynamic FA profiling revealed identical patterns of signal enhancement at 8 AM and 8 PM in *Bmal1<sup>fl/fl</sup>* Tie2-Cre<sup>+</sup> mice (Figure 5.17). The profile quantification produced overlapping signal intensity plots, with the peak of signal intensity occurring at 4.5 minutes at both 8 AM and 8 PM (Figure 5.18A). Correspondingly, there was no significant difference in the area under the respective curves and thus the vascular leakage (Figure 5.18B). Similar to this, the patterns of signal enhancement at 8 AM and 8 PM were comparable also in *Bmal1<sup>wt/fl</sup>* Tie2-Cre<sup>+</sup> animals (Figure 5.19). Quantified signal intensity profiles showed very little separation between 8 AM and 8 PM, with no significant differences at any time points following the fluorescein injection, although the profile plots were not completely overlapping. Like in *Bmal1<sup>fl/fl</sup>* Tie2-Cre<sup>+</sup> mice, the peak of signal intensity was also observed at 4.5 minutes in *Bmal1<sup>wt/fl</sup>* Tie2-Cre<sup>+</sup> mice at both 8 AM and 8 PM, but the overall signal intensity appeared to be slightly lower (Figure 5.20A). Furthermore, there was a modest, non-significant, increase of about 9% in the area under the curve at 8 PM (Figure 5.20B). To evaluate the effect of *Bmal1* gene copy number on the permeability changes, the signal intensity profiles at 8 AM and 8 PM were directly compared between *Bmal1<sup>fl/fl</sup>* Tie2-Cre<sup>+</sup> and *Bmal1<sup>wt/fl</sup>* Tie2-Cre<sup>+</sup> mice. Although the signal intensity was significantly increased up to 5.5 minutes after the fluorescein injection at 8 AM in *Bmal1<sup>fl/fl</sup>* Tie2-Cre<sup>+</sup> animals (Figure 5.21A), suggesting that vascular leakage might be increased, this was not reflected by a significant difference in the area under the curve (Figure 5.21B). At 8 PM, the signal intensity profiles of both genotypes were virtually identical (Figure 5.22A), with equal areas under the respective curves (Figure 5.22B). In summary, these results propose that the iBRB permeability cycling is under circadian control of the *Bmal1* gene expressed in endothelial cells, with the loss of one copy of the gene being sufficient to reduce, if not completely prevent, the changes in vascular leakage at 8 AM and 8 PM.

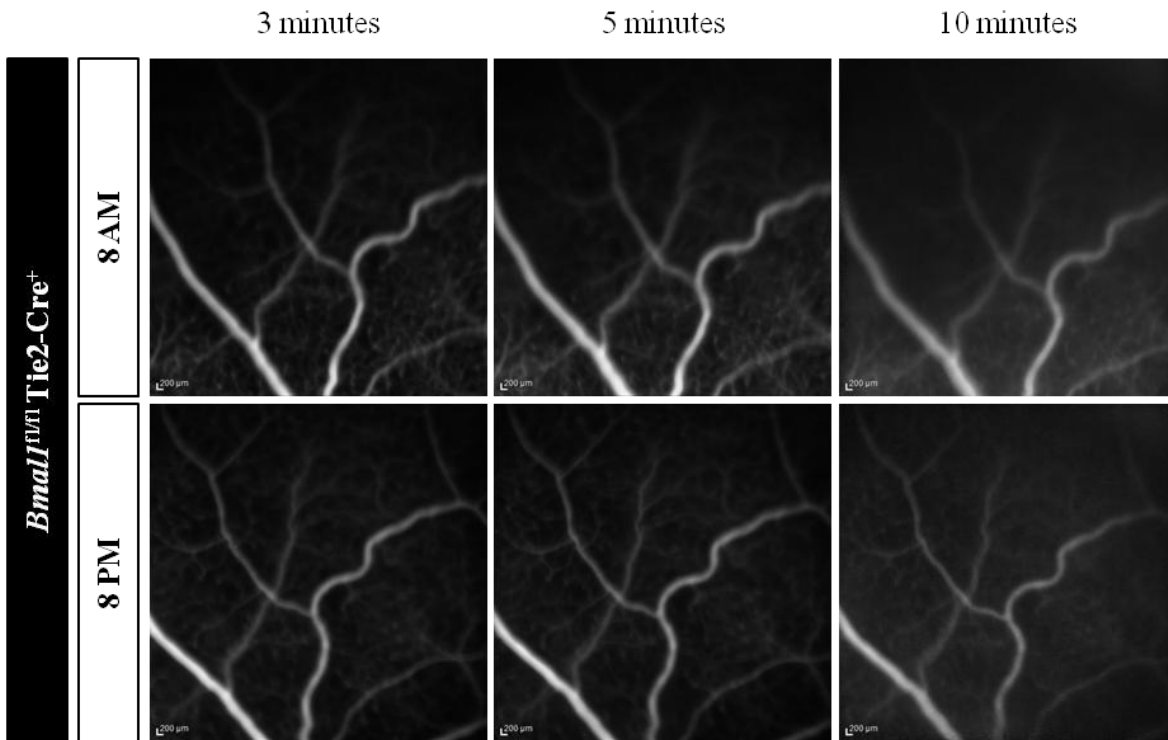


**Figure 5.17:** Partial dynamic FA profiles *in vivo* in *Bmal1<sup>fl/fl</sup>* Tie2-Cre<sup>+</sup> mice at 8 AM and 8 PM.

Representative partial dynamic FA profiles of *Bmal1<sup>fl/fl</sup>* Tie2-Cre<sup>+</sup> mice obtained at 8 AM and 8 PM, respectively, are presented. Mice were injected (i.p.) with sodium fluorescein (100 mg/kg body weight) and FA images acquired at regular intervals (every 30 seconds) at 2-10 minutes post injection. Images captured at 3, 5 and 10 minutes after the injection are shown.

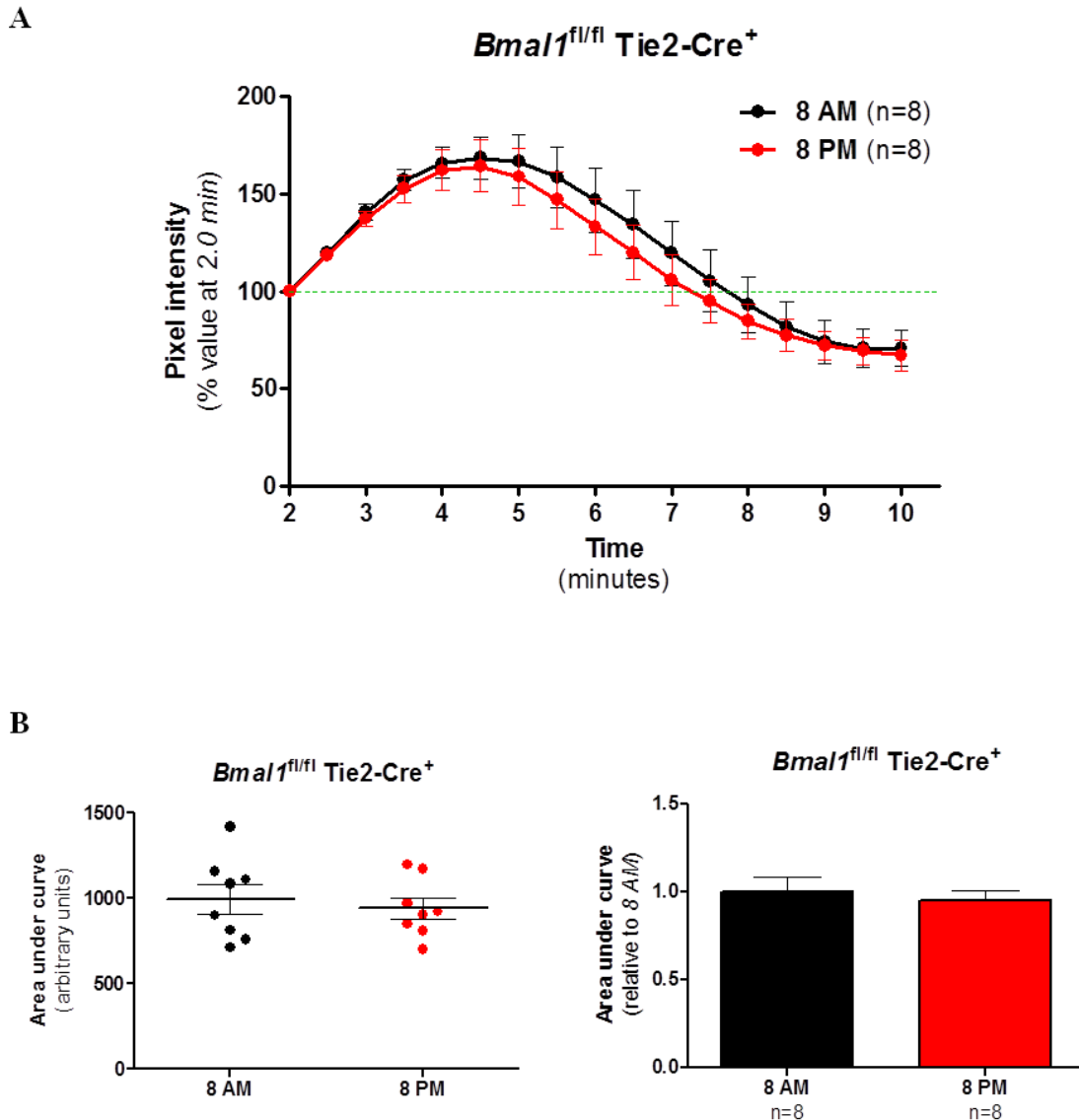


**Figure 5.18:** The iBRB permeability *in vivo* in *Bmal1<sup>fl/fl</sup> Tie2-Cre<sup>+</sup>* mice at 8 AM versus 8 PM.

Dynamic FA profiles were acquired in *Bmal1<sup>fl/fl</sup> Tie2-Cre<sup>+</sup>* mice at 8 AM or 8 PM. The minimum overlapping image area was identified in each case. The signal intensity in the selected region was measured in ImageJ, each value normalised to the starting point and expressed as % value at 2.0 min. Profile plot was obtained by plotting normalised pixel intensity against time (in minutes) (A). Area under this curve was quantified to represent leakage of the sodium fluorescein tracer (B). Data are presented as mean  $\pm$  SEM (n=8 animals per each time point). No significant differences between time points by Student's t test.

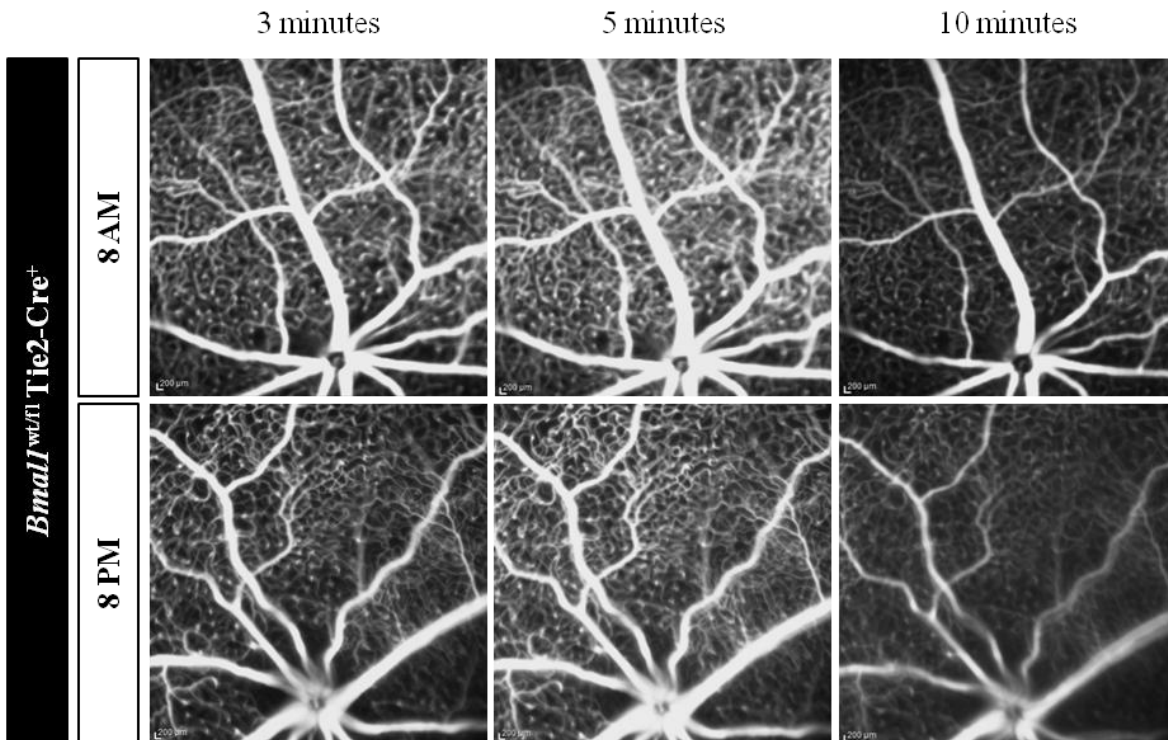


**Figure 5.19:** Partial dynamic FA profiles *in vivo* in *Bmal1<sup>wt/fl</sup>* Tie2-Cre<sup>+</sup> mice at 8 AM and 8 PM.

Representative partial dynamic FA profiles of *Bmal1<sup>wt/fl</sup>* Tie2-Cre<sup>+</sup> mice obtained at 8 AM and 8 PM, respectively, are presented. Mice were injected (i.p.) with sodium fluorescein (100 mg/kg body weight) and FA images acquired at regular intervals (every 30 seconds) at 2-10 minutes post injection. Images captured at 3, 5 and 10 minutes after the injection are shown.

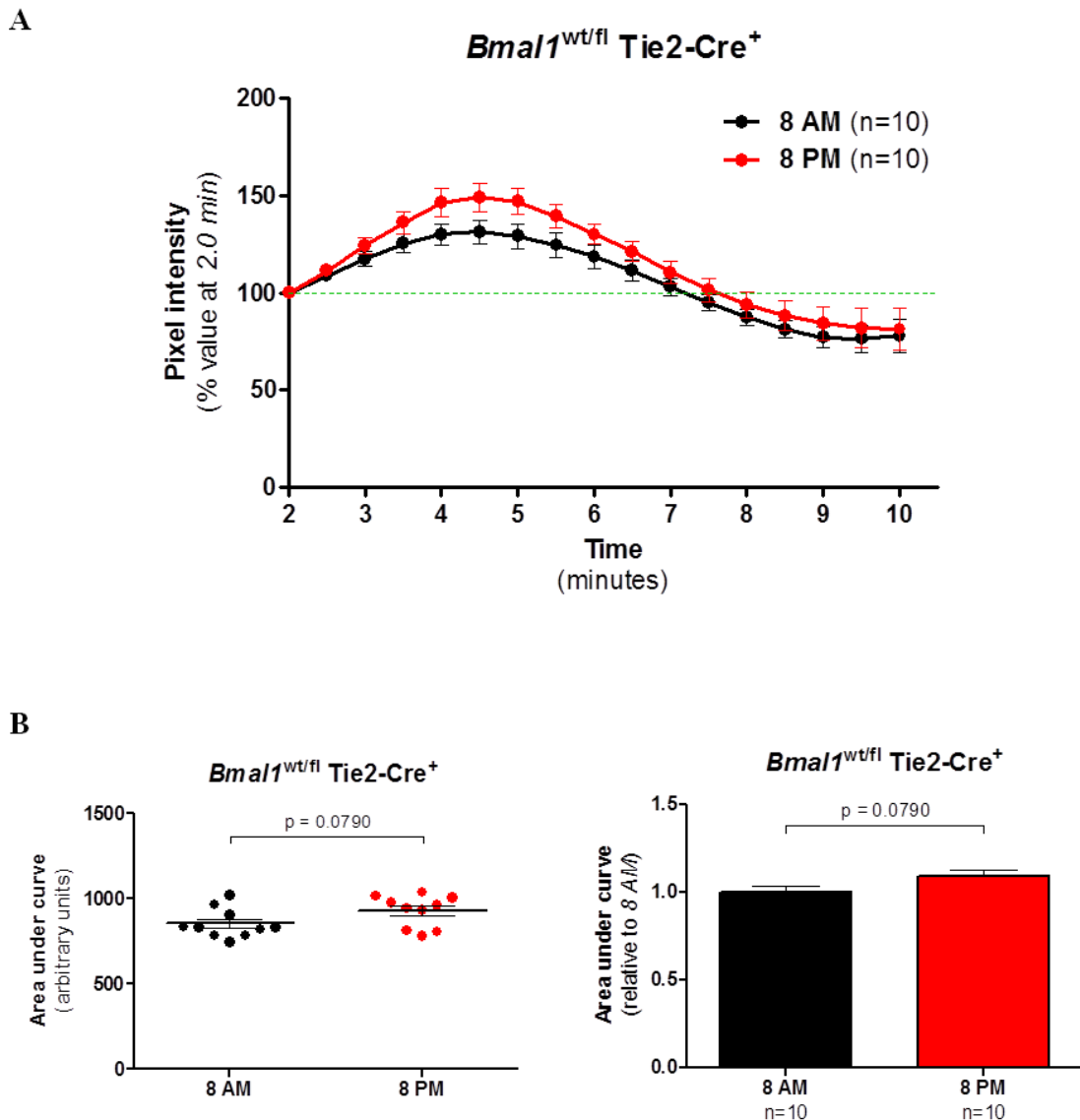
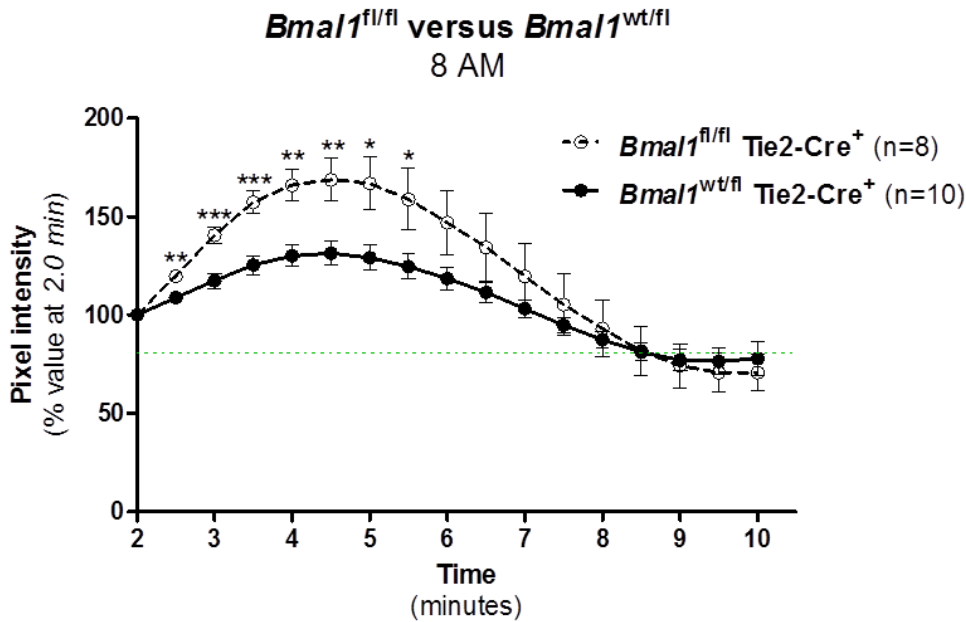


**Figure 5.20:** The iBRB permeability *in vivo* in *Bmal1*<sup>wt/fl</sup> Tie2-Cre<sup>+</sup> mice at 8 AM versus 8 PM.

Dynamic FA profiles were acquired in *Bmal1*<sup>wt/fl</sup> Tie2-Cre<sup>+</sup> mice at 8 AM or 8 PM. The minimum overlapping image area was identified in each case. The signal intensity in the selected region was measured in ImageJ, each value normalised to the starting point and expressed as % value at 2.0 min. Profile plot was obtained by plotting normalised pixel intensity against time (in minutes) (A). Area under this curve was quantified to represent leakage of the sodium fluorescein tracer (B). Data are presented as mean  $\pm$  SEM (n=10 animals per each time point). No significant differences between time points by Student's t test.

A



B

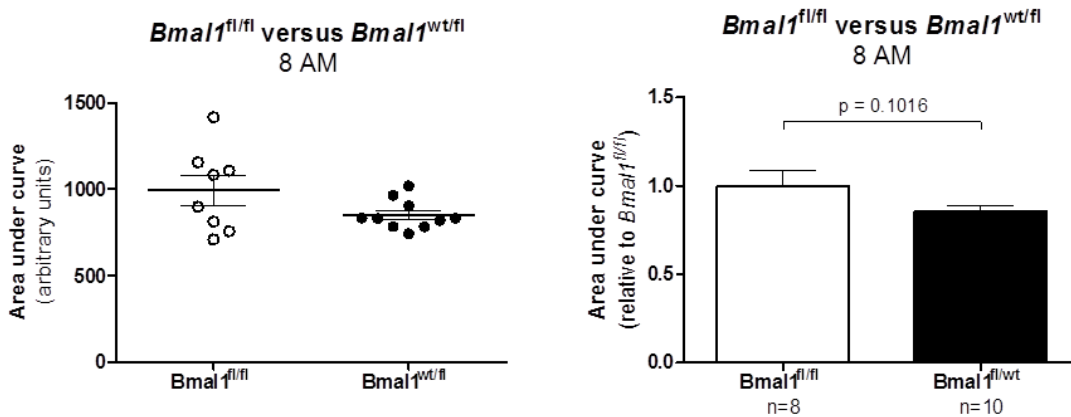
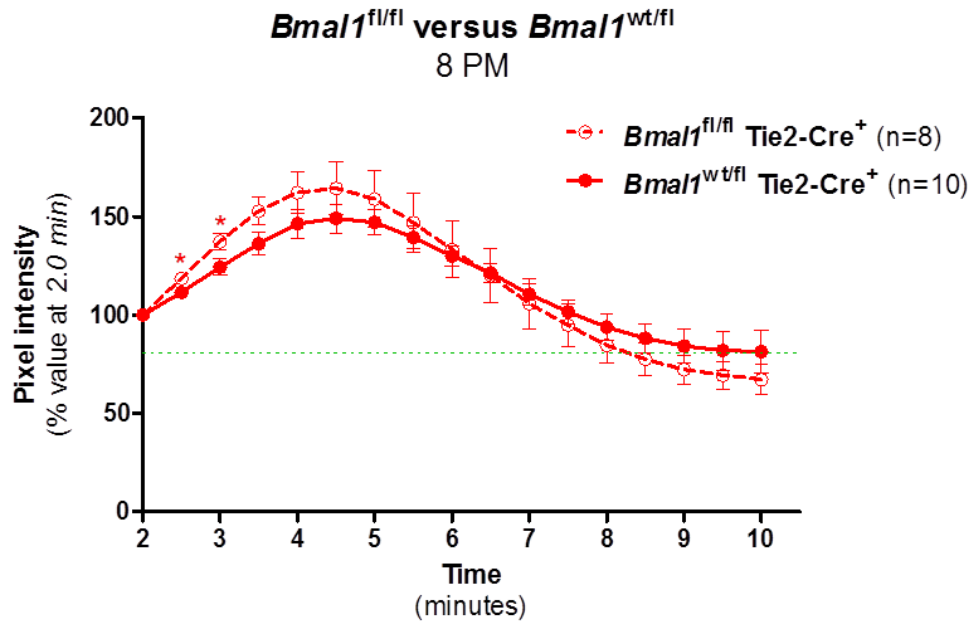


**Figure 5.21:** Effect of *Bmal1* gene copy number on iBRB permeability *in vivo* at 8 AM. Dynamic FA profiles were acquired in *Bmal1*<sup>fl/fl</sup> Tie2-Cre<sup>+</sup> mice or age-matched *Bmal1*<sup>wt/fl</sup> Tie2-Cre<sup>+</sup> at 8 AM. The minimum overlapping image area was identified in each case. The signal intensity in the selected region was measured in ImageJ, each value normalised to the starting point and expressed as % value at 2.0 min. Profile plot was obtained by plotting normalised pixel intensity against time (in minutes) (A). Area under this curve was quantified to represent leakage of the sodium fluorescein tracer (B). Data are presented as mean  $\pm$  SEM (n=8-10 animals per each genotype). \*p<0.05, \*\*p<0.01, \*\*\*p<0.001 by Student's t test compared to *Bmal1*<sup>wt/fl</sup> Tie2-Cre<sup>+</sup>.



A



B

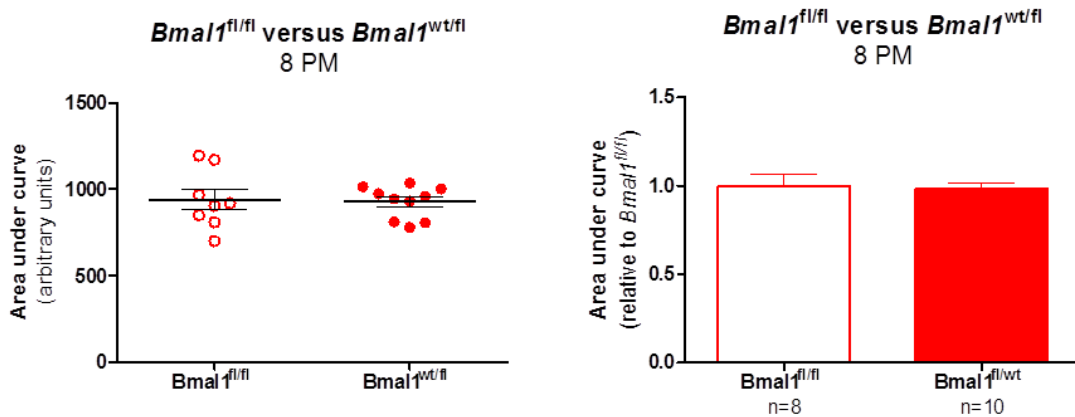


**Figure 5.22:** Effect of *Bmal1* gene copy number on iBRB permeability *in vivo* at 8 PM. Dynamic FA profiles were acquired in *Bmal1*<sup>fl/fl</sup> Tie2-Cre<sup>+</sup> mice or age-matched *Bmal1*<sup>wt/fl</sup> Tie2-Cre<sup>+</sup> at 8 PM. The minimum overlapping image area was identified in each case. The signal intensity in the selected region was measured in ImageJ, each value normalised to the starting point and expressed as % value at 2.0 min. Profile plot was obtained by plotting normalised pixel intensity against time (in minutes) (A). Area under this curve was quantified to represent leakage of the sodium fluorescein tracer (B). Data are presented as mean ± SEM (n=10 animals per each time point). \*p<0.05 by Student's t test compared to *Bmal1*<sup>wt/fl</sup> Tie2-Cre<sup>+</sup>.

### 5.3 Discussion

Based on previous results showing that the RPE underwent periodic changes in its activity that could affect the production of VEGF and/or other local factors, the iBRB permeability was examined *in vitro* and *in vivo*. The role of VEGF as an inducer of ocular angiogenesis and vascular leakage has been extensively described in the literature (reviewed in Klaassen et al., 2013). For instance, it is known to down-regulate the expression of tight junction proteins and promote their phosphorylation followed by ubiquitination, internalisation and degradation of junctional complexes. Furthermore, it also increases transcellular vesicular transport *in vitro* and *in vivo*, which contributes to the VEGF-induced iBRB permeability (Feng et al., 1999a; Feng et al., 1999b; Hofman et al., 2000). In line with these reports, it was observed that VEGF treatment could significantly impair barrier properties *in vitro*, by decreasing the electrical resistance of endothelial cells cultured on permeable membrane supports. The earliest significant changes were detected after 12 hours of VEGF treatment, corresponding to the time required for the VEGF-induced signal transduction cascade to go to completion and modulate cell function. In addition, VEGF administration to either the apical or basolateral surface of the endothelial cell monolayer had comparable effects on the electrical resistance, pointing towards an equal distribution of VEGFRs on both sides of polarised endothelial cells. This is unlike observations by Hudson et al. (2014), who reported a highly polarised VEGFR distribution, resulting in differential apicobasal VEGF signalling. However, their studies relied on the use of primary brain endothelial cells which may better reflect physiological endothelial barrier properties compared to the bEnd.3 cell line representing a rather limited model of vascular blood-neural barriers as these cells might never achieve a complete polarisation to acquire barrier characteristics comparable with primary cells. Moreover, whether the observed changes in electrical resistance were reflected by some other functional outcomes, such as increased paracellular permeability to solutes, was not examined in the present study. Similarly, the role of transcellular transport in the VEGF-induced reduction in barrier properties of cell monolayers was not addressed. Nonetheless, VEGF treatment was found to down-regulate the expression of tight junction proteins claudin-5 and ZO-1, with no detectable effects on occludin. Despite the decrease in claudin-5 levels not reaching statistical significance, it is necessary to point out the outlier in lane 1 which, if not taken into consideration during data analysis, would give rise to a much more convincing reduction of around 50% in claudin-5 at both time points examined, matching more closely the pattern of ZO-1 expression. In addition, the observed decrease in tight junction protein levels seemed to be transient, as ZO-1 showed maximum down-regulation at 12 hours, but appeared to slowly increase at 24 hours. Thus, to reliably

establish the time when the expression levels of these tight junction proteins would return back to baseline (if at all), an extended duration of VEGF treatment would be required. Occludin levels were not affected by VEGF exposure under given experimental conditions, although its expression was quite variable. However, different tight junction proteins might follow different kinetics of their response to growth factors, such as VEGF. Therefore, a longer treatment would once again be necessary to confirm whether VEGF indeed had no effects on occludin or whether down-regulation of occludin was delayed and occurred after the initial claudin-5 and ZO-1 decrease or was in fact dependent on the down-regulation of these. Moreover, the exact mechanism by which VEGF reduced the tight junction protein expression in this case is not clear. mRNA levels would need to be analysed to determine whether VEGF regulated tight junctions at the transcriptional level or exerted its effects by controlling protein stability through the various post-translational modifications causing their removal from a functional junctional complex at the plasma membrane followed by their degradation. Nonetheless, these results suggest that the VEGF-induced changes in electrical resistance *in vitro* are mediated by decreased claudin-5 and ZO-1 levels.

The iBRB permeability *in vivo* was found to cycle periodically during the day, increasing in the evening, with the barrier tightness corresponding to the phagocytically active period of the RPE in the morning. Furthermore, these changes did not depend on the age of an animal and were observed universally across three wild-type mouse strains, including the CD1 albino mice. In their case, however, the effects were less pronounced and associated with a much slower signal clearance attributable to the lack of RPE pigmentation in these animals, leading to increased light scattering and signal interference from the choroid. Additional data suggested that these functional changes in the iBRB permeability were accompanied, at the molecular level, by decreased expression of tight junction proteins in the evening (especially claudin-5), were reflected by increased extravasation of biotin into deeper retinal layers at 8 PM and were supported at the ultrastructural level by electron microscopy. The detailed mechanism of this physiological regulation of tight junctions, however, needs to be further investigated. As previously alluded to, tight junctions can be rapidly modified by multiple local factors. Importantly, the phagocytically active period of the RPE in the morning has been associated with inflammasome formation and subsequent IL-18 release. IL-18 in turn has been shown to regulate VEGF production *in vitro* and *in vivo* as well as directly increase the tight junction protein expression in endothelial cells. In line with these observed barrier-modulating properties of IL-18, increased vascular leakage was detected in *IL18<sup>-/-</sup>* mice compared to age-matched controls at 8 AM and even more so at 8 PM, suggesting that the iBRB permeability could be, at least to some extent, mediated

by IL-18. However, whether IL-18 exerted its effects directly by control of tight junction formation or indirectly via its regulation of VEGF and/or other factors was not determined. Nonetheless, IL-18 had no effect on the periodic iBRB permeability cycling. Moreover, the assembly of an inflammasome alone has been proposed to be sufficient to decrease VEGF secretion by the RPE *in vitro* (Mohr et al., 2015). To address the role of the inflammasome complex in the regulation of the iBRB permeability, a similar set of experiments could be performed in *Asc*<sup>-/-</sup> and *Nlrp3*<sup>-/-</sup> mice. Furthermore, the retinal levels of IL-18, VEGF and possibly other factors would need to be analysed in order to provide further evidence of their involvement in the control of vascular leakage. In addition, the role of pericytes and glial cells, that form a part of the NVU supporting the function of endothelial cells, tight junction formation and the maintenance of the iBRB integrity, could be explored.

As mentioned before, many functions throughout the body are controlled by circadian rhythms driven by feedback loops of the core circadian genes. *Bmal1* is a transcription factor that binds to E-box sequences of other core circadian genes as well as a number of circadian clock-regulated genes to initiate their expression. Interestingly, the claudin-5 promoter region was found to contain three E-box sequences (Burek and Förster, 2009), indicating that claudin-5 could be under a direct control of the circadian clock. Consistent with this, it was observed that a complete lack of *Bmal1* in endothelial cells prevented the periodic iBRB permeability cycling as the differences in vascular leakage between 8 AM and 8 PM were no longer detected in *Bmal1*<sup>fl/fl</sup> Tie2-Cre<sup>+</sup> mice. Moreover, a loss of only one copy of the *Bmal1* gene was sufficient to substantially reduce, if not entirely stop, the cycling. As the permeability changes have been suggested to be facilitated by regulation of tight junction protein expression, it seems likely that *Bmal1* can directly control the tight junction transcription (or at least claudin-5). However, this would require further evidence of a direct binding of *Bmal1* to the claudin-5 gene promoter as well as the analysis of tight junction protein and mRNA expression in *Bmal1*<sup>fl/fl</sup> Tie2-Cre<sup>+</sup> and *Bmal1*<sup>wt/fl</sup> Tie2-Cre<sup>+</sup> animals. In addition, a direct comparison of vascular leakage in *Bmal1*<sup>fl/fl</sup> Tie2-Cre<sup>+</sup> and *Bmal1*<sup>wt/fl</sup> Tie2-Cre<sup>+</sup> animals at 8 AM and 8 PM to evaluate the effect of the *Bmal1* gene copy number demonstrated no significant differences in the vascular permeability, though a modest increase in signal intensity was observed in *Bmal1*<sup>fl/fl</sup> Tie2-Cre<sup>+</sup> mice at 8 AM. Based on these results, a model of the physiological regulation of the iBRB permeability in retinal homeostasis could be proposed whereby tight junction (most importantly claudin-5) expression at the transcriptional level is under the circadian control of a local pacemaker in endothelial cells, with the barrier properties being further modulated by local factors, such

as VEGF and IL-18, most likely through regulating the post-translational modifications affecting the stability of the junctional complexes.

The main conclusions inferred from experiments presented in this section are as follows:

- VEGF decreases endothelial electrical resistance *in vitro*
- VEGF decreases tight junction protein expression in endothelial cells *in vitro*
- the iBRB permeability cycles periodically *in vivo*, increasing at 8 PM
  - these changes were independent of the animal age
  - these changes were universally observed across several different mouse strains
- IL-18 regulates the iBRB permeability *in vivo* without affecting the cycling
- the periodic cycling of the iBRB permeability is under circadian control

## Chapter 6

### **General discussion and future perspectives**

## 6 GENERAL DISCUSSION AND FUTURE PERSPECTIVES

---

### 6.1 Therapeutic potential of IL-18 in neovascular AMD

Neovascular (wet) AMD affects around 10-15% of all AMD patients and is characterised by an acute vision loss due to CNV. The current therapies targeting VEGF bioactivity have proven highly efficient in the disease treatment over the past years. However, they rely on regular intraocular injections that can be both uncomfortable for the patient and may be accompanied by severe side effects (CATT Research Group et al., 2011). Previous studies from our lab demonstrated that the NLRP3 inflammasome and its effector cytokine IL-18 had a protective role in a mouse model of wet AMD (Doyle et al., 2012). In addition, direct exogenous administration of mature recombinant IL-18 attenuated the development of experimental laser-induced CNVs and enhanced the effects of anti-VEGFs (Doyle et al., 2014). This suggested that IL-18 might represent a novel therapeutic strategy, used either alone or as a combination therapy with anti-VEGFs, and may be of a particular benefit for patients who do not respond to the current treatment.

Utilising a new genetic mouse model of spontaneous neovascularisation, the JR5558 strain, to further evaluate the therapeutic potential of IL-18, the results presented herein provide evidence that IL-18 could indeed be considered as an alternative approach to the treatment of wet AMD. Systemic IL-18 administration was efficient to prevent both progression of developing neovascular lesions in this animal model, as well as enhance regression of the fully established ones. Based on the results from mouse models, a tolerability and efficacy study in non-human primates (cynomolgus monkeys, *Macaca fascicularis*) was initiated in collaboration with GSK for the use of intravitreally administered clinical grade human IL-18 (SB-485232) in a laser-induced model of neovascular AMD. IL-18 showed a very clear activity in reducing leakage from grade IV CNV lesions, even though its effects were not as pronounced as those of Lucentis<sup>®</sup> (ranibizumab), one of the currently used anti-VEGFs (Doyle et al., 2015).

In line with previously published reports (Doyle et al., 2012; Shen et al., 2014), the results presented in this study suggest that IL-18 exerts its anti-angiogenic and anti-permeability properties, in part, via decreasing the rate of VEGF production by the RPE. Moreover, this might be mediated post-transcriptionally as IL-18 treatment was shown to have no effect on VEGF-A mRNA expression *in vitro*. Interestingly, IL-18 could decrease the expression levels, both mRNA and protein, of VEGFR2 in retinal endothelial cells, without affecting VEGFR1 or VEGFR3 (Doyle et al., 2015). Therefore, in conjunction with lowering levels of secreted VEGF, the ability of IL-18 to reduce VEGFR2 expression in parallel indicates

that IL-18 could effectively interfere with the VEGF signal transduction cascade and hence the capacity of endothelial cells to respond in a pro-angiogenic manner to any remaining VEGF. Furthermore, as the current therapies target and block the VEGFR2 specifically, it can be speculated that the enhanced effects of anti-VEGFs when used in combination with IL-18, as observed by Doyle et al. (2014), are facilitated by the ability of IL-18 to decrease VEGFR2 expression, thus reducing the number of available targets for anti-VEGFs and rendering them more effective. In addition, it was demonstrated that IL-18 could promote the wound-healing process in the RPE as well as directly regulate levels of tight junction proteins in endothelial cells.

Importantly, additional evidence is provided to confirm that IL-18 does not cause RPE cell degeneration and death *in vitro* or *in vivo*. This was also supported by observations in the non-human primate model, in which RPE cells maintained their characteristic honeycomb structure, with no evidence of cellular dysmorphia after exposure to IL-18. No toxic effects to either the retina or the RPE were associated with IL-18 administration and there were no signs of apoptotic (blebbing cells) or necrotic (swollen cells) phenotypes in any cell type. Similarly, histopathologic assessment of monkey retinal sections following IL-18 injection revealed no abnormalities (Doyle et al., 2015).

Interestingly, patients with certain autoinflammatory diseases, including systemic juvenile idiopathic arthritis and adult-onset Still's disease, are distinguished by unusually elevated serum levels of IL-18. They typically suffer from fevers, skin rashes, arthritis, adenopathy (large or swollen lymph nodes) and organomegaly (abnormal enlargement of organs), and can develop a life-threatening hyperinflammatory state known as macrophage activation syndrome. However, AMD is not a prominent feature of these diseases and patients do not routinely receive retinal screening. In their recent report, Canna et al. (2017) propose that chronic IL-18 exposure in the context of systemic inflammation does not act as a potent inducer of RPE toxicity or aberrant choroidal vascular homeostasis, which could promote macular degeneration and lead to CNV development, respectively. They carried out an extensive ophthalmic evaluation to screen for subclinical pathology in a group of patients with chronic massive elevation of serum IL-18 and observed no adverse effects on the patients' visual abilities. None of the patients were found to have retinal abnormalities or drusen, their retinas appeared healthy and all ophthalmic examinations were documented to be normal. Thus, despite being systemically exposed to very high IL-18 levels for multiple years, there was no evidence of retinal pathology in these patients, which provided further reassurance against the potentially toxic effects of IL-18 and supported the idea that the use of exogenous IL-18 to treat ophthalmologic conditions might be well-tolerated. In addition,



the AMD prevalence was shown to decrease among patients with other diseases associated with increased IL-18 levels, such as rheumatic disease and uveitis (McGeer and Sibley, 2005; Fox et al., 2017).

Taken together, all these results provide strong evidence that IL-18 can be considered as a safe and relatively effective intravitreal immunotherapy for the treatment of wet AMD that could be used alongside the current therapeutic approaches. Human IL-18 (SB-485232, GSK) is a clinically enabled investigational drug that has been administered systemically in more than 170 patients with various types of advanced cancer. It has been well-tolerated at biologically active doses and some common side effects included chills, fever, headache, fatigue, nausea and hypotension (Herzyk et al., 2003; Robertson et al., 2006; Robertson et al., 2008; Srivastava et al., 2010; Robertson et al., 2013; Simpkins et al., 2013; Robertson et al., 2018). However, despite having an excellent safety profile in numerous clinical trials as a systemic infusion, IL-18 has never been tested as a direct intravitreal injection for any ocular condition. Thus, before it can be translated to clinic, it first needs to be enabled for intraocular administration in human subjects. Nonetheless, clinical deployment of IL-18 for neovascular AMD has the potential to lead to a new adjuvant immunotherapy-based strategy and as a small biotherapeutic agonist could eventually pave the way for a slow release encapsulated treatment for this severe form of central blindness.

## **6.2 A novel link between POS phagocytosis and inflammasome activation in the RPE**

The RPE is metabolically a highly active tissue that serves many important roles in order to maintain a healthy ocular microenvironment and retinal homeostasis. Most importantly, the proper visual function of retinal photoreceptors is critically dependent on the support provided by healthy RPE layer. In recent years, components of the NLRP3 inflammasome complex and its effector cytokines have been detected in and around the RPE of patients with both dry and wet AMD. However, whether their presence implies a causative role in AMD development and/or progression has not been satisfactorily confirmed. In addition, their role in the normal RPE homeostasis is unknown.

The present study provides evidence of a complex relationship that exists inside the RPE between POS phagocytosis and inflammasome activation. Unlike immune cells, in which autophagy has been proposed to be a negative regulator of the inflammasome formation, activation of the inflammasome complex in RPE cells seems to go in hand with the POS phagocytosis-related autophagy induction. However, additional experiments are necessary to further examine the details of this complex crosstalk between the POS phagocytosis and inflammasome assembly. Apart from mimicking the *in vivo* situation by POS treatment of

hfRPE cells, autophagy can be initiated by pharmacological intervention and the response of the inflammasome complex can be further evaluated. Utilising genetically modified animals with a systemic and/or RPE-specific lack of the inflammasome components and/or autophagy machinery might allow to study the interdependence of the two processes.

Furthermore, the functional relevance of the inflammasome complex assembly in the RPE in response to the POS phagocytosis requires further investigations. As suggested in the present study, the POS phagocytosis, autophagy induction and inflammasome activation might function as important regulators of VEGF secretion by the RPE. This could in turn have an effect on the local microenvironment in the retina as well as stabilisation of the underlying choroid, thus regulating functions of the neighbouring cell types. It is also well established that only a single inflammasome complex can form in a cell at any given time (Fernandes-Alnemri et al., 2007). This is mainly caused by the large size of the assembled inflammasome (Cai et al., 2014; Lu et al., 2014), which could take up as much as one tenth of an RPE cell volume. Thus, the effects of the inflammasome formation on the function and maintenance of the oBRB integrity warrant further exploration. It could be speculated that potential weakening of its barrier properties due to the presence of such a big complex might facilitate export of degraded waste products derived from processing of ingested POSs and/or allow transient paracellular delivery of essential blood-borne material to the retina.

Importantly, a central role for caspases has previously been proposed in the interplay of complex pathways, including autophagy, apoptosis and inflammasome. RPE cells were found to express caspase-1, -3 and -8 at different levels and their expression changed in response to the POS phagocytosis. Therefore, it can be hypothesised that some form of a caspase switch might exist in the RPE, potentially regulating the cell metabolic functions and/or directing the cell fate towards different types of death once a certain intracellular threshold level is reached. Clearly, this represents a promising new avenue of studying the mechanism(s) underlying the development and progression of AMD and could be easily explored in a number of available animal models of the disease.

### **6.3 Circadian regulation of the iBRB permeability in retinal homeostasis**

The inner retinal microvasculature serves the essential role of supplying nutrients to the inner layers of the retina. The blood flow through these vessels is autoregulated by local factors to meet the varying metabolic requirements of different cell types, most importantly the retinal neurons. To protect the delicate tissue of the retina from blood-borne toxicity and maintain homeostasis of the neuronal microenvironment, tight junctions have evolved

between endothelial cells lining the inner retinal blood vessels to regulate the paracellular transport and form the iBRB. The barrier permeability and breakdown of its integrity have been extensively studied in relation to retinal pathology and were found to be controlled by many disease-associated factors that can directly or indirectly influence the formation of tight junctions. Down-regulation and/or degradation of tight junctions by such agents is known to cause reversible or irreversible opening of the intercellular spaces, leading to the leakage of fluids and harmful blood components, which can subsequently result in retinal oedema and neuronal cell death. Therefore, the iBRB has been considered to act as a "brick wall", preventing any substances in the systemic circulation from entering the vulnerable environment of the retina. However, details of the physiological regulation of its barrier properties and permeability in normal retinal homeostasis are poorly understood.

The results presented in this study provide a novel insight into the iBRB permeability control mechanism and suggest that, rather than a "brick wall", the iBRB is physiologically a very dynamic structure characterised by periodic changes of its barrier properties in order to maintain retinal homeostasis. Importantly, this barrier permeability cycling represents a universal phenomenon in mice and was observed across multiple strains. Clearly, it would be interesting to explore whether these findings could translate in a similar way into other species and/or apply to humans. Moreover, the exact functional relevance of the observed periodic changes in barrier properties remains to be elucidated. It could be speculated that this cyclic modulation of the iBRB might be required for the maintenance of normal retinal function, allowing selective passage of substances from the blood to the retina at specific times of the day as necessary. For example, the mechanism of POS disc renewal is still not fully understood. POSs are composed primarily of triglycerides and cholesterol which are not naturally produced in the retina. Thus, it could be hypothesised that the regulated time-specific iBRB opening might be crucial to provide material required in the replenishment process. In addition, the iBRB represents a significant impediment to successful delivery of therapeutics to the retina. Therefore, these results might have major clinical implications for drug delivery and development of novel treatment strategies for ocular diseases. Proper timing of the therapeutic administration in coordination with the barrier permeability could significantly increase delivery of systemically-administered drugs to the retina and enhance treatment efficacy in many retinal diseases.

Based on the findings of the present study, a model of the physiological iBRB regulation was proposed, suggesting that the periodic iBRB permeability cycling is under the control of a local circadian oscillator which exists in endothelial cells and the barrier properties can be further modulated by local factors present in the retina at specific times of the day, such

as IL-18 and VEGF. Interestingly, a relationship between circadian rhythms and vascular function is not an entirely new concept, as melanopsin has recently been shown to mediate the light-dependent relaxation of blood vessels (Sikka et al., 2014). Circadian rhythms are well-known to regulate a number of biochemical, physiological and behavioural functions throughout the body and are intertwined with most cellular metabolic processes. Although the daily iBRB permeability changes observed in the present study were not affected by animal age, it is generally accepted that there is a decline in circadian rhythms with aging, concomitant with disturbances of the overall metabolic tissue homeostasis. The reasons of this, however, remain unknown (Tevy et al., 2013). Nevertheless, it would imply that the circadian control of the iBRB permeability would deteriorate with increasing age, stopping the natural cycling in barrier properties. As a result, this could lead to a permanent opening of the iBRB and a subsequent leakage of blood components into the retina disrupting the local homeostasis. Interestingly, it has been proposed that the decline in circadian rhythms might underlie the pathology associated with age-related diseases. As described before, AMD is the leading cause of central vision loss and blindness in the elderly, with age being the major risk factor for disease development. In addition, several environmental factors, such as cigarette smoking and unhealthy diet, have also been implicated in its progression. Thus, it seems plausible that a decrease in circadian control of the iBRB permeability due to advanced age, combined with increased vascular leakage of harmful blood components known to promote oxidative stress, may induce retinal damage as observed in AMD. To this end, several animal models have been established and are currently under evaluation. Generally, they combine RNAi technology to down-regulate expression of a tight junction component claudin-5 with dietary intervention, feeding the animals cholesterol-enriched high-fat diet. One approach relies on the subretinal administration of adeno-associated viral (AAV) vectors to deliver claudin-5 siRNA to the retina, leading to locally reduced claudin-5 levels at the injection site accompanied by increased vascular leakage. Alternatively, a novel, recently-described, inducible endothelial cell-specific claudin-5 knockdown mouse model has been utilised, causing a widespread endothelial claudin-5 down-regulation and increased iBRB permeability throughout the retina (Greene et al., 2017). Both models mimicked the pathology observed in dry AMD and were associated with accumulation of cholesterol in the RPE. Nonetheless, the latter provides more experimental flexibility as it allows for controlled, reversible, tissue-specific suppression of claudin-5 and can be used to characterise not only the terminal stages of geographic atrophy, but also to investigate the early changes leading to disease development. Moreover, it provides the advantage of easier manipulation to study any potential treatment interventions. Despite this, they both

represent novel models of geographic atrophy that reflect, in a more physiological way, the pathology associated with dry AMD. Furthermore, re-introducing the rhythmicity to the iBRB permeability regulation appears to be a reasonable strategy to treat dry AMD and/or other age-related diseases and new approaches are being developed at the moment in order to provide a potential therapy for geographic atrophy, especially considering the current limited availability of treatments for dry AMD.

## **References**

## REFERENCES

---

- Abbas, A.K., Lichtman, A.H. & Pillai, S. 2010. *Cellular and Molecular Immunology* (updated 6th ed.) (Saunders Elsevier).
- Abbott, N.J. 2002. Astrocyte-endothelial interactions and blood-brain barrier permeability. *J Anat*, 200(6), 629-638.
- Abbott, N.J., Rönnbäck, L. & Hansson, E. 2006. Astrocyte-endothelial interactions at the blood-brain barrier. *Nat Rev Neurosci*, 7(1), 41-53.
- Access Economics. 2010. The global economic cost of visual impairment. Available online: <http://www.icoph.org/resources/146/The-Global-Economic-Cost-of-VisualImpairment.html> (accessed on 17 September 2014).
- Age-Related Eye Disease Study Research Group. 2000. Risk factors associated with age-related macular degeneration. A case-control study in the age-related eye disease study: Age-related eye disease study report number 3. *Ophthalmology*, 107(12), 2224-2232.
- Ahnelt, P. & Kolb, H. 1994a. Horizontal cells and cone photoreceptors in primate retina: a Golgi-light microscopic study of spectral connectivity. *J Comp Neurol*, 343(3), 387-405.
- Ahnelt, P. & Kolb, H. 1994b. Horizontal cells and cone photoreceptors in human retina: a Golgi-electron microscopic study of spectral connectivity. *J Comp Neurol*, 343(3), 406-427.
- Ajami, B., Bennett, J.L., Krieger, C., Tetzlaff, W. & Rossi, F.M. 2007. Local self-renew can sustain CNS microglia maintenance and function throughout adult life. *Nat Neurosci*, 10(12), 1538-1543.
- Akuffo, K.O., Nolan, J., Stack, J., Moran, R., Feeney, J., Kenny, R.A., Peto, T., Dooley, C., O'Halloran, A.M., Cronin, H. & Beatty, S. 2015. Prevalence of age-related macular degeneration in the Republic of Ireland. *Br J Ophthalmol*, 99(8), 1037-1044.
- AMD Gene Consortium. 2013. Seven new loci associated with age-related macular degeneration. *Nat Genet*, 45(4), 433-439.
- Ames, A. 3rd, Li, Y.Y., Heher, E.C. & Kimble, C.R. 1992. Energy metabolism of rabbit retina as related to function: high cost of Na<sup>+</sup> transport. *J Neurosci*, 12(3), 840-853.
- Anand-Apte, B. & Hollyfield, J.G. 2010. Developmental anatomy of the retinal and choroidal vasculature. In *Encyclopedia of the Eye*, eds. J. Besharse and D. Bok (Academic Press, Elsevier Books, London), 9-15.
- Anderson, B. Jr & Saltzman, H.A. 1964. Retinal oxygen utilization measured by hyperbaric blackout. *Arch Ophthalmol*, 72, 792-795.
- Anderson, D.H., Talaga, K.C., Rivest, A.J., Barron, E., Hageman, G.S. & Johnson, L.V. 2004. Characterization of beta amyloid assemblies in drusen: the deposits associated with aging and age-related macular degeneration. *Exp Eye Res*, 78(2), 243-256.
- Anderson, O.A., Finkelstein, A. & Shima, D.T. 2013. A2E induces IL-1 $\beta$  production in retinal pigment epithelial cells via the NLRP3 inflammasome. *PLoS One*, 8(6), e67263.
- Angleton, J.K. & Wensel, T.G. 1994. Enhancement of rod outer segment GTPase accelerating protein activity by the inhibitory subunit of cGMP phosphodiesterase. *J Biol Chem*, 269(23), 16290-16296.
- Antonelli-Orlidge, A., Smith, S.R. & D'Amore, P.A. 1989. Influence of pericytes capillary endothelial cell growth. *Am Rev Respir Dis*, 140(4), 1129-1131.
- Antonopoulos, C., Russo, H.M., El Sanadi, C., Martin, B.N., Li, X., Kaiser, W.J., Mocarski, E.S. & Dubyak, G.R. 2015. Caspase-8 as an effector and regulator of NLRP3 inflammasome signaling. *J Biol Chem*, 290(33), 20167-20184.
- Armulik, A., Genové, G., Mäe, M., Nisancioglu, M.H., Wallgard, E., Niaudet, C., He, L., Norlin, J., Lindblom, P., Strittmatter, K., Johansson, B.R. & Betsholtz, C. 2010. Pericytes regulate the blood-brain barrier. *Nature*, 468(7323), 557-561.
- Ardeljan, D. & Chan, C.C. 2013. Aging is not a disease: distinguishing age-related macular degeneration from aging. *Prog Retin Eye Res*, 37, 68-89.
- Babelova, A., Moreth, K., Tsalastra-Greul, W., Zeng-Brouwers, J., Eickelberg, O., Young, M.F., Bruckner, P., Pfeilschifter, J., Schaefer, R.M., Gröne, H.J. & Schaefer, L. 2009. Biglycan, a danger signal that activates the NLRP3 inflammasome via toll-like and P2X receptors. *J Biol Chem*, 284(36), 24035-24048.

- Bamias, G., Corridoni, D., Pizarro, T.T. & Cominelli, F. 2012. New insights into the dichotomous role of innate cytokines in gut homeostasis and inflammation. *Cytokine*, 59(3), 451-459.
- Bauernfeind, F.G., Horvath, G., Stutz, A., Alnemri, E.S., MacDonald, K., Speert, D., Fernandes-Alnemri, T., Wu, J., Monks, B.G., Fitzgerald, K.A., Hornung, V. & Latz, E. 2009. Cutting edge: NF-kappaB activating pattern recognition and cytokine receptors license NLRP3 inflammasome activation by regulating NLRP3 expression. *J Immunol*, 183(2), 787-791.
- Beatty, S., Koh, H., Phil, M., Henson, D. & Boulton, M. 2000. The role of oxidative stress in the pathogenesis of age-related macular degeneration. *Surv Ophthalmol*, 45(2), 115-134.
- Belenky, M.A., Smeraski, C.A., Provencio, I., Sollars, P.J. & Pickard, G.E. 2003. Melanopsin retinal ganglion cells receive bipolar and amacrine cell synapses. *J Comp Neurol*, 460(3), 380-393.
- Bell, R.D., Winkler, E.A., Sagare, A.P., Singh, I., LaRue, B., Deane, R. & Zlokovic, B.V. 2010. Pericytes control key neurovascular functions and neuronal phenotype in the adult brain and during brain aging. *Neuron*, 68(3), 409-427.
- Bergmann, M., Schütt, F., Holz, F.G. & Kopitz, J. 2004. Inhibition of the ATP-driven proton pump in RPE lysosomes by the major lipofuscin fluorophore A2-E may contribute to the pathogenesis of age-related macular degeneration. *FASEB J*, 18(3), 562-564.
- Bernardos, R.L., Barthel, L.K., Meyers, J.R. & Raymond, P.A. 2007. Late-stage neuronal progenitors in the retina are radial Müller glia that function as retinal stem cells. *J Neurosci*, 27(26), 7028-7040.
- Berson, D.M., Dunn, F.A. & Takao, M. 2002. Phototransduction by retinal ganglion cells that set the circadian clock. *Science*, 295(5557), 1070-1073.
- Besharse, J.C. 1982. Chapter 3 The daily light-dark cycle and rhythmic metabolism in the photoreceptor - pigment epithelial complex. *Prog Retin Res*, 1(0), 81-124.
- Besharse, J.C. & Hollyfield, J.G. 1979. Turnover of mouse photoreceptor outer segments in constant light and darkness. *Invest Ophthalmol Vis Sci*, 18(10), 1019-1024.
- Besharse, J.C., Hollyfield, J.G. & Rayborn, M.E. 1977. Photoreceptor outer segments: accelerated membrane renewal in rods after exposure to light. *Science*, 196(4289), 536-538.
- Bok, D. 1993. The retinal pigment epithelium: a versatile partner in vision. *J Cell Sci Suppl*, 17: 189-195.
- Boraschi, D. & Dinarello, C.A. 2006. IL-18 in autoimmunity: review. *Eur Cytokine Netw*, 17(4), 224-252.
- Boulton, M. & Dayhaw-Barker, P. 2001. The role of the retinal pigment epithelium: topographical variation and ageing changes. *Eye (Lond.)*, 15(Pt 3), 384-389.
- Boycott, B.B. & Wässle, H. 1974. The morphological types of ganglion cells of the domestic cat's retina. *J Physiol*, 240(2), 397-419.
- Brandstetter, C., Mohr, L.K., Latz, E., Holz, F.G. & Krohne, T.U. 2015. Light induces NLRP3 inflammasome activation in retinal pigment epithelial cells via lipofuscin-mediated photooxidative damage. *J Mol Med (Berl)*, 93(8), 905-916.
- Bressler, S.B., Maguire, M.G., Bressler, N.M. & Fine, S.L. 1990. Relationship of drusen and abnormalities of the retinal pigment epithelium to the prognosis of neovascular macular degeneration. The Macular Photocoagulation Study Group. *Arch Ophthalmol*, 108(10), 1442-1447.
- Bright Focus Foundation. Available online: <https://www.brightfocus.org/macular/article/age-related-macular-facts-figures> (accessed on 11 September 2017).
- Bringmann, A., Pannicke, T., Grosche, J., Francke, M., Wiedemann, P., Skatchkov, S.N., Osborne, N.N. & Reichenbach, A. 2006. Müller cells in the healthy and diseased retina. *Prog Retin Eye Res*, 25(4), 397-424.
- Brown, T.M., Tsujimura, S., Allen, A.E., Wynne, J., Bedford, R., Vickery, G., Vugler, A. & Lucas, R.J. 2012. Melanopsin-based brightness discrimination in mice and humans. *Curr Biol*, 22(12), 1134-1141.
- Burek, M. & Förster, C.Y. 2009. Cloning and characterization of the murine claudin-5 promoter. *Mol Cell Endocrinol*, 298(1-2), 19-24.
- Byrne, B.G., Dubuisson, J.F., Joshi, A.D., Persson, J.J. & Swanson, M.S. 2013. Inflammasome components coordinate autophagy and pyroptosis as macrophage responses to infection. *MBio*, 4(1), e00620-e00612.
- Cai, X., Chen, J., Xu, H., Liu, S., Jiang, Q.X., Halfmann, R. & Chen, Z.J. 2014. Prion-like polymerization underlies signal transduction in antiviral immune defense and inflammasome activation. *Cell*, 156(6), 1207-1222.



- Campbell, M. & Doyle, S.L. 2013. An eye on the future of inflammasomes and drug development in AMD. *J Mol Med (Berl)*, 91(9), 1059-1070.
- Campbell, M., Humphries, M.M., Kiang, A.S., Nguyen, A.T., Gobbo, O.L., Tam, L.C., Suzuki, M., Hanrahan, F., Ozaki, E., Farrar, G.J., Kenna, P.F. & Humphries, P. 2011. Systemic low-molecular weight drug delivery to pre-selected neuronal regions. *EMBO Mol Med*, 3(4), 235-245.
- Campbell, M., Nguyen, A.T., Kiang, A.S., Tam, L.C., Gobbo, O.L., Kerskens, C., Ni Dhubhghaill, S., Humphries, M.M., Farrar, G.J., Kenna, P.F. & Humphries, P. 2009. An experimental platform for systemic drug delivery to the retina. *Proc Natl Acad Sci USA*, 106(42), 17817-17822.
- Canna, S.W., Shi, G., Gery, I. & Sen, H.N. 2017. Chronic, systemic interleukin-18 does not promote macular degeneration or choroidal neovascularization. *Invest Ophthalmol Vis Sci*, 58(3), 1764-1765.
- CATT Research Group, Martin, D.F., Maguire, M.G., Ying, G.S., Grunwald, J.E., Fine, S.L. & Jaffe, G.J. 2011. Ranibizumab and bevacizumab for neovascular age-related macular degeneration. *N Engl J Med*, 364(20), 1897-1908.
- Chen, C.K., Burns, M.E., He, W., Wensel, T.G., Baylor, D.A. & Simon, M.I. 2000. Slowed recovery of rod photoresponse in mice lacking the GTPase accelerating protein RGS9-1. *Nature*, 403(6769), 557-560.
- Chen, C.K., Eversole-Cire, P., Zhang, H., Mancino, V., Chen, Y.J., He, W., Wensel, T.G. & Simon, M.I. 2003. Instability of GGL domain-containing RGS proteins in mice lacking the G protein beta-subunit Gbeta5. *Proc Natl Acad Sci USA*, 100(11), 6604-6609.
- Chen, C.K., Inglese, J., Lefkowitz, R.J. & Hurley, J.B. 1995. Ca<sup>2+</sup>-dependent interaction of recoverin with rhodopsin kinase. *J Biol Chem*, 270(30), 18060-18066.
- Chen, M. & Xu, H. 2015. Parainflammation, chronic inflammation, and age-related macular degeneration. *J Leukoc Biol*, 98(5), 713-725.
- Clemons, T.E., Milton, R.C., Klein, R., Seddon, J.M., Ferris, F.L. 3rd & Age-Related Eye Disease Study Research Group. 2005. Risk factors for the incidence of advanced age-related macular degeneration in the age-related eye disease study (AREDS) AREDS report no. 19. *Ophthalmology*, 112(4), 533-539.
- Compan, V., Baroja-Mazo, A., Lopez-Castejon, G., Gomez, A.I., Martinez, C.M., Angosto, D., Montero, M.T., Herranz, A.S., Bazan, E., Reimers, D., Mulero, V. & Pelegrin, P. 2012. Cell volume regulation modulates NLRP3 inflammasome activation. *Immunity*, 37(3), 487-500.
- Crabb, J.W., Miyagi, M., Gu, X., Shadrach, K., West, K.A., Sakaguchi, H., Kamei, M., Hasan, A., Yan, L., Rayborn, M.E., Salomon, R.G. & Hollyfield, J.G. 2002. Drusen proteome analysis: An approach to the etiology of age-related macular degeneration. *Proc Natl Acad Sci USA*, 99(23), 14682-14687.
- Crooks, J. & Kolb, H. 1992. Localization of GABA, glycine, glutamate and tyrosine hydroxylase in the human retina. *J Comp Neurol*, 315(3), 287-302.
- Cruz, C.M., Rinna, A., Forman, H.J., Ventura, A.L., Persechini, P.M. & Ojcius, D.M. 2007. ATP activates a reactive oxygen species-dependent oxidative stress response and secretion of proinflammatory cytokines in macrophages. *J Biol Chem*, 282(5), 2871-2879.
- Cunha-Vaz, J.G., Shakib, M. & Ashton, N. 1966. Studies on the permeability of the blood-retinal barrier. I. On the existence, development, and site of a blood-retinal barrier. *Br J Ophthalmol*, 50(8), 441-453.
- Curcio, C.A., Sloan, K.R., Kalina, R.E. & Hendrickson, A.E. 1990. Human photoreceptor topography. *J Comp Neurol*, 292(4), 497-523.
- Czeisler, C.A., Shanahan, T.L., Klerman, E.B., Martens, H., Brotman, D.J., Emens, J.S., Klein, T. & Rizzo, J.F. 3rd. 1995. Suppression of melatonin secretion in some blind patients by exposure to bright light. *N Engl J Med*, 332(1), 6-11.
- Dacey, D.M. 1993. The mosaic of midget ganglion cells in the human retina. *J Neurosci*, 13(12), 5334-5355.
- Dacey, D.M., Liao, H.W., Peterson, B.B., Robinson, F.R., Smith, V.C., Pokorny, J., Yau, K.W. & Gamlin, P.D. 2005. Melanopsin-expressing ganglion cells in primate retina signal colour and irradiance and project to the LGN. *Nature*, 433(7027), 749-754.
- Daneman, R., Zhou, L., Kebede, A.A. & Barres, B.A. 2010. Pericytes are required for blood-brain barrier integrity during embryogenesis. *Nature*, 468(7323), 562-566.
- Das, A.V., Mallya, K.B., Zhao, X., Ahmad, F., Bhattacharya, S., Thoreson, W.B., Hegde, G.V. & Ahmad, I. 2006. Neural stem cell properties of Müller glia in the mammalian retina: regulation by Notch and Wnt signaling. *Dev Biol*, 299(1), 283-302.
- Dasari, B., Prasanthi, J.R., Marwarha, G., Singh, B.B. & Ghribi, O. 2011. Cholesterol-enriched diet causes age-related macular degeneration-like pathology in rabbit retina. *BMC Ophthalmol*, 11, doi:10.1186/1471-2415-11-22.

- Davenport, C.M., Detwiler, P.B. & Dacey, D.M. 2008. Effects of pH buffering on horizontal and ganglion cell light responses in primate retina: evidence for the proton hypothesis of surround formation. *J Neurosci*, 28(2), 456-464.
- D'Cruz, P.M., Yasumura, D., Weir, J., Matthes, M.T., Abderrahim, H., LaVail, M.M. & Vollrath, D. 2000. Mutation of the receptor tyrosine kinase gene *Mertk* in the retinal dystrophic RCS rat. *Hum Mol Genet*, 9(4), 645-651.
- DeBault, L.E. & Cancilla, P.A. 1980. Gamma-glutamyl transpeptidase in isolated brain endothelial cells: induction by glial cells in vitro. *Science*, 207(4431), 653-655.
- de Jong, P.T. 2016. A historical analysis of the quest for the origins of aging macula disorder, the tissues involved, and its terminology. *Ophthalmol Eye Dis*, 8(Suppl 1), 5-14.
- Dhingra, A., Lyubarsky, A., Jiang, M., Pugh, E.N. Jr, Birnbaumer, L., Sterling, P. & Vardi, N. 2000. The light response of ON bipolar neurons requires G $\alpha$ o. *J Neurosci*, 20(24), 9053-9058.
- Díaz-Coránguez, M., Ramos, C. & Antonetti, D.A. 2017. The inner blood-retinal barrier: Cellular basis and development. *Vision Res*, 139, 123-137.
- Dib, B., Lin, H., Maidana, D.E., Tian, B., Miller, J.B., Bouzika, P., Miller, J.W. & Vavvas, D.G. 2015. Mitochondrial DNA has a pro-inflammatory role in AMD. *Biochim Biophys Acta*, 1853(11 Pt A), 2897-2906.
- Dinarello, C.A., Novick, D., Kim, S. & Kaplanski, G. 2013. Interleukin-18 and IL-18 binding protein. *Front Immunol*, 4, 289.
- Distler, C. & Dreher, Z. 1996. Glia cells of the monkey retina--II. Müller cells. *Vision Res*, 36(16), 2381-2394.
- Dostert, C., Pétrilli, V., Van Bruggen, R., Steele, C., Mossman, B.T. & Tschopp, J. 2008. Innate immune activation through Nalp3 inflammasome sensing of asbestos and silica. *Science*, 320(5876), 674-677.
- Doyle, S.E., Castrucci, A.M., McCall, M., Provencio, I. & Menaker, M. 2006. Nonvisual light responses in the Rpe65 knockout mouse: rod loss restores sensitivity to the melanopsin system. *Proc Natl Acad Sci USA*, 103(27), 10432-10437.
- Doyle, S.L., Campbell, M., Ozaki, E., Salomon, R.G., Mori, A., Kenna, P.F., Farrar, G.J., Kiang, A.S., Humphries, M.M., Lavelle, E.C., O'Neill, L.A.J., Hollyfield, J.G. & Humphries, P. 2012. NLRP3 has a protective role in age-related macular degeneration through the induction of IL-18 by drusen components. *Nat Med*, 18(5), 791-798.
- Doyle, S.L., López, F.J., Celkova, L., Brennan, K., Mulfaul, K., Ozaki, E., Kenna, P.F., Kurali, E., Hudson, N., Doggett, T., Ferguson, T.A., Humphries, P., Adamson, P. & Campbell, M. 2015. IL-18 immunotherapy for neovascular AMD: tolerability and efficacy in nonhuman primates. *Invest Ophthalmol Vis Sci*, 56(9), 5424-5430.
- Doyle, S.L., Ozaki, E., Brennan, K., Humphries, M.M., Mulfaul, K., Keaney, J., Kenna, P.F., Maminishkis, A., Kiang, A.S., Saunders, S.P., Hams, E., Lavelle, E.C., Gardiner, C., Fallon, P.G., Adamson, P., Humphries, P. & Campbell, M. 2014. IL-18 attenuates experimental choroidal neovascularization as a potential therapy for wet age-related macular degeneration. *Sci Transl Med*, 6(230), 230ra44.
- Dowling, J.K. & O'Neill, L.A. 2012. Biochemical regulation of the inflammasome. *Crit Rev Biochem Mol Biol*, 47(5), 424-443.
- Dreher, Z., Robinson, S.R. & Distler, C. 1992. Müller cells in vascular and avascular retinæ: a survey of seven mammals. *J Comp Neurol*, 323(1), 59-80.
- Duewell, P., Kono, H., Rayner, K.J., Sirois, C.M., Vladimer, G., Bauernfeind, F.G., Abela, G.S., Franchi, L., Nuñez, G., Schnurr, M., Espevik, T., Lien, E., Fitzgerald, K.A., Rock, K.L., Moore, K.J., Wright, S.D., Hornung, V. & Latz, E. 2010. NLRP3 inflammasomes are required for atherogenesis and activated by cholesterol crystals. *Nature*, 464(7293), 1357-1361.
- Dyer, M.A. & Cepko, C.L. 2000. Control of Müller glial cell proliferation and activation following retinal injury. *Nat Neurosci*, 3(9), 873-880.
- Eisenbarth, S.C., Colegio, O.R., O'Connor, W., Sutterwala, F.S. & Flavell, R.A. 2008. Crucial role for the Nalp3 inflammasome in the immunostimulatory properties of aluminium adjuvants. *Nature*, 453(7198), 1122-1126.
- Edwards, A.O., Ritter, R. 3rd, Abel, K.J., Manning, A., Panhuysen, C. & Farrer, L.A. 2005. Complement factor H polymorphism and age-related macular degeneration. *Science*, 308(5720), 421-424.
- Farquhar, M.G. & Palade, G.E. 1963. Junctional complexes in various epithelia. *J Cell Biol*, 17, 375-412.

- Feher, J., Kovacs, I., Artico, M., Cavallotti, C., Papale, A. & Balacco Gabrieli, C. 2006. Mitochondrial alterations of retinal pigment epithelium in age-related macular degeneration. *Neurobiol Aging*, 27(7), 983-993.
- Feng, W., Yasumura, D., Matthes, M.T., LaVail, M.M. & Vollrath, D. 2002. Mertk triggers uptake of photoreceptor outer segments during phagocytosis by cultured retinal pigment epithelial cells. *J Biol Chem*, 277(19), 17016-17022.
- Feng, Y., Venema, V.J., Venema, R.C., Tsai, N., Behzadian, M.A. & Caldwell, R.B. 1999a. VEGF-induced permeability increase is mediated by caveolae. *Invest Ophthalmol Vis Sci*, 40(1), 157-167.
- Feng, Y., Venema, V.J., Venema, R.C., Tsai, N. & Caldwell, R.B. 1999b. VEGF induces nuclear translocation of Flk-1/KDR, endothelial nitric oxide synthase, and caveolin-1 in vascular endothelial cells. *Biochem Biophys Res Commun*, 256(1), 192-197.
- Fernandes-Alnemri, T., Wu, J., Yu, J.W., Datta, P., Miller, B., Jankowski, W., Rosenberg, S., Zhang, J. & Alnemri, E.S. 2007. The pyroptosome: a supramolecular assembly of ASC dimers mediating inflammatory cell death via caspase-1 activation. *Cell Death Differ*, 14(9), 1590-1604.
- Finnemann, S.C. 2003. Focal adhesion kinase signaling promotes phagocytosis of integrin-bound photoreceptors. *EMBO J*, 22(16), 4143-4154.
- Finnemann, S.C., Bonilha, V.L., Marmorstein, A.D. & Rodriguez-Boulan, E. 1997. Phagocytosis of rod outer segments by retinal pigment epithelial cells requires alpha(v)beta5 integrin for binding but not for internalization. *Proc Natl Acad Sci USA*, 94(24), 12932-12937.
- Finnemann, S.C., Leung, L.W. & Rodriguez-Boulan, E. 2002. The lipofuscin component A2E selectively inhibits phagolysosomal degradation of photoreceptor phospholipid by the retinal pigment epithelium. *Proc Natl Acad Sci USA*, 99(6), 3842-3847.
- Finnemann, S.C. & Silverstein, R.L. 2001. Differential roles of CD36 and alphavbeta5 integrin in photoreceptor phagocytosis by the retinal pigment epithelium. *J Exp Med*, 194(9), 1289-1298.
- Fischer, A.J. & Reh, T.A. 2001. Müller glia are a potential source of neural regeneration in the postnatal chicken retina. *Nat Neurosci*, 4(3), 247-252.
- Fisher, M. 2009. Pericyte signaling in the neurovascular unit. *Stroke*, 40(3 Suppl), S13-S15.
- Forrester, J.V., Dick, A.D., McMenamin, P.G. & Roberts, F. 2008. *The Eye: Basic Sciences in Practice* (3rd ed.) (Saunders Elsevier).
- Fox, A.R., Chew, E.Y., Meyerle, C., Vitale, S., Ferris, F.L., Nussenblatt, R.B. & Sen, H.N. 2017. Age-related macular degeneration in patients with uveitis. *Br J Ophthalmol*, 101(3), 342-347.
- Franze, K., Grosche, J., Skatchkov, S.N., Schinkinger, S., Foja, C., Schild, D., Uckermann, O., Travis K., Reichenbach, A. & Guck, J. 2007. Müller cells are living optical fibers in the vertebrate retina. *Proc Natl Acad Sci USA*, 104(20), 8287-8292.
- Freedman, M.S., Lucas, R.J., Soni, B., von Schantz, M., Muñoz, M., David-Gray, Z. & Foster, R. 1999. Regulation of mammalian circadian behavior by non-rod, non-cone, ocular photoreceptors. *Science*, 284(5413), 502-504.
- Frey, T. & Antonetti, D.A. 2011. Alterations to the blood-retinal barrier in diabetes: cytokines and reactive oxygen species. *Antioxid Redox Signal*, 15(5), 1271-1284.
- Fu, L. & Lee, C.C. 2003. The circadian clock: pacemaker and tumour suppressor. *Nat Rev Cancer*, 3(5), 350-361.
- Fu, Y. 2010. Phototransduction in rods and cones. In *Webvision: The Organization of the Retina and Visual System [Internet]*, eds. H. Kolb, E. Fernandez and R. Nelson (Salt Lake City, UT: University of Utah Health Sciences Center; 1995- ), available online: <https://www.ncbi.nlm.nih.gov/books/NBK52768/> (accessed on 08 March 2018).
- Fu, Y., Zhong, H., Wang, M.H., Luo, D.G., Liao, H.W., Maeda, H., Hattar, S., Frishman, L.J. & Yau, K.W. 2005. Intrinsically photosensitive retinal ganglion cells detect light with a vitamin A-based photopigment, melanopsin. *Proc Natl Acad Sci USA*, 102(29), 10339-10344.
- Gal, A., Li, Y., Thompson, D.A., Weir, J., Orth, U., Jacobson, S.G., Apfelstedt-Sylla, E. & Vollrath, D. 2000. Mutations in MERTK, the human orthologue of the RCS rat retinal dystrophy gene, cause retinitis pigmentosa. *Nat Genet*, 26(3), 270-271.
- Garcia, C.M., Darland, D.C., Massingham, L.J. & D'Amore, P.A. 2004. Endothelial cell-astrocyte interactions and TGF beta are required for induction of blood-neural barrier properties. *Brain Res Dev Brain Res*, 152(1), 25-38.

- Gardiner, T.A., Stitt, A.W. & Archer, D.B. 1995. Retinal vascular endothelial cell endocytosis increases in early diabetes. *Lab Invest*, 72(4), 439-444.
- Gass, J.D. 1999. Müller cell cone, an overlooked part of the anatomy of the fovea centralis: hypotheses concerning its role in the pathogenesis of macular hole and foveomacular retinoschisis. *Arch Ophthalmol*, 117(6), 821-823.
- Ginhoux, F., Greter, M., Leboeuf, M., Nandi, S., See, P., Gokhan, S., Mehler, M.F., Conway, S.J., Ng, L.G., Stanley, E.R., Samokhvalov, I.M. & Merad, M. 2010. Fate mapping analysis reveals that adult microglia derive from primitive macrophages. *Science*, 330(6005), 841-845.
- Gnanaguru, G., Choi, A.R., Amarnani, D. & D'Amore, P.A. 2016. Oxidized lipoprotein uptake through the CD36 receptor activates the NLRP3 inflammasome in human retinal pigment epithelial cells. *Invest Ophthalmol Vis Sci*, 57(11), 4704-4712.
- Goodyear, M.J., Crewther, S.G. & Junghans, B.M. 2009. A role for aquaporin-4 in fluid regulation in the inner retina. *Vis Neurosci*, 26(2), 159-165.
- Gooley, J.J., Lu, J., Chou, T.C., Scammell, T.E. & Saper, C.B. 2001. Melanopsin in cells of origin of the retinohypothalamic tract. *Nat Neurosci*, 4(12), 1165.
- Göz, D., Studholme, K., Lappi, D.A., Rollag, M.D., Provencio, I. & Morin, L.P. 2008. Targeted destruction of photosensitive retinal ganglion cells with a saporin conjugate alters the effects of light on mouse circadian rhythms. *PLoS One*, 3(9), e3153.
- Graham, D.M., Wong, K.Y., Shapiro, P., Frederick, C., Pattabiraman, K. & Berson, D.M. 2008. Melanopsin ganglion cells use a membrane-associated rhabdomeric phototransduction cascade. *J Neurophysiol*, 99(5), 2522-2532.
- Greene, C., Kealy, J., Humphries, M.M., Gong, Y., Hou, J., Hudson, N., Cassidy, L.M., Martiniano, R., Shashi, V., Hooper, S.R., Grant, G.A., Kenna, P.F., Norris, K., Callaghan, C.K., Islam, M.D., O'Mara, S.M., Najda, Z., Campbell, S.G., Pachter, J.S., Thomas, J., Williams, N.M., Humphries, P., Murphy, K.C. & Campbell, M. 2017. Dose-dependent expression of claudin-5 is a modifying factor in schizophrenia. *Mol Psychiatry*, 156.
- Gu, X., Meer, S.G., Miyagi, M., Rayborn, M.E., Hollyfield, J.G., Crabb, J.W. & Salomon, R.G. 2003. Carboxyethylpyrrole protein adducts and autoantibodies, biomarkers for age-related macular degeneration. *J Biol Chem*, 278(43), 42027-42035.
- Guo, H., Callaway, J.B. & Ting, J.P. 2015. Inflammasomes: mechanism of action, role in disease, and therapeutics. *Nat Med*, 21(7), 677-687.
- Güler, A.D., Ecker, J.L., Lall, G.S., Haq, S., Altimus, C.M., Liao, H.W., Barnard, A.R., Cahill, H., Badea, T.C., Zhao, H., Hankins, M.W., Berson, D.M., Lucas, R.J., Yau, K.W. & Hattar, S. 2008. Melanopsin cells are the principal conduits for rod-cone input to non-image-forming vision. *Nature*, 453(7191), 102-105.
- Hageman, G.S., Anderson, D.H., Johnson, L.V., Hancox, L.S., Taiber, A.J., Hardisty, L.I., Hageman, J.L., Stockman, H.A., Borchardt, J.D., Gehrs, K.M., Smith, R.J., Silvestri, G., Russell, S.R., Klaver, C.C., Barbazetto, I., Chang, S., Yannuzzi, L.A., Barile, G.R., Merriam, J.C., Smith, R.T., Olsh, A.K., Bergeron, J., Zernant, J., Merriam, J.E., Gold, B., Dean, M. & Allikmets, R. 2005. A common haplotype in the complement regulatory gene factor H (HF1/CFH) predisposes individuals to age-related macular degeneration. *Proc Natl Acad Sci USA*, 102(20), 7227-7232.
- Haines, J.L., Hauser, M.A., Schmidt, S., Scott, W.K., Olson, L.M., Gallins, P., Spencer, K.L., Kwan, S.Y., Noureddine, M., Gilbert, J.R., Schnetz-Boutaud, N., Agarwal, A., Postel, E.A. & Pericak-Vance, M.A. 2005. Complement factor H variant increases the risk of age-related macular degeneration. *Science*, 308(5720), 419-421.
- Halle, A., Hornung, V., Petzold, G.C., Stewart, C.R., Monks, B.G., Reinheckel, T., Fitzgerald, K.A., Latz, E., Moore, K.J. & Golenbock, D.T. 2008. The NALP3 inflammasome is involved in the innate immune response to amyloid-beta. *Nat Immunol*, 9(8), 857-865.
- Hama, K., Mizukawa, A. & Kosaka, T. 1978. Fine structure of the Müller cell revealed by high-voltage electron microscopy. *Sens Processes*, 2(4), 296-299.
- Hammer, M., Richter, S., Guehrs, K.H. & Schweitzer, D. 2006. Retinal pigment epithelium cell damage by A2-E and its photo-derivatives. *Mol Vis*, 12, 1348-1354.
- Hannibal, J., Hindersson, P., Knudsen, S.M., Georg, B. & Fahrenkrug, J. 2002. The photopigment melanopsin is exclusively present in pituitary adenylate cyclase-activating polypeptide-containing retinal ganglion cells of the retinohypothalamic tract. *J Neurosci*, 22(1), RC191.

- Hannibal, J., Hindersson, P., Ostergaard, J., Georg, B., Heegaard, S., Larsen, P.J. & Fahrenkrug, J. 2004. Melanopsin is expressed in PACAP-containing retinal ganglion cells of the human retinohypothalamic tract. *Invest Ophthalmol Vis Sci*, 45(11), 4202-4209.
- Hannibal, J., Kankipati, L., Strang, C.E., Peterson, B.B., Dacey, D. & Gamlin, P.D. 2014. Central projections of intrinsically photosensitive retinal ganglion cells in the macaque monkey. *J Comp Neurol*, 522(10), 2231-2248.
- Harris, J. 2013. Autophagy and IL-1 family cytokines. *Front Immunol*, 4, 83.
- Harris, J., Hartman, M., Roche, C., Zeng, S.G., O'Shea, A., Sharp, F.A., Lambe, E.M., Creagh, E.M., Golenbock, D.T., Tschopp, J., Kornfeld, H., Fitzgerald, K.A. & Lavelle, E.C. 2011. Autophagy controls IL-1beta secretion by targeting pro-IL-1beta for degradation. *J Biol Chem*, 286(11), 9587-9597.
- Hasegawa, E., Sweigard, H., Husain, D., Olivares, A.M., Chang, B., Smith, K.E., Birsner, A.E., D'Amato, R.J., Michaud, N.A., Han, Y., Vavvas, D.G., Miller, J.W., Haider, N.B. & Connor, K.M. 2014. Characterization of a spontaneous retinal neovascular mouse model. *PLoS One*, 9(9), e106507.
- Haseloff, R.F., Blasig, I.E., Bauer, H.C. & Bauer, H. 2005. In search of the astrocytic factor(s) modulating blood-brain barrier functions in brain capillary endothelial cells in vitro. *Cell Mol Neurobiol*, 25(1), 25-39.
- Hatori, M., Le, H., Vollmers, C., Keding, S.R., Tanaka, N., Buch, T., Waisman, A., Schmedt, C., Jegla, T. & Panda, S. 2008. Inducible ablation of melanopsin-expressing retinal ganglion cells reveals their central role in non-image forming visual responses. *PLoS One*, 3(6), e2451.
- Hattar, S., Kumar, M., Park, A., Tong, P., Tung, J., Yau, K.W. & Berson, D.M. 2006. Central projections of melanopsin-expressing retinal ganglion cells in the mouse. *J Comp Neurol*, 497(3), 326-349.
- Hattar, S., Liao, H.W., Takao, M., Berson, D.M. & Yau, K.W. 2002. Melanopsin-containing retinal ganglion cells: architecture, projections, and intrinsic photosensitivity. *Science*, 295(5557), 1065-1070.
- Hattar, S., Lucas, R.J., Mrosovsky, N., Thompson, S., Douglas, R.H., Hankins, M.W., Lem, J., Biel, M., Hofmann, F., Foster, R.G. & Yau, K.W. 2003. Melanopsin and rod-cone photoreceptive systems account for all major accessory visual functions in mice. *Nature*, 424(6944), 76-81.
- He, L. & Marneros, A.G. 2013. Macrophages are essential for the early wound healing response and the formation of a fibrovascular scar. *Am J Pathol*, 182(6), 2407-2417.
- He, W., Cowan, C.W. & Wensel, T.G. 1998. RGS9, a GTPase accelerator for phototransduction. *Neuron*, 20(1), 95-102.
- Herzyk, D.J., Bugelski, P.J., Hart, T.K. & Wier, P.J. 2003. Preclinical safety of recombinant human interleukin-18. *Toxicol Pathol*, 31(5), 554-561.
- Hildebrand, G.D. & Fielder, A.R. 2011. Anatomy and physiology of the retina. In *Pediatric Retina*, eds. J.D. Reynolds and S.E. Olitsky (Springer-Verlag Berlin Heidelberg), 39-65.
- Hirasawa, H. & Kaneko, A. 2003. pH changes in the invaginating synaptic cleft mediate feedback from horizontal cells to cone photoreceptors by modulating Ca<sup>2+</sup> channels. *J Gen Physiol*, 122(6), 657-671.
- Hoegen, T., Tremel, N., Klein, M., Angele, B., Wagner, H., Kirschning, C., Pfister, H.W., Fontana, A., Hammerschmidt, S. & Koedel, U. 2011. The NLRP3 inflammasome contributes to brain injury in pneumococcal meningitis and is activated through ATP-dependent lysosomal cathepsin B release. *J Immunol*, 187(10), 5440-5451.
- Hofman, P., Blaauwgeers, H.G., Tolentino, M.J., Adamis, A.P., Nunes Cardozo, B.J., Vrensen, G.F. & Schlingemann, R.O. 2000. VEGF-A induced hyperpermeability of blood-retinal barrier endothelium in vivo is predominantly associated with pinocytotic vesicular transport and not with formation of fenestrations. Vascular endothelial growth factor-A. *Curr Eye Res*, 21(2), 637-645.
- Holler, N., Zaru, R., Micheau, O., Thome, M., Attinger, A., Valitutti, S., Bodmer, J.L., Schneider, P., Seed, B. & Tschopp, J. 2000. Fas triggers an alternative, caspase-8-independent cell death pathway using the kinase RIP as effector molecule. *Nat Immunol*, 1(6), 489-495.
- Holz, F.G., Bindenwald-Wittich, A., Fleckenstein, M., Dreyhaupt, J., Scholl, H.P., Schmitz-Valckenberg, S. & FAM-Study Group. 2007. Progression of geographic atrophy and impact of fundus autofluorescence patterns in age-related macular degeneration. *Am J Ophthalmol*, 143(3), 463-472.
- Holz, F.G., Schütt, F., Kopitz, J., Eldred, G.E., Kruse, F.E., Völcker, H.E. & Cantz, M. 1999. Inhibition of lysosomal degradative functions in RPE cells by a retinoid component of lipofuscin. *Invest Ophthalmol Vis Sci*, 40(3), 737-743.

- Hornung, V., Bauernfeind, F., Halle, A., Samstad, E.O., Kono, H., Rock, K.L., Fitzgerald, K.A. & Latz, E. 2008. Silica crystals and aluminum salts activate the NALP3 inflammasome through phagosomal destabilization. *Nat Immunol*, 9(8), 847-856.
- Hopkins, J.M. & Boycott, B.B. 1995. Synapses between cones and diffuse bipolar cells of a primate retina. *J Neurocytol*, 24(9), 680-694.
- Howard, J., Blakeslee, B. & Laughlin, S.B. 1987. The intracellular pupil mechanism and photoreceptor signal: noise ratios in the fly *Lucilia cuprina*. *Proc R Soc Lond B Biol Sci*, 231(1265), 415-435.
- Hu, G. & Wensel, T.G. 2002. R9AP, a membrane anchor for the photoreceptor GTPase accelerating protein, RGS9-1. *Proc Natl Acad Sci USA*, 99(15), 9755-9760.
- Hudson, N., Powner, M.B., Sarker, M.H., Burgoyne, T., Campbell, M., Ockrim, Z.K., Martinelli, R., Futter, C.E., Grant, M.B., Fraser, P.A., Shima, D.T., Greenwood, J. & Turowski, P. 2014. Differential apicobasal VEGF signaling at vascular blood-neural barriers. *Dev Cell*, 30(5), 541-552.
- Jager, R.D., Mieler, W.F. & Miller, J.W. 2008. Age-related macular degeneration. *N Engl J Med*, 358(24), 2606-2617.
- Jain, R.K. & Booth, M.F. 2003. What brings pericytes to tumor vessels? *J Clin Invest*, 112(8), 1134-1136.
- Janzer, R.C. & Raff, M.C. 1987. Astrocytes induce blood-brain barrier properties in endothelial cells. *Nature*, 325(6101), 253-257.
- Jarrett, S.G. & Boulton, M.E. 2012. Consequences of oxidative stress in age-related macular degeneration. *Mol Aspects Med*, 33(4), 399-417.
- Jayaram, H., Jones, M.F., Eastlake, K., Cottrill, P.B., Becker, S., Wiseman, J., Khaw, P.T. & Limb, G.A. 2014. Transplantation of photoreceptors derived from human Muller glia restore rod function in the P23H rat. *Stem Cells Transl Med*, 3(3), 323-333.
- Johnson, L.V., Leitner, W.P., Rivest, A.J., Staples, M.K., Radeke, M.J. & Anderson, D.H. 2002. The Alzheimer's A beta -peptide is deposited at sites of complement activation in pathologic deposits associated with aging and age-related macular degeneration. *Proc Natl Acad Sci USA*, 99(18), 11830-11835.
- Jones, S.A., Mills, K.H. & Harris, J. 2013. Autophagy and inflammatory diseases. *Immunol Cell Biol*, 91(3), 250-258.
- Kaarniranta, K., 2010. Autophagy--hot topic in AMD. *Acta Ophthalmol*, 88(4), 387-388.
- Kaarniranta, K., Salminen, A., Haapasalo, A., Soininen, H. & Hiltunen, M. 2011. Age-related macular degeneration (AMD): Alzheimer's disease in the eye? *J Alzheimers Dis*, 24(4), 615-631.
- Kaarniranta, K., Sinha, D., Blasiak, J., Kauppinen, A., Veréb, Z., Salminen, A., Boulton, M.E. & Petrovski, G. 2013. Autophagy and heterophagy dysregulation leads to retinal pigment epithelium dysfunction and development of age-related macular degeneration. *Autophagy*, 9(7), 973-984.
- Kahlenberg, J.M. & Dubyak, G.R. 2004. Mechanisms of caspase-1 activation by P2X7 receptor-mediated K<sup>+</sup> release. *Am J Physiol Cell Physiol*, 286(5), C1100-1108.
- Kalloniatis, M., Marc, R.E. & Murry, R.F. 1996. Amino acid signatures in the primate retina. *J Neurosci*, 16(21), 6807-6829.
- Kamermans, M., Fahrenfort, I., Schultz, K., Janssen-Bienhold, U., Sjoerdsma, T. & Weiler, R. 2001. Hemichannel-mediated inhibition in the outer retina. *Science*, 292(5519), 1178-1180.
- Kandel, E.R., Schwartz, J.H. & Jessell, T.M. 2000. *Principles of Neural Science* (4th ed.) (New York: McGraw-Hill), 503-517.
- Kaneko, A. & Tachibana, M. 1986. Effects of gamma-aminobutyric acid on isolated cone photoreceptors of the turtle retina. *J Physiol*, 373, 443-461.
- Kaneko, H., Dridi, S., Tarallo, V., Gelfand, B.D., Fowler, B.J., Cho, W.G., Kleinman, M.E., Ponicsan, S.L., Hauswirth, W.W., Chiodo, V.A., Karikó, K., Yoo, J.W., Lee, D.K., Hadziahmetovic, M., Song, Y., Misra, S., Chaudhuri, G., Buaas, F.W., Braun, R.E., Hinton, D.R., Zhang, Q., Grossniklaus, H.E., Provis, J.M., Madigan, M.C., Milam, A.H., Justice, N.L., Albuquerque, R.J., Blandford, A.D., Bogdanovich, S., Hirano, Y., Witta, J., Fuchs, E., Littman, D.R., Ambati, B.K., Rudin, C.M., Chong, M.M., Provost, P., Kugel, J.F., Goodrich, J.A., Dunaief, J.L., Baffi, J.Z. & Ambati, J. 2011. DICER1 deficit induces Alu RNA toxicity in age-related macular degeneration. *Nature*, 471(7338), 325-330.
- Karunadharma, P.P., Nordgaard, C.L., Olsen, T.W. & Ferrington, D.A. 2010. Mitochondrial DNA damage as a potential mechanism for age-related macular degeneration. *Invest Ophthalmol Vis Sci*, 51(11), 5470-5479.

- Kauppinen, A., Niskanen, H., Suuronen, T., Kinnunen, K., Salminen, A. & Kaarniranta, K. 2012. Oxidative stress activates NLRP3 inflammasomes in ARPE-19 cells--implications for age-related macular degeneration (AMD). *Immunol Lett*, 147(1-2), 29-33.
- Kawamura, S. 1992. Light-sensitivity modulating protein in frog rods. *Photochem Photobiol*, 56(6), 1173-1180.
- Kawamura, S. 1993. Rhodopsin phosphorylation as a mechanism of cyclic GMP phosphodiesterase regulation by S-modulin. *Nature*, 362(6423), 855-857.
- Keeler, C.E. 1927. Iris movements in blind mice. *Am J Physiol*, 81, 107-112.
- Keeler, C.E., Sutcliffe, E. & Chaffee, E.L. 1928. Normal and "rodless" retinæ of the house mouse with respect to the electromotive force generated through stimulation by light. *Proc Natl Acad Sci USA*, 14(6), 477-484.
- Keresztes, G., Martemyanov, K.A., Krispel, C.M., Mutai, H., Yoo, P.J., Maison, S.F., Burns, M.E., Arshavsky, V.Y. & Heller, S. 2004. Absence of the RGS9. Gbeta5 GTPase-activating complex in photoreceptors of the R9AP knockout mouse. *J Biol Chem*, 279(3), 1581-1584.
- Kevany, B.M., & Palczewski, K. 2010. Phagocytosis of retinal rod and cone photoreceptors. *Physiology (Bethesda)*, 25(1), 8-15.
- Kim, J.Y., Zhao, H., Martinez, J., Doggett, T.A., Kolesnikov, A.V., Tang, P.H., Ablonczy, Z., Chan, C.C., Zhou, Z., Green, D.R. & Ferguson, T.A. 2013. Noncanonical autophagy promotes the visual cycle. *Cell*, 154(2), 365-376.
- Kindzelskii, A.L., Elnor, V.M., Elnor, S.G., Yang, D., Hughes, B.A. & Petty, H.R. 2004. Toll-like receptor 4 (TLR4) of retinal pigment epithelial cells participates in transmembrane signaling in response to photoreceptor outer segments. *J Gen Physiol*, 124(2), 139-149.
- Klaassen, I., Van Noorden, C.J. & Schlingemann, R.O. 2013. Molecular basis of the inner blood-retinal barrier and its breakdown in diabetic macular edema and other pathological conditions. *Prog Retin Eye Res*, 34, 19-48.
- Klein, R.J., Zeiss, C., Chew, E.Y., Tsai, J.Y., Sackler, R.S., Haynes, C., Henning, A.K., SanGiovanni, J.P., Mane, S.M., Mayne, S.T., Bracken, M.B., Ferris, F.L., Ott, J., Barnstable, C. & Hoh, J. 2005. Complement factor H polymorphism in age-related macular degeneration. *Science*, 308(5720), 385-389.
- Klenchin, V.A., Calvert, P.D. & Bownds, M.D. 1995. Inhibition of rhodopsin kinase by recoverin. Further evidence for a negative feedback system in phototransduction. *J Biol Chem*, 270(27), 16147-16152.
- Klettner, A., Kauppinen, A., Blasiak, J., Roeder, J., Salminen, A. & Kaarniranta, K. 2013. Cellular and molecular mechanisms of age-related macular degeneration: from impaired autophagy to neovascularization. *Int J Biochem Cell Biol*, 45(7), 1457-1467.
- Kolb, H. 1970. Organisation of the outer plexiform layer of the primate retina: electron microscopy of Golgi-impregnated cells. *Philos Trans R Soc Lond B Biol Sci*, 258(823), 261-283.
- Kolb, H. 2001a (updated 2007). Inner plexiform layer. In *Webvision: The Organization of the Retina and Visual System [Internet]*, eds. H. Kolb, E. Fernandez and R. Nelson (Salt Lake City, UT: University of Utah Health Sciences Center; 1995- ), available online: <https://www.ncbi.nlm.nih.gov/books/NBK11536/> (accessed on 19 March 2018).
- Kolb, H. 2001b (updated 2007). Glial cells of the retina. In *Webvision: The Organization of the Retina and Visual System [Internet]*, eds. H. Kolb, E. Fernandez and R. Nelson (Salt Lake City, UT: University of Utah Health Sciences Center; 1995- ), available online: <https://www.ncbi.nlm.nih.gov/books/NBK11516/> (accessed on 25 March 2018).
- Kolb, H. 2005a (updated 2007). Gross anatomy of the eye. In *Webvision: The Organization of the Retina and Visual System [Internet]*, eds. H. Kolb, E. Fernandez and R. Nelson (Salt Lake City, UT: University of Utah Health Sciences Center; 1995- ), available online: <https://www.ncbi.nlm.nih.gov/books/NBK11534/> (accessed on 15 February 2018).
- Kolb, H. 2005b (updated 2012). Simple anatomy of the retina. In *Webvision: The Organization of the Retina and Visual System [Internet]*, eds. H. Kolb, E. Fernandez and R. Nelson (Salt Lake City, UT: University of Utah Health Sciences Center; 1995- ), available online: <https://www.ncbi.nlm.nih.gov/books/NBK11533/> (accessed on 15 February 2018).
- Kolb, H. 2005c (updated 2007). Facts and figures concerning the human retina. In *Webvision: The Organization of the Retina and Visual System [Internet]*, eds. H. Kolb, E. Fernandez and R. Nelson

- (Salt Lake City, UT: University of Utah Health Sciences Center; 1995- ), available online: <https://www.ncbi.nlm.nih.gov/books/NBK11556/> (accessed on 15 February 2018).
- Kolb, H. 2005d (updated 2012). Photoreceptors. In *Webvision: The Organization of the Retina and Visual System [Internet]*, eds. H. Kolb, E. Fernandez and R. Nelson (Salt Lake City, UT: University of Utah Health Sciences Center; 1995- ), available online: <https://www.ncbi.nlm.nih.gov/books/NBK11522/> (accessed on 03 March 2018).
- Kolb, H. 2005e (updated 2007). Outer plexiform layer. In *Webvision: The Organization of the Retina and Visual System [Internet]*, eds. H. Kolb, E. Fernandez and R. Nelson (Salt Lake City, UT: University of Utah Health Sciences Center; 1995- ), available online: <https://www.ncbi.nlm.nih.gov/books/NBK11518/> (accessed on 12 March 2018).
- Kolb, H. 2005f (updated 2007). Feedback loops in the retina. In *Webvision: The Organization of the Retina and Visual System [Internet]*, eds. H. Kolb, E. Fernandez and R. Nelson (Salt Lake City, UT: University of Utah Health Sciences Center; 1995- ), available online: <https://www.ncbi.nlm.nih.gov/books/NBK11514/> (accessed on 17 March 2018).
- Kolb, H. 2005g (updated 2007). Roles of amacrine cells. In *Webvision: The Organization of the Retina and Visual System [Internet]*, eds. H. Kolb, E. Fernandez and R. Nelson (Salt Lake City, UT: University of Utah Health Sciences Center; 1995- ), available online: <https://www.ncbi.nlm.nih.gov/books/NBK11514/> (accessed on 23 March 2018).
- Kolb, H., Cuenca, N., Wang, H.H. & Dekorver, L. 1990. The synaptic organization of the dopaminergic amacrine cell in the cat retina. *J Neurocytol*, 19(3), 343-366.
- Kolb, H., Linberg, K.A. & Fisher, S.K. 1992. Neurons of the human retina: a Golgi study. *J Comp Neurol*, 318(2), 147-187.
- Kolb, H., Nelson, R. & Mariani, A. 1981. Amacrine cells, bipolar cells and ganglion cells of the cat retina: a Golgi study. *Vision Res*, 21(7), 1081-1114.
- Kolb, H. & West, R.W. 1977. Synaptic connections of the interplexiform cell in the retina of the cat. *J Neurocytol*, 6(2), 155-170.
- Kosmidou, C., Efstathiou, N.E., Hoang, M.V., Notomi, S., Konstantinou, E.K., Hirano, M., Takahashi, K., Maidana, D.E., Tsoka, P., Young, L., Gragoudas, E.S., Olsen, T.W., Morizane, Y., Miller, J.W. & Vavvas, D.G. 2017. Issues with the specificity of immunological reagents for NLRP3: Implications for age-related macular degeneration. *Sci Rep*, 8(1), 461.
- Kouyama, N. & Marshak, D.W. 1992. Bipolar cells specific for blue cones in the macaque retina. *J Neurosci*, 12(4), 1233-1252.
- Krispel, C.M., Chen, D., Melling, N., Chen, Y.J., Martemyanov, K.A., Quillinan, N., Arshavsky, V.Y., Wensel, T.G., Chen, C.K. & Burns, M.E. 2006. RGS expression rate-limits recovery of rod photoresponses. *Neuron*, 51(4), 409-416.
- Krohne, T.U., Stratmann, N.K., Kopitz, J. & Holz, F.G. 2010. Effects of lipid peroxidation products on lipofuscinogenesis and autophagy in human retinal pigment epithelial cells. *Exp Eye Res*, 90(3), 465-471.
- Kroll, S., Phillips, W.J. & Cerione, R.A. 1989. The regulation of the cyclic GMP phosphodiesterase by the GDP-bound form of the alpha subunit of transducin. *J Biol Chem*, 264(8), 4490-4497.
- Kuffler, S.W. 1953. Discharge patterns and functional organization of mammalian retina. *J Neurophysiol*, 16(1), 37-68.
- Kur, J., Newman, E.A. & Chan-Ling, T. 2012. Cellular and physiological mechanisms underlying blood flow regulation in the retina and choroid in health and disease. *Prog Retin Eye Res*, 31(5), 377-406.
- Kühn, H. & Wilden, U. 1987. Deactivation of photoactivated rhodopsin by rhodopsin-kinase and arrestin. *J Recept Res*, 7(1-4), 283-298.
- Labin, A.M. & Ribak, E.N. 2010. Retinal glial cells enhance human vision acuity. *Phys Rev Lett*, 104(15), 158102.
- LaVail, M.M. 1976. Rod outer segment disk shedding in rat retina: relationship to cyclic lighting. *Science*, 194(4269), 1071-1074.
- LaVail, M.M. 1980. Circadian nature of rod outer segment disc shedding in the rat. *Invest Ophthalmol Vis Sci*, 19(4), 407-411.
- Lee, S.W., Kim, W.J., Choi, Y.K., Song, H.S., Son, M.J., Gelman, I.H., Kim, Y.J. & Kim, K.W. 2003. SSeCKS regulates angiogenesis and tight junction formation in blood-brain barrier. *Nat Med*, 9(7), 900-906.



- Lehmann, G.L., Benedicto, I., Philp, N.J. & Rodriguez-Boulan, E. 2014. Plasma membrane protein polarity and trafficking in RPE cells: past, present and future. *Exp Eye Res*, 126, 5-15.
- Lightman, S. & Greenwood, J. 1992. Effect of lymphocytic infiltration on the blood-retinal barrier in experimental autoimmune uveoretinitis. *Clin Exp Immunol*, 88(3), 473-477.
- Lin, H. & Clegg, D.O. 1998. Integrin alphavbeta5 participates in the binding of photoreceptor rod outer segments during phagocytosis by cultured human retinal pigment epithelium. *Invest Ophthalmol Vis Sci*, 39(9), 1703-1712.
- Lin, H., Xu, H., Liang, F.Q., Gupta, P., Havey, A.N., Boulton, M.E. & Godley, B.F. 2011. Mitochondrial DNA damage and repair in RPE associated with aging and age-related macular degeneration. *Invest Ophthalmol Vis Sci*, 52(6), 3521-3529.
- Liu, R.T., Gao, J., Cao, S., Sandhu, N., Cui, J.Z., Chou, C.L., Fang, E. & Matsubara, J.A. 2013. Inflammatory mediators induced by amyloid-beta in the retina and RPE in vivo: implications for inflammasome activation in age-related macular degeneration. *Invest Ophthalmol Vis Sci*, 54(3), 2225-2237.
- Liu, R.T., Wang, A., To, E., Gao, J., Cao, S., Cui, J.Z. & Matsubara, J.A. 2014. Vinpocetine inhibits amyloid-beta induced activation of NF- $\kappa$ B, NLRP3 inflammasome and cytokine production in retinal pigment epithelial cells. *Exp Eye Res*, 127, 49-58.
- Lopez-Castejon, G., Luheshi, N.M., Compan, V., High, S., Whitehead, R.C., Flitsch, S., Kirov, A., Prudovsky, I., Swanton, E. & Brough, D. 2013. Deubiquitinases regulate the activity of caspase-1 and interleukin-1 $\beta$  secretion via assembly of the inflammasome. *J Biol Chem*, 288(4), 2721-2733.
- Lu, A., Magupalli, V.G., Ruan, J., Yin, Q., Atianand, M.K., Vos, M.R., Schröder, G.F., Fitzgerald, K.A., Wu, H. & Egelman, E.H. 2014. Unified polymerization mechanism for the assembly of ASC-dependent inflammasomes. *Cell*, 156(6), 1193-1206.
- Lucas, R.J., Douglas, R.H. & Foster, R.G. 2001. Characterization of an ocular photopigment capable of driving pupillary constriction in mice. *Nat Neurosci*, 4(6), 621-626.
- Lucas, R.J. & Foster, R.G. 1999. Neither functional rod photoreceptors nor rod or cone outer segments are required for the photic inhibition of pineal melatonin. *Endocrinology*, 140(4), 1520-1524.
- Lucas, R.J., Freedman, M.S., Muñoz, M., Garcia-Fernández, J.M. & Foster, R.G. 1999. Regulation of the mammalian pineal by non-rod, non-cone, ocular photoreceptors. *Science*, 284(5413), 505-507.
- Lucas, R.J., Hattar, S., Takao, M., Berson, D.M., Foster, R.G. & Yau, K.W. 2003. Diminished pupillary light reflex at high irradiances in melanopsin-knockout mice. *Science*, 299(5604), 245-247.
- Luibl, V., Isas, J.M., Kaye, R., Glabe, C.G., Langen, R. & Chen, J. 2006. Drusen deposits associated with aging and age-related macular degeneration contain nonfibrillar amyloid oligomers. *J Clin Invest*, 116(2), 378-385.
- Makino, E.R., Handy, J.W., Li, T. & Arshavsky, V.Y. 1999. The GTPase activating factor for transducin in rod photoreceptors is the complex between RGS9 and type 5 G protein beta subunit. *Proc Natl Acad Sci USA*, 96(5), 1947-1952.
- Mandel, L.J., Bacallao, R. & Zampighi, G. 1993. Uncoupling of the molecular 'fence' and paracellular 'gate' functions in epithelial tight junctions. *Nature*, 361(6412), 552-555.
- Mariani, A.P. 1984. Bipolar cells in monkey retina selective for the cones likely to be blue-sensitive. *Nature*, 308(5955), 184-186.
- Mariani, A.P. 1990. Amacrine cells of the rhesus monkey retina. *J Comp Neurol*, 301(3), 382-400.
- Mariathasan, S., Weiss, D.S., Newton, K., McBride, J., O'Rourke, K., Roose-Girma, M., Lee, W.P., Weinrauch, Y., Monack, D.M. & Dixit, V.M. 2006. Cryopyrin activates the inflammasome in response to toxins and ATP. *Nature*, 440(7081), 228-232.
- Marneros, A.G. 2013. NLRP3 inflammasome blockade inhibits VEGF-A-induced age-related macular degeneration. *Cell Rep*, 4(5), 945-958.
- Martinon, F., Pétrilli, V., Mayor, A., Tardivel, A. & Tschopp, J. 2006. Gout-associated uric acid crystals activate the NALP3 inflammasome. *Nature*, 440(7081), 237-241.
- Masland, R.H. 2001. The fundamental plan of the retina. *Nat Neurosci*, 4(9), 877-886.
- Masland, R.H. & Tauchi, M. 1986. The cholinergic amacrine cell. *Trends Neurosci*, 9, 218-223.
- McGeer, P.L. & Sibley, J. 2005. Sparing of age-related macular degeneration in rheumatoid arthritis. *Neurobiol Aging*, 26(8), 1199-1203.
- Medzhitov, R. 2008. Origin and physiological roles of inflammation. *Nature*, 454(7203), 428-435.

- Melyan, Z., Tarttelin, E.E., Bellingham, J., Lucas, R.J. & Hankins, M.W. 2005. Addition of human melanopsin renders mammalian cells photoreceptive. *Nature*, 433(7027), 741-745.
- Miao, E.A., Leaf, I.A., Treuting, P.M., Mao, D.P., Dors, M., Sarkar, A., Warren, S.E., Wewers, M.D. & Aderem, A. 2010. Caspase-1-induced pyroptosis is an innate immune effector mechanism against intracellular bacteria. *Nat Immunol*, 11(12), 1136-1142.
- Millen, A.E., Volland, R., Sondel, S.A., Parekh, N., Horst, R.L., Wallace, R.B., Hageman, G.S., Chappell, R., Blodi, B.A., Klein, M.L., Gehrs, K.M., Sarto, G.E., Mares, J.A. & CAREDS Study Group. 2011. Vitamin D status and early age-related macular degeneration in postmenopausal women. *Arch Ophthalmol*, 129(4), 481-489.
- Mitter, S.K., Rao, H.V., Qi, X., Cai, J., Sugrue, A., Dunn, W.A. Jr, Grant, M.B. & Boulton, M.E. 2012. Autophagy in the retina: a potential role in age-related macular degeneration. *Adv Exp Med Biol*, 723: 83-90.
- Mizushima, N. & Komatsu, M. 2011. Autophagy: renovation of cells and tissues. *Cell*, 147(4), 728-741.
- Mohr, L.K., Hoffmann, A.V., Brandstetter, C., Holz, F.G. & Krohne, T.U. 2015. Effects of inflammasome activation on secretion of inflammatory cytokines and vascular endothelial growth factor by retinal pigment epithelial cells. *Invest Ophthalmol Vis Sci*, 56(11), 6404-6413.
- Mullins, R.F., Russell, S.R., Anderson, D.H. & Hageman, G.S. 2000. Drusen associated with aging and age-related macular degeneration contain proteins common to extracellular deposits associated with atherosclerosis, elastosis, amyloidosis, and dense deposit disease. *FASEB J*, 14(7), 835-846.
- Muñoz-Planillo, R., Kuffa, P., Martínez-Colón, G., Smith, B.L., Rajendiran, T.M. & Núñez, G. 2013. K<sup>+</sup> efflux is the common trigger of NLRP3 inflammasome activation by bacterial toxins and particulate matter. *Immunity*, 38(6), 1142-1153.
- Murakami, Y., Matsumoto, H., Roh, M., Giani, A., Kataoka, K., Morizane, Y., Kayama, M., Thanos, A., Nakatake, S., Notomi, S., Hisatomi, T., Ikeda, Y., Ishibashi, T., Connor, K.M., Miller, J.W. & Vavvas, D.G. 2014. Programmed necrosis, not apoptosis, is a key mediator of cell loss and DAMP-mediated inflammation in dsRNA-induced retinal degeneration. *Cell Death Differ*, 21(2), 270-277.
- Murakami, T., Ockinger, J., Yu, J., Byles, V., McColl, A., Hofer, A.M. & Horng, T. 2012. Critical role for calcium mobilization in activation of the NLRP3 inflammasome. *Proc Natl Acad Sci USA*, 109(28), 11282-11287.
- Mure, L.S., Rieux, C., Hattar, S. & Cooper, H.M. 2007. Melanopsin-dependent nonvisual responses: evidence for photopigment bistability in vivo. *J Biol Rhythms*, 22(5), 411-424.
- Murphy-Ulrich, J.E. & Poczatek, M. 2000. Activation of latent TGF-beta by thrombospondin-1: mechanisms and physiology. *Cytokine Growth Factor Rev*, 11(1-2), 59-69.
- Nagai, N., Lundh von Leithner, P., Izumi-Nagai, K., Hosking, B., Chang, B., Hurd, R., Adamson, P., Adamis, A.P., Foxton, R.H., Ng, Y.S. & Shima, D.T. 2014. Spontaneous CNV in a novel mutant mouse is associated with early VEGF-A-driven angiogenesis and late-stage focal edema, neural cell loss, and dysfunction. *Invest Ophthalmol Vis Sci*, 55(6), 3709-3719.
- Nagelhus, E.A., Horio, Y., Inanobe, A., Fujita, A., Haug, F.M., Nielsen, S., Kurachi, Y. & Ottersen, O.P. 1999. Immunogold evidence suggests that coupling of K<sup>+</sup> siphoning and water transport in rat retinal Müller cells is mediated by a coenrichment of Kir4.1 and AQP4 in specific membrane domains. *Glia*, 26(1), 47-54.
- Nakahira, K., Haspel, J.A., Rathinam, V.A., Lee, S.J., Dolinay, T., Lam, H.C., Englert, J.A., Rabinovitch, M., Cernadas, M., Kim, H.P., Fitzgerald, K.A., Ryter, S.W. & Choi, A.M. 2011. Autophagy proteins regulate innate immune responses by inhibiting the release of mitochondrial DNA mediated by the NALP3 inflammasome. *Nat Immunol*, 12(3), 222-230.
- Nakamura, Y., McGuire, B.A. & Sterling, P. 1980. Interplexiform cell in cat retina: identification by uptake of gamma-[3H]aminobutyric acid and serial reconstruction. *Proc Natl Acad Sci USA*, 77(1), 658-661.
- Nakanishi, K., Yoshimoto, T., Tsutsui, H. & Okamura, H. 2001a. Interleukin-18 regulates both Th1 and Th2 responses. *Annu Rev Immunol*, 19, 423-474.
- Nakanishi, K., Yoshimoto, T., Tsutsui, H. & Okamura, H. 2001b. Interleukin-18 is a unique cytokine that stimulates both Th1 and Th2 responses depending on its cytokine milieu. *Cytokine Growth Factor Rev*, 53-72.
- Nandrot, E.F., Anand, M., Almeida, D., Atabai, K., Sheppard, D. & Finnemann, S.C. 2007. Essential role for MFG-E8 as ligand for alpha5beta1 integrin in diurnal retinal phagocytosis. *Proc Natl Acad Sci USA*, 104(29), 12005-12010.

- Nandrot, E.F. & Finnemann, S.C. 2008. Lack of alphavbeta5 integrin receptor or its ligand MFG-E8: distinct effects on retinal function. *Ophthalmic Res*, 40(3-4), 120-123.
- Nandrot, E.F., Silva, K.E., Scelfo, C. & Finnemann, S.C. 2012. Retinal pigment epithelial cells use a MerTK-dependent mechanism to limit the phagocytic particle binding activity of  $\alpha\beta 5$  integrin. *Biol Cell*, 104(6), 326-341.
- National Council for the Blind of Ireland. 2011. The economic impact of vision impairment and blindness in the Republic of Ireland. Available online: [http://www.ncbi.ie/files/Cost\\_of\\_Sight\\_Loss\\_Full\\_Report\\_July\\_2011.pdf](http://www.ncbi.ie/files/Cost_of_Sight_Loss_Full_Report_July_2011.pdf) (accessed on 18 September 2014).
- National Council for the Blind of Ireland. 2012. The cost of blindness in the Republic of Ireland 2010-2020. Available online: [https://www.ncbi.ie/sites/default/files/cost\\_of\\_blindness\\_pdf\\_nov\\_2012.pdf](https://www.ncbi.ie/sites/default/files/cost_of_blindness_pdf_nov_2012.pdf) (accessed on 17 September 2014).
- Nawy, S. 1999. The metabotropic receptor mGluR6 may signal through G(o), but not phosphodiesterase, in retinal bipolar cells. *J Neurosci*, 19(8), 2938-2944.
- Nawy, S. & Jahr, C.E. 1990. Suppression by glutamate of cGMP-activated conductance in retinal bipolar cells. *Nature*, 346(6281), 269-271.
- Nelson, R. & Kolb, H. 1985. A17: a broad-field amacrine cell in the rod system of the cat retina. *J Neurophysiol*, 54(3), 592-614.
- Nguyen-Legros, J. & Hicks, D. 2000. Renewal of photoreceptor outer segments and their phagocytosis by the retinal pigment epithelium. *Int Rev Cytol*, 196, 245-313.
- Nita, M., Grzybowski, A., Ascaso, F.J. & Huerva, V. 2014. Age-related macular degeneration in the aspect of chronic low-grade inflammation (pathophysiological parainflammation). *Mediators Inflamm*, 2014, 930671.
- Niven, J.E. & Laughlin, S.B. 2008. Energy limitation as a selective pressure on the evolution of sensory systems. *J Exp Biol*, 211(Pt 11), 1792-1804.
- Noël, A., Jost, M., Lambert, V., Lecomte, J. & Rakic, J.M. 2007. Anti-angiogenic therapy of exudative age-related macular degeneration: current progress and emerging concepts. *Trends Mol Med*, 13(8), 345-352.
- Nomura, A., Shigemoto, R., Nakamura, Y., Okamoto, N., Mizuno, N. & Nakanishi, S. 1994. Developmentally regulated postsynaptic localisation of a metabotropic glutamate receptor in rat rod bipolar cells. *Cell*, 77(3), 361-369.
- Nordgaard, C.L., Karunadharm, P.P., Feng, X., Olsen, T.W. & Ferrington, D.A. 2008. Mitochondrial proteomics of the retinal pigment epithelium at progressive stages of age-related macular degeneration. *Invest Ophthalmol Vis Sci*, 49(7), 2848-2855.
- Ooto, S., Akagi, T., Kageyama, R., Akita, J., Mandai, M., Honda, Y. & Takahashi, M. 2004. Potential for neural regeneration after neurotoxic injury in the adult mammalian retina. *Proc Natl Acad Sci USA*, 101(37), 13654-13659.
- Osanai, M., Takasawa, A., Murata, M. & Sawada, N. 2017. Claudins in cancer: bench to bedside. *Pflugers Arch*, 469(1), 55-67.
- Osterberg, G. 1935. Topography of the layer of rods and cones in the human retina. *Acta Ophthalmol Suppl*, 6, 1-103.
- Palm, E. 1947. On the occurrence in the retina of conditions corresponding to the blood-brain barrier. *Acta Ophthalmol (Copenh)*, 25(1), 29-35.
- Panda, S., Nayak, S.K., Campo, B., Walker, J.R., Hogenesch, J.B. & Jegla, T. 2005. Illumination of the melanopsin signaling pathway. *Science*, 307(5709), 600-604.
- Panda, S., Provencio, I., Tu, D.C., Pires, S.S., Rollag, M.D., Castrucci, A.M., Pletcher, M.T., Sato, T.K., Wiltshire, T., Andahazy, M., Kay, S.A., Van Gelder, R.N. & Hogenesch, J.B. 2003. Melanopsin is required for non-image-forming photic responses in blind mice. *Science*, 301(5632), 525-527.
- Panda, S., Sato, T.K., Castrucci, A.M., Rollag, M.D., DeGrip, W.J., Hogenesch, J.B., Provencio, I. & Kay, S.A. 2002. Melanopsin (Opn4) requirement for normal light-induced circadian phase shifting. *Science*, 298(5601), 2213-2216.
- Panda-Jonas, S., Jonas, J.B. & Jakobczyk-Zmija, M. 1996. Retinal pigment epithelial cell count, distribution, and correlations in normal human eyes. *Am J Ophthalmol*, 121(2), 181-189.
- Pardridge, W.M. 2005. Molecular biology of the blood-brain barrier. *Mol Biotechnol*, 30(1), 57-70.
- Parekh, N., Volland, R.P., Moeller, S.M., Blodi, B.A., Ritenbaugh, C., Chappell, R.J., Wallace, R.B., Mares, J.A. & CAREDS Research Study Group. 2009. Association between dietary fat intake and age-related

- macular degeneration in the carotenoids in age-related eye disease study (CAREDS): An ancillary study of the women's health initiative. *Arch Ophthalmol*, 127(11), 1483-1493.
- Pascolini, D. & Mariotti, S.P. 2012. Global estimates of visual impairment: 2010. *Br J Ophthalmol*, 96, 614-618.
- Pauleikhoff, D., Barondes, M.J., Minassian, D., Chisholm, I.H. & Bird, A.C. 1990. Drusen as risk factors in age-related macular disease. *Am J Ophthalmol*, 109(1), 38-43.
- Paulson, O.B. & Newman, E.A. 1987. Does the release of potassium from astrocyte endfeet regulate cerebral blood flow? *Science*, 237(4187), 896-898.
- Pennesi, M.E., Neuringer, M. & Courtney, R.J. 2012. Animal models of age related macular degeneration. *Mol Aspects Med*, 33(4), 487-509.
- Perez-Leon, J.A., Warren, E.J., Allen, C.N., Robinson, D.W. & Brown, R.L. 2006. Synaptic inputs to retinal ganglion cells that set the circadian clock. *Eur J Neurosci*, 24(4), 1117-1123.
- Pétrilli, V., Papin, S., Dostert, C., Mayor, A., Martinon, F. & Tschopp, J. 2007. Activation of the NALP3 inflammasome is triggered by low intracellular potassium concentration. *Cell Death Differ*, 14(9), 1583-1589.
- Picaud, S., Pattnaik, B., Hicks, D., Forster, V., Fontaine, V., Sahel, J. & Dreyfus, H. 1998. GABAA and GABAC receptors in adult porcine cones: evidence from a photoreceptor-glia co-culture model. *J Physiol*, 513(Pt 1), 33-42.
- Piippo, N., Korkmaz, A., Hytti, M., Kinnunen, K., Salminen, A., Atalay, M., Kaarniranta, K. & Kauppinen, A. 2014. Decline in cellular clearance systems induces inflammasome signaling in human ARPE-19 cells. *Biochim Biophys Acta*, 1843(12), 3038-3046.
- Plafker, S.M., O'Mealey, G.B. & Szweda, L.I. 2012. Mechanisms for countering oxidative stress and damage in retinal pigment epithelium. *Int Rev Cell Mol Biol*, 298, 135-177.
- Poitry-Yamate, C.L., Poitry, S. & Tsacopoulos, M. 1995. Lactate released by Müller glial cells is metabolized by photoreceptors from mammalian retina. *J Neurosci*, 15(7 Pt 2), 5179-5191.
- Poltorak, A., He, X., Smirnova, I., Van Huffel, C., Du, X., Birdwell, D., Alejos, E., Silva, M., Galanos, C., Freudenberg, M., Ricciardi-Castagnoli, P., Layton, B. & Beutler, B. 1998. Defective LPS signaling in C3H/HeJ and C57BL/10ScCr mice: mutations in Tlr4 gene. *Science*, 282(5396), 2085-2088.
- Poor, S.H., Qiu, Y., Fassbender, E.S., Shen, S., Woolfenden, A., Delpero, A., Kim, Y., Buchanan, N., Gebuhr, T.C., Hanks, S.M., Meredith, E.L., Jaffee, B.D. & Dryja, T.P. 2014. Reliability of the mouse model of neovascularization induced by laser photocoagulation. *Invest Ophthalmol Vis Sci*, 55(10), 6525-6534.
- Pourcho, R.G. 1982. Dopaminergic amacrine cells in the cat retina. *Brain Res*, 252(1), 101-109.
- Pourcho, R.G. & Goebel, D.J. 1983. Neuronal subpopulations in cat retina which accumulate the GABA agonist, (3H)muscimol: a combined Golgi and autoradiographic study. *J Comp Neurol*, 219(1), 25-35.
- Pourcho, R.G. & Goebel, D.J. 1985. A combined Golgi and autoradiographic study of (3H)glycine-accumulating amacrine cells in the cat retina. *J Comp Neurol*, 233(4), 473-480.
- Pournaras, C.J., Rungger-Brändle, E., Riva, C.E., Hardarson, S.H. & Stefansson, E. 2008. Regulation of retinal blood flow in health and disease. *Prog Retin Eye Res*, 27(3), 284-330.
- Prager, P., Hollborn, M., Steffen, A., Wiedemann, P., Kohen, L. & Bringmann, A. 2016. P2Y1 receptor signaling contributes to high salt-induced priming of the NLRP3 inflammasome in retinal pigment epithelial cells. *PLoS One*, 11(10), e0165653.
- Provencio, I., Jiang, G., De Grip, W.J., Hayes, W.P. & Rollag, M.D. 1998. Melanopsin: An opsin in melanophores, brain, and eye. *Proc Natl Acad Sci USA*, 95(1), 340-345.
- Provencio, I., Rodriguez, I.R., Jiang, G., Hayes, W.P., Moreira, E.F. & Rollag, M.D. 2000. A novel human opsin in the inner retina. *J Neurosci*, 20(2), 600-605.
- Provencio, I., Rollag, M.D. & Castrucci, A.M. 2002. Photoreceptive net in the mammalian retina. This mesh of cells may explain how some blind mice can still tell day from night. *Nature*, 415(6871), 493.
- Provis, J.M. 2001. Development of the primate retinal vasculature. *Prog Ret Eye Res*, 20, 799-821.
- Purnyn, H. 2013. The mammalian retina: structure and blood supply. *Neurophysiol*, 45(3), 266- 276.
- Qiu, X., Kumbalasisri, T., Carlson, S.M., Wong, K.Y., Krishna, V., Provencio, I. & Berson, D.M. 2005. Induction of photosensitivity by heterologous expression of melanopsin. *Nature*, 433(7027), 745-749.
- Rajamäki, K., Nordström, T., Nurmi, K., Åkerman, K.E., Kovanen, P.T., Öörni, K. & Eklund, K.K. 2013. Extracellular acidosis is a novel danger signal alerting innate immunity via the NLRP3 inflammasome. *J Biol Chem*, 288(19), 13410-13419.

- Rapaport, D.H., Rakic, P., Yasamura, D. & LaVail, M.M. 1995. Genesis of the retinal pigment epithelium in the macaque monkey. *J Comp Neurol*, 363(3), 359-376.
- Reese, T.S. & Karnovsky, M.J. 1967. Fine structural localization of a blood-brain barrier to exogenous peroxidase. *J Cell Biol*, 34(1), 207-217.
- Reichenbach, A., Hagen, E., Schippel, K., Brückner, G., Reichelt, W. & Leibnitz, L. 1988. Cytotopographical specialization of enzymatically isolated rabbit retinal Müller (glial) cells: structure, ultrastructure, and 3H-ouabain binding sites. *Z Mikrosk Anat Forsch*, 102(6), 897-912.
- Reichenbach, A., Schneider, H., Leibnitz, L., Reichelt, W., Schaaf, P. & Schümann, R. 1989. The structure of rabbit retinal Müller (glial) cells is adapted to the surrounding retinal layers. *Anat Embryol (Berl)*, 180(1), 71-79.
- Reichenbach, A., Wurm, A., Pannicke, T., Iandiev, I., Wiedenmann, P. & Bringmann, A. 2007. Müller cells as players in retinal degeneration and edema. *Graefes Arch Clin Exp Ophthalmol*, 245(5), 627-636.
- Ribatti, D., Nico, B., Crivellato, E., Artico, M. 2006. Development of the blood-brain barrier: a historical point of view. *Anat Rec B New Anat*, 289(1), 3-8.
- Robertson, M.J., Kirkwood, J.M., Logan, T.F., Koch, K.M., Kathman, S., Kirby, L.C., Bell, W.N., Thurmond, L.M., Weisenbach, J. & Dar, M.M. 2008. A dose-escalation study of recombinant human interleukin-18 using two different schedules of administration in patients with cancer. *Clin Cancer Res*, 14(11), 3462-3469.
- Robertson, M.J., Kline, J., Struemper, H., Koch, K.M., Bauman, J.W., Gardner, O.S., Murray, S.C., Germaschewski, F., Weisenbach, J., Jonak, Z. & Toso, J.F. 2013. A dose-escalation study of recombinant human interleukin-18 in combination with rituximab in patients with non-Hodgkin lymphoma. *J Immunother*, 36(6), 331-341.
- Robertson, M.J., Mier, J.W., Logan, T., Atkins, M., Koon, H., Koch, K.M., Kathman, S., Pandite, L.N., Oei, C., Kirby, L.C., Jewell, R.C., Bell, W.N., Thurmond, L.M., Weisenbach, J., Roberts, S. & Dar, M.M. 2006. Clinical and biological effects of recombinant human interleukin-18 administered by intravenous infusion to patients with advanced cancer. *Clin Cancer Res*, 12(14 Pt 1), 4265-4273.
- Robertson, M.J., Stamatkin, C.W., Pelloso, D., Weisenbach, J., Prasad, N.K. & Safa, A.R. 2018. A dose-escalation study of recombinant human interleukin-18 in combination with ofatumumab after autologous peripheral blood stem cell transplantation for lymphoma. *J Immunother*, 41(3), 151-157.
- Rodieck, R.W., Binmoeller, K.F. & Dineen, J. 1985. Parasol and midget ganglion cells of the human retina. *J Comp Neurol*, 233(1), 115-132.
- Ruby, N.F., Brennan, T.J., Xie, X., Cao, V., Franken, P., Heller, H.C. & O'Hara, B.F. 2002. Role of melanopsin in circadian responses to light. *Science*, 298(5601), 2211-2213.
- Rungger-Brändle, E., Messerli, J.M., Niemeyer, G. & Eppenberger, H.M. 1993. Confocal microscopy and computer-assisted image reconstruction of astrocytes in the mammalian retina. *Eur J Neurosci*, 5(8), 1093-1106.
- Ryan, S.J. 1979. The development of an experimental model of subretinal neovascularization in disciform macular degeneration. *Trans Am Ophthalmol Sol*, 77, 707-745.
- Ryan, S.J. 1980. Subretinal neovascularization after argon laser photocoagulation. *Albrecht Von Graefes Arch Klin Exp Ophthalmol*, 215(1), 29-42.
- Ryan, S.J. 1982. Subretinal neovascularization. Natural history of an experimental model. *Arch Ophthalmol*, 100(11), 1804-1809.
- Ryeom, S.W., Sparrow, J.R. & Silverstein, R.L. 1996. CD36 participates in the phagocytosis of rod outer segments by retinal pigment epithelium. *J Cell Sci*, 109(Pt 2), 387-395.
- Sagaties, M.J., Raviola, G., Schaeffer, S. & Miller, C. 1987. The structural basis of the inner blood-retina barrier in the eye of *Macaca mulatta*. *Invest Ophthalmol Vis Sci*, 28(12), 2000-2014.
- Sagulenko, V., Thygesen, S.J., Sester, D.P., Idris, A., Cridland, J.A., Vajjhala, P.R., Roberts, T.L., Schroder, K., Vince, J.E., Hill, J.M., Silke, J. & Stacey, K.J. 2013. AIM2 and NLRP3 inflammasomes activate both apoptotic and pyroptotic death pathways via ASC. *Cell Death Differ*, 20(9), 1149-1160.
- Saint-Geniez, M. & D'Amore, P.A. 2004. Development and pathology of the hyaloid, choroidal and retinal vasculature. *Int J Dev Biol*, 48(8-9), 1045-1058.
- Sakamoto, K., Liu, C., Kasamatsu, M., Pozdeyev, N.V., Iuvone, P.M. & Tosini, G. 2005. Dopamine regulates melanopsin mRNA expression in intrinsically photosensitive retinal ganglion cells. *Eur J Neurosci*, 22(12), 3129-3136.

- Sakamoto, K., Liu, C. & Tosini, G. 2004. Classical photoreceptors regulate melanopsin mRNA levels in the rat retina. *J Neurosci*, 24(43), 9693-9697.
- Sarks, S.H., Van Driel, D., Maxwell, L. & Killingsworth, M. 1980. Softening of drusen and subretinal neovascularization. *Trans Ophthalmol Soc UK*, 100(3), 414-422.
- Schroder, K. & Tschoop, J. 2010. The inflammasomes. *Cell*, 140(6), 821-832.
- Schulz, C., Gomez Perdiguero, E., Chorro, L., Szabo-Rogers, H., Cagnard, N., Kierdorf, K., Prinz, M., Wu, B., Jacobsen, S.E., Pollard, J.W., Frampton, J., Liu, K.J. & Geissmann, F. 2012. A lineage of myeloid cells independent of Myb and hematopoietic stem cells. *Science*, 336(6077), 86-90.
- Schütt, F., Davies, S., Kopitz, J., Holz, F.G. & Boulton, M.E. 2000. Photodamage to human RPE cells by A2-E, a retinoid component of lipofuscin. *Invest Ophthalmol Vis Sci*, 41(8), 2303-2308.
- Schwartz, E.A. 1982. Calcium-independent release of GABA from isolated horizontal cells of the toad retina. *J Physiol*, 323, 211-227.
- Sekaran, S., Lupi, D., Jones, S.L., Sheely, C.J., Hattar, S., Yau, K.W., Lucas, R.J., Foster, R.G. & Hankins, M.W. 2005. Melanopsin-dependent photoreception provides earliest light detection in the mammalian retina. *Curr Biol*, 15(12), 1099-1107.
- Shakib, M. & Cunha-Vaz, J.G. 1966. Studies on the permeability of the blood-retinal barrier. IV. Junctional complexes of the retinal vessels and their role in the permeability of the blood-retinal barrier. *Exp Eye Res*, 5(3), 229-234.
- Shapley, R. & Perry, V.H. 1986. Cat and monkey retinal ganglion cells and their visual functional roles.
- Shen, J., Choy, D.F., Yoshida, T., Iwase, T., Hafiz, G., Xie, B., Hackett, S.F., Arron, J.R. & Campochiaro, P.A. 2014. Interleukin-18 has antipermeability and antiangiogenic activities in the eye: reciprocal suppression with VEGF. *J Cell Physiol*, 229(8), 974-983.
- Shi, C.S., Shenderov, K., Huang, N.N., Kabat, J., Abu-Asab, M., Fitzgerald, K.A., Sher, A. & Kehrl, J.H. 2012. Activation of autophagy by inflammatory signals limits IL-1 $\beta$  production by targeting ubiquitinated inflammasomes for destruction. *Nat Immunol*, 13(3), 255-263.
- Shi, G., Chen, S., Wandu, W.S., Ogbeifun, O., Nugent, L.F., Maminishkis, A., Hinshaw, S.J., Rodriguez, I.R. & Gery, I. 2015. Inflammasomes induced by 7-ketocholesterol and other stimuli in RPE and in bone marrow-derived cells differ markedly in their production of IL-1 $\beta$  and IL-18. *Invest Ophthalmol Vis Sci*, 56(3), 1658-1664.
- Shiells, R.A. & Falk, G. 1990. Glutamate receptors of rod bipolar cells are linked to a cyclic GMP cascade via a G-protein. *Proc Biol Sci*, 242(1304), 91-94.
- Shimada, K., Crother, T.R., Karlin, J., Dagvadorj, J., Chiba, N., Chen, S., Ramanujan, V.K., Wolf, A.J., Vergnes, L., Ojcius, D.M., Rentsendorj, A., Vargas, M., Guerrero, C., Wang, Y., Fitzgerald, K.A., Underhill, D.M., Town, T. & Arditi, M. 2012. Oxidized mitochondrial DNA activates the NLRP3 inflammasome during apoptosis. *Immunity*, 36(3), 401-414.
- Sikka, G., Hussmann, G.P., Pandey, D., Cao, S., Hori, D., Park, J.T., Stepan, J., Kim, J.H., Barodka, V., Myers, A.C., Santhanam, L., Nyhan, D., Halushka, M.K., Koehler, R.C., Snyder, S.H., Shimoda, L.A. & Berkowitz, D.E. 2014. Melanopsin mediates light-dependent relaxation in blood vessels. *Proc Natl Acad Sci USA*, 111(50), 17977-17982.
- Simpkins, F., Flores, A., Chu, C., Berek, J.S., Lucci, J. 3rd, Murray, S., Bauman, J., Struemper, H., Germaschewski, F., Jonak, Z., Gardner, O., Toso, J. & Coukos, G. 2013. Chemoimmunotherapy using pegylated liposomal doxorubicin and interleukin-18 in recurrent ovarian cancer: a phase I dose-escalation study. *Cancer Immunol Res*, 1(3), 168-178.
- Singhal, S., Bhatia, B., Jayaram, H., Becker, S., Jones, M.F., Cottrill, P.B., Khaw, P.T., Salt, T.E. & Limb, G.A. 2012. Human Müller glia with stem cell characteristics differentiate into retinal ganglion cell (RGC) precursors in vitro and partially restore RGC function in vivo following transplantation. *Stem Cells Transl Med*, 1(3), 188-199.
- Skiba, N.P., Hopp, J.A. & Arshavsky, V.Y. 2000. The effector enzyme regulates the duration of G protein signaling in vertebrate photoreceptors by increasing the affinity between transducin and RGS protein. *J Biol Chem*, 275(42), 32716-32720.
- Spadoni, I., Fornasa, G. & Rescigno, M. 2017. Organ-specific protection mediated by cooperation between vascular and epithelial barriers. *Nat Rev Immunol*, 17(12), 761-773.
- Sparrow, J.R. & Boulton, M. 2005. RPE lipofuscin and its role in retinal pathobiology. *Exp Eye Res*, 80(5), 595-606.

- Srivastava, S., Salim, N. & Robertson, M.J. 2010. Interleukin-18: biology and role in the immunotherapy of cancer. *Curr Med Chem*, 17(29), 3353-3357.
- Steinberg, R.H., Fisher, S.K. & Anderson, D.H. 1980. Disc morphogenesis in vertebrate photoreceptors. *J Comp Neurol*, 190(3), 501-508.
- Steinberg, R.H., Wood, I. & Hogan, M.J. 1977. Pigment epithelial ensheathment and phagocytosis of extrafoveal cones in human retina. *Philos Trans R Soc Lond B Biol Sci*, 277(958), 459-474.
- Stone, J. & Dreher, Z. 1987. Relationship between astrocytes, ganglion cells and vasculature of the retina. *J Comp Neurol*, 255(1), 35-49.
- Strauss, O. 2005. The retinal pigment epithelium in visual function. *Physiol Rev*, 85(3), 845-881.
- Strauss, O. 2011. The retinal pigment epithelium. In *Webvision: The Organization of the Retina and Visual System [Internet]*, eds. H. Kolb, E. Fernandez and R. Nelson (Salt Lake City, UT: University of Utah Health Sciences Center; 1995- ), available online: <https://www.ncbi.nlm.nih.gov/books/NBK54392/> (accessed on 28 March 2018).
- Streilein, J.W. 2003. Ocular immune privilege: the eye takes a dim but practical view of immunity and inflammation. *J Leukoc Biol*, 74(2), 179-185.
- Strowig, T., Henao-Mejia, J., Elinav, E. & Flavell, R. 2012. Inflammasomes in health and disease. *Nature*, 481(7381), 278-286.
- Sui, G.Y., Liu, G.C., Liu, G.Y., Gao, Y.Y., Deng, Y., Wang, W.Y., Tong, S.H. & Wang, L. 2013. Is sunlight exposure a risk factor for age-related macular degeneration? A systematic review and meta-analysis. *Br J Ophthalmol*, 97(4), 389-394.
- Takano, K., Kojima, T., Sawada, N. & Himi, T. 2014. Role of tight junctions in signal transduction: an update. *EXCLI J*, 13, 1145-1162.
- Tarallo, V., Hirano, Y., Gelfand, B.D., Dridi, S., Kerur, N., Kim, Y., Cho, W.G., Kaneko, H., Fowler, B.J., Bogdanovich, S., Albuquerque, R.J., Hauswirth, W.W., Chiodo, V.A., Kugel, J.F., Goodrich, J.A., Ponicsan, S.L., Chaudhuri, G., Murphy, M.P., Dunaief, J.L., Ambati, B.K., Ogura, Y., Yoo, J.W., Lee, D.K., Provost, P., Hinton, D.R., Núñez, G., Baffi, J.Z., Kleinman, M.E. & Ambati, J. 2012. DICER1 loss and Alu RNA induce age-related macular degeneration via the NLRP3 inflammasome and MyD88. *Cell*, 149(4), 847-859.
- Taylor, A.W. 2009. Ocular immune privilege. *Eye (Lond)*, 23(10), 1885-1889.
- Tevy, M.F., Giebultowicz, J., Pincus, Z., Mazzocchi, G. & Vinciguerra, M. 2013. Aging signaling pathways and circadian clock-dependent metabolic derangements. *Trends Endocrinol Metab*, 24(5), 229-237.
- Thoreson, W.B. & Mangel, S.C. 2012. Lateral interactions in the outer retina. *Prog Retin Eye Res*, 31(5), 407-441.
- Tobe, T., Ortega, S., Luna, J.D., Ozaki, H., Okamoto, N., Derevanik, N.L., Vinoses, S.A., Basilico, C. & Campochiaro, P.A. 1998. Targeted disruption of the FGF2 gene does not prevent choroidal neovascularization in a murine model. *Am J Pathol*, 153(5), 1641-1646.
- Tout, S., Chan-Ling, T., Holländer, H. & Stone, J. 1993. The role of Müller cells in the formation of the blood-retinal barrier. *Neuroscience*, 55(1), 291-301.
- Travis, G.H., Golczak, M., Moise, A.R. & Palczewski, K. 2007. Diseases caused by defects in the visual cycle: retinoids as potential therapeutic agents. *Annu Rev Pharmacol Toxicol*, 47, 469-512.
- Tsang, S.H., Burns, M.E., Calvert, P.D., Gouras, P., Baylor, D.A., Goff, S.P. & Arshavsky, V.Y. 1998. Role for the target enzyme in deactivation of photoreceptor G protein in vivo. *Science*, 282(5386), 117-121.
- Tschopp, J. & Schroder, K. 2010. NLRP3 inflammasome activation: The convergence of multiple signalling pathways on ROS production? *Nat Rev Immunol*, 10(3), 210-215.
- Tseng, W.A., Thein, T., Kinnunen, K., Lashkari, K., Gregory, M.S., D'Amore, P.A. & Ksander, B.R. 2013. NLRP3 inflammasome activation in retinal pigment epithelial cells by lysosomal destabilization: implications for age-related macular degeneration. *Invest Ophthalmol Vis Sci*, 54(1), 110-120.
- Tu, D.C., Owens, L.A., Anderson, L., Golczak, M., Doyle, S.E., McCall, M., Menaker, M., Palczewski, K. & Van Gelder, R.N. 2006. Inner retinal photoreception independent of the visual retinoid cycle. *Proc Natl Acad Sci USA*, 103(27), 10426-10431.
- Vandenabeele, P., Galluzzi, L., Vanden Berghe, T. & Kroemer, G. 2010. Molecular mechanisms of necroptosis: an ordered cellular explosion. *Nat Rev Mol Cell Biol*, 11(10), 700-714.
- Van Hook, M.J., Wong, K.Y. & Berson, D.M. 2012. Dopaminergic modulation of ganglion-cell photoreceptors in rat. *Eur J Neurosci*, 35(4), 507-518.

- van Meer, G. & Simons, K. 1986. The function of tight junctions in maintaining differences in lipid composition between the apical and the basolateral cell surface domains of MDCK cells. *EMBO J*, 5(7), 1455-1464.
- Vardi, N. & Morigiwa, K. 1997. ON cone bipolar cells in rat express the metabotropic receptor mGluR6. *Vis Neurosci*, 14(4), 789-794.
- Vecino, E., Rodriguez, F.D., Ruzafa, N., Pereiro, X. & Sharma, S.C. 2016. Glia-neuron interactions in the mammalian retina. *Prog Retin Eye Res*, 51, 1-40.
- Verweij, J., Hornstein, E.P. & Schnapf, J.L. 2003. Surround antagonism in macaque cone photoreceptors. *J Neurosci*, 23(32), 10249-10257.
- Verweij, J., Kamermans, M. & Spekrijse, H. 1996. Horizontal cells feed back to cones by shifting the cone calcium-current activation range. *Vision Res*, 36(24), 3943-3953.
- Vessey, J.P., Stratis, A.K., Daniels, B.A., Da Silva, N., Jonz, M.G., Lalonde, M.R., Baldrige, W.H. & Barnes, S. 2005. Proton-mediated feedback inhibition of presynaptic calcium channels at the cone photoreceptor synapse. *J Neurosci*, 25(16), 4108-4117.
- Vinding, T. 1990. Occurrence of drusen, pigmentary changes and exudative changes in the macula with reference to age-related macular degeneration. An epidemiological study of 1000 aged individuals. *Acta Ophthalmol (Copenh)*, 68(4), 410-414.
- Vives-Bauza, C., Anand, M., Shiraz, A.K., Magrane, J., Gao, J., Vollmer-Snarr, H.R., Manfredi, G. & Finnemann, S.C. 2008. The age lipid A2E and mitochondrial dysfunction synergistically impair phagocytosis by retinal pigment epithelial cells. *J Biol Chem*, 283(36), 24770-24780.
- Voigt, T. & Wässle, H. 1987. Dopaminergic innervation of A II amacrine cells in mammalian retina. *J Neurosci*, 7(12), 4115-4128.
- Vollrath, D., Feng, W., Duncan, J.L., Yasumura, D., D'Cruz, P.M., Chappelow, A., Matthes, M.T., Kay, M.A., LaVail, M.M. 2001. Correction of the retinal dystrophy phenotype of the RCS rat by viral gene transfer of Mertk. *Proc Natl Acad Sci USA*, 98(22), 12584-12589.
- Vroman, R., Klaassen, L.J., Howlett, M.H., Cenedese, V., Klooster, J., Sjoerdsma, T. & Kamermans, M. 2014. Extracellular ATP hydrolysis inhibits synaptic transmission by increasing pH buffering in the synaptic cleft. *PLoS Biol*, 12(5), e1001864.
- Wang, A.L., Lukas, T.J., Yuan, M., Du, N., Tso, M.O. & Neufeld, A.H. 2009. Autophagy, exosomes and drusen formation in age-related macular degeneration. *Autophagy*, 5(4), 563-564.
- Wang, K., Yao, Y., Zhu, X., Zhang, K., Zhou, F. & Zhu, L. 2017. Amyloid  $\beta$  induces NLRP3 inflammasome activation in retinal pigment epithelial cells via NADPH oxidase- and mitochondria-dependent ROS production. *J Biochem Mol Toxicol*, 31(6), doi: 10.1002/jbt.21887.
- Wang, L., Clark, M.E., Crossman, D.K., Kojima, K., Messinger, J.D., Mobley, J.A. & Curcio, C.A. 2010. Abundant lipid and protein components of drusen. *PLoS One*, 5(4), e10329.
- Wang, Y., Hanus, J.W., Abu-Asab, M.S., Shen, D., Ogilvy, A., Ou, J., Chu, X.K., Shi, G., Li, W., Wang, S. & Chan, C.C. 2016. NLRP3 upregulation in retinal pigment epithelium in age-related macular degeneration. *Int J Mol Sci*, 17(1), pii: E73.
- Watanabe, T. & Raff, M.C. 1988. Retinal astrocytes are immigrants from the optic nerve. *Nature*, 332(6167), 834-837.
- Whitcup, S.M., Sodhi, A., Atkinson, J.P., Holers, V.M., Sinha, D., Rohrer, B. & Dick, A.D. 2013. The role of the immune response in age-related macular degeneration. *Int J Inflam*, 2013, 348092.
- Wilden, U., Hall, S.W. & Kühn, H. 1986. Phosphodiesterase activation by photoexcited rhodopsin is quenched when rhodopsin is phosphorylated and binds the intrinsic 48-kDa protein of rod outer segments. *Proc Natl Acad Sci USA*, 83(5), 1174-1178.
- Winkler, B.S., Boulton, M.E., Gottsch, J.D. & Sternberg, P. 1999. Oxidative damage and age-related macular degeneration. *Mol Vis*, 5, 32.
- Wislocki, G.B. & Ladman, A.J. 1955. The demonstration of a blood-ocular barrier in the albino rat by means of the intravitam deposition of silver. *J Biophys Biochem Cytol*, 1(6), 501-510.
- Wong, K.Y., Dunn, F.A., Graham, D.M. & Berson, D.M. 2007. Synaptic influences on rat ganglion-cell photoreceptors. *J Physiol*, 582(Pt 1), 279-296.
- Wong, W.L., Su, X., Li, X., Cheung, C.M., Klein, R., Cheng, C.Y. & Wong, T.Y. 2014. Global prevalence of age-related macular degeneration and disease burden projection for 2020 and 2040: A systematic review and meta-analysis. *Lancet Glob Health*, 2(2), e106-116.



- World Health Organization. Available online: <http://www.who.int/blindness/causes/priority/en/index7.html> (accessed on 5 September 2017).
- World Health Organization. Available online: <http://www.who.int/blindness/causes/en/> (accessed on 5 September 2017).
- Wu, H., Che, X., Zheng, Q., Wu, A., Pan, K., Shao, A., Wu, Q., Zhang, J. & Hong, Y. 2014. Caspases: a molecular switch node in the crosstalk between autophagy and apoptosis. *Int J Biol Sci*, 10(9), 1072-1083.
- Xu, H., Chen, M. & Forrester, J.V. 2009. Para-inflammation in the aging retina. *Prog Retin Eye Res*, 28(5), 348-368.
- Xue, T., Do, M.T., Riccio, A., Jiang, Z., Hsieh, J., Wang, H.C., Merbs, S.L., Welsbie, D.S., Yoshioka, T., Weissgerber, P., Stolz, S., Flockerzi, V., Freichel, M., Simon, M.I., Clapham, D.E. & Yau, K.W. 2011. Melanopsin signalling in mammalian iris and retina. *Nature*, 479(7371), 67-73.
- Yamasaki, K., Muto, J., Taylor, K.R., Cogen, A.L., Audish, D., Bertin, J., Grant, E.P., Coyle, A.J., Misaghi, A., Hoffman, H.M. & Gallo, R.L. 2009. NLRP3/cryopyrin is necessary for interleukin-1beta (IL-1beta) release in response to hyaluronan, an endogenous trigger of inflammation in response to injury. *J Biol Chem*, 284(19), 12762-12771.
- Yamazaki, S., Goto, M. & Menaker, M. 1999. No evidence for extraocular photoreceptors in the circadian system of the Syrian hamster. *J Biol Rhythms*, 14(3), 197-201.
- Yang, Z. & Klionsky, D.J. 2010. Mammalian autophagy: core molecular machinery and signaling regulation. *Curr Opin Cell Biol*, 22(2), 124-131.
- Yazdi, A.S., Guarda, G., Riteau, N., Drexler, S.K., Tardivel, A., Couillin, I. & Tschopp, J. 2010. Nanoparticles activate the NLR pyrin domain containing 3 (Nlrp3) inflammasome and cause pulmonary inflammation through release of IL-1 $\alpha$  and IL-1 $\beta$ . *Proc Natl Acad Sci USA*, 107(45), 19449-19454.
- Young, R.W. 1967. The renewal of photoreceptor cell outer segments. *J Cell Biol*, 33(1), 61-72.
- Young, R.W. 1971. The renewal of rod and cone outer segments in the rhesus monkey. *J Cell Biol*, 49(2), 303-318.
- Young, R.W. 1976. Visual cells and the concept of renewal. *Invest Ophthalmol Vis Sci*, 15(9), 700-725.
- Young, R.W. & Bok, D. 1969. Participation of the retinal pigment epithelium in the rod outer segment renewal process. *J Cell Biol*, 42(2), 392-403.
- Yu, D.Y. & Cringle, S.J. 2001. Oxygen distribution and consumption within the retina in vascularised and avascular retinas and in animal models of retinal disease. *Prog Retin Eye Res*, 20(2), 175-208.
- Zaidi, F.H., Hull, J.T., Peirson, S.N., Wulff, K., Aeschbach, D., Gooley, J.J., Brainard, G.C., Gregory-Evans, K., Rizzo, J.F. 3rd, Czeisler, C.A., Foster, R.G., Moseley, M.J. & Lockley, S.W. 2007. Short-wavelength light sensitivity of circadian, pupillary, and visual awareness in humans lacking an outer retina. *Curr Biol*, 17(24), 2122-2128.
- Zarbin, M.A. 2004. Current concepts in the pathogenesis of age-related macular degeneration. *Arch Ophthalmol*, 122(4), 598-614.
- Zhou, R. & Caspi, R.R. 2010. Ocular immune privilege. *F1000 Biol Rep*, 2(3).
- Zhou, R., Tardivel, A., Thorens, B., Choi, I. & Tschopp, J. 2010. Thioredoxin-interacting protein links oxidative stress to inflammasome activation. *Nat Immunol*, 11(2), 136-140.
- Zhou, R., Yazdi, A.S., Menu, P. & Tschopp, J. 2011. A role for mitochondria in NLRP3 inflammasome activation. *Nature*, 469(7329), 221-225.

# **Appendix**

# IL-18 Immunotherapy for Neovascular AMD: Tolerability and Efficacy in Nonhuman Primates

Sarah L. Doyle,<sup>1</sup> Francisco J. López,<sup>2</sup> Lucia Celkova,<sup>3</sup> Kiva Brennan,<sup>1</sup> Kelly Mulfaul,<sup>1</sup> Ema Ozaki,<sup>3</sup> Paul F. Kenna,<sup>3,4</sup> Edit Kurali,<sup>5</sup> Natalie Hudson,<sup>3</sup> Teresa Doggett,<sup>6</sup> Thomas A. Ferguson,<sup>6</sup> Peter Humphries,<sup>3</sup> Peter Adamson,<sup>7,8</sup> and Matthew Campbell<sup>3</sup>

<sup>1</sup>Department of Clinical Medicine, School of Medicine, Trinity College Dublin, Dublin, Ireland

<sup>2</sup>Ophthalmology Discovery Performance Unit, GlaxoSmithKline, King of Prussia, Pennsylvania, United States

<sup>3</sup>Ocular Genetics Unit, Smurfit Institute of Genetics, Trinity College Dublin, Dublin, Ireland

<sup>4</sup>The Research Foundation, Royal Victoria Eye and Ear Hospital, Adelaide Road, Dublin, Ireland

<sup>5</sup>Statistics Consulting Group, Quantitative Science, PTS, GlaxoSmithKline, King of Prussia, Pennsylvania, United States

<sup>6</sup>Department of Ophthalmology and Visual Science, Washington University School of Medicine, St. Louis, Missouri, United States

<sup>7</sup>Ophthalmology Discovery Performance Unit, GlaxoSmithKline, Stevenage, United Kingdom

<sup>8</sup>Ocular Biology and Therapeutics, Institute of Ophthalmology, University College London, London, United Kingdom

Correspondence: Sarah L. Doyle, Department of Clinical Medicine, School of Medicine, Trinity College Dublin, Dublin 2, Ireland; sarah.doyle@tcd.ie.

Matthew Campbell, Ocular Genetics Unit, Smurfit Institute of Genetics, Trinity College Dublin, Dublin 2, Ireland; matthew.campbell@tcd.ie.

Submitted: May 13, 2015

Accepted: June 27, 2015

Citation: Doyle SL, López FJ, Celkova L, et al. IL-18 immunotherapy for neovascular AMD: tolerability and efficacy in nonhuman primates. *Invest Ophthalmol Vis Sci.* 2015;56:5424–5430. DOI:10.1167/iovs.15-17264

**PURPOSE.** Age-related macular degeneration is the most common form of central retinal blindness in the elderly. Of the two end stages of disease, neovascular AMD—although the minority form—is the most severe. Current therapies are highly successful at controlling progression of neovascular lesions; however, a significant number of patients remain refractory to treatment and the development of alternative and additive therapies to anti-VEGFs is essential.

**METHODS.** In order to address the translational potential of interleukin (IL)-18 for use in neovascular AMD, we initiated a nonhuman primate tolerability and efficacy study for the use of intravitreally (IVT) administered clinical grade human IL-18 (SB-485232). Cynomolgus monkeys were injected IVT with increasing doses of human IL-18 (two each at 1000, 3000, and 10,000 ng per eye). In tandem, 21 monkeys were administered nine laser burns in each eye prior to receiving IL-18 as an IVT injection at a range of doses. Fundus fluorescein angiography (FFA) was performed on days 8, 15, and 22 post injection and the development of neovascular lesions was assessed.

**RESULTS.** We show intravitreal, mature, recombinant human IL-18 is safe and can reduce choroidal neovascular lesion development in cynomolgus monkeys.

**CONCLUSIONS.** Based on our data comparing human IL-18 to current anti-VEGF-based therapy, clinical deployment of IL-18 for neovascular AMD has the potential to lead to a new adjuvant immunotherapy-based treatment for this severe form of central blindness.

Keywords: interleukin-18, immunotherapy, age-related macular degeneration

It is estimated that 1 in 10 people aged older than 55 years show early signs of AMD. In 10% of patients with AMD, blood vessels sprout from underlying choroidal vasculature disrupting retinal tissue integrity, leading to vision loss. Although less common, the neovascular form of the disease, termed “wet” AMD, is the most severe form and is termed a priority eye disease by the World Health Organization. Wet AMD can be treated acutely with regular intraocular injections of antibodies or fusion proteins directed against VEGF.<sup>1</sup> These treatments have revolutionized AMD therapy, stabilizing the areas of choroidal neovascularization (CNV) and delaying further neovascularization. However, there is no end stage to treatment as patients require regular injections to sustain efficacy and there is a proportion of patients who will remain refractory to treatment. Evidence also suggests that long-term use of “anti-VEGFs” is damaging to the retina due to the role of VEGFs as a neuronal survival factor and long-term progression of underlying AMD continues.<sup>2</sup> These data illustrate the critical requirement for the development of new therapeutic targets and novel strategies for the treatment and management of AMD. Indeed

other mechanistic approaches which do not target VEGF—but used in combination with anti-VEGF therapeutics such as anti-PDGF aptamers (Fovista; Ophthotech Corp., New York, NY, USA)—have proved successful in clinical studies to date,<sup>3</sup> and are currently undergoing phase III studies in neovascular AMD. The use of anti-PDGF aptamers, dosed between anti-VEGF doses, sensitizes the infiltrating choroidal neovessels to the anti-VEGF therapeutic resulting in enhanced efficacy and demonstrating effective interaction between two independent mechanisms. Here we provide evidence that interleukin-18 (IL-18) can be considered as a safe and relatively effective intravitreal immunotherapy for the treatment of wet AMD that could now be used alongside current therapeutic approaches.

## MATERIALS AND METHODS

### Mice

JR5558 mice that harbored the Rd8 mutation were bred at GSK and shipped to Trinity College Dublin for experimentation.

Mice were housed in a specific pathogen-free environment throughout the course of treatment and were used between the ages of 3 and 8 weeks. Animals were injected intraperitoneally with mouse IL-18.

### Western Blot and Antibodies

We grew retinal microvascular endothelial cells (RMVECs) to confluency and treated them with vehicle or hIL-18 (10, 100, 1000 ng/mL) for 6 or 24 hours as indicated. Cells were then treated with VEGF (0.1, 0.3, 1, 3, 10, 30, 100 ng/mL) for an additional 24 hours. Cells were lysed in RIPA buffer (plus protease inhibitors; Roche, Dublin, Ireland). Protein concentrations were measured by BCA assay and equal amounts of protein were separated by SDS-PAGE gel electrophoresis, transferred to PVDF membrane, and incubated with VEGFR2 (Cell Signaling Technology, Inc., Beverly, MA, USA) or  $\beta$ -actin (Abcam, Cambridge, UK) and visualized by autoradiography.

### Quantitative Polymerase Chain Reaction

We grew RMVECs to confluency and treated them with vehicle or hIL-18 (50 ng/mL) for 4, 8, or 24 hours as indicated. Using a commercial kit (RNeasy Isolation kit; Qiagen, Venlo, Limburg, The Netherlands), RNA was extracted according to the manufacturer's protocol. Relative expression of VEGF-A and VEGFR-1, -2, and -3 was analyzed by quantitative PCR. We prepared cDNA from 20 ng/mL total RNA using an archive kit (High-Capacity cDNA; Applied Biosystems, Waltham, MA, USA). A real-time PCR platform (AB7900FAST; Applied Biosystems) was used for all PCRs in triplicate. Changes in expression were calculated by the change in threshold ( $\Delta\Delta C_T$ ) method with *Gapdh* as an endogenous control for gene-expression analysis and were normalized to results obtained with vehicle treated cells.

### Electroretinography

We dark-adapted JR5558 mice overnight and prepared them for ERG under dim red light. Electroretinogram responses were recorded simultaneously from both mouse eyes by means of gold wire electrodes (Roland Consulting GmbH, Havel, Germany) using topical eye gel (Vidisc; Dr. Mann Pharma, Berlin, Germany) as a conducting agent in addition to maintaining corneal hydration.

### Monkey Tolerability Study

Female cynomolgus monkeys ( $n=2$  per dose) were administered ascending doses (1000, 3000, and 10,000 ng) of IL-18 (SB-485232) and vehicle control (25 mM sodium acetate, 0.1 M EDTA), 6% (wt/vol) sucrose and 0.05% Tween 80 at pH 4) by IVT injection (50  $\mu$ L per eye) and followed for 15 days. After enucleation, eyes were fixed in 3% glutaraldehyde for a minimum of 24 hours, followed by transfer to 10% neutral buffered formalin before processing and staining with hematoxylin and eosin. Images represent a section of the retina in the region of the macula from the eye of a single monkey administered either vehicle control or IL-18 by IVT injection. Monkeys used were bred in captivity and were of Vietnamese origin. Animals were aged <3 years at time of study. All relevant ethical approval documentation was obtained before study initiation.

### Monkey Efficacy Study

A total of 21 male cynomolgus monkeys (*Macaca fascicularis*) aged 2 to 4 years and weighing 2 to 5 kg were obtained from Covance Research Products. Animals were fed Certified Primate Diet #2055C (Harlan Laboratories, Inc., Indianapolis, IN, USA) with access to water ad libitum and maintained at 18

to 26°C, with a relative humidity of 30% to 70%, a minimum of 10 air changes/hour, and a 12-hour light/12-hour dark cycle. Prior to IVT injections, the eyes were anesthetized using topical anesthetic (0.5% proparacaine, Bausch & Lomb Pharmaceuticals, Tampa, FL, USA), cleaned with 1% povidone iodine (prepared with sterile saline and 10% povidone iodine, Bausch & Lomb Pharmaceuticals), and rinsed with sterile saline. The periorbital region was cleaned with a dilute, 1% povidone-iodine solution. Doses were administered by intravitreal injection using a 1-mL syringe and a 30-G (injections) or 25-G (implants) needle. Injections were made into the inferior aspect of the eye. A topical antibiotic (Tobrex, 0.3%, Alcon, Fort Worth, TX, USA) was instilled in each eye following the intravitreal injection. For laser photocoagulation, the macula of each eye was targeted with a 532-nm diode green laser (OcuLight GL; IRIDEX Corp, Inc., Mountain View, CA, USA) using a slit lamp delivery system and a Kaufman-Wallow plano fundus contact lens (Ocular Instruments Inc., Bellevue, WA, USA). Animals were anesthetized and nine areas symmetrically placed in the macula of each eye. The laser parameters included a 75- $\mu$ m spot size and 0.1-second duration. The power setting was assessed by the ability to produce a blister and a small hemorrhage. If hemorrhage was not observed with the first laser treatment, a second laser spot was placed adjacent to the first following the same laser procedure, except at a higher wattage. For areas not adjacent to the fovea, the initial power setting was 500 mW; if a second spot was placed, the power was set to 650 mW. For the area adjacent to the fovea, the power setting was 400 mW for initial treatment and 550 mW for secondary treatment. At the discretion of the vitreoretinal surgeon, power settings were further adjusted based on observations at the time of photocoagulation. Fundus fluorescein angiography was conducted on days 8, 15, 22, and occasionally 29 following laser photocoagulation. Animals fasted for at least 2 hours prior to being anesthetized, and the eyes were dilated with a mydriatic agent. Animals were intubated due to the possibility of emesis following the fluorescein injection. Images were taken at the start and end of the intravenous fluorescein injection. Following fluorescein injection, a rapid series (approximately from dye appearance through 35 seconds) of stereo photographs of the posterior pole were taken of the right eye followed by a stereo pair of the posterior pole of the left eye. Additional stereo pairs were taken of both eyes at approximately 1 to 2 and 5 minutes after fluorescein injection. Between approximately 2 and 5 minutes after fluorescein injection, nonstereoscopic photographs were taken of two midperipheral fields (temporal and nasal) of each eye. Images of FFA were evaluated according to the following grading system which has been described previously<sup>4</sup>: grade I, no hyperfluorescence; grade II, hyperfluorescence without leakage; grade III, early- or midtransit hyperfluorescence and late leakage; grade IV, bright early- or midtransit hyperfluorescence and late leakage outside the borders of the treated area. Since grade IV lesions most closely resemble CNV seen in various human retinal disorders, including AMD, incidence of grade IV lesions was compared between groups. This analysis was performed by a masked observer. All animal procedures were ethically reviewed and approved according to the British Home Office Animals Scientific Procedures Act 1986 and were performed in accordance with European Directive 86/609/EEC, the GSK Policy on the Care, Welfare and Treatment of Animals, and the ARVO Statement for the Use of Animals in Ophthalmic and Vision Research.

### Statistical Methods

The number of grade 4 lesions (0–9) per eye (the response Y) was modeled using a truncated Poisson distribution. The

experimental design took advantage of historical controls provided by Covance (Covance database; Covance, Madison, WI, USA). Bayesian simulations were performed to determine group sample sizes that would ensure at least 80% power to detect a decreasing dose-related trend in the response; 1000 datasets from a 4-parameter logistic function with known parameters (Min and Max parameters set to historical positive and negative controls in the Covance database, Hill slope = -1, ED99 = 100) were simulated and a Bayesian (truncated) Poisson linear regression model with informative prior on the Maximum parameter (corresponding to the mean of the historical Vehicle data) was fit to each dataset. The posterior probability ( $P$ ) of a decreasing dose-related trend (negative slope) was calculated and the number of datasets ( $n$ ) with  $P > 80\%$  was recorded. The group sample size was calibrated to keep the power ( $n/1000$ )  $> 80\%$ .

Final data analysis was conducted using a Bayesian (truncated) Poisson linear regression model with informative prior information from the Covance database. This model was fitted to all the data. The posterior probabilities of a decreasing dose-related trend (negative slope) were calculated as well as the posterior probability of the response at the maximal dose  $Y_{dmax} < 1$  (efficacy similar to Lucentis). The Bayesian simulation work was carried out using the BRUGS package in R 3.1.1 (available in the public domain at <https://cran.r-project.org/web/packages/BRugs/index.html>) calling OpenBugs 3.2.3 in the background. The final data analysis was carried out in R.

## RESULTS

### IL-18 Prevents Spontaneous Neovascular Lesion Development

We previously reported that the proinflammatory cytokine IL-18 could prevent CNV, in a laser-induced mouse model of the condition.<sup>5</sup> The laser-induced CNV model was established as a highly reproducible model in nonhuman primates; however, its use in the mouse eye is less straightforward and appears susceptible to variability as highlighted by Poor et al.<sup>6</sup> in a comprehensive study reported in 2014. Therefore, we assessed the efficacy response of mouse IL-18 (SB-528775; Glaxo-SmithKline [GSK], Stevenage, UK) on the formation of neovascular lesions in the central region of the retinas of the recently described JR5558 mice, which develop bilateral spontaneous CNV and retinal angiomatous proliferation (RAP; Figs. 1A, 1B).<sup>7,8</sup> Interleukin 18 was administered by intraperitoneal (IP) injection at doses of 0.1 or 1 mg/kg for 4 days either as lesions developed (between 3–4 weeks old) or when the lesions were fully established (8–10 weeks old), to assess the effect of IL-18 on the progression and regression of established lesions, respectively. Administration of IL-18 prevented both progression (Fig. 1C) and enhanced regression (Fig. 1D) of spontaneous neovascular lesions in the eyes of JR5558 mice as determined by fundus fluorescein angiography (FFA) on day 5. It is notable that in mouse models, anti-VEGF therapeutic approaches are not capable of regressing established lesions and that such effects are only observed when anti-VEGF therapeutics are used in combination with other agents targeting other mechanisms such as PDGF.<sup>9</sup> Electroretinography measures photoreceptor rod and cone function. No changes in rod or cone function were observed in these mice post IL-18 treatment, as assessed by ERG (Figs. 1E, 1F), indicating no obvious deleterious effects as a consequence of IL-18 treatment. The observation that IL-18 treatment did not improve rod and cone function is consistent with the JR5558 phenotype of microvascular dysfunction and not retinal degeneration in the short term.

### IL-18 Reduces Expression Levels of VEGFR2

Previously we observed that IL-18 could inhibit the secretion of VEGF from both endothelial and RPE cells.<sup>4</sup> This appears to be regulated at a posttranscriptional level as IL-18 had no effect on VEGF-A mRNA expression (Fig. 2A) in retinal microvascular endothelial cells (RMVECs). To delve deeper into the effect of IL-18 on the VEGF signaling cascade, we measured mRNA levels of VEGF receptors on RMVECs (Figs. 2B–D). Interleukin 18 treatment inhibited VEGFR-2 expression specifically (Fig. 2C). Consequently, levels of basal and VEGF-induced VEGFR-2 protein decreased with IL-18 pretreatment in a time- and dose-dependent manner (Figs. 2E, 2F). Therefore, in conjunction with lowering levels of secreted VEGF,<sup>4,10</sup> the ability of IL-18 to lower VEGFR-2 expression in parallel indicates that IL-18 would effectively reduce VEGF signal transduction, and hence, the ability of endothelial cells to respond in a proangiogenic manner to any remaining VEGF.

### Mature IL-18 Is Safe and Reduces Development of Laser-Induced CNV in Cynomolgus Monkeys

Our data pertaining to a role for IL-18 in regulating neovascularization was supported by independent reports in the literature,<sup>10,11</sup> and strongly indicated that IL-18 could have some therapeutic benefit in neovascular AMD, in contrast to a report by Ambati et al.<sup>12</sup> Human IL-18 (SB-485232, GSK) is a clinically enabled investigational drug that has been injected systemically in  $>170$  cancer patients with an excellent safety profile, with numerous on-going studies.<sup>13,14</sup> We sought to examine the tolerability and efficacy of SB-485232 in a nonhuman primate model of neovascular AMD. Human IL-18 has been reported to have bioactivity in cynomolgus monkeys.<sup>15</sup> The laser-induced CNV model in nonhuman primates is a well-established robust model for screening therapeutic efficacy of drugs directed at neovascular AMD, albeit most of these studies have directly targeted the VEGF pathway.<sup>15</sup> Monkeys were injected intravitreally (IVT) with IL-18 (0.01, 0.2, 1, 2.5, and 10  $\mu$ g) post induction of laser lesions and FFA was performed on days 8, 15, and 22 (Fig. 3A). Following Bayesian analysis, the estimated probabilities for the existence of a dose-dependent, linear reduction in grade IV lesion counts (those which most likely resemble human neovascular AMD lesions) were 0.77, 0.97 and 0.9 for days 8, 15, and 22, respectively. In short, the data indicate that there is a 77%, 97%, and 90% probability that IL-18 is inducing a dose-dependent reduction in grade IV lesion counts when compared with vehicle control at days 8, 15, and 22 post laser. In Figure 3B, the horizontal red line in the plot depicts the estimated number of grade IV lesions in vehicle injected eyes and the prior historical controls for vehicle-treated eyes at the laboratory conducting these studies, and the horizontal green line depicts worst case scenario (one lesion as grade IV) observed in eyes injected with Lucentis (Fig. 3B). In contrast, the Bayesian assessment of whether the IL-18 data would be equivalent to the worst-case scenario of the Lucentis treatment indicated a low chance for IL-18 being similar to the worst case scenario for Lucentis with a 51%, 16%, and 17% chance for the 8, 15, and 22 days, respectively. Overall, the data demonstrate very clear IL-18 activity in reducing leakage from grade IV lesions, but this activity is not as pronounced as that of Lucentis. An interesting observation is the fact that the 10- $\mu$ g dose appeared to be less efficacious than the 1- and 2.5- $\mu$ g/eye doses. Interleukin 18 is approximately 95% homologous with the cynomolgus protein and, hence, is immunogenic in cynomolgus monkeys.<sup>16</sup> The apparent reduced efficacy of the 10- $\mu$ g dose when compared with lower doses may likely be due to this response which effectively neutralizes the bioactivity of IL-18. In addition, in flatmounts stained for F-actin, RPE cells appeared to

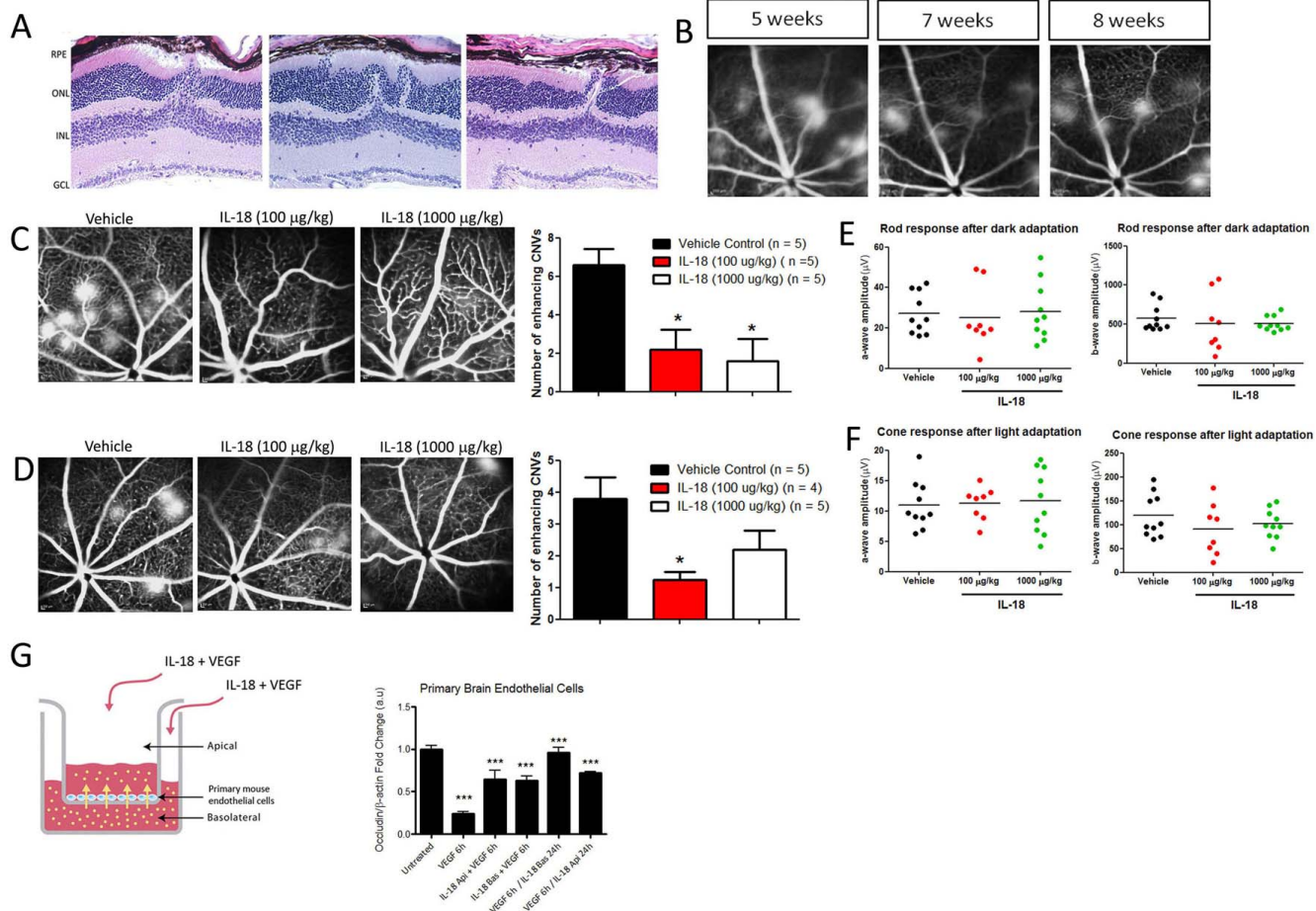


**FIGURE 1.** Interleukin 18 prevents spontaneous neovascular lesion development. (A) Representative histopathological analysis of JR5558 mouse retinas at 5 weeks old. (B) Progression of neovascular lesion development in single JR5558 mouse from 5 up to and including 8 weeks old. (C) Fundus fluorescein angiography in vehicle control, IL-18 (1000 µg/kg) or (100 µg/kg) injected 3- or (D) 8-week-old JR5558 mice ( $\times 4$  on consecutive days; FFA performed on day 5). Number of fluorescein enhancing lesions was significantly decreased in IL-18 injected mice (*right histogram*).  $^*P < 0.05$ , ANOVA ( $n = 5$  mice per group and data representative of four independent experiments). (E) Rod and (F) Cone photoreceptor electroretinography (ERG) a-wave (*left*) and b-wave (*right*) of JR5558 mice injected with IL-18 (100 µg/kg or 1000 µg/kg) for 4 consecutive days ( $n = 4/5$  mice per group). (G) Primary mouse brain microvascular endothelial cells were grown to confluence on the apical chamber of a 0.4-µm Transwell filter. Mouse IL-18 (50 ng/mL) and VEGF (50 ng/mL) were added to the apical and basolateral chambers. Levels of occludin transcript were measured post treatment of cells with VEGF for 6 hours post treatment of cells with IL-18 and VEGF together in the apical chamber, IL-18/VEGF in the basolateral chamber for 6 or 24 hours. Data representative of means  $\pm$  SEM, one-way ANOVA with Tukey posttest,  $P < 0.05$  representing significance and data representative of two independent experiments.  $^{***}P < 0.001$ .

maintain their honeycomb structure with no evidence of cellular dysmorphia observed at any dose or any time point post IVT injection of IL-18 (Fig. 4A). Furthermore, postmortem analysis of nonlasered ocular tissues 15 days post injection showed no toxic effect to either the retina or RPE, with no apoptotic (blebbing cells) or necrotic (swollen cells) phenotypes evident in any cell type at any dose (1, 3 or 10 µg IL-18; Figs. 4B–D). Additionally, histopathologic assessment of cynomolgus monkey retinal sections was carried out 15 days post IVT injection of IL-18 (1000, 3000, and 10,000 ng) and with no abnormal findings reported (Fig. 4E). Pharmacokinetic plasma analysis of IL-18 showed detectable and dose-proportional levels of IL-18 up to and including 7 days post IVT injection in all animals injected with the 10-µg dose of IL-18 (Supplementary Figs. S1, S2).

**DISCUSSION**

We live in an aging society, with the US population aged older than 65 years expected to double by 2050. Consistent with this

trend, the prevalence of age-related conditions is also increasing rapidly.<sup>17</sup> Age-related macular degeneration is already the most common cause of central retinal vision loss in those aged older than 50 years globally and this figure is predicted to increase by 50% by 2020.<sup>1</sup> In fact, estimates of the global cost of visual impairment due to AMD alone are \$343 billion (US), including \$255 billion in direct health care costs.<sup>16</sup> These statistics are stark and indicate the very substantial societal burden assumed by this condition, not only in relation to the negative impact on the quality of life of the affected individuals, but also the associated increased costs in health and home care. Current state-of-the-art “anti-VEGF” therapies can involve monthly intraocular injections, which are a significant burden for patients and caregivers, and it is clear that improvements in treatment duration is a key market driver. Furthermore, there is also a need to provide alternative treatment options to subjects not responding to anti-VEGF therapies.<sup>18</sup> Here we present data that indicates that mouse IL-18 inhibits vascular leakage in a mouse model of spontaneous neovascularization. We also present data indicating that human

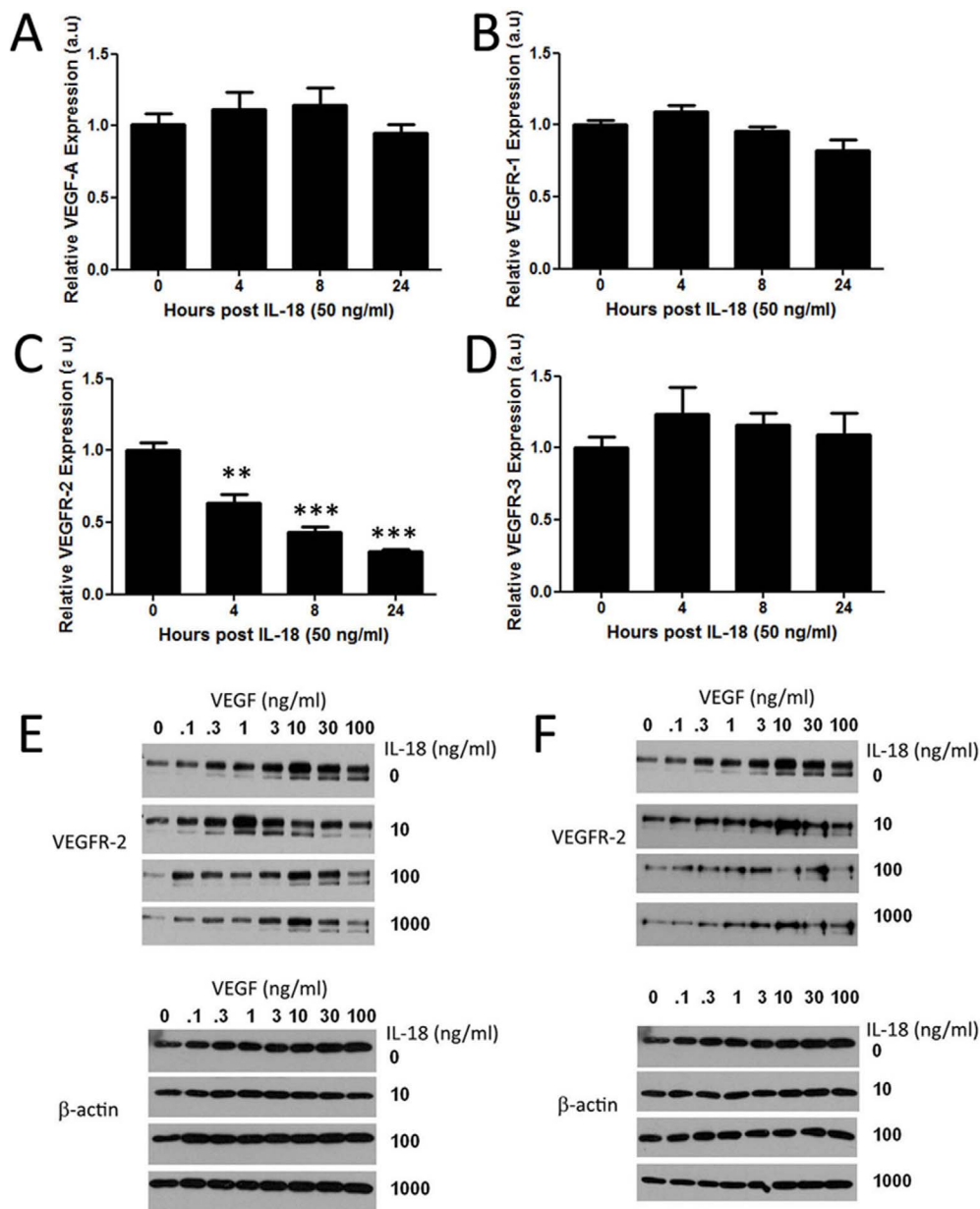


**FIGURE 2.** Interleukin 18 inhibits the expression of VEGFR2. (A) Vascular endothelial growth factor-A; (B) VEGFR-1; (C) VEGFR-2; (D) VEGFR-3 transcript levels in confluent RMVECs stimulated with IL-18 (50 ng/mL) for 0, 4, 8 and 24 hours, ( $n = 3$  biological replicates).  $**P < 0.01$ ,  $***P < 0.001$ , ANOVA. (E) Vascular endothelial growth factor-2 protein expression in confluent RMVECs stimulated with IL-18 for 6 hours prior to VEGF treatment or (F) 24 hours prior to VEGF treatment. These experiments were run alongside each other so the top blot (i.e., VEGF stimulation alone, in the absence of IL-18 treatment) is the matching control for each panel. They have been included as reference blots in each of the figure subsets.

recombinant IL-18 is safe and has disease modifying efficacy in the nonhuman primate eye, can reduce CNV development in this species compared with vehicle control, and may now have major therapeutic utility as an adjunctive immunotherapy in the first instance in the context of neovascular AMD.

**Limitations of Results and Interpretation**

The main limitation of this study has been the small numbers of animals used overall; however, given the nature of the study and the species used, we have had to refine the scope of the work, such that the minimum possible number of nonhuman primates required to show an efficacy response were used. In effect, in conjunction with GSK statisticians, a Bayesian approach was adopted for the design and implementation of

the adaptive efficacy study. While it is abundantly clear that IL-18 is not as efficacious when compared with Lucentis in preventing CNV development, it certainly has a significant modifying effect on CNV lesion development when compared with vehicle control-injected eyes. In this regard, it is interesting to note that effective combinatorial approaches currently in development such as anti-PDGF aptamers have absolutely no impact on any preclinical CNV model when used alone. The mechanism of action of IL-18 is vastly different to current proven strategies, yet alone, it can reduce grade IV CNV development, and if used as an adjunctive therapy clinically, could yield important improvements in clinical disease management. However, given the limitations in all animal models of AMD, the only way we will now be able to

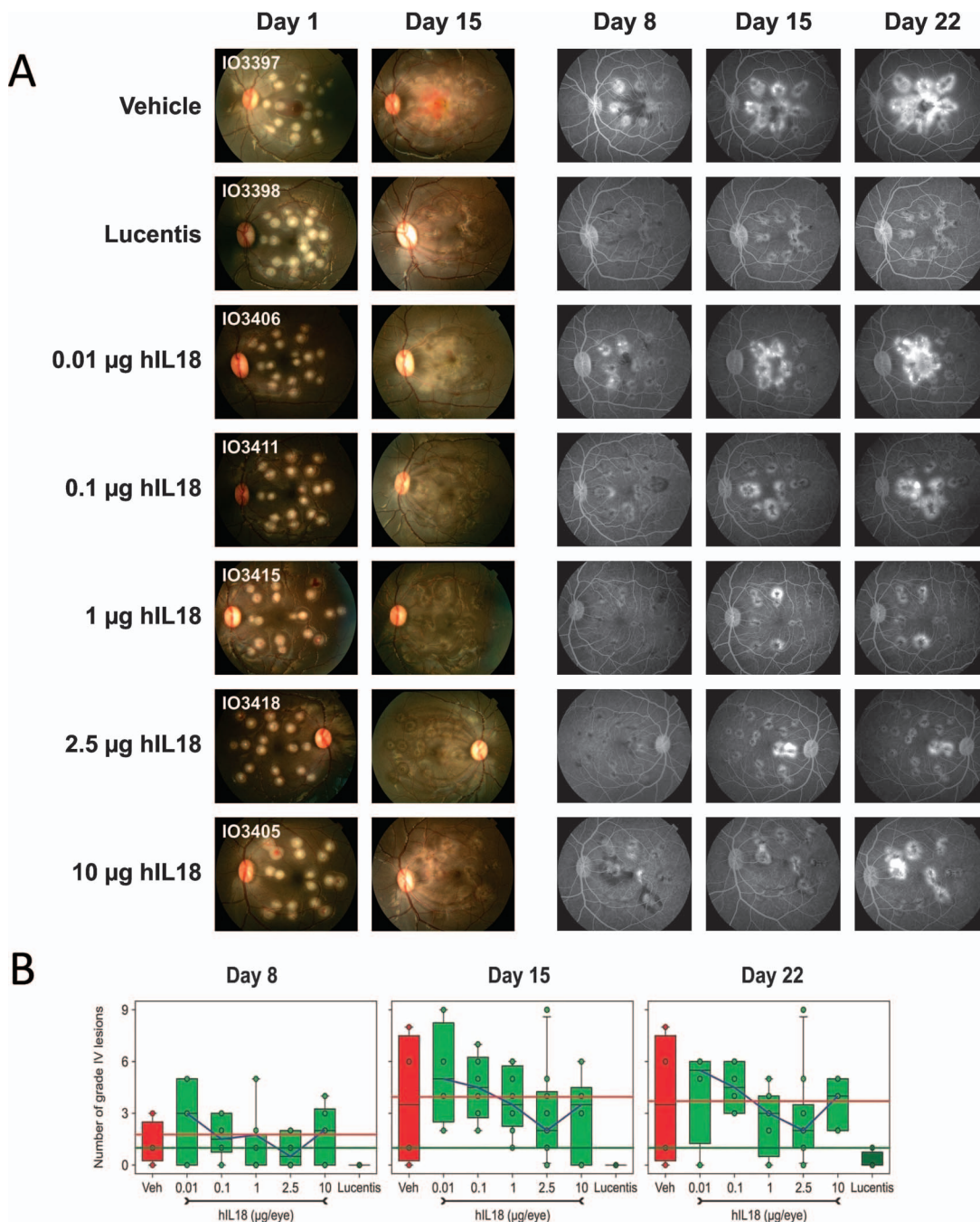


**FIGURE 3.** Mature IL-18 reduces development of laser induced choroidal neovascularization in cynomolgus monkeys. **(A)** Grade IV lesion development post IVT injection of IL-18. *Columns 1 and 2:* Fundus photographs of monkeys post IVT injection of IL-18 (10, 100, 1000, 2500, and 10,000 ng). *Columns 3–5:* Fundus fluorescein angiography post IVT injection of 10, 100, 1000, 2500, and 10,000 ng IL-18. **(B)** Bayesian analysis of grade IV lesion development post IVT injection of IL-18. Vehicle ( $n = 2$ ); 0.01 µg ( $n = 2$ ); 0.1 µg ( $n = 3$ ); 1 µg ( $n = 4$ ); 2.5 µg ( $n = 5$ ); 10 µg ( $n = 3$ ); Lucentis ( $n = 2$ ).

assess the clinical utility of IL-18 is through robust clinical studies.

**Steps That Need to Be Taken for the Findings to Be Applied in the Clinic**

As a small biotherapeutic agonist, IL-18 has the potential to eventually pave the way for a slow release encapsulated immunotherapeutic adjunctive strategy for neovascular AMD. The next step in the translational pipeline to clinic involves

enabling IL-18 for IVT injection in human subjects. Currently, this developmental drug is being used in numerous clinical trials as a systemic infusion for cancer patients and has an excellent safety profile; however, it has never been tested as an IVT injection for any ocular condition. We are now working toward obtaining a full good laboratory practice compliant nonhuman primate safety toxicology assessment of IL-18 post IVT injection based on our observations to date. In that regard, we envision clinical application of this developmental drug upon completion of these studies in the short term.



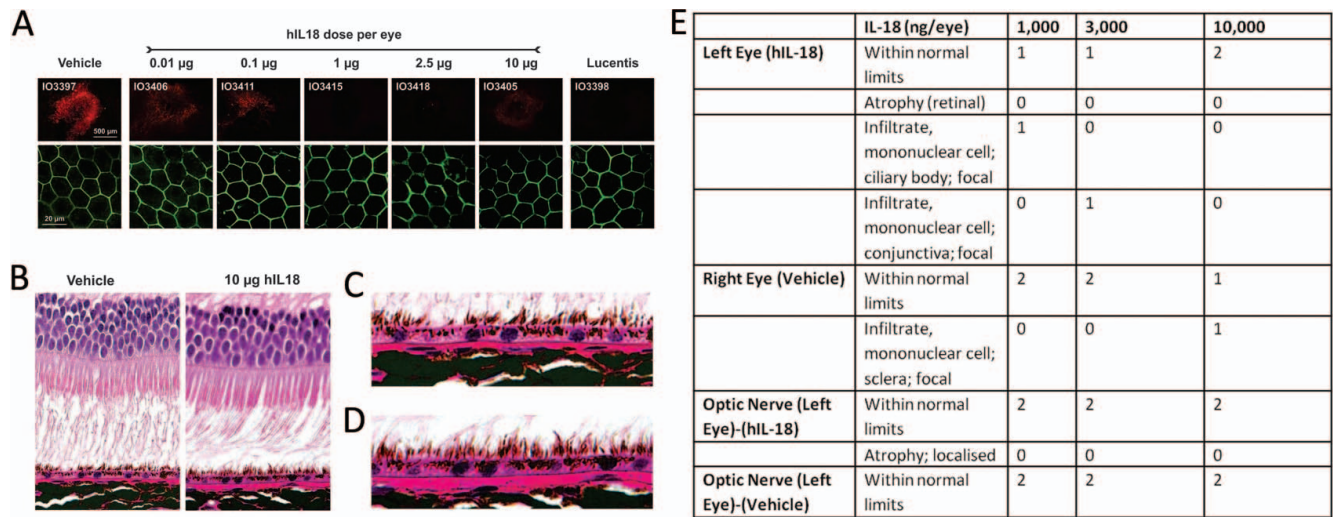


FIGURE 4. Mature IL-18 does not induce RPE cell death in cynomolgus monkeys. (A) Immunohistochemical analysis of flatmounts stained for isolectin (top row, red) or phalloidin (F-actin, bottom row, green) post IVT injection of vehicle control or IL-18 (10, 100, 1000, 2500, and 10,000 ng) or Lucentis. (B) Histopathological analysis of RPE and photoreceptor outer segments (OS) post intravitreal injection of vehicle control or IL-18 (10,000 ng), (C) vehicle control, and (D) IL-18 (10,000 ng) in high magnification. (E) Histopathological assessment of cynomolgus monkey retinal sections 15 days post IVT injection of IL-18 (1000, 3000, 10,000 ng human IL-18).

**Acknowledgments**

We thank Caroline Woods, Charles Murray, and David Flynn for animal husbandry. We also acknowledge Anran Wang and John Peterson for their help running the simulations for the Bayesian design of the primate study.

Supported by Enterprise Ireland, GSK, Science Foundation Ireland (12/YI/B2614) and BrightFocus Foundation. The Ocular Genetics Unit at TCD is supported by SFI, the Health Research Board of Ireland, Irish Research Council for Science Engineering and Technology, and the European Research Council.

Disclosure: **S.L. Doyle**, P; **F.J. López**, GlaxoSmithKline (F); **L. Celkova**, None; **K. Brennan**, None; **K. Mulfaul**, None; **E. Ozaki**, None; **P.F. Kenna**, GlaxoSmithKline (F); **E. Kurali**, None; **N. Hudson**, None; **T. Doggett**, None; **T.A. Ferguson**, None; **P. Humphries**, P; **P. Adamson**, GlaxoSmithKline (F); **M. Campbell**, GlaxoSmithKline (F), P

**References**

- Rein, DB, Wittenborn JS, Zhang X, et al. Forecasting age-related macular degeneration through the year 2050: the potential impact of new treatments. *Arch Ophthalmol.* 2009; 127:533-540.
- Rofagha, S, Bhisitkul, RB, Boyer, DS, Sadda, SR, Zhang, K. Seven-year outcomes in ranibizumab-treated patients in ANCHOR, MARINA, and HORIZON: a multicenter cohort study (SEVEN-UP). *Ophthalmology.* 2013;120:2292-2299.
- Patel S. Combination therapy for age-related macular degeneration. *Retina.* 2009;(suppl 6):S45-S48.
- Doyle, SL, Campbell, M, Ozaki, E, et al. NLRP3 plays a protective role during the development of age related macular degeneration through the induction of IL-18 by drusen components. *Nat Med.* 2012;18:791-798.
- Doyle, SL, Ozaki E, Brennan K, et al. IL-18 attenuates experimental choroidal neovascularization as a potential therapy for wet age-related macular degeneration. *Sci Transl Med.* 2014;6:230ra244.
- Poor SH, Qui Y, Fassbender ES, et al. Reliability of the mouse model of choroidal neovascularization induced by laser photocoagulation. *Invest Ophthalmol Vis Sci.* 2014;55:6525-5634.

- Nagai N, Lundh von Leithner P, Izumi-Nagai K, et al. Spontaneous CNV in a novel mutant mouse is associated with early VEGF-A-driven angiogenesis and late-stage focal edema, neural cell loss, and dysfunction. *Invest Ophthalmol Vis Sci.* 2014;55:3709-3719.
- Hasegawa E, Sweigard H, Husain D, et al. Characterization of a spontaneous retinal neovascular mouse model. *PLoS One.* 2014;9:e106507.
- Jo N, Mailhos C, Ju M, et al. Inhibition of platelet-derived growth factor B signaling enhances the efficacy of anti-vascular endothelial growth factor therapy in multiple models of ocular neovascularization. *Am J Pathol.* 2006;168:2036-2053.
- Shen J, Choy DF, Yoshida T, et al. Interleukin-18 has anti-permeability and antiangiogenic activities in the eye: reciprocal suppression with VEGF. *J Cell Physiol.* 2014;229: 974-983.
- Cao R, Farnebo J, Kurimoto M, Cao Y. Interleukin-18 acts as an angiogenesis and tumor suppressor. *FASEB J.* 1999;13:2195-2202.
- Hirano Y, Yasuma T, Mizutani T, et al. IL-18 is not therapeutic for neovascular age-related macular degeneration. *Nat Med.* 2014;20:1372-1375.
- Srivastava S, Salim N, Robertson MJ. Interleukin-18: biology and role in the immunotherapy of cancer. *Curr Med Chem.* 2010;17:3353-3357.
- Herzyk DJ, Bugelski PJ, Hart TK, Wier PJ. Preclinical safety of recombinant human interleukin-18. *Toxicol Pathol.* 2003;31: 554-561.
- Nork TM, Dubielzig RR, Christian BJ, et al. Prevention of experimental choroidal neovascularization and resolution of active lesions by VEGF trap in nonhuman primates. *Arch Ophthalmol.* 2011;129:1042-1052.
- Access Economics. *The Global Economic Cost of Visual Impairment.* New York: AMD Alliance International; 2010.
- Vincent GK, Velkoff VA. *The Next Four Decades, The Older Population in the United States: 2010 to 2050, Population Estimates and Projections.* Washington, DC: US Census Bureau; 2010.
- Kudelka, MR, Grossniklaus, HE Mandell, KJ. Emergence of dual VEGF and PDGF antagonists in the treatment of exudative age-related macular degeneration. *Expert Rev Ophthalmol.* 2013; 8:475-484.